

**Winter College on Optics and Photonics**  
**7 - 25 February 2000**

**1218-22**

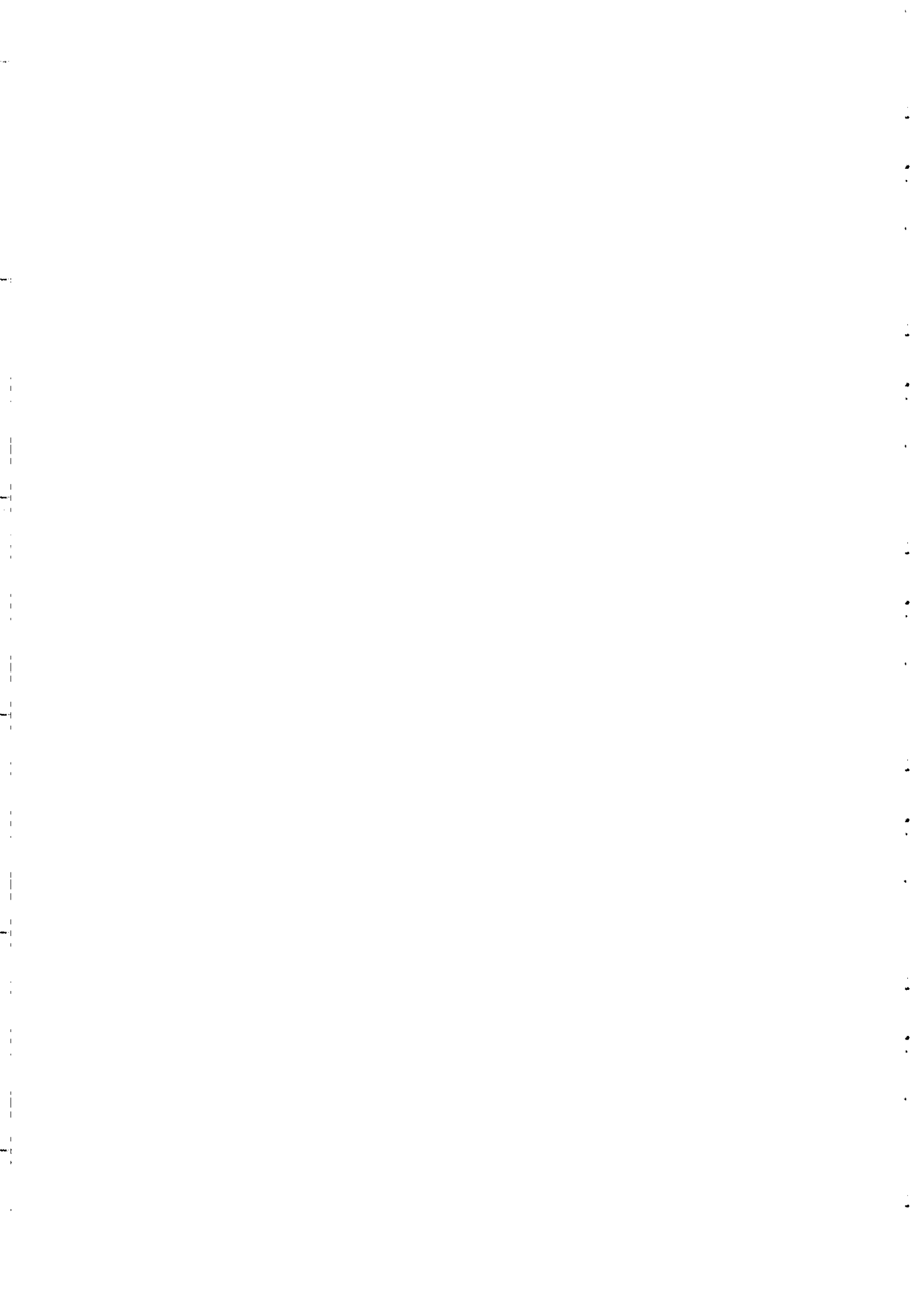
---

"Fundamentals of Photonic Bloch Waves"  
"Photonic Crystal Fibers & Devices"  
"Band Edge Effects & Related Devices"

**P. St. J. RUSSELL**  
**Department of Physics**  
**University of Bath**  
**United Kingdom**

---

***Please note: These are preliminary notes intended for internal distribution only.***

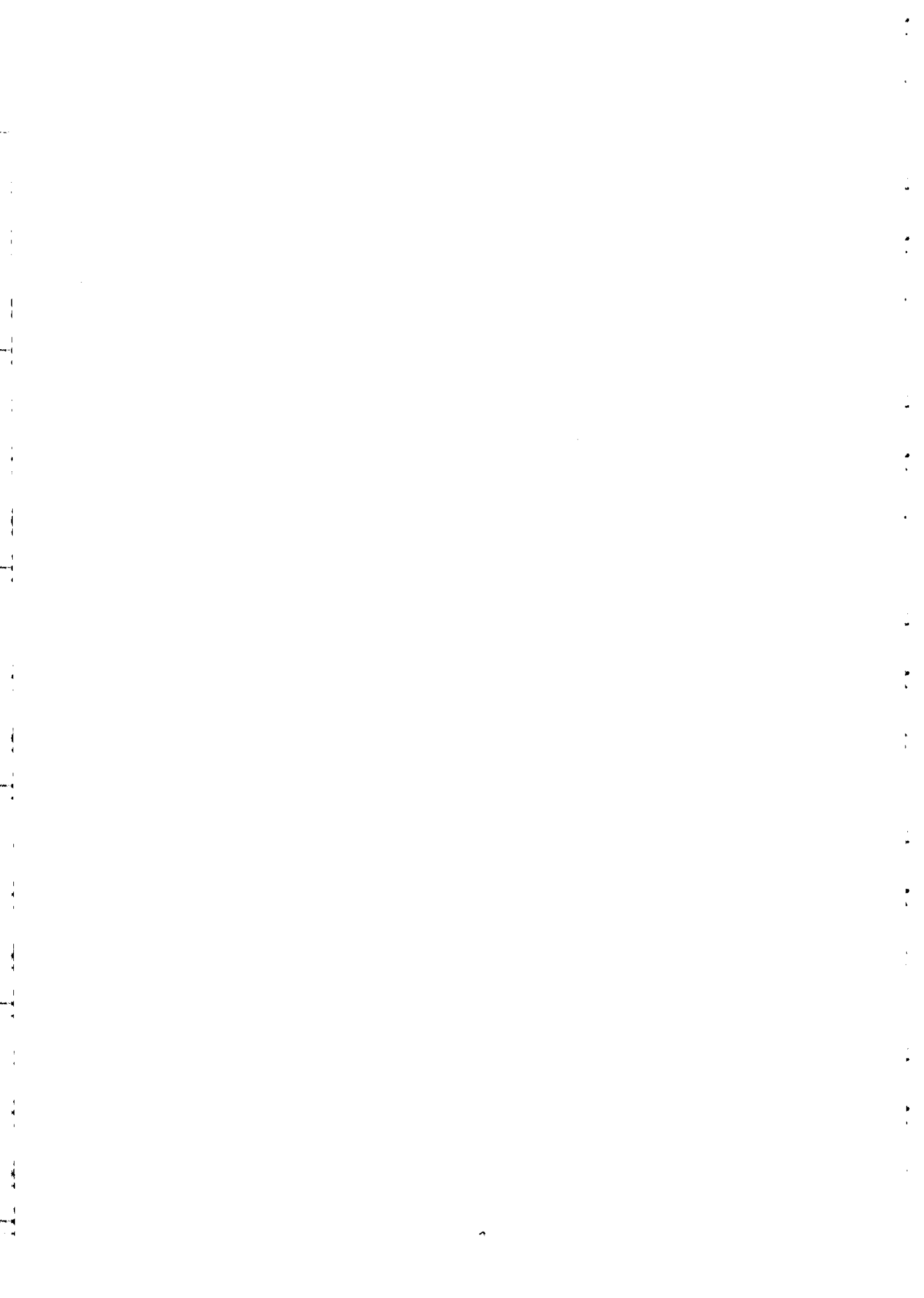


FUNDAMENTALS OF PHOTONIC BLOCH WAVES  
PHOTONIC CRYSTAL FIBERS AND DEVICES  
BAND EDGE EFFECTS AND RELATED DEVICES

P.St.J. Russell

Department of Physics, University of Bath, Bath BA2 7AY, United Kingdom  
Tel +44 1225 826946, Fax +44 1225 826110, Email pypsjr@bath.ac.uk

- P0. P.St.J. Russell, T.A. Birks and F.D. Lloyd-Lucas, "Photonic Bloch Waves and Photonic Band Gaps," in *Confined Electrons and Photons: New Physics and Applications*, E. Burstein & C. Weisbuch (editors), pp 585-633, Plenum Press, 1995
- P1. J.C. Knight, T.A. Birks, P.St.J. Russell and D.M. Atkin, "All-silica single-mode fiber with photonic crystal cladding," *Opt. Lett.* **21** (1547-1549) 1996; Errata, *Opt.Lett.* **22** (484-485) 1997
- P2. T.A. Birks, J.C. Knight and P.St.J. Russell, "Endlessly single-mode photonic crystal fibre," *Optics Letters*, **22** (961-963) 1997
- P3. J.C. Knight, T.A. Birks, R.F. Cregan, P.St.J. Russell and J.-P. de Sandro, "Large mode area photonic crystal fibre," *Electron. Lett.* **34** (1347-1348) 1998
- P4. P.St.J. Russell, T.A. Birks, J.C. Knight, R.F. Cregan and J.-P. De Sandro, "Silica/air photonic crystal fibres," *Jap. J. Appl. Phys.* **37** Suppl. 37-1, (45-48) 1998
- P5. J.C. Knight, T.A. Birks, R.F. Cregan, P.St.J. Russell and J.-P. De Sandro, "Photonic crystals as optical fibres – physics and applications," *Optical Materials* **11** (143-151) 1998
- P6. P.St.J. Russell, J.C. Knight, B.J. Mangan, R.F. Cregan and T.A. Birks, "Microscopic glass fibre crystals: the world's longest holes," *New Frontiers Exhibition 1998*, Royal Society, London
- P7. D. Mogilevtsev, T.A. Birks and P.St.J. Russell, "Group-velocity dispersion in photonic crystal fibres," *Opt. Lett.* **23** (1662-1664) 1998
- P8. D. Mogilevtsev, T.A. Birks and P.St.J. Russell, "Localised function method for modelling defect modes in 2-D photonic crystals," *IEEE JLT special issue on EM crystal structures, synthesis and applications*, **17** (2078-2081) 1999
- P9. *Don't Make Waves, Control 'Em* by Charles T. Whipple, *Photonic Spectra*, March 1999, pp110-116
- P10. *A New Way to Guide Light in Optical Fibers* by Barbara Goss Levi, *Physics Today*, December 1999, (21-23)
- P11. *Holey Light* by Philip Ball, *New Scientist*, June 12 1999, pp 36-39
- P12. J.C. Knight, J. Broeng, T.A. Birks and P.St.J. Russell, "Photonic band gap guidance in optical fibers," *Science* **282** (1476-1478) 1998
- P13. R.F. Cregan, B.J. Mangan, J.C. Knight, T.A. Birks, P.St.J. Russell, P.J. Roberts and D.C. Allan, "Single-mode photonic band gap guidance of light in air," *Science* **285** (1537-1539) 1999
- P14. P.St.J. Russell and T.A. Birks, "Bloch wave optics in photonic crystals: Physics and applications," in *Photonic Band Gap Materials* (Editor: C.M. Soukoulis) Kluwer 1996, pp 71-91
- P15. D.M. Atkin, P.St.J. Russell, T.A. Birks & P.J. Roberts, "Photonic band structure of guided Bloch modes in high index films fully etched through with periodic microstructure," *J.Mod.Opt.* **43** (1035-1053) 1996
- P16. P.St.J. Russell, D.M. Atkin and T.A. Birks, "Bound modes of photonic crystal waveguides," in *Microcavities and Photonic Bandgaps: Physics and Applications* (Eds: J.G. Rarity & C. Weisbuch), Kluwer 1996, pp 203-218
- P17. P.St.J. Russell, S. Tredwell and P.J. Roberts, "Full photonic bandgaps and spontaneous emission control in 1-D multilayer dielectric structures," *Opt. Commun.* **160** (66-71) 1999
- P18. W.F. Liu, P.St.J. Russell and L. Dong, "Acousto-optic superlattice modulator using fibre Bragg grating," *Opt. Lett.* **22** (1515-1517) 1997
- P19. P.St.J. Russell and T.A. Birks, "Hamiltonian optics in non-uniform photonic crystals," *IEEE JLT special issue on EM crystal structures, synthesis and applications*, **17** (1982-1988) 1999



## PHOTONIC BLOCH WAVES AND PHOTONIC BAND GAPS

Philip St.J. Russell, Timothy A. Birks and F. Dominic Lloyd-Lucas

Optoelectronics Research Centre,  
University of Southampton,  
Hants SO9 5NH, United Kingdom

### 1. INTRODUCTION

Photonic band gap materials are dielectrics with a synthetic, three dimensional, multiply periodic microstructure (lattice constant of order the optical wavelength) whose distinguishing feature is a very large modulation depth of refractive index. When appropriately designed, these "photonic crystals" exhibit ranges of optical frequency where light cannot exist - the photonic band gaps<sup>7</sup>. The current interest in these materials<sup>1-22</sup> has led us to re-appraise propagation in structures that, while not exhibiting a *complete* photonic band gap (PBG), nevertheless display anomalous and intriguing propagation effects in the vicinity of their Bragg conditions<sup>54-58</sup>. In most cases, around each Bragg condition appear incomplete momentum and energy gaps (i.e., ranges of, respectively, wavevector and frequency where propagation is forbidden) with widths that are given approximately by the product of the index difference with, respectively, the vacuum wavevector and  $h$  times the optical frequency. With the exception of the multi-layer dielectric stack, most conventional electromagnetic gratings, such as those encountered in holography<sup>27</sup>, waveguides<sup>45</sup>, distributed feedback lasers<sup>35,37,38</sup>, acousto-optic<sup>47</sup> and x-ray<sup>61</sup> diffraction, consist of weak periodic perturbations about a mean refractive index. In these gratings, while strong spatial and temporal dispersion are present around each Bragg condition, the ranges of angles and frequencies over which this occurs are very narrow; and although PBG's do appear, they are incomplete and mostly very weak.

It was in this context that Yablonovitch posed the question: By analogy with electronic band gaps, would a full photonic band gap appear in a multiply periodic three-dimensional structure if the refractive index were very strongly modulated? As we now know<sup>7</sup>, state-of-the-art optics was unable to answer the question immediately, because although large modulation depths were well known and accepted in the solid state physics of electrons, where the lattice potential is often both very deeply modulated and highly non-sinusoidal<sup>23</sup>, they were encountered in optics only in the form of *singly* periodic multi-layer stacks. Commonly-used and well-understood perturbation approaches<sup>27</sup>, in which the field in a singly periodic structure is Fourier decomposed into a finite set of plane waves coupled together by the lattice, were not immediately applicable to the full vector case of multiply periodic three-dimensional structures. The high modulation depth of index in PBG structures also means that even the concept of average index is of limited usefulness; as we shall see, this is because the expectation value of the refractive index can deviate

hugely from its mean value via re-distribution of the photon probability function (or optical intensity) into regions of higher or lower dielectric constant<sup>5</sup>. Indeed, this redistribution, which depends on  $\omega$ , lies behind all the complex and curious types of behaviour encountered in photonic band gap materials.

The field of photonic band structure is a hybrid, drawing on the resources of two major disciplines: optics and electronic band theory. Electronic band theory is rich in concepts<sup>23-25</sup> (such as density of states and effective mass) not widely used in optics, where the emphasis is more on wave propagation<sup>43-50</sup>. On the other hand, conventional optics provides a range of ideas (such as rays, diffraction, refraction and interference) that are essential if photonic band gap materials are to be used in real systems, where propagation in the vicinity of the band gap must be well understood. For example, the effective mass method<sup>23,25</sup> turns out to be useful for treating the propagation of Bloch rays in photonic band gap structures with slowly-varying non-uniformities, whereas generalised versions of refraction and dispersion<sup>57</sup> are needed to treat wave behaviour at sharp interfaces between different periodic media.

The theme of this chapter is thus the development of an approach to propagation in periodic optical media that uses Bloch waves instead of plane waves; and the goal is to provide the basis for a full "quantum photo-dynamical" (QPD) description of light in PBG structures, where the density of photonic states is controlled by the presence of a dielectric "crystal" lattice.

The simplicity of the multi-layer dielectric stack, and the availability of exact analytical solutions for the Bloch waves it supports<sup>28,29</sup>, make it an ideal vehicle for illustrating the physics of photonic band gaps. A major aim of this chapter is to reinterpret the behaviour of the multi-layer stack within the framework of photonic band structure, making use of versatile intuitive graphical tools such as wavevector ( $k-k$ ), Brillouin ( $\omega-k$ ) and band-edge diagrams. The physical origins of energy and momentum band gaps are discussed, together with concepts like effective mass, group and phase velocity, and density of states of "valence" and "conduction" photons. The link between photonic Bloch waves and traditional plane wave optics is also explored, the effects of optical nonlinearities and gain briefly touched upon, and a number of unusual structures and devices described.

*Note that there is a list of mathematical symbols in Appendix A1.*

## 1.1 List of Chapter Headings

1. Introduction
  - 1.1 List of chapter headings
  - 1.2 Essential background material
    - 1.2.1 Three regimes of behaviour
    - 1.2.2 Hard and soft reflections
    - 1.2.3 Brewster's angle
    - 1.2.4 Two parallel interfaces
    - 1.2.5 Anti-reflection condition
    - 1.2.6 Micro-cavity resonators in two and three dimensions
2. Photons and Electrons
  - 2.1 Wave equation for electrons and photons
  - 2.2 Effective mass of electrons and photons in uniform isotropic media
3. Analysis of Singly Periodic Structures
  - 3.1 Translation matrix formalism
  - 3.2 Normalised parameters
4. Singly Periodic Structures at Normal Incidence ( $\beta = 0$ )
  - 4.1 Brillouin diagrams
  - 4.2 Group velocity and density of states
  - 4.3 Expectation values of potential: Electrons and photons
  - 4.4 Origins of band gaps

5. The Wavevector Diagram
  6. Singly Periodic Structures at Oblique Incidence ( $\beta > 0$ )
    - 6.1 Band-edge diagrams
    - 6.2 Photonic band gaps and windows
    - 6.3 Points of zero band gap width
    - 6.4 Brillouin diagrams for finite  $\beta$
  7. Two-Dimensional Propagation
    - 7.1 Effective mass method for non-uniform periodic structures
    - 7.2 Illustrations from experiments on planar waveguides
  8. Extensions to Multiply Periodic Structures
  9. Miscellaneous Topics
    - 9.1 Localised modes, defects and surface-guided states
    - 9.2 Effects of optical gain: Lasers
    - 9.3 Effects of optical nonlinearity: Gap solitons
    - 9.4 Applications of photonic band gap materials
  10. In Conclusion
  11. Acknowledgements
  12. References and Reading Guide
- Appendices
- A1. Main Mathematical Symbols and Their Meanings
  - A2. Translation Matrix Elements
  - A3. Bessel Function Solutions
    - A3.1 Nearly-free photons: Green's function solution
    - A3.2 Tight binding

## 1.2 Essential Background Material

A range of elementary results can be derived by considering the reflection and refraction of a plane wave incident on the interface between two isotropic dielectric media<sup>43,44</sup>. Since a good intuitive understanding of the physics of this phenomenon is vital in the ensuing treatment of photonic band structure, it will now be briefly discussed; for a more detailed account, the reader is referred to any standard optics textbook such as Born and Wolf<sup>44</sup>. The electric field of a linearly polarised electromagnetic wave in medium  $j$  may be written in the form:

$$\mathbf{E}_j = \mathbf{E}_{j0} \exp[-j(\beta z \pm p_j y) + j\omega t] \quad (1)$$

where

$$p_j = \sqrt{k^2 n_j^2 - \beta^2} \quad (2)$$

is the wavevector component - normal to the interface - of the field within each medium,  $k = \omega/c$  is the vacuum wavevector at optical frequency  $\omega/2\pi$ ,  $n_j$  the refractive index and  $\beta$  the wavevector along the interface, whose normal points in the  $y$  direction. Convention defines a *transverse electric* (TE, or  $s$ -polarised) wave as one whose electric field is parallel to the interface, and a *transverse magnetic* (TM, or  $p$ -polarised) wave as one whose electric field points in the  $(y,z)$  plane. Equation (2) is a consequence of the requirement that the wavevector must have a magnitude equal to  $kn_j$ ; this gives rise to the very useful *wavevector diagram*, which is the locus of allowed wavevectors at fixed optical frequency. For isotropic media, it is a circle of radius  $kn_j$ , and for two different media, two concentric circles appear (see Figure 1;  $n_1 > n_2$  is assumed throughout this chapter). In any collision of a plane wave with a plane parallel interface, the momentum along the interface is conserved; this is another way of saying that the effective wavelength along the interface of all the participating waves must be identical, i.e., that they must be phase-matched. A line drawn normal to the interface, displaced from the origin by  $\beta$ , intersects

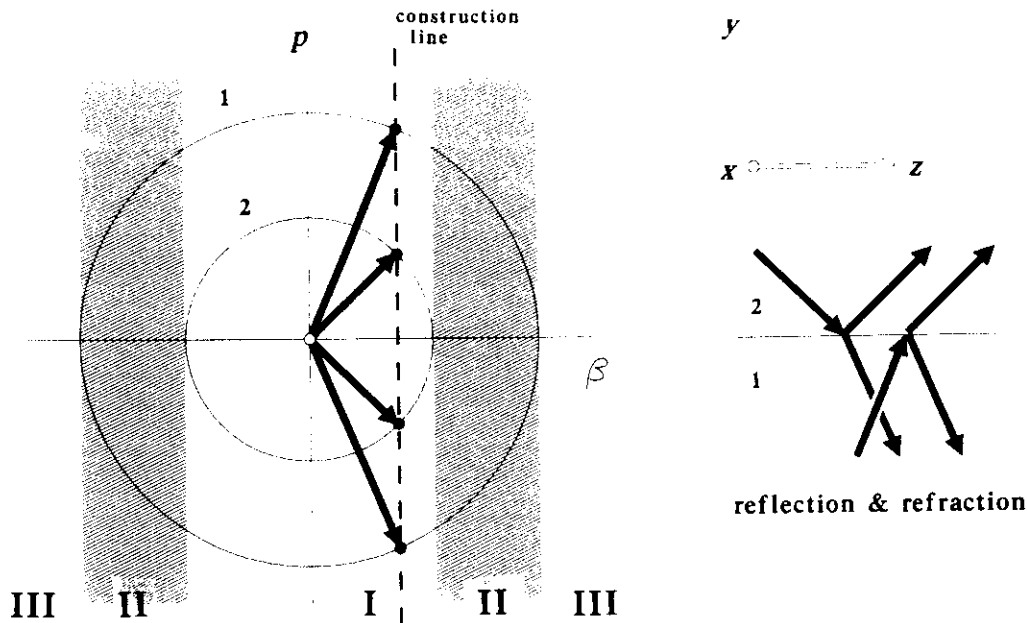


**Figure 1.** Interface between two media of refractive indices  $n_1 > n_2$ , together with the related wavevector diagram. Three regions (I, II and III) exist, corresponding to reflection/refraction, total internal reflection, and cut-off. A simple construction yields all the real-valued wavevectors that may exist at fixed wavevector  $\beta$  along the interface (illustrated for region I). The ray directions of the plane waves in real space are sketched on the right hand side.

the circles at a number of points, giving the complete set of wavevectors satisfying this interface condition.

**1.2.1 Three regimes of behaviour.** Note that three distinct regions of behaviour exist. In the first (region I:  $0 < \beta < kn_2$ ) both refraction and reflection occur: light propagates in both media. In the second (region II:  $kn_2 < \beta < kn_1$ ), total internal reflection occurs: light propagates only in the high index medium. In the third (region III:  $kn_1 < \beta$ ) the light is evanescent in both media: it is cut-off from propagation. On the boundary between regions I and II the angle between the wavevector on the high index circle and the vertical axis is the *critical angle*.

**1.2.2 Hard and soft reflections.** A very important physical quantity is the phase change upon reflection. For incidence from the low index side (medium 2), a phase retardation of  $\pi$  occurs throughout region I (in regions II and III the light is cut-off); the associated reflection is sometimes described as *hard*. For incidence from the high index side (medium 1), the phase change is zero in region I, and varies smoothly from zero to a retardation of  $\pi$  across region II; in region I the reflection is sometimes described as *soft*.

**1.2.3 Brewster's angle.** The magnitude of the reflection can go to zero in the case of TM polarisation; this occurs in region I at Brewster's angle, when the refracted and reflected wavevectors are at right angles. Under these circumstances, the electric dipoles of the refracted and reflected waves are orthogonal, resulting in zero reflected power. It is easy to show (see Figure 2) that the Brewster condition is satisfied when:



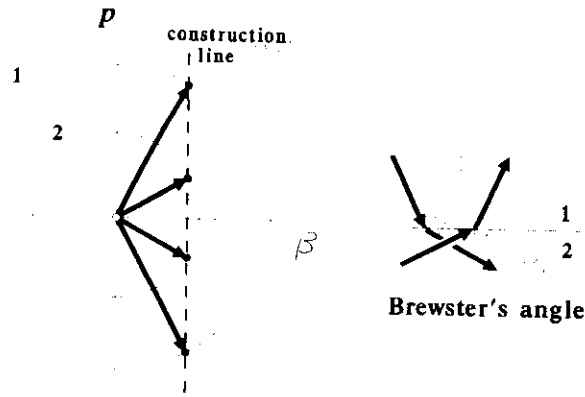


**Figure 2.** In region I, when the reflected and refracted rays are orthogonal, the dipoles excited by the refracted wave are unable to radiate into a reflected wave, resulting in zero reflection. This occurs at Brewster's angle.

$$\beta = \frac{kn_1n_2}{\sqrt{n_1^2+n_2^2}}; \quad (3)$$

this condition applies irrespective of whether the light is incident from the low or the high index medium. No Brewster phenomenon occurs in regions II and III. Note that as the index difference tends to zero, the Brewster angle occurs at close to  $45^\circ$  as should be expected.

**1.2.4 Two parallel interfaces.** When a second parallel interface is introduced, a number of new phenomena occur, the most important for our purposes being a) guided modes, b) anti-reflections and c) tunnelling across low index layers. Guided modes can form in region II for a high index layer bounded by low index media (Figure 3a). They occur when the round-trip phase change across the layer, including the phase retardation upon total internal reflection at the interfaces, equals a multiple of  $2\pi$ . They may be viewed as isolated micro-resonances of the layer, and in this respect bear some resemblance to electrons trapped in atomic orbitals. Their dispersion relation takes the form (an excellent derivation is available in Kogelnik's chapter in reference 45):

$$p_1 h_1 - 2 \arctan \left[ \frac{\xi_2 \sqrt{-p_2^2}}{\xi_1 p_1} \right] = m\pi \quad (4)$$

where  $h_1$  is the layer thickness,  $m$  the mode order and the  $\xi_j$  contain the polarization dependence:

$$\xi_j = 1 \text{ (TE) or } 1/n_j^2 \text{ (TM)}. \quad (5)$$

Retaining these factors allows both the TE and TM cases to be covered in a single analysis.

Note that, unlike in the electron case, light cannot be trapped at  $\beta=0$  in a high index layer since total internal reflection is impossible in dielectrics at normal incidence. Tunnelling through a thin low index layer sandwiched between two high index media can occur in region II (Figure 3b); this is important if two or more identical high index layers are brought in close proximity. Resonant tunnelling of light between waveguide micro-resonances can then occur, as will be discussed in more detail in section 6.

**1.2.5 Anti-reflection condition.** A single layer will exhibit zero reflection when the round-trip phase change in region I is an odd multiple of  $\pi$ , i.e., when the waves reflected from each interface interfere destructively; since the optical round-trip across any

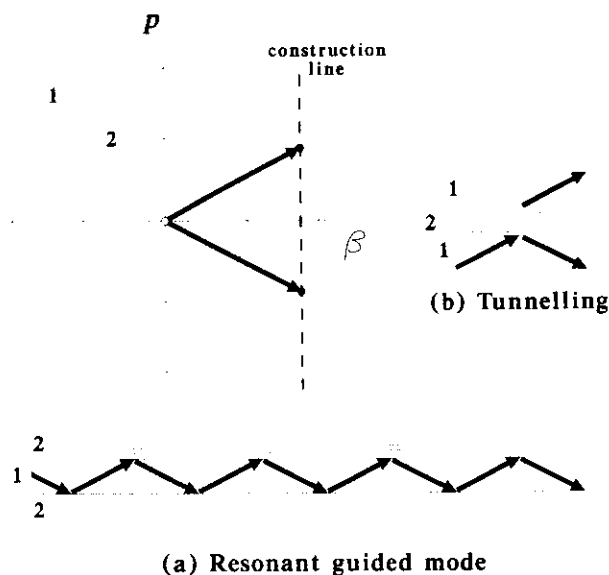


**Figure 3.** In region II: (a) a single layer of high index, sandwiched between two media of lower index, will support guided modes in its "potential well" for discrete values of  $\beta$ ; (b) on the other hand, if the indices are the opposite way around, tunnelling of photons through the low index "potential barrier" is possible.

layer (of high or low index) always contains one hard and one soft reflection, the anti-reflection condition is<sup>44</sup>:

$$2p_i h_i - \pi = (2m-1)\pi \Rightarrow p_i h_i = m\pi \quad (6)$$

which shows that, at normal incidence, the layer must be a multiple of half a wavelength thick. In the same way it may be shown that layers whose round-trip phase change is an even multiple of  $\pi$  reflect strongly.

**1.2.6 Micro-cavity resonators in two and three dimensions.** A single island of high index material imbedded in a low index background (Figure 4a) will support a large

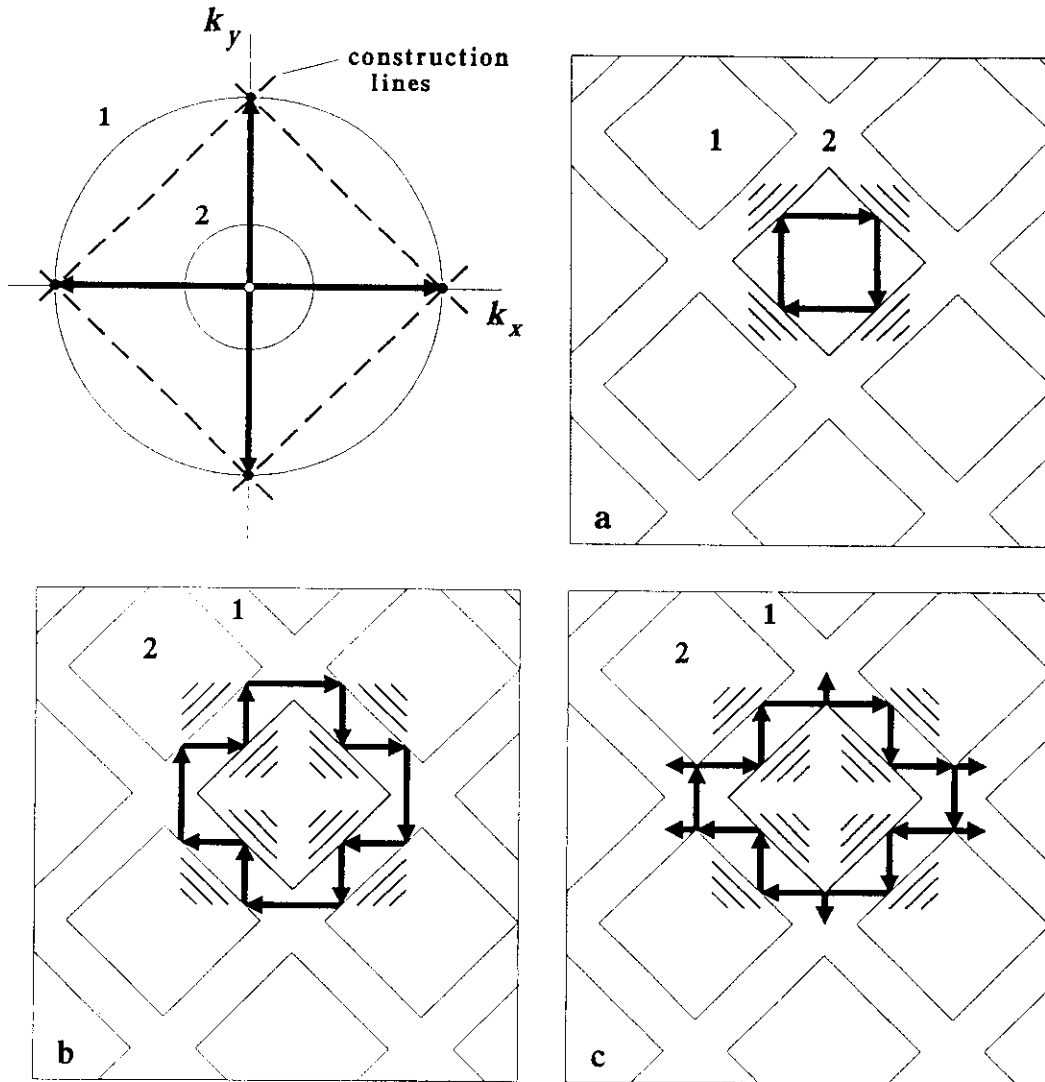


**Figure 4.** Cubic arrays of square unit cells (GaAs/air, critical angle  $16.6^\circ$ ), together with their wavevector diagram for horizontal and vertical rays. *High index islands* (a): Certain closed ray paths (of which one is illustrated) can be found for which the round-trip phase change is a multiple of  $2\pi$ ; these represent leaky isolated resonances (see text). An array of identical micro-resonators will be able to "talk" to one another through their evanescent external fields, creating the conditions for resonant tunnelling. *Low index islands* (b)&(c): If the high and low index regions are reversed, bound ray paths are much more difficult to find (particularly for rays at arbitrary angles to the horizontal), and any resulting micro-resonances will have very low Q factors.

number of bound rays, i.e., rays which are trapped by total internal reflection (TIR). If closed paths can be found for which (at a given frequency) the round-trip phase change is a multiple of  $2\pi$ , then localised resonances will appear. The Q-factor of these resonances will depend on the rate of leakage of energy into the low index surrounding medium. This in turn is governed by the width of the angular plane wave spectrum of the beamlet surrounding the trapped ray. For a very small resonator, this is large, and a significant number of plane waves will approach the boundaries *outside* the range of TIR. A square resonator of GaAs surrounded by air is depicted in Figure 4a, together with its wavevector diagram. The larger the index contrast, the smaller the inner circle, and the larger the number of rays within the high index material that are confined (in other words, the wider the range of total internal reflection). A perfectly confining resonator would be one for which there is no inner circle, resulting in a TIR range of  $360^\circ$ . This occurs when the

resonator is surrounded by a perfect metal (dielectric constant negative).

The impossibility of realising perfect resonators using dielectrics means that the conditions for resonant tunnelling, across a periodic array of identical high index islands, are only ever approximately attained. Even so, under the correct excitation conditions (frequency and wavevector), the light will tend to be pulled into the high index regions, resulting in a local narrowing of the band gap and a radical shifting of its mean position (caused by a sudden change in perceived refractive index). The higher the index contrast, the more dramatic is this effect. It is therefore desirable, for attainment of a good band gap, to avoid the appearance of micro-resonances as far as possible - one does not wish to prevent the natural tendency of the light to redistribute itself into high and low index regions on (respectively) the low and high frequency sides of the band gap (see section 4.4). As Yablonovitch has demonstrated, micro-resonances may be avoided by building structures in which low index islands are imbedded in a high index medium (Figure 4b&c). This results in a high degree of interconnection between the high index regions, effectively reducing the probability of finding strong micro-resonances - and even if they do exist, they will have very low Q factors owing to the high probability of finding unbound rays.

## 2. PHOTONS AND ELECTRONS

In this section, comparisons between electrons and photons are drawn in a number of contexts relevant to the chapter's aims, with special reference to the wave equation and the concept of effective mass in uniform isotropic media.

### 2.1 Wave Equation for Electrons and Photons

Schrödinger's equation, in time-independent form, for electrons of total energy  $H_e$  in an arbitrary potential  $U$  is:

$$\left[ -\frac{\hbar^2}{2m_e} \nabla^2 + U(\mathbf{r}) \right] \psi = H_e \psi \quad (7)$$

where  $m_e$  is the electron rest mass. In the absence of free charges in non-magnetic materials, Maxwell's equations (SI units) take the form<sup>26</sup>:

$$\begin{aligned} \nabla \times \mathbf{E} &= -\mu_o \frac{\partial \mathbf{H}}{\partial t} \\ \nabla \times \mathbf{H} &= \epsilon_o \epsilon_r \frac{\partial \mathbf{E}}{\partial t} \end{aligned} \quad (8)$$

$$\nabla \cdot (\epsilon_o \epsilon_r \mathbf{E}) = 0, \quad \nabla \cdot (\mu_o \mathbf{H}) = 0$$

where the electric and magnetic fields are  $\mathbf{E}$  and  $\mathbf{H}$ , the free space magnetic permeability and dielectric susceptibility  $\mu_o$  and  $\epsilon_o$  and the relative dielectric constant is  $\epsilon_r$ . Noting from (1) that  $\partial/\partial t \equiv j\omega$ , the following time-independent wave equation for the electric field  $\mathbf{E}$  is obtained after some straightforward manipulation:

$$\left[ -\nabla^2 - k^2 \{ \epsilon_r(\mathbf{r}) - 1 \} \right] \mathbf{E} - \nabla \left[ \{ \nabla \ln \epsilon_r(\mathbf{r}) \} \cdot \mathbf{E} \right] = k^2 \mathbf{E}. \quad (9)$$

The terms in (9) may be regrouped in a number of equivalent ways; we have chosen to separate out the dielectric susceptibility ( $\epsilon_r - 1$ ) and interpret it as being related to potential

energy. A dimensionally accurate comparison may be obtained by using the arbitrarily defined mass:

$$m_o = \hbar\omega/2c^2 \quad (10)$$

which yields:

$$\left[ -\frac{\hbar^2}{2m_o} \nabla^2 + U_o(\mathbf{r}) \right] \mathbf{E} - \frac{\hbar^2}{2m_o} \nabla \left[ \{\nabla \ln \epsilon_r(\mathbf{r})\} \cdot \mathbf{E} \right] = H_o \mathbf{E} \quad (11)$$

where

$$U_o(\mathbf{r}) = -\hbar\omega[\epsilon_r(\mathbf{r})-1], \quad H_o = \hbar\omega \quad (12)$$

are the potential and total energy terms respectively; the subscript "o" means optical. The definition of "potential energy" yields  $U_o=0$  in vacuum, which seems reasonable; note also that  $U_o$  is negative in a dielectric material. This implies that, unlike electrons which are free only if  $H_e$  exceeds  $U$ , photons are free in a dielectric at *all* energies since both  $U_o$  and  $H_o$  scale with optical frequency. Photons can of course be trapped (also at all energies) in a cavity filled with dielectric and surrounded by a perfect metal for which  $\epsilon_r < -1$ ; however, this type of cavity has little practical utility since metals exhibit high dissipative losses at optical frequencies. The other obvious difference between electrons and photons lies in the vector nature of the optical fields, which produces an extra non-zero term if the susceptibility has a non-zero gradient in the direction of the electric field - something which will normally happen in photonic band gap materials. Its effect is to couple together the cartesian field components, making the calculation of band structure for photons significantly more difficult than for electrons. If it did not exist, each field component would satisfy a scalar Helmholtz equation independently, greatly reducing the complexity of the problem; the electron and photon wave equations would then be formally identical at constant optical frequency.

## 2.2 Effective Mass of Electrons and Photons in Uniform Isotropic Media

It is known that the electronic effective mass is profoundly affected by the presence of a periodic potential<sup>23</sup>; in order to understand the implications of this for photons in PBG materials it is essential first to explore and understand the comparison in the simpler non-periodic case of a uniform isotropic medium. The matrix elements of the reciprocal effective mass tensor are given by:

$$\frac{1}{m_{ij}^*} = \frac{1}{\hbar^2} \frac{\partial^2 H}{\partial k_i \partial k_j} = \frac{1}{\hbar} \frac{\partial^2 \omega}{\partial k_i \partial k_j} \quad (13)$$

Evaluation of the effective mass tensor thus requires an exact knowledge of the dispersion relations, which take the simple forms:

$$H_e = \frac{\hbar^2(k_x^2 + k_y^2 + k_z^2)}{2m_e} + U \quad (14)$$

for electrons and

**Table I.** Electrons and Photons in Isotropic Uniform Media

<i>compared item</i>	<i>electrons</i>	<i>photons</i>
particle type	fermion	boson
occupancy per state	two (opposite spins)	limited only by material breakdown or nonlinearity
fields	scalar	vector
potential energy	$U \sim$ constant (effective one-electron potential)	$U_o = -\hbar\omega(\epsilon_r - 1)$ (our chosen definition)
total energy	$H_e$ variable	$H_o = \hbar\omega$
dispersion relation	$k^2 = 2m_e(H_e - U)/\hbar^2$	$k^2 = (\omega n/c)^2$
effective mass	rest mass $m_e$ (scalar)	$\infty$ (direction of travel) $2m_o n$ (for deflection)
evanescence at normal incidence (i.e., $\beta=0$ )?	yes (if $H_e$ small enough)	impossible in dielectrics
polarisation effects	none	Brewster's angle
critical angle $\theta_c$	$\arcsin \sqrt{[(H_e - U_1)/(H_e - U_2)]}$ depends on $H_e$	$\arcsin (n_2/n_1)$ independent of $H_o$
in potential well at $\beta=0$	tight binding to free electrons as $H_e$ rises	no binding possible in dielectrics
in potential well at $\beta > 0$	tight binding to free electrons as $H_e$ rises	discrete tightly bound modes beyond $\theta_c$

$$H_o = \frac{\hbar c}{n} \sqrt{k_x^2 + k_y^2 + k_z^2} \quad (15)$$

for photons, where  $n$  is the refractive index. Deriving the reciprocal effective mass tensor is straightforward, and after diagonalisation leads to the principal forms:

$$[1/\mathbf{m}_e^*] = (1/m_e) \mathbf{I} \quad (16)$$

for electrons (where  $\mathbf{I}$  is the identity matrix) and

$$[1/\mathbf{m}_o^*] = \frac{1}{2m_o n} \begin{bmatrix} 1 & 0 & 0 \\ 0 & 1 & 0 \\ 0 & 0 & 0 \end{bmatrix} \quad (17)$$

for photons travelling in the  $z$ -direction (the quantity  $m_o$  was defined in (10)). The electron effective mass is, as expected, a scalar quantity equal to the rest mass; electrons can be accelerated equally easily in any direction, including the direction in which they are moving. For photons, however, the situation is considerably more complicated. It turns out that the effective mass is *infinite in the direction of propagation*, and equal to  $2m_o n$  in the two directions orthogonal to this; the implication is that photons can be deflected but not accelerated. The profound differences between photons and electrons are all the more

extraordinary when one considers that the only difference is a square root in the dispersion relation! The comparison between electrons and photons in uniform isotropic media is summarised in Table I.

### 3. ANALYSIS OF SINGLY PERIODIC STRUCTURES

We present now a full two-dimensional treatment (using the translation matrix method<sup>29</sup>) of singly periodic multi-layer structures, with an emphasis on re-interpretation (using the concepts of photonic band structure) and building up intuition. Periodic structuring of a medium can affect the density of states profoundly, either reducing it to zero within the photonic band gaps, or increasing it and creating new states with unusual properties in the vicinity of the photonic band gaps. A full two-dimensional treatment permits the building up of a canon of basic concepts useful for understanding these effects (and others) in more complicated multiply-periodic two and three dimensional structures. It provides an excellent introduction to the subject, illustrating simply and precisely a number of key physical concepts such as the tightly bound and nearly-free photon approximations, the Brillouin diagram, the constant energy (wavevector) diagram, the factors governing the appearance and disappearance of the band gaps, and the role of effective mass. In the alternative language of optics, photonic Bloch waves are the *normal optical modes* of a periodic structure, in the same sense that plane waves are the normal modes of free space.

#### 3.1 Translation Matrix Formalism

*This section contains a detailed mathematical account of the translation matrix method, and may be omitted at a first reading; it provides a source of the mathematical tools needed if the reader wishes at some later date to treat a specific case.*

We consider a periodic medium composed of alternating planar layers with constant refractive indices  $n_1$  and  $n_2$  ( $n_1 > n_2$ ) and widths  $h_1$  and  $h_2$ . The stack period  $\Lambda$  is the sum of  $h_1$  and  $h_2$ . The same geometry as in section 1.2 is used: cartesian axes are oriented with  $y$  normal to the layer boundaries and  $z$  along the layers (Figure 5); there is no field variation with  $x$ . As already pointed out, one key feature of the planar geometry is the separation of the electric field into TM and TE polarization states, with  $E_x = H_y = H_z = 0$  and  $H_x = E_y = E_z = 0$  respectively. In each case, all field components can be expressed in terms of the surviving  $x$  component (denoted here by  $f$ ), which itself satisfies a Helmholtz equation in each layer ( $j = 1, 2$ ):

$$\frac{d^2 f_j}{dy^2} + (k^2 n_j^2 - \beta^2) f_j = 0 \quad (18)$$

(where  $\beta$  is the propagation constant in the  $z$  direction) with scalar boundary conditions at the interfaces:

$$f_1 = f_2, \quad \xi_1 \frac{df_1}{dy} = \xi_2 \frac{df_2}{dy}; \quad (19)$$

the TE and TM polarisation parameters  $\xi_j$  are defined in (5). The general solution for the field distribution  $f_j^N(y)$  in the  $j$ -th layer of the  $N$ -th period is a superposition of the two field expressions in (1), and can be written in the form:

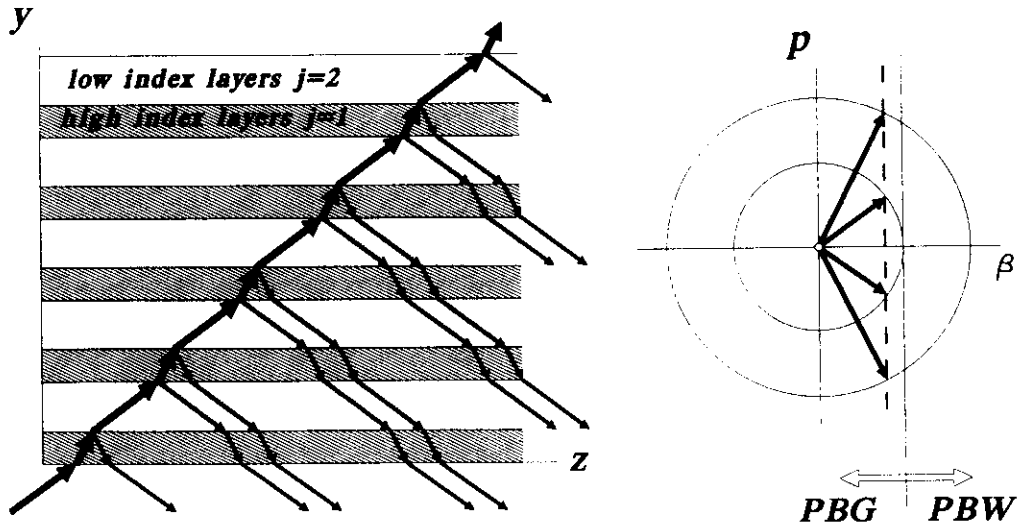


**Figure 5.** Geometry of multi-layer stack ( $n_1 > n_2$ ), and the related wavevector diagram. The directions of the rays in each layer are easily predicted using the wavevector diagram at constant  $\beta$ . Under the first Born approximation, the reflections at each interface are very weak, the incident ray can be assumed undepleted, and single scattering dominates. The primary ray is illustrated with a somewhat thicker line.

$$f_j^N(y) = a_j^N \cos[p_j(y - y_j^N)] + b_j^N \frac{\sin[p_j(y - y_j^N)]}{\xi_j p_j \Lambda}, \quad (20)$$

where  $a_j^N$  and  $b_j^N$  are arbitrary constants,  $y_j^N$  is the value of  $y$  at the centre of the  $j$ -th layer of the  $N$ -th period, and  $p_j$  was defined in (2). In departure from previous treatments (e.g. reference 29), the functions in (20) have been carefully chosen for algebraic convenience. They are entirely real for all real values of  $\beta^2$  even if  $p_j$  is imaginary, are well-behaved as  $p_j^2$  changes sign, and retain two degrees of freedom in the special case  $p_j=0$ . Also, waves within a stop-band are specified by entirely real values of the two constants  $a_j^N$  and  $b_j^N$ , which have the same units. A two-component state vector made up of these constants completely specifies the field in the stack. The state vector in one layer can be expressed in terms of the state vector in the corresponding layer in the previous period by operation with a  $2 \times 2$  translation matrix:

$$\begin{pmatrix} a_j^{N+1} \\ b_j^{N+1} \end{pmatrix} = \mathbf{M} \begin{pmatrix} a_j^N \\ b_j^N \end{pmatrix}. \quad (21)$$

By expressing the fields in (20) with respect to a local origin in the centre of a layer (instead of, for example, at the edge), the symmetry of the structure is maximally exploited, leading to a matrix  $\mathbf{M}$  with eigenvalues and eigenvectors in a particularly simple form:

$$\mathbf{M} = \begin{pmatrix} A & B \\ C & A \end{pmatrix}, \quad (22)$$

where the elements are given in Appendix A1. The eigenvalues and eigenvectors are:



$$\lambda_{\pm} = A \pm \sqrt{BC}; \quad (23)$$

$$(f_{\pm}) = \begin{pmatrix} \sqrt{B} \\ \pm\sqrt{C} \end{pmatrix}, \quad (24)$$

where  $BC = A^2 - 1$  and  $\det[\mathbf{M}] = 1$ , i.e.,  $\mathbf{M}$  is unimodular. This implies that the product of the eigenvalues  $\lambda_+$  and  $\lambda_-$  is unity, so that they can without loss of generality be written as

$$\lambda_{\pm} = \exp(\pm jk_y \Lambda), \quad (25)$$

where  $k_y$  is to be determined. Thus the state vector of each component field satisfies

$$\begin{pmatrix} a_j^{N+1} \\ b_j^{N+1} \end{pmatrix} = \begin{pmatrix} a_j^N \\ b_j^N \end{pmatrix} \exp(\pm jk_y \Lambda). \quad (26)$$

The general field in the structure (for given  $\omega$ ,  $\beta$  and polarization) is expressible as a superposition of two Bloch waves with field distributions:

$$f_{\pm}(y)e^{-j\beta z} = B_{\pm}(y) \exp[-j(\beta z \pm k_y y)], \quad (27)$$

where the function  $B_{\pm}(y)$  is periodic with period  $\Lambda$  and the Bloch wavevector  $k_y$  is given by:

$$k_y = \frac{\cos^{-1} A}{\Lambda}. \quad (28)$$

If  $k_y$  is real, the Bloch waves in (27) are progressive and may transport energy normal to the layers as well as along them. If, however, values of  $\omega$  and  $\beta$  exist for which the magnitude of  $A$  exceeds 1 (or  $BC < 0$ ),  $k_y$  has an imaginary part. The Bloch waves are then evanescent, growing or decaying exponentially from period to period normal to the layers, while progressing along them. If the structure is infinite (in the  $y$ -direction), these waves cannot be supported and no real states exist; the ranges of  $\omega$  and  $\beta$  where this occurs are the photonic band gaps. In a truncated structure, however, they play the role of tunnelling fields; for example, for incidence of a travelling plane wave, the stack behaves as a familiar multi-layer reflector. If the external field is itself evanescent, and matches to a Bloch wave decaying into the stack, a photonic surface wave can form (see section 9.1). The band edges between real and virtual states (i.e., travelling and evanescent Bloch waves) occur when  $A = \pm 1$ ; an equivalent condition is  $BC = 0$ .

Each Bloch wave can alternatively be expanded in terms of an infinite number of plane waves whose wavevectors are related by Floquet's theorem:

$$\mathbf{k}_n = \beta \hat{\mathbf{z}} + (k_y + nK) \hat{\mathbf{y}} \quad (29)$$

where  $K = 2\pi/\Lambda$  is the reciprocal lattice wavevector (or grating vector). This permits us to express  $B_{\pm}(y)$  in the general form:

$$B_{\pm}(y) = \sum_n S_n^{\pm} \exp(-jnKy) \quad (30)$$

where the  $S_n^\pm$  are the complex plane wave amplitudes. Equations (28) and (29) may be used directly to plot the Brillouin and wavevector diagrams for the structure, as is done in later sections.

### 3.2 Normalised Parameters

An appropriate set of normalised parameters for the multi-layer stack treated above includes just three normalised parameters: a normalised frequency  $\nu$ , an index ratio  $n_R$  and an relative thickness  $\tau$ :

$$\nu = kn_{av}\Lambda, \quad n_R = (n_2/n_1), \quad \tau = (h_2/\Lambda), \quad (31)$$

where  $n_{av}$  is the weighted average index, defined by:

$$n_{av} = (n_1h_1 + n_2h_2)/\Lambda \quad (32)$$

and the indices of the layers are  $n_1 > n_2$ . For convenience, a normalised version of  $\beta$  will occasionally be used, in the form

$$b = \beta\Lambda. \quad (33)$$

As we shall sometimes discuss electrons in a stack of alternating high and low potentials  $U_2$  and  $U_1$ , the following definition of average potential will be useful:

$$U_{av} = (U_1h_1 + U_2h_2)/\Lambda. \quad (34)$$

In the next three sections, we use the above analytical expressions for  $k_y$  to explore the behaviour of Bloch waves in singly periodic structure as a function of frequency and  $\beta$ . In section 4, Brillouin diagrams for electrons and photons at  $\beta=0$  are discussed, together with the physical origins of the band gaps and some other issues. In section 5, the wavevector diagram at constant  $\omega$  and variable  $\beta$  is introduced, and in section 6 the behaviour at oblique incidence treated.

## 4. SINGLY PERIODIC STRUCTURES AT NORMAL INCIDENCE ( $\beta = 0$ )

### 4.1 Brillouin Diagrams

The Brillouin diagram<sup>23,24</sup> for electrons is a plot of all the permitted real wavevectors as a function of electron energy. The photonic equivalent is a plot of wavevector  $k_y$  as a function of optical frequency. These diagrams are plotted in Figure 6 for normal incidence in a particular case (oblique incidence is treated in section 6). For very weak modulation ( $n_1 \approx n_2 \approx n_{av}$  and  $U_1 \approx U_2 \approx U_{av}$ ), the diagram reduces to a series of parabolae for electrons:

$$h_e = \frac{2m_e\Lambda^2}{\hbar^2} H_e = u_{av} + (k_y + 2n\pi)^2 \quad (35)$$

$$u_{av} = \frac{2m_e\Lambda^2}{\hbar^2} U_{av}$$

where  $h_e$  is the normalised total electron energy, and to a series of straight lines of slope  $\pm 1$  for photons:

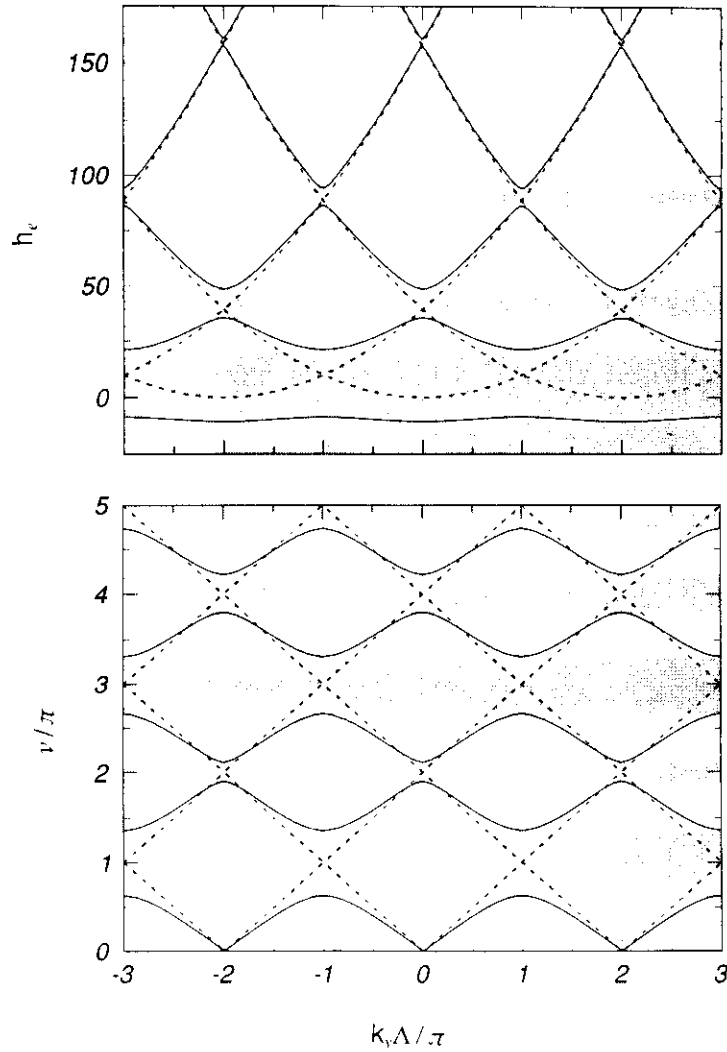


**Figure 6.** Brillouin zone diagrams for  $\beta = 0$  (normal incidence) on a multi-layer stack for electrons (upper) and photons (lower). The dotted lines are asymptotes, corresponding to a structure with the same average properties but a very weak modulation. In the electron case,  $\tau = 0.5$ ,  $u_2 = 25$  and  $u_1 = -25$ . In the photon case,  $\tau = 0.741$  and  $n_R = 0.286$  and the integers on the  $v/\pi$  axis correspond to the Bragg conditions; the band gaps are all of comparable width (because "potential" and "total" energies both scale with frequency), and the asymptotes straight lines as expected. In the electron case, the band gaps narrow with increasing  $h_e$ , and the asymptotes are parabolic; note the appearance of a band window - a region where propagation is unexpectedly allowed - below the base of the parabolae.

$$v = \pm(k_y \Lambda + 2n\pi) . \quad (36)$$

The integer  $n$  in each case refers to the  $n$ -th plane wave in the expansion in (30). When the single-pass optical path length across a unit cell, calculated using the components of wavevector  $p_1$  and  $p_2$  normal to each layer, is equal to an integral number  $m$  times  $\pi$ , the  $m$ -th order Bragg condition is satisfied:

$$p_1(1-\tau)\Lambda + p_2\tau\Lambda = m\pi . \quad (37)$$

This condition originally arose in x-ray diffraction<sup>59-63</sup>, where the modulation depth of the periodic scattering potential is very weak, and in fact it assumes that the *first Born approximation* holds, i.e., that each interface contributes only a very weak reflection and that secondary and higher order reflections are negligible (see Figure 5 for an illustration of this). This is clearly not the case in a photonic band gap structure with very high modulation depths, when the Bragg condition becomes uncertain, spreading out over a range of frequencies (as discussed in section 4.4 below). Thus band gaps form at the intersections of the parabolae and straight lines, and a band window appears (for the parameters chosen) in the normally forbidden energy range  $H_e < U_{av}$  for electrons (Figure 6).

#### 4.2 Group Velocity and Density of States

Just as for electrons in a finite crystal, the photonic states in a finite periodic structure are quantized (although they may be smeared out by strong coupling to the outside world). The density of states becomes large at the band edges since the wavevector  $k_y$  there changes rapidly with frequency; states that would appear within the band gap if no periodicity were present are pushed to higher and lower frequencies, where they cluster in large numbers at the band edges. By reducing the density of states to zero within the band gap, the formation of photons is blocked, which can be used to suppress an unwanted radiative electronic transition<sup>7</sup>. The zero slope at the band edges implies that the group velocity vanishes, which makes sense since within the band gap photons cannot travel. There is of course a reciprocal relationship between density of states and group velocity<sup>23</sup>; however, unlike in the electron case when two electrons are permitted per state, each state can accommodate as many photons as desired (before the material becomes nonlinear or breaks down).

#### 4.3 Expectation Values of Potential: Electrons and Photons

It will be useful, as preparation for the discussion of the origin of band gaps in section 4.4, to have supplemented the Brillouin diagram with plots of the *expectation value* of potential for both electrons and photons in a simple stack of alternating layers of high and low potential; this quantity varies according to how strongly the photons/electrons are redistributed within the unit cell. It also provides graphic illustration of some of the essential similarities and differences between electrons and photons in a periodic potential. For simplicity, normal incidence ( $\beta = 0$ ) is assumed in each case, rendering the photonic solutions for TE and TM polarization identical. To facilitate the comparison, the wave equation is recast in a one-dimensional form common to electrons and photons:

$$\left[ -\Lambda^2 \frac{d^2}{dy^2} + u(y) \right] \psi = e \psi \quad (38)$$

where the normalised potential energy  $u(y)$  is given by:

$$u(y) = \frac{2m\Lambda^2}{\hbar^2} U(y) \quad \text{or} \quad -v^2 \{e_r(y) - 1\} / n_{av}^2 \quad (39)$$

and the normalised energy eigenvalue  $e$  by:

$$e = h_e \quad \text{or} \quad v^2 / n_{av}^2 \quad (40)$$

for electrons and photons respectively. The expectation value of  $u(y)$  in each case is:

$$\langle u \rangle = \frac{\langle \psi | u | \psi \rangle}{\langle \psi | \psi \rangle} \quad (41)$$

where the averaging is carried out over a unit cell. Inside the stop-bands, where the fields

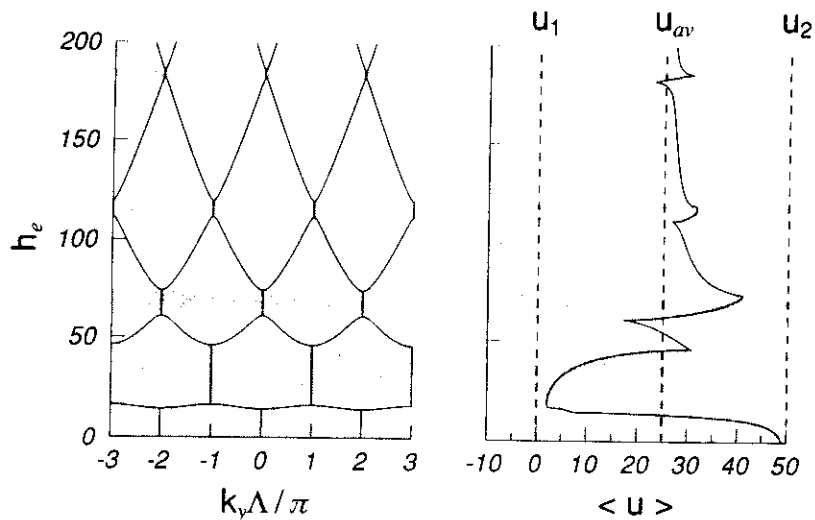


**Figure 7.** Wavevectors  $k_y\Lambda/\pi$  and expectation values of potential energy  $\langle u \rangle$  for electrons, plotted against energy eigenvalue  $h_e$  ( $\tau = 0.5$ ,  $u_1 = 0$  and  $u_2 = 50$ ). The upper and lower bounds of  $\langle u \rangle$  are constant ( $\propto$  lattice potentials). Note that  $\langle u \rangle$  is consistently low on the low  $e$  side of the band gaps, that the effect of the periodic potential diminishes with increasing total energy, leading to  $\langle u \rangle \rightarrow u_{av}$  at high energies.

are evanescent, expectation values cannot be calculated (the field grows/decays from cell to cell) because there are no real states; however, in the interests of following the redistribution of photons, the fields  $\psi$  in (41) are multiplied by  $\exp(\pm\alpha y)$ , where  $\alpha = \text{Im}(k_y)$  is the evanescent decay rate of the Bloch wave. This compensates for the exponential growth/decay of the field from cell to cell.

First, for electrons, the Brillouin diagram is plotted in the form  $h_e$  versus  $k_y\Lambda/\pi$  (Figure 7). When the total energy  $h_e$  is less than  $\langle u \rangle$ , the waves are evanescent. The

lower and upper bounds on  $\langle u \rangle$  are given by the minimum and maximum potential energies present in the lattice:  $u_1$  and  $u_2$  respectively. For total energies  $h_e < u_2$ , the tight binding approximation holds, and substantial variations in  $\langle u \rangle$  occur as the electrons shift between regions of high and low potential energies. As  $h_e$  increases, the number of cycles of field within the layers increases, and  $\langle u \rangle$  tends towards the mean value  $u_{av}$ . The expectation potential is consistently lower on the low energy band gap edges, and higher on the high energy band gap edges. At higher electron energies, the presence of the periodic potential becomes less and less important, and the fluctuations in  $\langle u \rangle$  smaller and smaller; this reflects the fact that  $u(y)$  is independent of  $e$  for electrons.

Second, for photons, the upper and lower bounds of the potential scale with the

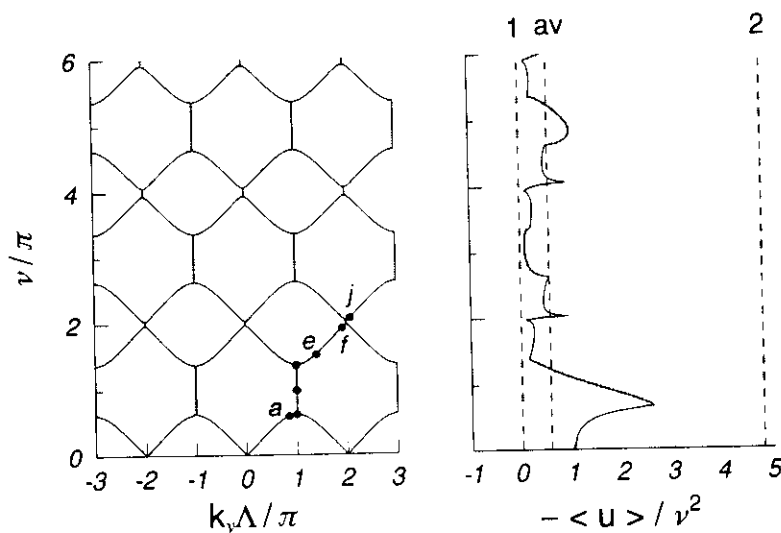


**Figure 8.** Wavevectors  $k_y\Lambda/\pi$  and expectation values of the dielectric susceptibility  $\langle \epsilon_r - 1 \rangle / n_{av}^2$ , plotted against  $\nu/\pi$  ( $\tau = 0.7878$ ,  $n_1 = 3.5$  and  $n_2 = 1$ ). The upper and lower bounds of  $\langle \epsilon_r - 1 \rangle$  are  $(n_1^2 - 1)$  and  $(n_2^2 - 1)$  respectively. Note that, unlike in the electron case,  $\langle \epsilon_r - 1 \rangle$  is not consistently low on the low  $e$  side of the band gaps. The microscopic field intensity profiles for the five marked points ( $a$  to  $e$  from low to high frequencies) are available in Figure 9, together with the profiles for five similar points ( $f$  to  $j$  - not marked in owing to lack of space) around the second-order band gap at  $\nu/\pi = 2$ .

optical frequency ( $\propto k$ ), so it is more convenient to plot  $\langle \epsilon_r - 1 \rangle$ , which we normalise to  $n_{av}^2$ ; for consistency with Figure 6 the quantity  $e$  is replaced with  $\nu/\pi$ . The diagram (Figure 8) is very different; unlike in the electronic case, tight binding and nearly free energy regions cannot co-exist on the same diagram, since the ratio between potential and total energy does not alter with increasing  $\nu$ . Note that for photons the expectation value of dielectric constant does not change consistently from high to low across the band gaps. Illustrative field intensity profiles across the unit cells for different points on the diagram are given in Figure 9.

We note in conclusion that a completely different comparison may be made at constant optical frequency (i.e.,  $k = \text{constant}$ ). Under these circumstances, a diagram formally identical with the electron case in Figure 7 may be obtained for photons when

$\beta > 0$ , in which case for TE polarization (38) can be rearranged as:

$$\left[ -\Lambda^2 \frac{d^2}{dy^2} + u'(y) \right] \psi = e' \psi \quad (42)$$

where  $u' = -k^2 \epsilon_r$  and  $e' = -\beta^2$ . Under these circumstances the "potential energy" is independent of the "total energy". We emphasise that this makes use of a completely different analogy to that in section 2 and the rest of this section.

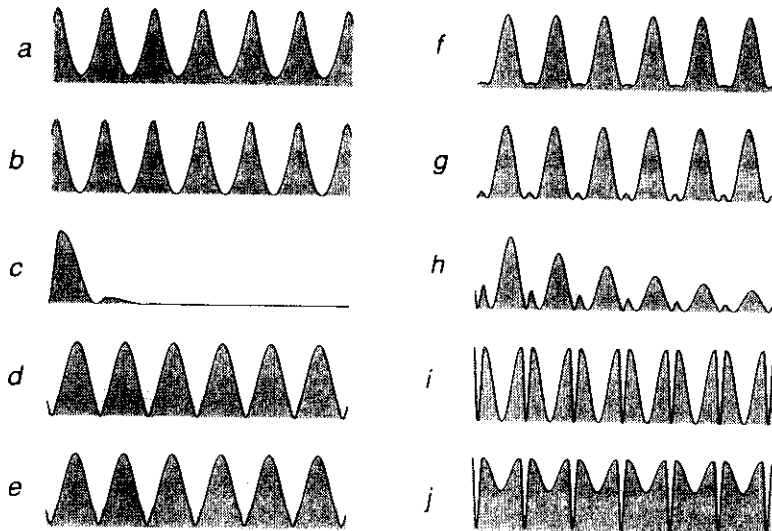


**Figure 9.** Field intensity distributions at points in Figure 8, as the first and second order Bragg conditions are traversed (a to j). The redistribution of photons into high and low index regions gives rise to frequency-dependent expectation values of dielectric constant (also Figure 8), and can be used to explain to appearance of a photonic band gap.

#### 4.4 Origins of Band Gaps

The accepted characteristic of a band gap is that it appears in regions where propagation is normally allowed (although see section 6.2). This statement is equally true of electrons in a semiconductor and photons in a PBG material. It is interesting at this point to ask why electrons in the valence band have restricted mobility (proportional to the reciprocal of the effective mass), while photons in a photonic "valence" band are free to move. The essential reason is that for photons the potential and total energy both scale with frequency; thus for  $\beta = 0$  it is not possible to move from nearly free (conduction) to tightly bound (valence) photons by changing the total energy. If, however, the optical frequency is fixed and  $\beta$  is varied instead, a perfect analogy with electronic band theory is obtained as pointed out above (in equation (42)).

Perhaps the simplest qualitative explanation of band gap formation starts with field microstructure. As the Bragg condition is approached, the periodic structure becomes resonantly imaged by the light<sup>5</sup>. This occurs as the wavelets reflected at successive grating

planes become more and more in phase, allowing them to build up into a strong reflected wave which interferes with the incident wave to produce a periodic image. If this image is invariant as the light progresses through the grating, it is a picture of a Bloch wave. The band gap then arises through the interplay of two sometimes conflicting requirements: 1) the light must produce an image with the same period as the structure; and 2) it must achieve this despite being redistributed by interference into regions of high or low dielectric constant.

As the band edge is approached for normal incidence ( $\beta = 0$ ) and the image becomes resonant with the periodic structure, the expectation value of dielectric constant  $\langle \epsilon_r \rangle$  increases or reduces according to the position of the fringes relative to the grating planes (section 4.3; Figure 8). At exact Bragg incidence,  $\lambda/2n_{av} = \Lambda$ , suggesting that a perfect image can form; however, if this were so, interference would push  $\langle \epsilon_r \rangle$  away

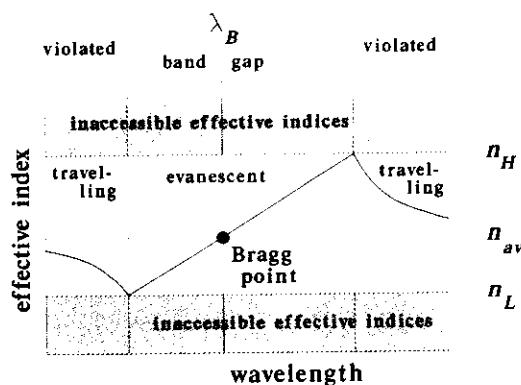


**Figure 10.** Diagram illustrating how wavelength-dependent changes in effective refractive index permit the Bragg condition to smear out over a band gap - a range of wavelengths limited by the degree to which photons are redistributed into high and low index regions.

to higher or lower values, thus altering the fringe period and ruining the image. What happens in practice is that the fringe pattern forms neither in nor out-of-phase with the grating, allowing  $\langle \epsilon_r \rangle$  to reduce or increase until the correct period is found, i.e., until the real part of  $k\sqrt{\langle \epsilon_r \rangle}$  exactly equals  $K/2$ . The penalty for this trickery is that the associated Bloch wave becomes evanescent - a consequence of the fact that a true image cannot form at an arbitrary phase to an object. Exactly on the band edges, it may be shown that  $k\sqrt{\langle \epsilon_r \rangle} = mK/2$  where  $m$  is the order of the Bragg condition; outside the band gap, moving away from the Bragg condition, fringes of the correct period are produced, but the image becomes increasingly less visible (this trend is apparent in Figure 9). Note that within the band gap, because the image is highly visible, the fields are zero at one or more points within each unit cell; this forbids energy flow across the layers, which is another way of stating that the group velocity normal to the planes goes to zero<sup>56,57</sup>. The position of the band edges can be crudely explained by generalising the first order Bragg condition



to allow for wavelength-dependent changes in effective index  $n_{\text{eff}}$ :

$$\lambda = 2 n_{\text{eff}}(\lambda) \Lambda \quad (43)$$

which is based on the notion that  $\sqrt{\langle \epsilon_r \rangle}$  is related in some monotonic (but not straightforward) manner to  $n_{\text{eff}}$ . This generalised Bragg condition is satisfied over a range of wavelengths given by the maximum and minimum values of  $2\Lambda\sqrt{\langle \epsilon_r \rangle}$ , yielding the positions of the band edges; the concept is illustrated in Figure 10. The fringes are out-of-phase with the grating at the high frequency band edge (photons concentrated in low index regions), and in-phase at the low frequency band edge (concentrated in high index regions). Note that these simple arguments are less useful at higher order Bragg conditions, when the field microstructure becomes much more complicated; indeed, the band gap can shrink to zero (see section 6.3) for a number of reasons.

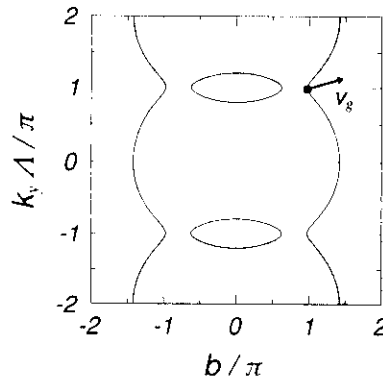


**Figure 11.** Example of wavevector diagram. The upper and lower shaded regions are higher order Brillouin zones, which are exact replicas of the first zone. A single point on a curve within the first zone brings with it all corresponding points within all the other zones; the wavevectors associated with these points are those of the complete set of plane waves needed to form a Bloch wave - see (30). The group velocity of the Bloch wave points in the direction of the normal (equation (44)).

## 5. THE WAVEVECTOR DIAGRAM

Most of the important features of two-dimensional propagation of photonic Bloch waves in periodic structures are usefully summarised on a wavevector diagram<sup>56</sup>, which is a plot of the loci of allowed real values of  $k_y$  against  $\beta$  for a given  $\omega$  and polarization; it may be calculated using (28) and (29). A simple example is given in Figure 11. The resulting curves are known in x-ray diffraction as dispersion surfaces<sup>61</sup>, and are related to constant energy surfaces in electronic band theory<sup>23</sup>. The diagrams are symmetric in  $\beta$ , periodic in  $k_y$ , because of the Floquet/Bloch theorem, and symmetric in  $k_y$ , since for every value of  $k_y$  there is a value  $-k_y$  corresponding to a Bloch wave progressing in the opposite

direction. The diagram reveals the location of the stop-bands for a particular stack. A particularly useful feature of the diagram is its ability to predict the direction of the group velocity, via the relationship:

$$\mathbf{v}_g = \nabla_{\mathbf{k}} \omega(\mathbf{k}) \quad (44)$$

which shows that  $\mathbf{v}_g$  is oriented normal to the curves in wavevector space, pointing in the direction of increasing frequency (note that it ceases to have an obvious meaning for evanescent waves, when the wavevector is complex).

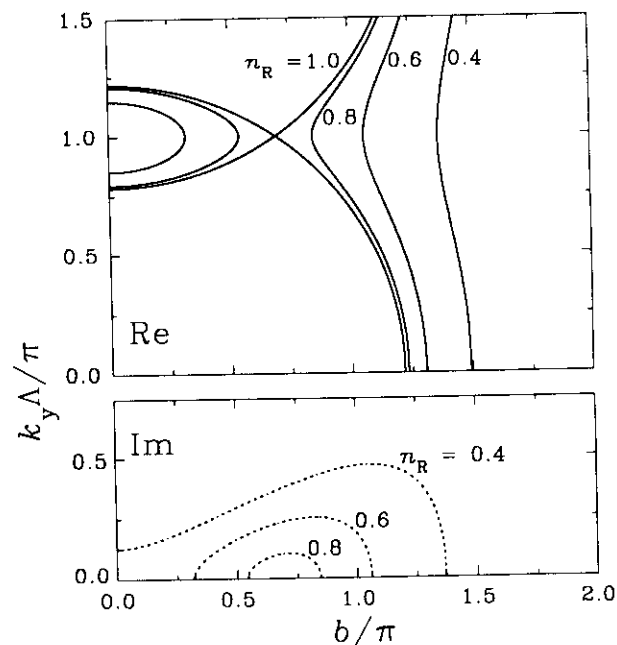


**Figure 12.** Portion of the wavevector diagram at  $\nu = 1.21\pi$  for  $n_R = 1, 0.8, 0.6$  and  $0.4$ , keeping  $n_{av}$  constant by adjusting  $\tau$  appropriately. At  $n_R = 0.4$  the left hand branch of the stop band has vanished and the right hand pass band has considerably narrowed. The imaginary parts of  $k_y \Lambda / \pi$  for pure real  $\beta$  are also plotted.

In Figure 12 the diagram is plotted for a variety of values of  $n_R$ . Notice how it is possible to suppress the inner (left hand) stop-band branch at high modulation depths (e.g.,  $n_R = 0.4$ ), when the right hand stop-band branches become squashed-up and steep, lying well outside the circle corresponding to the average index in the stack (this is linked to the appearance of photonic band windows, and is discussed in more detail in section 6.2). For  $\beta$  values within a stop-band, it is also instructive to plot the imaginary part of  $k_y$ , which gives the decay rate of the Bloch mode field in the  $y$  direction.

It is of critical importance in optics to be able to predict what waves will be excited inside a periodic structure for an arbitrary incident wave. The wavevector diagram is ideal for this purpose; by superimposing the diagrams for each medium, and requiring the wavevector components tangential to the local boundary to be conserved, the complete set of travelling waves on each side of the boundary can be found<sup>57</sup>. The direction in which

the light proceeds within the grating is then given by the normal to the dispersion surfaces. The method is described in more detail in section 7.2, where it is used extensively in the discussion of devices and two-dimensional propagation.

## 6. SINGLY PERIODIC STRUCTURES AT OBLIQUE INCIDENCE ( $\beta > 0$ )

In this section, the effect of oblique incidence ( $\beta > 0$ ) on the band gap widths and positions is explored. This is an important issue if singly periodic stacks are to be used in the control of spontaneous emission in lasers<sup>37-40</sup> (see also other chapters in this volume). In the ensuing sub-sections, band-edge diagrams are discussed, the idea of a photonic band window introduced, the conditions causing the PBG to shrink to zero identified, and finally the Brillouin diagram at  $\beta = \text{constant}$  is used to illustrate how under these conditions photons can resemble electrons.

### 6.1 Band-Edge Diagrams

It is useful to know in detail how light will behave in frequency regions outside the main photonic band gap. For example, although the creation of a photonic band gap may successfully suppress an intermediate radiative transition in an up-conversion laser, higher order band gaps could, if not properly understood and controlled, interfere with the laser's performance. For this and many other reasons, it is useful to plot the band edge positions on a diagram of normalised frequency versus  $\beta$ . The band edges are located at points where the product of off-diagonal matrix elements is zero, i.e.,  $BC = 0$  in (23). The resulting diagram (Figure 13) divides up into three main regions: a photonic band gap region where free propagation is normally expected but gaps appear; a photonic band window region where the norm is evanescent but windows appear (the light being tightly bound inside each high index layer); and a cut-off region where propagation never occurs. The first two of these regions have analogies in the nearly free electron and tight binding models of electronic band theory<sup>23,24</sup>.

### 6.2 Photonic Band Gaps and Windows

Two complementary views of photonic band structure are possible: It is either a sequence of band gaps in a frequency range where light is otherwise free to propagate; or a sequence of band windows in a frequency range where light is otherwise localised, i.e., evanescent. Which of these views is most appropriate depends on our understanding of the words "otherwise free to propagate" and "otherwise localised." One interpretation makes use of the average index; however, as already mentioned, it is difficult to assign this a useful value owing to redistribution of photons into regions of high and low dielectric constant (for example, the multi-layer stack whose one-branch wavevector diagram is given in Figure 12 with  $n_R = 0.4$  can be viewed as a material with a refractive index that depends strongly on angle). Even so, some qualitative observations based on refractive index may be made. It is clear that tight binding cannot exist in the range  $0 < \beta < kn_2$ , where the light is free to propagate in both layers; this is definitely a photonic band gap region. If, however,  $\beta$  exceeds  $kn_2$ , the light in the low index layers is evanescent, and each high index layer will support a micro-resonance (a waveguide mode). The light is then able to progress across the layers by a process of resonant tunnelling<sup>52</sup>. As the value of  $\beta$  increases, the light is more and more tightly bound inside each high index layer, and this tunnelling process becomes more difficult and slower; its efficacy depends on the width of the low index layers, i.e., the geometry of the stack. At infinite interlayer (atomic) spacing, the bound states correspond exactly to guided modes, with infinitely

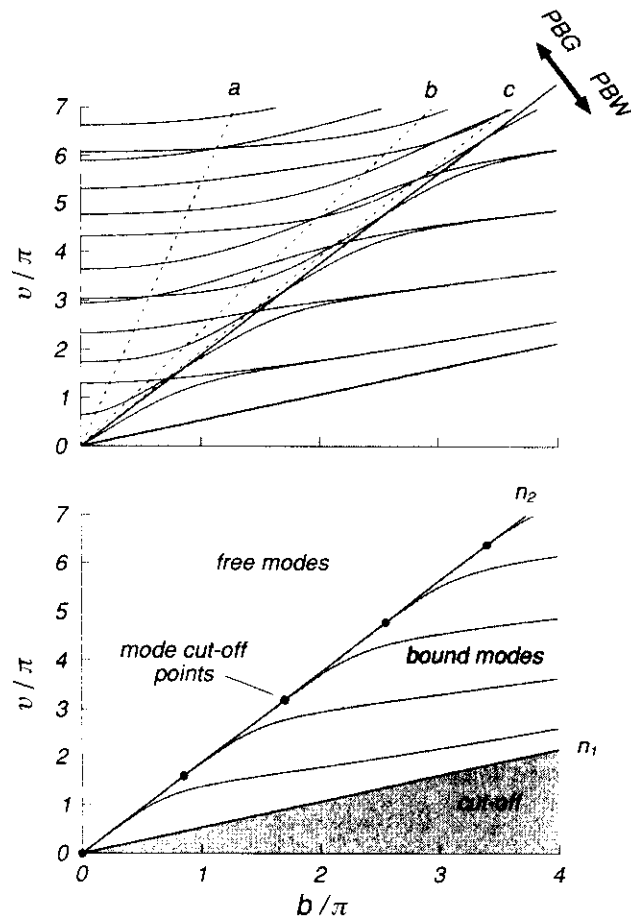


**Figure 13.** *Upper:* Band-edge diagram (TM polarization) in a multi-layer stack with  $\tau = 0.65$  and  $n_R = 0.286$ ; *Lower:* guided modes of a single high index layer; note free, bound (only points lying on the curves are permitted) and cut-off regions. Regions where propagation is forbidden are shaded. The higher order bound modes turn on at different values of  $\nu/\pi$ . In the stack, photonic band gaps (Bragg conditions) form in the free region and photonic band windows (resonant tunnelling between bound modes) form in the bound region. The transition occurs at  $\beta = kn_2$ . The band gaps shrink to zero at the Brewster condition (dotted line *c*), and at anti-resonances (two illustrative sequences indicated by the dotted lines *a* and *b*); see section 6.3 for details.

sharp micro-resonant frequencies. As the interlayer spacing falls, the bound states begin to interact, their resonances smearing out over a range of frequencies to form a photonic band window. If the interlayer spacing is small so that considerable overlap exists between the photonic "orbitals," photons are relatively free to travel across the layers: the nearly-

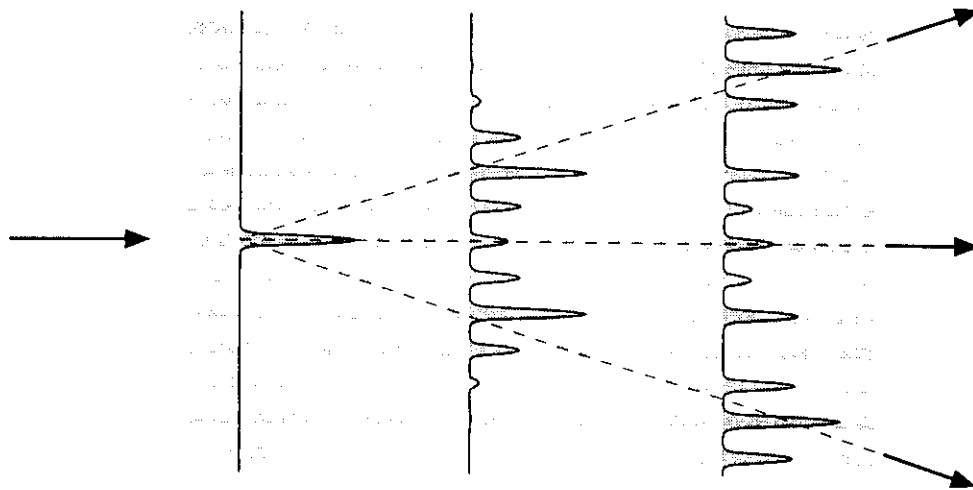
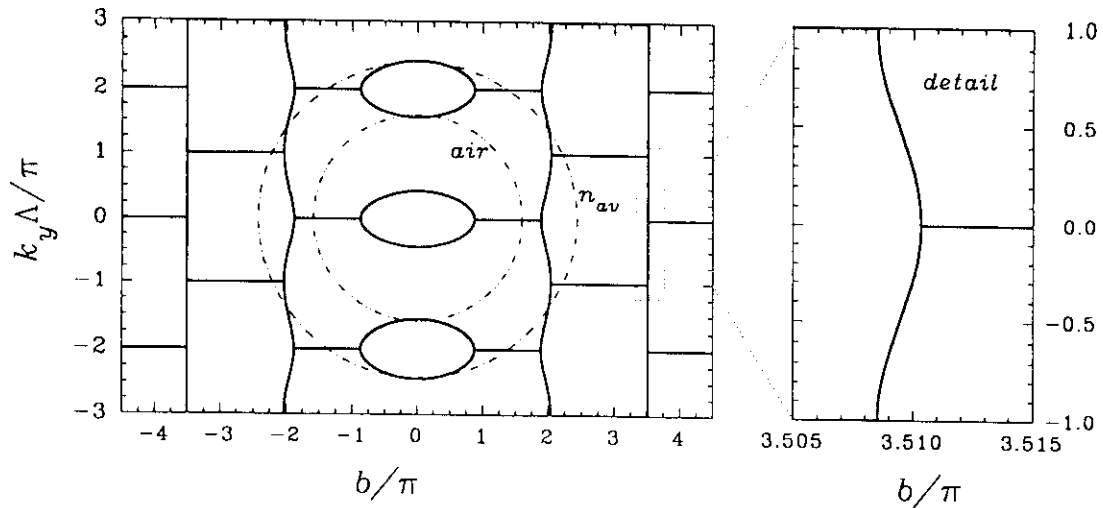


**Figure 14.** Upper (a): Wavevector diagram for  $\tau = 0.35$ ,  $n_R = 0.4$ ,  $\nu = 0.97\pi$ ; resonant tunnelling between the high index layers is very slow in the tightly squashed-up pass band near  $b/\pi = 3.5$ , and less so in the band near  $b/\pi = 2$ . Lower (b): A schematic diagram of the tunnelling process for excitation of a single "waveguide"; note that two pulses emerge above and below the initial guide, in the vicinity of which some light remains (group velocity is horizontal at  $k_y\Lambda/\pi = \pm 1$  &  $0$ ).

free photon approximation then becomes valid again.

In the tight-binding PBW regime, the group velocity direction (but not its magnitude) changes very little over each half of the Brillouin zone (Figure 14a). This creates, in optical terms, a highly anomalous situation where the phase velocity changes rapidly (thereby permitting good spatial resolution of small objects) while the group velocity is constant in direction (thereby avoiding Fresnel diffraction). This provides a physical basis from which to interpret an experiment on an array of parallel channel waveguides reported by Garmire et al<sup>52</sup>. In that experiment, light was coupled into a single central waveguide, and tunneled sideways into the neighbouring guides; the waveguide array is thus "imaged" by the light, while the group velocity slowly carries the power sideways across the waveguides via resonant tunnelling (Figure 14b). An alternative interpretation of this experiment in terms of spatial Wannier functions is briefly introduced in section 7.2.

Finally, we should like to mention the possibility of creating a PBW in a metal

containing a periodic array of dielectric micro-cavities<sup>5</sup>. If these micro-cavities can "talk to each other," light will be able to tunnel through the metal in narrow frequency ranges around the resonant frequencies of the cavities. Alternatively described, a PBW will open up in regions of the spectrum where certain photonic states, their periodic field intensities peaking in the interstices between the metal walls of the cavities, are able to sneak through the structure without attenuation. In a real metal at optical frequencies, dissipation is likely to be a problem, but the concept is nonetheless valid.

### 6.3 Points of Zero Band Gap Width

It is important to understand the physical circumstances under which an otherwise wide photonic band gap can close up. Two different things can cause this to happen. The first is co-incidence of a Bragg condition (37) and the Brewster condition (3), which occurs when the rays in each layer are incident on the interfaces at Brewster's angle, reducing the reflection at each interface to zero; this happens only when the light is  $p$ -polarized (TM case). The second effect is more subtle, but just as simple; and it is even more important, since it occurs for both TE and TM polarized light. It happens when the anti-reflection condition discussed in section 1.2.5 applies concurrently to both layers; this occurs when the optical path lengths across each layer are separately a multiple of  $\pi$  ( $m_1\pi$  and  $m_2\pi$  in layers 1 and 2,  $m_1$  and  $m_2$  being integers). At the same time, as stated mathematically in (37), the  $m$ -th order Bragg condition occurs when the single-pass optical path length across a unit cell is equal to  $m\pi$ . The points of zero stop-band width (Figure 13) therefore occur when both these conditions are simultaneously satisfied, i.e., when:

$$\frac{p_1 h_1}{m_1} = \frac{p_2 h_2}{m_2} = \pi, \quad m_1 + m_2 = m. \quad (45)$$

Solving these equations yields:

$$b = \frac{\pi m_1}{1-\tau} \sqrt{\frac{\alpha^2 - n_R^2}{n_R^2 - 1}} = \sqrt{\frac{\alpha^2 - n_R^2}{\alpha^2 - 1}} \quad (46)$$

where

$$\alpha = m_2(1-\tau)/m_1\tau \quad (47)$$

is used for convenience of notation. This corresponds to a situation where the total reflection from each unit cell is zero, i.e., when an anti-reflection resonance appears simultaneously in each layer. These points of zero stop-band width are much more common at higher frequencies, which explains why complete photonic band gaps are much more difficult (if not impossible) to find in higher order energy bands. In both cases,

$$\mathbf{M} = \mathbf{M}' = \pm \begin{pmatrix} 1 & 0 \\ 0 & 1 \end{pmatrix}, \quad (48)$$

and the multi-layer structure behaves as a uniform medium with an average index different from  $n_{av}$  but no Bragg reflection. It may be possible to defeat (or at least mitigate) this effect by constructing more complicated unit cells with more than two different materials, such that the ratios of optical thicknesses are never simultaneously rational numbers.

## 6.4 Brillouin Diagrams for finite $\beta$

We now turn our attention to the Brillouin diagram for photons under the slightly artificial circumstance when the momentum  $\beta$  along the layers is constant but not zero (Figure 15). This form of oblique incidence turns out to be useful for illustrating how photons can become increasingly free as their total energy increases; the photonic states track along a vertical line in the band edge diagram (Figure 13). As the energy  $H_0$  increases, the real photonic states move from being first cut off, to being concentrated in narrow band windows within an otherwise cut off region, to being permitted everywhere except within the photonic band gaps; the photons become increasingly less tightly bound.

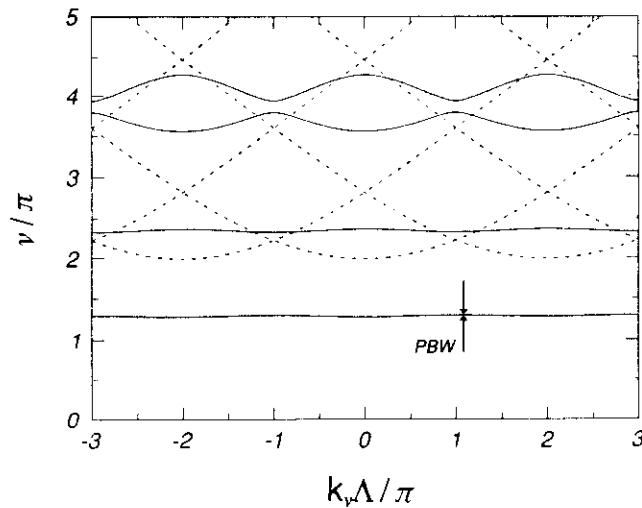


**Figure 15.** Brillouin diagram for photons at  $b = \beta\Lambda = 1.988\pi$ , with  $\tau = 0.741$  and  $n_R = 0.286$  (TE polarisation); the dotted lines are asymptotes, corresponding to a structure with the same average index but a very weak modulation ( $n_R \rightarrow 1$ ). The diagram is reminiscent of the electron case at normal incidence (Figure 6), although the asymptotes are this time *hyperbolic* with frequency; the pass bands widen with increasing frequency, and a band window opens up below the base of the hyperbolae (section 6.2).

As before, it is useful to plot the Brillouin diagram for the case when the scattering from each interface is vanishingly small; under these circumstances, the relationship between  $\nu$ ,  $\beta$  and  $k_y$  for the  $n$ -th plane wave in the expansion (30) is given simply by:

$$\nu = \sqrt{b^2 + (k_y \Lambda + 2n\pi)^2}. \quad (49)$$

Note that for  $b^2 > \nu^2$ , the photons cannot normally (see section 6.2) propagate into the stack, although they will still progress along it with wavevector  $\beta$ . The appearance of real wavevectors within the cut-off region is intriguing, as it is reminiscent of the behaviour of electrons discussed in Figure 6. These wavevectors are caused, as discussed in section 6.2, by the excitation of sharp micro-resonances where the light is concentrated almost entirely

within the high index layers. This permits a real wave to exist for combinations of energy and wavevector where, based on a mean index  $n_{av}$ , evanescence would normally be expected.

## 7. TWO-DIMENSIONAL PROPAGATION

The aim in this section is to discuss the main features of two-dimensional propagation in singly periodic media, and to present some illustrative experimental results taken from work on periodic planar waveguides. First of all a Newtonian effective mass method is developed to handle the propagation of light in structures with a slowly varying average dielectric constant. Experimental results are then presented on this phenomenon, together with examples of refraction, diffraction and interference. Extensive use is made of the wavevector diagram introduced in section 5. All the tools used can be extended without difficulty to multiply periodic structures whose wavevector diagrams are known.

### 7.1 Effective Mass Method For Non-Uniform Periodic Structures

Near a band edge, the effect of the lattice potential on the motion of an electron can be represented by replacing the electron rest mass with an effective mass  $m_e^*$ . If the electron is subjected to an external force, its motion can then be modelled by Newton's laws for a particle with mass  $m_e^*$ . This effective mass method is also known to be very useful in analysing the behaviour of electrons in *non-uniform* crystals containing slow variations in mean potential, such as can happen around dislocations, inclusions and other structural defects<sup>23,25</sup>. Under these circumstances, in the absence of an external electric field, the total electron energy is constant. We now develop an equivalent method for photonic Bloch waves in a periodic structure with a slowly varying average dielectric constant (the photonic equivalent of potential - see (12)), and illustrate it in the next section with experimental results on periodic planar waveguides. In both cases it is the curvatures of the  $H-k$  Brillouin diagram that determine the elements of the reciprocal effective mass tensor, via the formula stated in (13).

We have already seen in section 2.2 that there is a profound difference between the effective masses of electrons and photons in uniform isotropic media; for photons, a straightforward adaptation of (13) to the one-dimensional isotropic case leads to an effective mass of infinity, since the curvature of the  $\omega-k$  diagram for free photons is then zero. Although this reflects the fact that photons cannot be accelerated or decelerated in a one-dimensional isotropic system, it is of little practical significance since to test it would require the creation of a force field for photons - something which is trivial for electrons (simply apply a voltage) but which is unknown for photons. As already pointed out (section 2.2), however, photons may be deflected, when they exhibit a finite effective mass of  $2m_0n$ .

In periodic media, however, it turns out that electrons can acquire some of the properties of photons (e.g., very large effective mass in the direction of motion), and vice-versa (e.g., finite effective mass in the direction of motion). In a PBG dielectric a slowly varying average dielectric constant at fixed optical frequency plays the same role for photons as an electric field does for electrons, permitting an effective mass to be defined and a Newtonian model of their motion to be constructed. Note that other forms of non-uniformity (pitch, refractive index difference) result in a *variable* effective mass and cannot be treated using this approach. At constant optical frequency, the "mass"  $m_0$  and the total energy  $H_0$  in (11) are constant, while the mean value of the potential  $U_0$  is allowed to vary slowly. For formal simplicity, we restrict the analysis to the TE case when the wave equation is scalar. The Hamiltonian may then be written:



$$H_o = \frac{1}{2} \{\mathbf{p}\}^T [1/m_o^*] \{\mathbf{p}\} + W_o(\mathbf{r}) \quad (49)$$

where  $\{\mathbf{p}\}$  is the momentum and  $W_o$  is the slowly varying potential left behind after taking account of the periodic potential  $U_o$  by using  $m_o^*$  rather than  $m_o$  (i.e., the total potential is  $W_o + U_{oo}$ , where  $U_{oo}$  is the mean value of  $U_o$ ). Deriving Hamilton's equations of motion is now straightforward:

$$\begin{aligned} \{\dot{\mathbf{p}}\} &= -\nabla H_o = -\nabla W_o, \\ \{\dot{\boldsymbol{\rho}}\} &= \nabla_p H_o = [1/m_o^*] \{\mathbf{p}\} \end{aligned} \quad (50)$$

where  $\{\boldsymbol{\rho}\}$  is the position vector and  $\nabla_p$  represents the gradient in momentum space. After differentiating the second equation and rearranging we obtain Newton's equations of motion with a force  $-\nabla_p W_o$ :

$$\{\ddot{\boldsymbol{\rho}}\} = -[1/m_o^*] \nabla W_o \quad (51)$$

Notice that, owing to the tensor nature of the reciprocal effective mass, the acceleration is not necessarily in the direction of the changing potential.

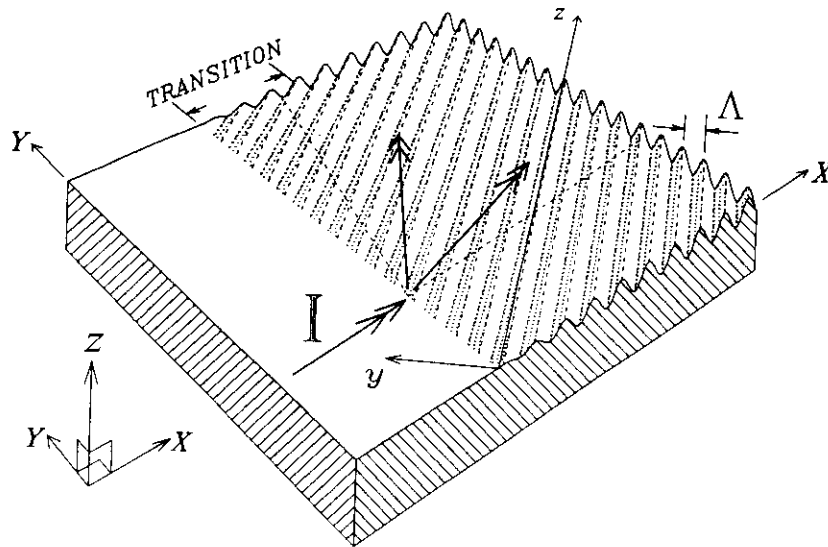


**Figure 16.** Sketch of the experimental set-up for exciting two-dimensional guided Bloch waves in a periodic planar waveguide (140 nm thick film of  $Ta_2O_5$ , on a glass substrate, with an etched corrugation of period 300 nm). A guided mode is launched by prism coupling.

## 7.2 Illustrations From Experiments On Planar Waveguides

Periodic planar waveguides are ideal for studying Bloch wave propagation in two dimensions<sup>54-58</sup>. A sketch of the experimental set-up for excitation (by prism coupling) of a typical corrugated planar waveguide is given in Figure 16; a narrow beam is launched in the non-periodic guide region, travelling towards the periodic region, where it excites guided two-dimensional Bloch waves that can be observed (via the scattered light from the

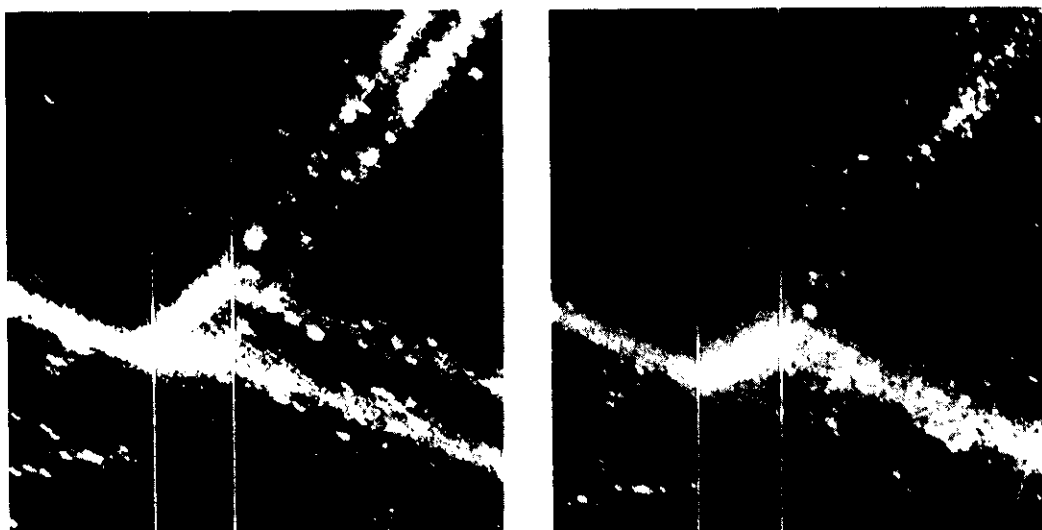
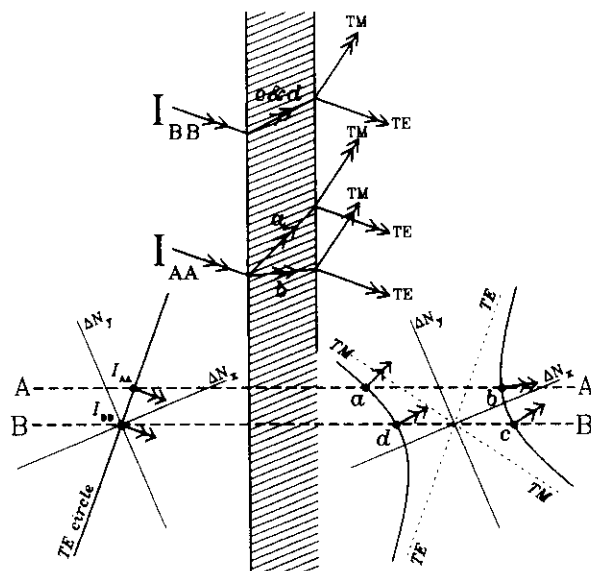


**Figure 17.** *Upper:* Double ( $I_{AA}$ ) and single ( $I_{BB}$ ) negative refraction at a parallel slab containing a singly periodic structure; note the use of the wavevector diagram to match the boundary conditions. Because the conversion is TE/TM, the asymptotic circles that cross at the stop-band centre have different radii; this causes an asymmetric stop-band. *Lower:* Photographs of the effect in a corrugated planar waveguide (slab width 1 mm). The grating lines are slanted upwards to the right as shown schematically.

inevitably imperfect guide) by eye. In the experiments described in this section, the waveguide is formed from a layer  $\sim 140$  nm thick of  $\text{Ta}_2\text{O}_5$  (index 2.12), deposited by rf sputtering onto a glass substrate (index 1.472). For these parameters, solutions of (4) yield guided mode refractive indices of 1.775 (TE) and 1.569 (TM) at 632.8 nm. The waveguides were etched with a periodic pattern to form a corrugated upper surface with

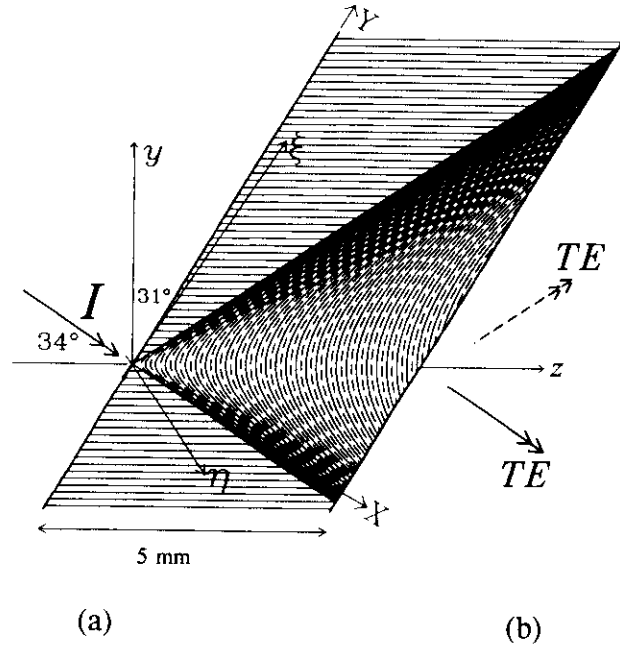
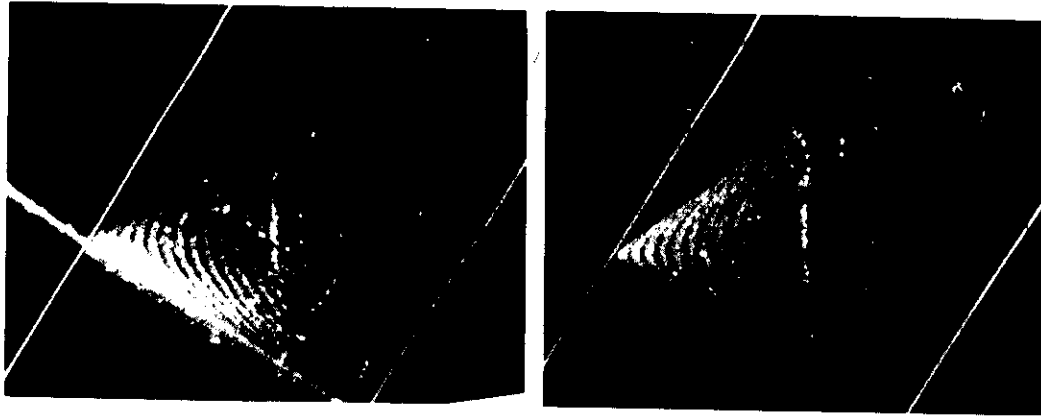


**Figure 18.** Point influence function for the fields in a singly-periodic medium (grating lines horizontal). Note how the power spreads out over a region bounded by the upper and lower Bragg angles (upper and lower edges of triangular region containing the fringes), and how interference occurs owing to spatial superposition of Bloch waves from opposite sides of the stop-band.

a pitch of 300 nm.

Two things are needed to understand completely the propagation of a wave: its phase velocity (for boundary condition matching); and its group velocity (for predicting where it's going). Both are available simultaneously on the wavevector diagram for the periodic waveguide. As explained in section 5, the phase velocity is given by  $(\omega/|\mathbf{k}|^2)\mathbf{k}$ , where  $\mathbf{k}$  is the vector between the origin of wavevector space and a point on the wavevector diagram; and the group velocity points normal to the curves, in the direction

of increasing frequency (denoted by double-headed arrows in the figures in this section). Since the waveguide supports both TE and TM modes, Bragg conditions exist for TE/TE, TE/TM, TM/TE and TM/TM modal coupling. In Figure 17 the collision of a narrow TE-polarized guided-beam with a parallel-sided periodic region is illustrated; the coupling is between TE and TM polarized guided modes. The beams incident from the uniform region have wavevectors that sit on the arc of the TE circle (points  $I_{AA}$  off-Bragg and  $I_{BB}$  on-Bragg in the figure). The Bloch waves excited within the grating are found by matching

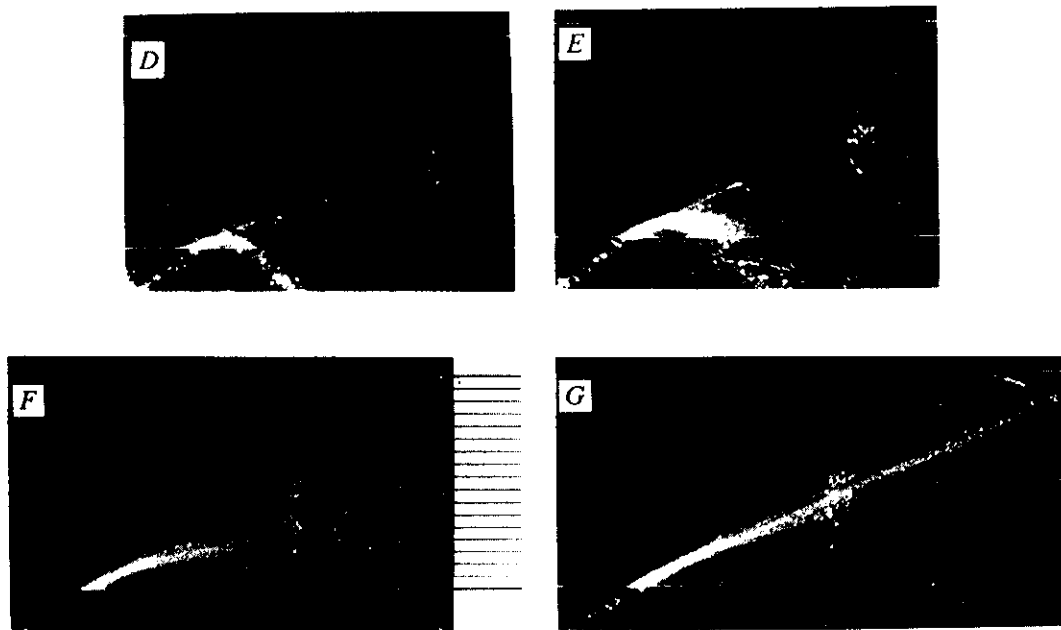


**Figure 19a.** Propagation of Bloch waves in grating with non-uniform average refractive index. In the experiment,  $n_{av}$  peaked in the centre of the parallel-sided periodic region 1.5 mm thick (see case *F* for orientation of grating lines). The conversion is TE-TM. The cases *D-G* are for different mean angles of incidence of a bundle of convergent rays. Notice the curved paths taken by the rays; the average index "hill" is viewed as a potential barrier by the light. See Figure 19b for the results of an effective mass analysis.

wavevector components along the boundary. A simple graphical construction (similar to the one used in section 1.2) achieves this; construction lines AA and BB are drawn normal to the boundary, passing through points  $I_{AA}$  and  $I_{BB}$ . These intersect with the stop-band branches in reciprocal space at the points associated with the Bloch waves excited inside the periodic structure. The normals to the stop-band branches at these points lie parallel to the group velocities of the Bloch waves, i.e., their rays. Notice that *single negative* refraction occurs on-Bragg (both Bloch waves sharing the same ray paths), and that *double*

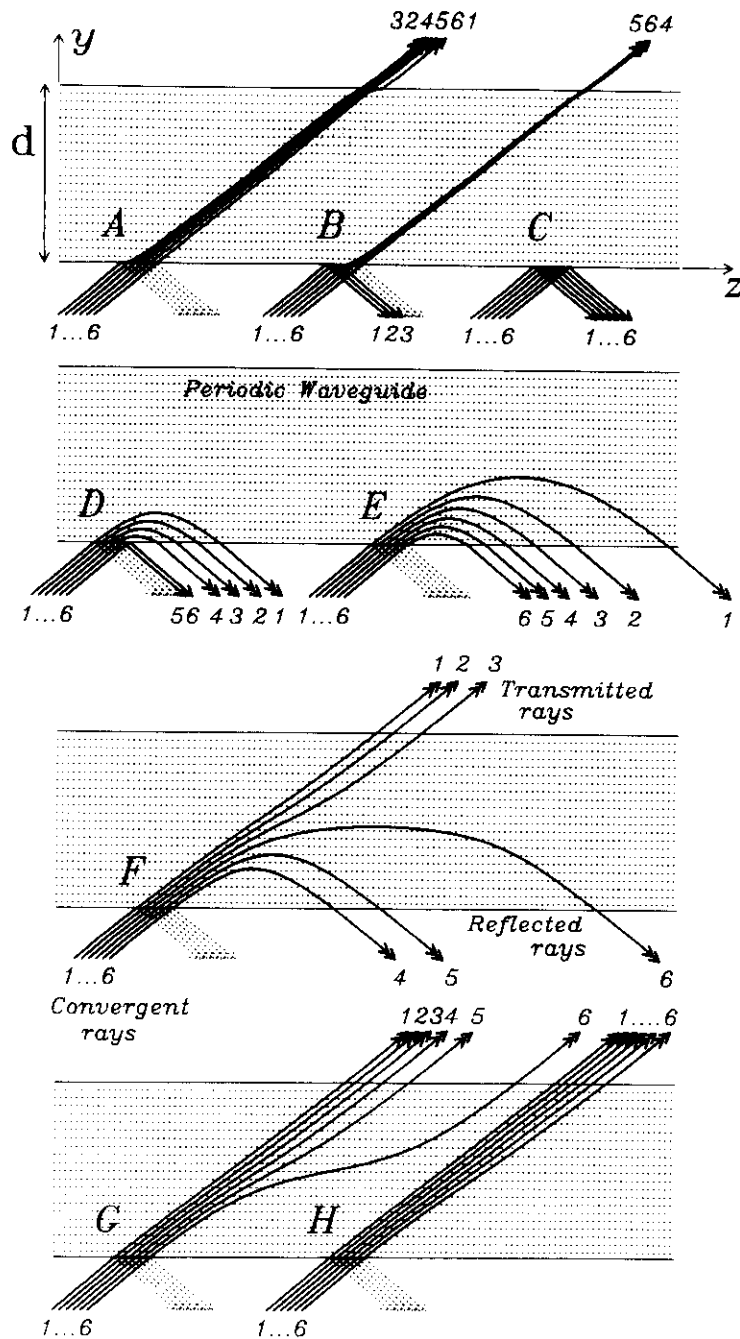


**Figure 19b.** The photographed behaviour in Figure 19a is qualitatively well predicted by a simple ray tracing procedure, based on the effective mass method described in the text. The sketches *A-H* are for different mean angles of incidence of a bundle of convergent rays. Cases *D-G* correspond most closely to the four experimental cases.

*negative* refraction occurs off-Bragg (each Bloch wave having a different ray path). Note that the behaviour is a sensitive function of the incident angle. At the output surface, the same boundary matching procedure yields the directions of the exit beams.

When the incident beam is tightly focused, its angular plane wave spectrum can spread over the entire stop-band<sup>57,58</sup>. By analogy with electronic band theory<sup>23,25</sup>, this type of excitation is approximately described by a kind of incomplete "spatial Wannier function", i.e., the integral of all the photonic Bloch states present in the stop-band portion of a Brillouin zone. In a weak singly periodic structure, these functions take the form of Bessel functions, and may be interpreted as point influence (Green's) functions (Appendix A3.1)<sup>55</sup>. They describe the diffractive spreading that occurs after point excitation of a grating. An example of one of these functions in operation is given in Figure 18, where a grating with a slanted input boundary is excited with a narrow focused beam; the spreading out over a triangular region bounded by the upper and lower Bragg angles is plain. Notice the fine periodic pattern in the photograph; this is caused by the interference of Bloch waves<sup>57</sup>. Since both branches of the stop-band are excited simultaneously in Figure 18, sharp interference fringes form between Bloch waves on opposite sides. These fringes have a spatial period  $\Lambda_f = 2\pi/|\delta|$ , where  $\delta$  is the wavevector drawn between two points in reciprocal space associated with spatially coincident Bloch waves. The fringe orientation is normal to  $\delta$ . For a weak grating, the position of these fringes in space is accurately described by the zeros in the Bessel functions in Appendix A3.1. An intriguing situation arises when the group velocities of both Bloch waves point across the fringes; this appears to violate power conservation. In fact, no visible fringes (in the form of spatial variations in power density) form in the total field under these circumstances; instead, a kind of virtual interference somewhat akin to the "interference" of orthogonally polarized waves takes place<sup>57</sup>. In the photographs, the fringe visibility was enhanced by using a polarizer to block out the scattering from the upward or downward constituent plane waves of the fields.

In strongly modulated structures, interference may be suppressed owing to the disappearance of the left hand stop-band branch; as we have already seen, the wavevector diagram then becomes quite distorted (Figure 14), with "photonic band window" regions (where the group velocity hardly changes direction over an entire half Brillouin zone, pointing only very slightly normal to the planes). This is the wavevector diagram's view of resonant tunnelling across a waveguide array. Under the tight-binding approximation, the Wannier function is a spot the size of a unit cell, i.e., approximately a waveguide mode. Once excited, this waveguide mode spreads out sideways into the adjacent guides (see Figure 14 and Appendix A3.2).

A simple example of propagation in a spatially non-uniform structure, illustrating use of the effective mass method, is given in Figures 19a&b. A region of periodic waveguide, with straight parallel boundaries and a slowly changing average index that peaks in the centre, is excited by a narrow focused beam (see figure caption for more details).

Note in conclusion that it is not possible to set up a simple Newtonian model for cases where the grating period and strength vary with position, because under these circumstances the curvature of the  $H_o - \mathbf{k}$  diagram (and hence the effective mass tensor) depends both on position and the previous history of the ray path. In this case, a split-step propagation method can be used, finite steps through real and reciprocal space being made alternately, matching ray direction and phase velocity in each cycle.

## 8. EXTENSION TO MULTIPLY PERIODIC STRUCTURES

There has already been a focused and successful effort in Europe and North America on calculating the photonic band structure of multiply periodic PBG structures in two and three dimensions<sup>1,7,9-22</sup>. This work is covered in other chapters within this volume. But how useful is the intuitive picture developed in this chapter for understanding the

behaviour of these more complicated media? The various tools we have introduced (Brillouin diagrams, wavevector diagrams, band edge diagrams) remain indispensable if all aspects of propagation are to be well understood. The tight-binding and nearly free approximations are also still valid, although the nature of the micro-resonances is

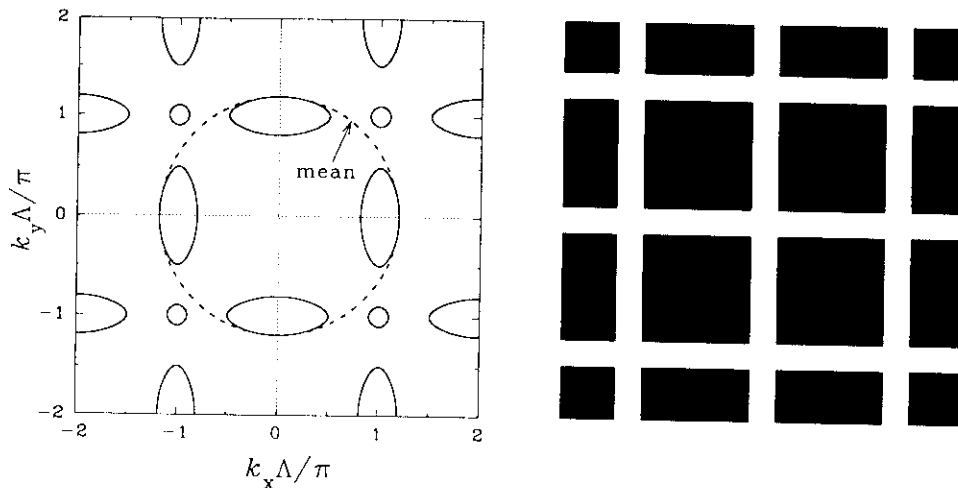


**Figure 20.** Wavevector diagram (left) for cubic lattice depicted on the right. The diagram was calculated using the method in references 16 & 22 for  $n_R = 0.47$ ,  $\tau = a_2/a_1 = 0.56$ ,  $\nu = 1.19\pi$ ,  $n_{av} = \sqrt{\{(a_1 n_1^2 + a_2 n_2^2)/A\}} = 1.8$  where  $a_1$  and  $a_2$  are the areas of the high and low index regions within a unit cell, whose area is  $A$ . For example, 400 nm wide square pillars of  $\text{Ta}_2\text{O}_5$ , separated by 200 nm air gaps would give this wavevector diagram at a wavelength of 1515 nm in vacuo.

considerably more complicated in three dimensions. Also, the second term in (11) can no longer be ignored - coupling between orthogonal field components occurs at the interfaces in the unit cells, resulting in polarization mixing. The tight-binding approximation can be usefully generalized to three dimensions, whether the picture is of coupled arrays of tubular waveguides, dielectric boxes, ellipsoids, spheres or more complicated entities. All these will support micro-resonances if excited appropriately (i.e., correct wavevector and frequency), in which case an analysis based on nearest-neighbour coupling can be used (see section 1.2.6).

Compared to the electronic case (with its simpler scalar wave equation), the calculation of photonic band structure is actually *easier* in one respect: the potential in each unit cell is precisely known, and does not change as the photons are redistributed (in the absence of optical nonlinearities). This means that band structure calculations for photons are actually more accurate.

The success of structures in which low index islands are surrounded by narrow seas of high index material (as in Yablonovitch's crystals<sup>7</sup>) may be due to the flattening of the Brillouin zone boundary owing to the absence of high-Q micro-resonances that would tend to pull (when resonant) the band gap edges together, at the same time forcing the band gap to lower or higher values.

Finally, the wavevector diagram generalises very nicely to multiply periodic structures in two dimensions, and an example of how it looks for a cubic lattice (calculated using the method reported by Pendry and MacKinnon<sup>16,22</sup>) is given in Figure 20. Some more examples are available, together with two-dimensional field intensity profiles, in

reference 5. A useful paper containing experimental results on propagation in doubly periodic planar waveguides has been written by Zengerle<sup>58</sup>.

## 9. MISCELLANEOUS TOPICS

In this section we briefly discuss the relevance of our results on singly-periodic structures to a variety of different circumstances, including the properties and control of surface states and defect modes, the effects on photonic band structure of optical nonlinearity and optical gain, the extension to multiply periodic structures, and applications of photonic band gap materials.

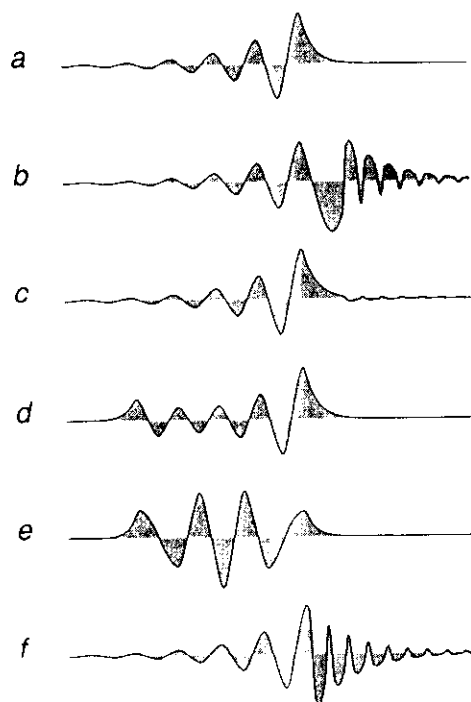


**Figure 21.** Different types of defect modes that can exist on or between multi-layer stacks: a) single surface guided mode (SGM); b) travelling waves bounded by Bragg reflection (high index intervening layer); c) two SGM's coupled by evanescent fields (low index intervening layer); d) two coupled SGM's on opposite sides of same stack; e) bound mode of finite stack formed from two travelling Bloch waves; f) SGM at the interface between two different multi-layer stacks.

### 9.1 Localised Modes, Defects and Surface-Guided States

As with any wave, Bloch waves can be quantized by truncating the medium in which they exist. This has the effect of reducing the spectral density of states (i.e., the number of states per unit frequency in a given volume of material) by localising them between the boundaries. Several other different sorts of localised modes can exist in multi-



layer stacks, however, as illustrated in Figure 21; most (not all) of these have been previously reported in the literature<sup>75-87</sup>. The range of possibilities is much richer than in isotropic media, mainly due to one thing: total reflection can be produced in ranges of  $\beta$  (the band gaps) where, based on  $n_{av}$ , the stack would be expected to be transparent. This

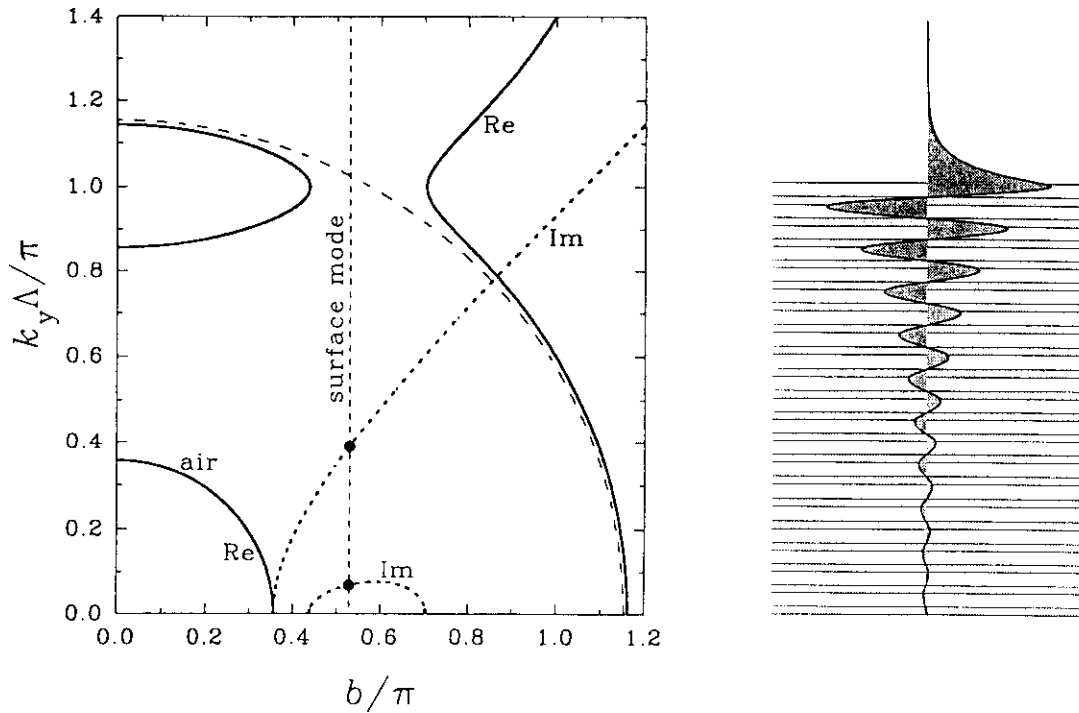


**Figure 22.** Wavevector diagram illustrating condition for formation of a particular surface guided mode ( $\tau = 0.59$ ,  $n_R = 0.84$ ,  $\nu = 1.15\pi$ ; last TE polarised; amplitude distribution depicted on the right). The parameters are for an AlAs/GaAlAs stack at 830 nm, and the thickness of the final high index layer, normalised to  $\Lambda$ , is 0.036. As the thickness of this layer is reduced, the  $\beta$  value of the mode moves from the right-hand side of the stop-band to the left.

means that a single interface mode in each polarisation state can exist between the surface of a stack and a medium of low refractive index. The general approach to finding the bound modes is straightforward provided the expressions for the field distributions are chosen carefully, with the field distribution in the defect layer between two stacks referred to the centre as in (20). For a single surface mode the analysis is particularly simple, leading to the following dispersion equation:

$$p_j(y_e - y_j) - \arctan \left[ \frac{\xi_e p_e \Lambda a_j + b_j}{\xi_j p_j \Lambda a_j - (\xi_e p_e / \xi_j p_j) b_j} \right] = m\pi \quad (52)$$

where the parameters with subscripts  $j$  are those belonging to the last partial layer of the stack, the position of the edge is  $y = y_e$  and the amplitude decay rate into the external isotropic medium is:

$$p_e = \sqrt{\beta^2 - (kn_e)^2} \quad (53)$$

where  $n_e$  is the external index and  $\xi_e = 1$  for TE and  $1/n_e^2$  for TM polarisation. The conditions for formation of a surface mode are best understood by reference to the wavevector diagram (Figure 22), because this reveals clearly the location of the band gaps

for a particular stack, and hence the ranges of  $\beta$  within which a surface wave can exist. They may form for values of  $\beta > kn_e$  that at the same time lie within a band gap of the stack, and they only exist if the final layer has an appropriate thickness. This means that they may easily be suppressed if desired (although perhaps not in both polarization states) by appropriately designing the stack. We plan to discuss these modes at length elsewhere. It is interesting to point out in addition that TE and TM surface plasmon modes with hugely different propagation constants can also exist at the interface between a metal and a stack; they may of course exist (since a metal forbids any propagation whatsoever) at normal incidence  $\beta = 0$ , creating a resonator with just one mode. Similar stationary localised modes can also exist at the interface between two different multi-layer stacks. Surface photonic states are directly analogous to the electronic surface states in the solid-state, and can appear on multiple quantum well structures<sup>83</sup>.

## 9.2 Effects of Optical Gain: Lasers

Since one of the major applications of photonic band gap materials is in lasers, it is worthwhile considering the effect that optical gain may have on the passive dispersion. It has been known for a long time that the  $\omega$ - $k$  relationship is strongly affected if the gain  $g$  (per unit length) and the grating strength  $\kappa$  (the well-known coupling constant defined in Appendix A3.1) are comparable, i.e., if:

$$\kappa/g \sim 1 \quad (54)$$

or smaller; this is commonly the case in a distributed feed-back (DFB) semiconductor laser<sup>35,37</sup>. Alterations in  $k_y$  for a given frequency  $\omega$  (Figure 23) will of course alter the frequencies at which a cavity will resonate, which might be of importance in some contexts such as dense wavelength-division-multiplexing applications. In contrast to DFB lasers, this is unlikely to be a matter of much concern in PBG materials where the grating strength (perhaps  $6\pi$  per  $\mu\text{m}$  in Yablonovitch's proposed PBG AlGaAs structures<sup>7</sup>) is certain to be much greater than the gain. Of more concern is unwanted lasing outside the band gap. DFB lasers in their purest form consist of a defect-free length of grating - a kind of one-dimensional PBG structure. Laser oscillation occurs at two frequencies symmetrically placed on either side of the band gap, where the photonic states are real while the reflection is still strong enough to provide substantial feedback. In materials with broad unwanted bands of high gain it may be difficult to produce a band gap wide enough to suppress lasing completely. The etching process used to produce a PBG in a semiconductor laser material will inevitably concentrate the gain in the high index regions. This will tend to favour Bloch modes whose photonic probability distribution peaks in the high gain regions, and may often result in suppression of laser oscillation on one side of the band gap. In the language of quantum photodynamics, the expectation value of the gain will be higher on one side of the band gap compared to the other. An early example of a related phenomenon is the Borrmann effect (1941), where x-rays experience anomalously low absorption at the Bragg condition in an  $\alpha$ -quartz crystal. This is caused by the x-ray Bloch waves on the inner stop-band branch (see Figure 11) experiencing less absorption than those on the outer branch, since their probability distributions peak *in between* the atoms where the absorption is concentrated<sup>31</sup>.

## 9.3 Effects of Optical Nonlinearity: Gap Solitons

The ability to pack as many photons as desired into each photonic state means that optical Kerr nonlinearities can become important at high optical intensities. If the nonlinear index change is comparable to the index modulation depth in the PBG material, the stop-

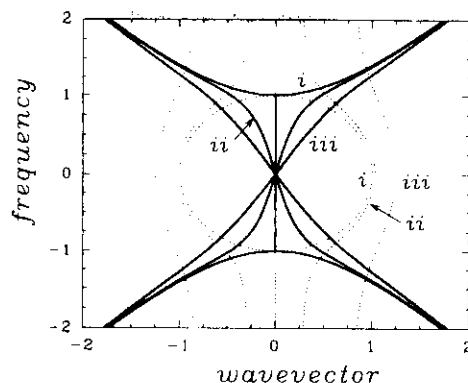


**Figure 23.** Stop band distortion in the presence of optical gain; the ratio of  $g/\kappa$  is 0, 0.25 and 0.75 respectively in the three cases *i*, *ii* and *iii*. The vertical axis is frequency deviation from the Bragg condition, normalised to half the band gap width, and the horizontal axis is  $k_y - K/2$ , normalised to the coupling constant  $\kappa$ . The full and dotted lines are based on the real and imaginary parts of  $k_y$ .

band branches become significantly distorted<sup>74</sup>; the dispersion and the nonlinearity are then closely entangled. As recently studied by John and Aközbek<sup>67</sup>, this can result in the appearance, within a linear three-dimensional photonic band gap, of real states induced by the nonlinearity. These densely occupied photonic states trapped by their own nonlinearity are in fact related to gap solitons<sup>68-73</sup>. The presence of optical nonlinearity outside the band gap in a region of strong spatial dispersion can also result in strong nonlinear beam-steering, since the group velocity of the Bloch waves is then a function of power.

We have seen that the effective mass of photons becomes small close to a band edge; this means that scattering centres that would have a negligible effect on free photons can strongly scatter a photon in a Bloch state. The interaction (collision cross-section) is greatly increased by the small group velocity (momentum) of the Bloch wave (photon). This has important implications in stimulated Brillouin scattering. Two travelling counter-propagating Bloch waves with frequencies close to the band edge on the same side of a band gap will be coupled together very strongly by a low frequency, low momentum acoustic wave<sup>32,33</sup>. This is because the expectation value of the momentum difference between backward and forward Bloch waves can itself be very small, and the coupling strength depends on the reciprocal of the group velocity, which also goes to zero at the band edge. Raman scattering may similarly be enhanced if the band gap is sufficiently large to allow both the Stokes and anti-Stokes Bloch waves to possess small group velocities close to the same band edge. Nonlinear interactions *across* a band gap are unlikely to be significant since the Bloch functions do not overlap strongly spatially.

#### 9.4 Applications of Photonic Band Gap Materials

Since PBG materials are essentially synthetic (although natural biology or bio-engineering may be able to contribute some useful structures), there has to be a good reason for going to the trouble (and expense) of making them. Hence the importance of the question: What use are they? Interpreted in the widest sense, they may be viewed as synthetic effective index media with highly unusual anisotropic refractive indices, diffractive properties and substantial ranges of angle and frequency where propagation is

forbidden. Independent control of phase and group velocity is possible, which is like saying that conventional optics (with only a restricted range of anisotropic molecular polarizabilities at its disposal - those naturally occurring in crystals) can be augmented or even superseded, with many new features.

A common problem in waveguide optics is creating phase-matched single modes in low and high index materials. In conventional guided wave optics, the mode indices

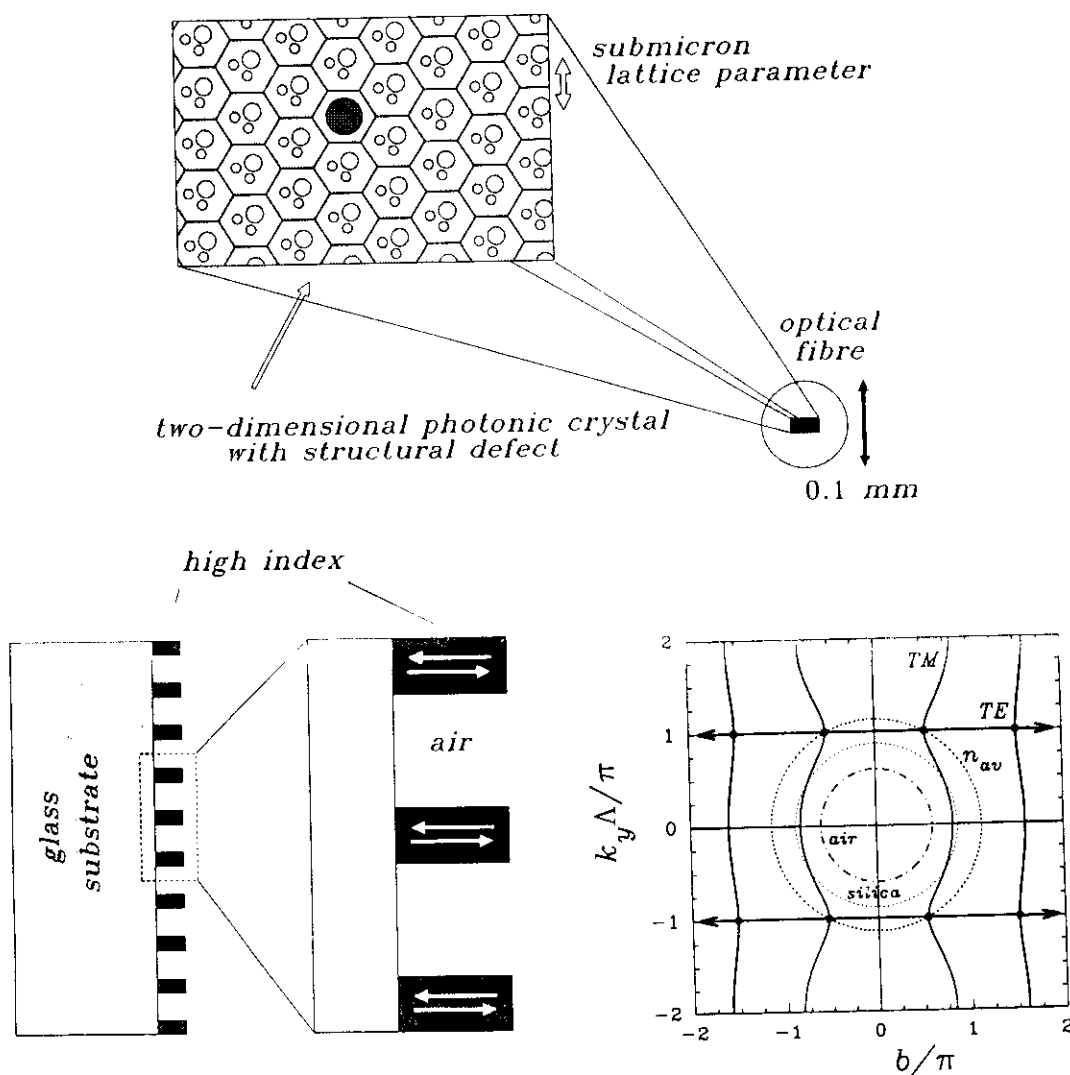


**Figure 24.** Two examples of structures that will exhibit unusual photonic band gap effects: (a) A holey fibre, whose core is a two-dimensional photonic crystal with structural defects where the light is trapped; strong anisotropy can be built in; and (b) A resonator made from a single periodically etched-through layer of dielectric material ( $\text{Ta}_2\text{O}_5$ , index 2.12) that completely confines light in a localised state. Its wavevector diagram is also shown; the group velocity at the Brillouin zone edge points normal to the layer, and the related Bloch wave cannot escape because its lowest order plane waves are totally internally reflected at the left and right boundaries.

must lie in between the substrate and the film index. Surface guided Bloch waves neatly side-step this restriction<sup>87</sup>, permitting for example a single surface mode on a high index multi-layer stack to be phase-matched to the light guided in a single-mode silica fibre, or enhancing the penetration of light into a low index external medium such as an aqueous solution containing some chemical to be sensed. This may have important potential

applications in biological and chemical sensing. Multi-layer stacks in AlGaAs, for example, can be designed to support surface Bloch modes with indices lying between air and the maximum index of the stack (around 3.5).

There are many potential uses of localised single states in PBG materials<sup>77</sup>. These can be created by introducing a structural defect at one point in a grating; this could be a slight local variation in average index or grating modulation depth. When appropriately designed, a single-mode photonic defect state appears that occupies a volume of space substantially larger than is possible in a conventional single-mode two-mirror lasing cavity. Single-frequency laser oscillation then becomes feasible in materials whose optical gain is normally too low.

The creation of a structural defect, by the addition of less/more high index material in a unit cell, results in localised modes whose frequency lies within the band gap close to the upper/lower band edge; these may be regarded as donor/acceptor states by analogy with semiconductors<sup>76</sup>. The process of donation and acceptance involves shifting a photon between a localised and an almost-localised state (just outside the band gap) at a different frequency. How this might be achieved is an interesting question - perhaps by the photonic crystal equivalent of an optical phonon?

Many interesting applications of PBG materials have already been reported<sup>4,5,9,17,39,40</sup>. Two examples from our own work of exotic structures with potentially useful properties are illustrated in Figure 24. The "holey" fibre (Figure 24a) is a glass optical fibre with a two-dimensional crystalline core region and a central defect that traps photons while permitting them to travel along the fibre axis. Many useful properties can be built into the crystal structure, such as various types of optical anisotropy, and very strong lateral confinement can be achieved in the photonic band window range of the band edge diagram (Figure 13). An unusual resonator forms if a high index film is etched with a periodic pattern as illustrated in Figure 24b. At the correct wavelength and film thickness, a tightly confined stationary optical mode exists, with zero group velocity along the film. This cavity, made entirely from a small volume of material, could have a very high Q and be phase-matched to an optical fibre mode.

In one important respect, band gap engineering - the optimisation of the performance of a PBG crystal by changing the geometry of the unit cell - may be somewhat easier for photons, at least at the design stage. This is because the "grainy-ness" of dielectric material is much less for photons than for electrons (atoms are not easily divisible!). Hence it is likely that new effects can be "engineered in" based on features fractions of a period in thickness; for example, anti-surface wave layers could be coated on to a multi-layer stack or a PBG crystal to prevent lasing in unwanted surface modes.

## 10. IN CONCLUSION

In moving away from a traditional plane wave approach towards one based on Bloch waves, photonic band theory provides an alternative conceptual framework for thinking about light in periodic structures, and provides the starting point for a full "quantum photo-dynamical" description of photons in PBG media. This is well illustrated by the discussion of electromagnetic wave propagation in singly-periodic structures presented here. For many years, the response of laser designers to a problem of lifetimes and unwanted transitions has been to try to alter the electronic properties of the material itself. This has paid off handsomely in the quaternary III-V system, and seems set to do so again in the II-VI system for blue lasers<sup>42</sup>. Photonic band gap materials offer an additional powerful means of altering the fluorescence properties of a material without having to tamper directly with its electronic structure. The implications of a Bloch wave approach, brought into the limelight by Yablonovitch's proposal that photonic band gaps

could exist by analogy with electronic band gaps, have still to be fully worked out. One immediate benefit, however, is a sea-change in approach within optics that seems certain to lead to new applications based on a re-interpretation of the physics of light in periodic structures.

## 11. ACKNOWLEDGEMENTS

The authors wish to thank Jacek Generowicz for carrying out the numerical modelling for Figure 20, Tim Sluckin and Chris Pannell for many useful discussions, and Dale Atkin for checking the manuscript. Partial support for the work on surface guided modes is provided by the U.S. Department of the Air Force through the European Office of Aerospace Research and Development, London, and the PBG fibre work is being supported by the Defence Research Agency, Malvern. The experimental results were obtained by Philip Russell at the Technische Universität Hamburg-Harburg in 1982-84, with the support of the Alexander von Humboldt Foundation. The Optoelectronics Research Centre is funded by the U.K. Science and Engineering Research Council.

## 12. REFERENCES AND READING GUIDE

*The references are sorted into subjects, so do not appear in numerical order in the text. The asterisked items are suggested sources for introductory reading or background material.*

### Photonic Band Gaps

- 1.\* W. van Haeringen and D. Lenstra (Editors), "Analogies in Optics and Microelectronics," Kluwer Academic Publishers, Dordrecht (1990).
- 2.\* S. John, "Localization of light," *Physics Today* **44** (32-40) 1991
- 3.\* I. Amato, "Designing crystals that say no to photons," *Science*, **255** (1512) 1992.
- 4.\* H.O. Everitt, "Applications of photonic band gap structures," *Optics and Photonics News* (20-23), November 1992.
- 5.\* P.St.J. Russell, "Photonic Band Gaps," *Physics World* **5** (37-42) 1992.
- 6.\* C.M. Bowden, J.P. Dowling and H.O. Everitt (Editors), "Development and Applications of Materials Exhibiting Photonic Band Gaps," feature section in *J. Opt. Soc. Am.* **10** (279-413) 1993.
- 7.\* E. Yablonovitch, "Photonic band gap structures," *J. Opt. Soc. Am.* **10** (283-295) 1993
- 8.\* Special issue of *J. Modern Optics* on Photonic band structure, to be published, 1994.
9. G. Kurizki and A.Z. Genack, "Suppression of molecular interactions in periodic dielectric structures," *Phys. Rev. Lett.* **61** (2269-2271) 1988.
10. K.M. Ho, C.T. Chan and C.M. Soukoulis, "Existence of a photonic band gap in periodic dielectric structures," *Phys. Rev. Lett.* **65** (3152-3155) 1990.
11. K.M. Leung and Y.F. Liu, "Full vector wave calculation of photonic band structures in face-centered-cubic dielectric media," *Phys. Rev. Lett.* **65** (2646-2649) 1990.
12. Z. Zhang and S. Satpathy, "Electromagnetic wave propagation in periodic structures: Bloch wave solution of Maxwell's equations," *Phys. Rev. Lett.* **65** 2650-2653) 1990.
13. M. Plihal and A.A. Maradudin, "Photonic band structure in two-dimensional systems: The triangular lattice," *Phys. Rev.* **B44** (8565-8571) 1991.
14. E. Yablonovitch and T.J. Gmitter, "Photonic band structure: The face-centered-cubic case employing nonspherical atoms," *Phys. Rev. Lett.* **67** (2295-2298) 1991.
15. P. R. Villeneuve and M. Piché, "Photonic band gaps in two-dimensional square lattices: Square and circular rods," *Phys. Rev.* **B46** (4973-4975) 1992.
16. J.B. Pendry and A. MacKinnon, "Calculation of photon dispersion relation," *Phys. Rev. Lett.*, **69** (2772-2775) 1992.
17. E.R. Brown, C.D. Parker and E. Yablonovitch, "Radiation properties of a planar antenna on a

- photonic-crystal substrate," *J. Opt. Soc. Am.* **10** (404-407) 1993.
18. S.Y. Lin and G. Arjavalingam, "Tunnelling of electromagnetic waves in two-dimensional photonic crystals," *Opt. Lett.* **18** (1666-1668) 1993.
  19. A.A. Maradudin and A.R. McGurn, "Photonic band structure of a truncated, two-dimensional, periodic dielectric medium," *J. Opt. Soc. Am.* **10** (307-313) 1993.
  20. R.D. Meade, A.M. Rappe, K.D. Brommer and J.D. Joannopolous, "Nature of the photonic band gap: some insights from a field analysis," *J. Opt. Soc. Am.*, **10** (328-332) 1993.
  21. H. S. Sözüer and J.W. Haus, "Photonic bands: simple-cubic lattice," *J. Opt. Soc. Am.* **10** (296-302) 1993.
  22. J.B. Pendry, "Photonic band structures," to be published in *J. Mod. Opt.*, 1994.

### Electrons in Solids

- 23.\* N.W. Ashcroft and N.D. Mermin, "Solid State Physics," Harcourt Brace College Publishers, Fort Worth (1976).
- 24.\* J.S. Blakemore, "Solid State Physics," Cambridge University Press, Cambridge, 1991.
- 25.\* H. Haken, "Quantum Field Theory of Solids," North-Holland, Amsterdam (1988).
25. C. Kittel, "Quantum Theory of Solids," John Wiley & Sons, New York (1987).

### Electromagnetic Waves and Periodic Structures

- 26.\* J.R. Reitz, F.J. Milford and R.W. Christy, "Foundations of Electromagnetic Theory," 3rd edition, Addison-Wesley Publishing Company, Massachusetts (1979).
- 27.\* L. Solymar and D.J. Cooke, "Volume Holography and Volume Gratings," Academic Press, London (1981).
- 28.\* P. Yeh, A. Yariv and C.-S. Hong, "Electromagnetic propagation in periodic stratified media. I & II," *J. Opt. Soc. Am.* **67** (423-448) 1977
- 29.\* P. Yeh, "Optical Waves in Layered Media," Wiley, New York (1988).
30. L. Brillouin, "Wave Propagation in Periodic Structures," McGraw-Hill, New York (1946); "Wave Propagation and Group Velocity," Academic Press, New York (1960).
31. P.St.J. Russell and L. Solymar, "Borrmann-like anomalous effects in volume holography," *Appl. Phys.* **22** (335-353) 1980.
32. P.St.J. Russell, "Bragg resonance of light in optical superlattices," *Phys. Rev. Lett.* **56** (596-599) 1986.
33. P.St.J. Russell, "Optical superlattices for modulation and deflection of light," *J. Appl. Phys.* **59** (3344-3355) 1986.
34. E.N. Economou and A. Zdetsis, "Classical wave propagation in periodic structures," *Phys. Rev.* **B40** (1334-1337) 1989.

### Distributed Feedback Lasers and Micro-Cavities

- 35.\* H. Kogelnik and C.V. Shank, "Coupled-wave theory of distributed feedback lasers," *J. Appl. Phys.* **43** (2327-2335) 1972.
- 36.\* D.S. Chemla (editor), "Optics of Nanostructures," special issue of *Physics Today* **46** (22-73) 1993.
- 37.\* F.K. Kneubühl, "Theories of Distributed Feedback Lasers," Harwood Academic Publishers, Switzerland (1993).
38. S.L. McCall and P.M. Platzman, "An optimised  $\pi/2$  distributed feedback laser," *IEEE J. Quant. Electr.* **QE-21** (1899-1904) 1985.
39. D.L. Bullock, C.-C. Shih and R.S. Margulies, "Photonic band structure investigation of two-dimensional Bragg reflector mirrors for semiconductor laser mode control," *J. Opt. Soc. Am.* **10** (399-403) 1993.
40. T. Erdogen, K.G. Sullivan and D.G. Hall, "Enhancement and inhibition of radiation in cylindrically symmetric periodic structures," *J. Opt. Soc. Am.* **10** (391-398) 1993
41. Y. Yamamoto and R.E. Slusher, "Optical processes in microcavities," *Physics Today* **46** (66-73) 1993.
42. N. Nakayama, S. Itoh, T. Ohata, K. Nakano, H. Okuyama, M. Ozawa, A. Ishibashi, M. Ikeda and Y. Mori, "Room temperature continuous operation of blue-green laser diodes," *Electr. Lett.* **29** (1488-1489) 1993.

## Optics, Waveguides and Optoelectronics

- 43.\* E. Hecht and A. Zajac, "Optics," Addison-Wesley Publishing Company, Massachusetts (1974).
- 44.\* M. Born and E. Wolf, "Principles of Optics," fifth edition, Pergamon Press, Oxford (1975).
- 45.\* T. Tamir (editor), "Integrated Optics," Springer-Verlag, Berlin (1979).
- 46.\* H. Haken, "Light," volume 1: Waves, Photons, Atoms, North Holland, Amsterdam (1981).
- 47.\* A. Korpel (Editor), "Selected Papers on Acoustooptics," SPIE Optical Engineering Press, volume MS16, Bellingham, Washington (1990).
- 48.\* D. Marcuse, "Theory of Dielectric Optical Waveguides," 2nd edition, Academic Press, Boston (1991).
- 49.\* A. Yariv, "Optical Electronics," 4th edition, Harcourt Brace College Publishers, Fort Worth, (1991).
- 50.\* H.A. Haus, "Waves and Fields in Optoelectronics," Prentice-Hall, Englewood Cliffs (1984).
51. J.A. Arnaud, "Beam and Fibre Optics," Academic Press, New York (1976).
52. E. Garmire, Semiconductor components for monolithic applications, in: "Integrated Optics," T. Tamir, ed., Springer-Verlag, Berlin (1979).
53. A.W. Snyder and J.D. Love, "Optical Waveguide Theory," Chapman and Hall, London (1983).
54. P.St.J. Russell and R. Ulrich, "Elementary and coupled waves in periodic planar waveguides," *2nd European Conference on Integrated Optics*, Florence, IEE Conf. Publication 227 (88-91) October 1983.
55. P.St.J. Russell, "Novel thick-grating beam-squeezing device in Ta<sub>2</sub>O<sub>5</sub> corrugated planar waveguide," *Electr. Lett.* **20** (72-73) 1984.
56. P.St.J. Russell, "Optics of Floquet-Bloch waves in dielectric gratings," *Appl. Phys.* **B39** (231-246) 1986.
57. P.St.J. Russell, "Interference of integrated Floquet-Bloch waves," *Phys. Rev. A* **33** (3232-3242) 1986.
58. R. Zengerle, "Light propagation in single and doubly periodic planar waveguides," *J. Mod. Opt.* **34** (1589-1617) 1987.

## X-ray Diffraction

- 59.\* J.M. Bijvoet, W.G. Burgers and G. Hägg, "Early Papers on Diffraction of X-rays by Crystals," A. Oosthoek's Uitgeversmaatschappij N.V., Utrecht (1969).
- 60.\* P.P. Ewald, "Fifty Years of X-ray Diffraction," A. Oosthoek's Uitgeversmaatschappij N.V., Utrecht (1962).
- 61.\* Z.G. Pinsker, "Dynamical Scattering of X-rays in Crystals," Springer-Verlag, Berlin (1978).
- 62.\* J.M. Cowley, "Diffraction Physics," second revised edition, North-Holland (1981).
63. C.G. Darwin, "The theory of x-ray reflexion," *Phil. Mag.* **27** (315-) 1914.

## Nonlinear Optics

- 64.\* Y.R. Shen, "Principles of Nonlinear Optics," Wiley Interscience, New York (1984).
- 65.\* A.D. Boardman, M. Bertolotti and T. Twardowski (editors), "Nonlinear Waves in Solid State Physics," NATO ASI Series: Series B: Physics, volume 247, Plenum, New York (1993).
- 66.\* P.N. Butcher and D. Cotter, "The Elements of Nonlinear Optics," Cambridge Studies in Modern Optics, volume 9, Cambridge University Press, Cambridge (1993).
- 67.\* S. John and N. Aközbeke, "Nonlinear optical solitary waves in a photonic band gap," *Phys. Rev. Lett.* **71** (1168-1171) 1993.
68. D.L. Mills and S.E. Trullinger, "Gap solitons in nonlinear periodic structures," *Phys. Rev. B* **36** (947-952) 1987.
69. W. Chen and D.L. Mills, "Gap solitons and the nonlinear optical response of superlattices," *Phys. Rev. Lett.* **58** (160-164) 1987.
70. J.E. Sipe and H.G. Winful, "Nonlinear Schrödinger solitons in a periodic structure," *Opt. Lett.* **13** (133-134) 1988.
71. C.M. de Sterke and J.E. Sipe, "Envelope-function approach for the electrodynamics of nonlinear periodic structures," *Phys. Rev.* **A38** (5149-5165) 1988.
72. A.B. Aceves and S. Wabnitz, "Self-induced transparency solitons in nonlinear refractive periodic media," *Phys. Lett.* **A141** (37-42) 1989.
73. D.N. Christodoulides and R.I. Joseph, "Slow Bragg solitons in nonlinear periodic structures," *Phys. Rev. Lett.* **62** (1746-1749) 1989.



74. P.St.J. Russell and J.-L. Archambault, "Field microstructure and temporal and spatial instability of photonic Bloch waves in nonlinear periodic media," to be published in *J. de Physique III*, 1994; see also paper FrD4, *International Quantum Electronics Conference, IQEC'92*, Vienna, Austria, June 1992.

### Surface States and Defects

- 75.\* P. Yeh, "Optical Waves in Layered Media," Wiley, New York (1988).
- 76.\* E. Yablonovitch, T.J. Gmitter, R.D. Meade, A.M. Rappe, K.D. Brommer and J.D. Joannopoulos, "Donor and acceptor modes in photonic band structure," *Phys. Rev. Lett.* **67** (3380-3383) 1991.
- 77.\* D.R. Smith, R. Dalichaouch, N. Kroll, S. Schultz, S.L. McCall and P.M. Platzman, "Photonic band structure and defects in one and two dimensions," *J. Opt. Soc. Am.* **10** (314-321) 1993.
78. P. Yeh, A. Yariv, A. Cho, "Optical surface waves in periodic layered media," *Appl. Phys. Lett.* **32** (104-105) 1978.
79. W. Ng, P. Yeh, P.C. Chen and A. Yariv, "Optical surface waves in periodic layered medium grown by liquid phase epitaxy," *Appl. Phys. Lett.* **32** (370-371) 1978.
80. A.A. Bulgakov and V.R. Kovtun, "Surface optical oscillations in a bounded layered periodic medium," *Opt. Spectrosc. (USSR)* **56** (471-472) 1984.
81. A.A. Bulgakov and V.R. Kovtun, "Study of surface optical oscillations in periodic multi-layer media," *Solid State Comm.* **56** (781-785) 1985.
82. S.D. Gupta and B. Buti, "Electromagnetic surface waves in periodic layered media," *Indian J. Pure & Appl. Phys.* **23** (452-457) 1985.
83. F. Huang, "Electronic surface states confined to the boundary of periodic multiple quantum wells," *Appl. Phys. Lett.* **57** (1669-1671) 1990.
84. R.D. Meade, K.D. Brommer, A.M. Rappe and J.D. Joannopoulos, "Electromagnetic Bloch waves at the surface of a photonic crystal," *Phys. Rev. A* **44** (10961-10964) 1991.
85. K.M. Leung, "Defect modes in photonic band structures: a Green's function approach using vector Wannier functions," *J. Opt. Soc. Am.* **10** (303-306) 1993.
86. R.P. Stanley, R. Houdré, U. Oesterle, M. Ilegems and C. Weisbuch, "Impurity modes in one-dimensional systems: The transition from photonic band gaps to microcavities," *Phys. Rev. A* **48** (2246-2249) 1993.
87. T.A. Birks, F.D. Lloyd-Lucas and P.St.J. Russell, "Applications of optical surface waves on multi-layer stacks," in preparation, 1994.

### APPENDIX A1. MAIN MATHEMATICAL SYMBOLS AND THEIR MEANINGS

#### Roman characters

$a_j^N$	amplitude of co-sinusoidal part of $f_j^N$ (equation (20))
$b$	normalised version of $\beta$ ( $= \beta\Lambda$ )
$b_j^N$	amplitude of sinusoidal part of $f_j^N$ (equation (20))
$A, B, C$	matrix elements in $\mathbf{M}$
$c$	velocity of light in vacuo
$e$	energy eigenvalue in effective mass discussion
$\mathbf{E}$	electric field vector
$\mathbf{E}_j$	electric field in medium $j$
$f_j$	electric (TE) or magnetic (TM) field in medium $j$
$h$	Planck's constant
$\hbar$	$h/2\pi$
$h_e$	normalised total electron energy
$h_j$	thickness of layer $j$
$H_e$	total electron energy
$H_o$	total photon energy $\hbar\omega$
$\mathbf{H}$	magnetic field vector
$k$	vacuum wavevector ( $= \omega/c$ )

$k_j$	cartesian component of wavevector $\mathbf{k}$ ( $j = x, y$ or $z$ )
$k_y$	base wavevector of Bloch wave
$K$	reciprocal lattice wavevector ( $= 2\pi/\Lambda$ )
$m$	integer representing mode order
$m_e$	electron rest mass
$m_o$	arbitrarily defined photon mass ( $= \hbar\omega/2c^2$ )
$m_{ij}^*$	effective mass tensor element
$\mathbf{M}$	translation matrix (over one period) between layers of medium 1
$\mathbf{M}'$	translation matrix (over one period) between layers of medium 2
$n$	refractive index; integer for $n$ -th plane wave in expansion
$n_{av}$	weighted mean index ( $= (n_1h_1 + n_2h_2)/\Lambda$ )
$n_j$	refractive index in medium $j$
$n_1$	high index medium
$n_2$	low index medium ( $n_1 > n_2$ )
$n_R$	index ratio $n_2/n_1 < 1$
$N$	integer representing $N$ -th period in multi-layer stack
$p_j$	wavevector component within layer $j$ , normal to interfaces
$t$	time
$u$	potential energy in effective mass discussion
$u_{av}$	normalised mean potential
$U$	electronic potential, in general spatially varying
$U_{av}$	weighted mean potential ( $= (U_1h_1 + U_2h_2)/\Lambda$ )
$U_1$	high potential medium
$U_2$	low potential medium ( $U_1 < U_2$ )
$U_o$	photon potential energy ( $= -\hbar\omega(\epsilon_r - 1)$ )
$\mathbf{v}_g$	group velocity
$x$	coordinate along which nothing varies in two dimensions
$y$	coordinate perpendicular to layers
$y_j^N$	value of $y$ at centre of layer of index $n_j$ in $N$ -th period
$z$	coordinate along layers

#### Greek characters

$\beta$	wavevector component along the layers ( $z$ direction)
$\epsilon_o$	dielectric permittivity of free space
$\epsilon_r$	relative dielectric constant
$\theta_c$	critical angle for total internal reflection (between ray and normal to interface)
$\Lambda$	period in multi-layer stack ( $= h_1 + h_2$ )
$\mu_o$	magnetic permeability of free space
$\nu$	normalised frequency ( $= kn_{av}\Lambda$ )
$\xi_j$	$= 1$ for TE polarised light $= 1/n_j^2$ for TM polarised light
$\tau$	relative thickness of layer 2 ( $= h_2/\Lambda$ )
$\psi$	general field amplitude
$\omega/2\pi$	optical frequency

## APPENDIX A2. TRANSLATION MATRIX ELEMENTS

The matrix  $\mathbf{M}_{21}$  relating the field in the 2nd layer to the field in the 1st layer is

$$\begin{pmatrix} a_2^N \\ b_2^N \end{pmatrix} = \mathbf{M}_{21} \begin{pmatrix} a_1^N \\ b_1^N \end{pmatrix} = \begin{pmatrix} A_{21} & B_{21} \\ C_{21} & D_{21} \end{pmatrix} \begin{pmatrix} a_1^N \\ b_1^N \end{pmatrix}, \quad (\text{A1})$$

where

$$\begin{aligned} A_{21} &= c_1 c_2 - (\xi_1 p_1 \Lambda / \xi_2 p_2 \Lambda) s_1 s_2, \\ B_{21} &= s_1 c_2 / (\xi_1 p_1 \Lambda) + c_1 s_2 / (\xi_2 p_2 \Lambda), \\ C_{21} &= -\xi_1 p_1 \Lambda s_1 c_2 - \xi_2 p_2 \Lambda c_1 s_2, \\ D_{21} &= c_1 c_2 - (\xi_2 p_2 \Lambda / \xi_1 p_1 \Lambda) s_1 s_2, \\ \det \mathbf{M}_{21} &= 1, \end{aligned} \quad (\text{A2})$$

where the terms  $s_j$  and  $c_j$  are shorthand for:

$$c_j = \cos(p_j h_j / 2), \quad s_j = \sin(p_j h_j / 2). \quad (\text{A3})$$

The matrix  $\mathbf{M}_{12}$  relating the field in the 1st layer of the  $(N+1)$ th period to the field in the 2nd layer of the  $N$ th period is then

$$\begin{pmatrix} a_1^{N+1} \\ b_1^{N+1} \end{pmatrix} = \mathbf{M}_{12} \begin{pmatrix} a_2^N \\ b_2^N \end{pmatrix} = \begin{pmatrix} D_{21} & B_{21} \\ C_{21} & A_{21} \end{pmatrix} \begin{pmatrix} a_2^N \\ b_2^N \end{pmatrix}. \quad (\text{A4})$$

The analysis can either be based on the translation matrix  $\mathbf{M} = \mathbf{M}_{12} \mathbf{M}_{21}$  (with a state vector representing the field in layers with index  $n_1$ ) or equivalently on the matrix  $\mathbf{M}' = \mathbf{M}_{21} \mathbf{M}_{12}$  (state vector representing the field in layers with index  $n_2$ ).  $\mathbf{M}$  is

$$\begin{pmatrix} a_1^{N+1} \\ b_1^{N+1} \end{pmatrix} = \mathbf{M} \begin{pmatrix} a_1^N \\ b_1^N \end{pmatrix} = \begin{pmatrix} A & B \\ C & D \end{pmatrix} \begin{pmatrix} a_1^N \\ b_1^N \end{pmatrix}, \quad (\text{A5})$$

where

$$A = D = A_{21} D_{21} + B_{21} C_{21}, \quad (\text{A6})$$

$$B = 2D_{21} B_{21}, \quad C = 2A_{21} C_{21}. \quad (\text{A7})$$

$A$  can be re-arranged as

$$A = \cos(p_1 h_1) \cos(p_2 h_2) - \frac{1}{2} \left( \frac{p_1 \xi_1}{p_2 \xi_2} + \frac{p_2 \xi_2}{p_1 \xi_1} \right) \sin(p_1 h_1) \sin(p_2 h_2) \quad (\text{A8})$$

but  $B$  and  $C$  are most conveniently expressed as the product of two factors as above. The elements of the alternative matrix  $\mathbf{M}'$  are:

$$A' = D' = A, \quad (\text{A9})$$

$$B' = 2A_{21}B_{21}, \quad C' = 2D_{21}C_{21}. \quad (\text{A10})$$

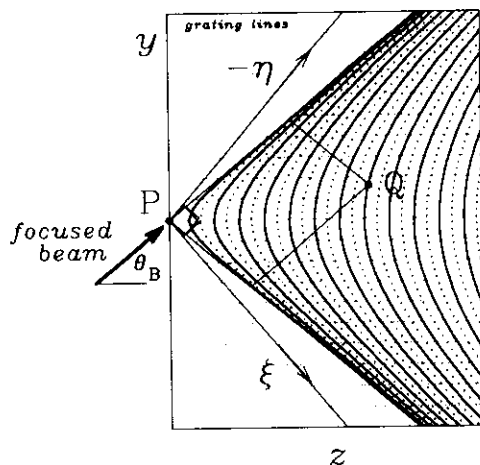


**Figure A1.** Geometry of Green's function for singly periodic structure in nearly free photon case; the position of the intensity peaks for the Bragg reflected and transmitted fields are given by the zeros and peaks in the Bessel functions (A11).

### APPENDIX A3. BESSEL FUNCTION SOLUTIONS

#### A3.1 Nearly-Free Photons: Green's Function Solution<sup>27,31</sup>

When (1) the index modulation is very weak, i.e.  $\epsilon_m = n_1^2 - n_2^2 \ll \epsilon_{av}$ , (2) the Bragg angle  $\theta_B = \arcsin(K/2kn_{av})$  lies in the mid-range between 0 and  $\pi$ , (3) a beam B is focused to a small point on the boundary at P (see Figure A1) and (4) its plane wave spectrum is centred at the Bragg angle, then the transmitted and Bragg reflected field intensities at an arbitrary point Q are given by:

$$T_{QP} = J_0^2 \left( \frac{2\kappa}{\sin\theta_B} \sqrt{\eta_Q \xi_Q} \right) \quad (\text{A11})$$

$$R_{QP} = \frac{\eta_Q}{\xi_Q} J_1^2 \left( \frac{2\kappa}{\sin\theta_B} \sqrt{\eta_Q \xi_Q} \right)$$

where the coordinates  $\xi$  and  $\eta$  are defined by:

$$\begin{pmatrix} \xi \\ \eta \end{pmatrix} = \begin{pmatrix} \sin\theta_B & -\cos\theta_B \\ -\sin\theta_B & -\cos\theta_B \end{pmatrix} \begin{pmatrix} z \\ y \end{pmatrix} \quad (\text{A12})$$

where  $\kappa = \epsilon_m k / 4n_{av}$  is known as the coupling constant. This solution arises when the incident beam B has an angular spectrum large enough to excite Bloch waves over each entire stop-band branch, while the stop-band itself is small, i.e., the beam B has an angular spectrum small enough for it not to diffract appreciably in the absence of a grating ( $\kappa \rightarrow 0$ ). The minimum feature size needed to excite this function is of order  $\Delta y = 2\pi/\kappa \sin\theta_B$ . Note that the form of the solution does not depend on the boundary slant angle, provided it does not cut into the triangular region bounded by the Bragg angles. Because they are obtained by integration over the entire stop-band, these functions are akin (though not identical) to Wannier functions in electronic band theory<sup>23,25</sup>. They are also Green's functions, and can be used to build up more complicated solutions by linear superposition; e.g., non-planar boundary shapes and non-uniform incident beams can be treated. The solution they represent is in the "nearly free photon" approximation.

### A3.2 Tight Binding

Excitation of a single waveguide in an array of parallel coupled channel waveguides (or a single tightly bound high index layer in a multi-layer stack - see section 6.2) results in lateral spreading out of power by resonant tunnelling. After propagating a distance  $z$ , the power in the  $n$ th channel (the entrant channel being  $n = 0$ , see Figure A2) is given by:

$$P_n(z) = J_n^2(2\kappa_c z) \quad (\text{A13})$$

where the inter-guide coupling constant  $\kappa_c$  is a function of the waveguide parameters<sup>52</sup>. The tight-binding approximation upon which this solution is based is common in waveguide optics, where it is formulated in terms of coupled mode theory. Again, because the structure is excited at one lattice point, the field at entry to the structure is akin to an electronic Wannier function.

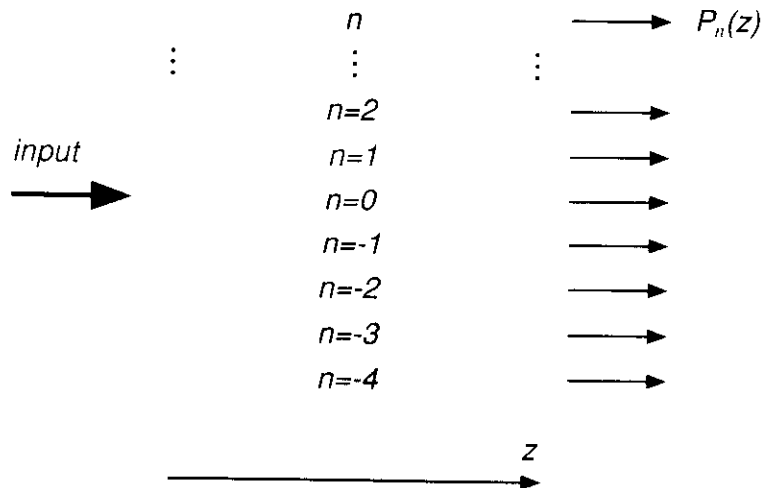
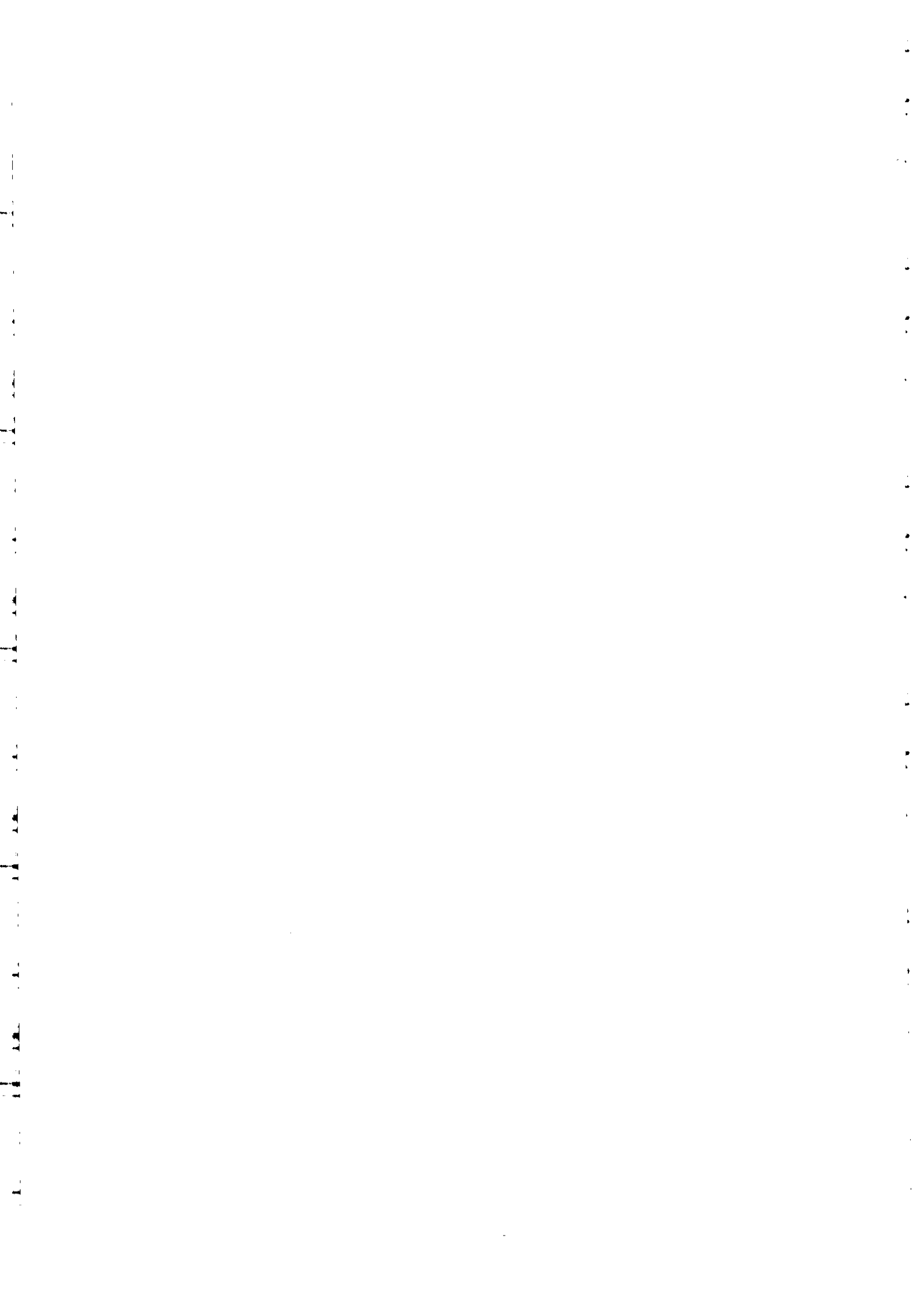


Figure A2. Geometry of the coupled waveguide array for the tight-binding Bessel function solution in (A13).



# All-silica single-mode optical fiber with photonic crystal cladding

J. C. Knight,\* T. A. Birks,\* P. St. J. Russell\* and D. M. Atkin

*Optoelectronics Research Centre, University of Southampton, Southampton, SO17 1BJ, UK*

Received April 8, 1996

We report the fabrication of a new type of optical waveguide: the photonic crystal fiber. It consists of a pure silica core surrounded by a silica-air photonic crystal material with a hexagonal symmetry. The fiber supports a single robust low-loss guided mode over a very broad spectral range of at least 458–1550 nm.  
© 1996 Optical Society of America

Substantial effort has been invested over the past few years in fabricating photonic crystals—materials that have a periodic modulation of the refractive index on the scale of the optical wavelength. The interest in such materials lies in their ability to interact unusually strongly with light of certain wavelengths: For example, appropriately designed structures can exhibit band gaps at optical frequencies (photonic band gaps).<sup>1</sup> Light that is incident upon a band-gap material from the outside would be totally reflected. Similarly, light that existed at a structural-defect site in such a material would be permanently trapped, being unable to propagate through the lattice. These properties make photonic crystals of both fundamental and technological interest. The observation of these effects requires a large variation in the refractive index, such that the photonic crystal must be formed of at least two bulk materials of different optical properties. Because of the difficulty of fabricating structures on the scale of an optical wavelength that are periodic in three dimensions, much recent experimental research has been aimed at producing materials with a two-dimensional variation by use of etching techniques in semiconductors<sup>2</sup> and glasses<sup>3</sup> to form structures that are periodic in a plane but are of limited extent in the third dimension. However, some of the most interesting effects in two-dimensional photonic crystals occur for waves that have a nonzero wave-vector component  $\beta$  normal to the periodic plane.<sup>4,5</sup> It is difficult if not impossible to study some of these effects by use of the previous structures, which are at most a few millimeters in depth (and usually much less). Here we describe the fabrication of a two-dimensional hexagonal silica-air photonic crystal that is extended into the third dimension. The structure is in the form of a fine silica fiber. Air holes arranged in a regular hexagonal pattern run the entire length of the fiber, which is many meters long. We investigate the properties of guided modes that are predicted to occur at purposely introduced lattice-defect sites (a lattice-defect site is any structural feature that breaks the regularity of the crystal lattice). By introducing a high-index defect site into the middle of the fiber during fabrication we have created a novel monomode optical fiber with a hexagonal symmetry.

We form the hexagonal unit cell on a macroscopic scale by drilling a hole of 16-mm diameter down the length of a 30-mm-diameter silica rod. Six flats are milled on the outside of the rod, forming a regular hexagon. This preform is then drawn on a fiber drawing tower at  $\sim 2000^\circ\text{C}$  to produce hexagonal cane of a diameter of 0.8 mm, which is cut to length and stacked to give the required crystal structure. This stack is again drawn on the tower, fusing the stacked canes together and reducing the pitch (center-to-center spacing) to  $\sim 50\ \mu\text{m}$ . Finally, a piece of this fused stack is drawn down again to yield the final fiber. During the three-stage drawing process the size of the unit cell is reduced by a factor of more than  $10^4$ , yielding a final pitch of  $\sim 2\ \mu\text{m}$ .

It has been predicted<sup>5</sup> that a hexagonal silica-air photonic crystal with a pitch of  $\sim 2\ \mu\text{m}$  will exhibit a band gap at a wavelength of  $1.5\ \mu\text{m}$  for certain values of  $\beta$  and for certain values of the air-filling fraction. In this case guidance could be achieved by introduction of any sort of defect into the periodic structure, which would have the effect of pulling a spatially localized mode from the band edge into the band-gap region. The fiber presented here does not rely on the existence of a complete band gap. We have demonstrated low-loss guidance by the photonic crystal in a different regime by purposely introducing a high-index defect into the center of the fiber. We do this at the stacking stage by replacing one of the hollow hexagonal canes with a similar cane that does not have a hole in the middle. In this case we expect any light with  $\beta$  greater than a certain value to be confined to the core, as the surrounding silica-air matrix has a reduced effective refractive index compared with the solid core. The fiber bears some resemblance to previously fabricated single-material fibers<sup>6</sup> but differs from them in having a periodic index modulation in the cladding region and a unique hexagonal symmetry.

A scanning electron micrograph of the fiber is shown in Fig. 1. The structure shown in the figure is virtually invariant over a length of several meters. The flat-to-flat width of the fiber shown is  $38\ \mu\text{m}$ , the pitch is  $2.3\ \mu\text{m}$ , and the solid core region is nominally  $4.6\ \mu\text{m}$  wide. The relative diameter of the air holes shown in the figure is smaller than in the original

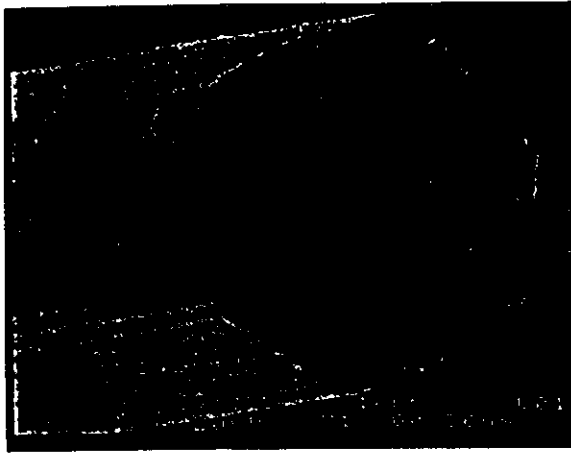


Fig. 1. Scanning electron micrograph of the photonic crystal fiber.

unit cell—this is caused by the effect of surface tension during the final stages of the drawing process. By varying the furnace temperature during the pulling process, we were able to exert some control over the relative size of the air holes in the final fiber and have drawn fiber with a pitch similar to that shown in Fig. 1 and with air holes of 0.2–1.2  $\mu\text{m}$  diameter. The fiber is quite robust and easy to handle despite its small size.

To investigate the guidance properties of the fiber, we coupled light from argon-ion (wavelength  $\lambda = 457.9$  nm), He-Ne (632.8 nm), Ti:sapphire (850 nm), and diode (1550 nm) lasers into one end of a 1-m length of fiber with an objective lens, using index-matching fluid to strip off light in cladding modes. It was relatively easy to achieve a coupling of more than 50% into the guided mode, comparable with that for standard monomode optical fiber. We then used a vidicon camera and photographic film to record the near- and far-field patterns of the guided mode at the output end of the fiber. Figure 2(a) shows a contour map of the near-field pattern at 632.8 nm that we recorded by imaging the output end of the fiber onto the vidicon camera, using a 60 $\times$  objective lens. The contour map is shown superimposed upon a portion of an approximately scaled scanning electron microscope picture of the fiber output surface to show the relative orientation of the modal field with respect to the fiber. The light is strongly confined to the core region, and the field pattern is dominated by minima occurring at the six nearest air holes. Figure 2(b) shows the Fourier transform of the recorded near-field pattern, which is strongly peaked in the center. The hexagonal nature of the guided mode is manifest as six symmetrically placed spots occurring around the central peak, with much weaker spots further from the center (not visible in Fig. 2).

Next we photographed the spatial far-field pattern falling upon a sheet of paper several centimeters from the far end of the fiber [Fig. 3(a)]. The observed pattern shows qualitative similarity to the Fourier transform of the observed near-field pattern shown in Fig. 2, as expected. The central part of the pattern has been overexposed in Fig. 3(b) to show the higher-order terms present on the fringes of the pattern, which demon-

strate the integrity of the periodic structure. This far-field pattern is independent of the way in which light is launched into the fiber and is unaffected by any bends imposed upon the fiber, implying that there is only a single low-loss guided mode. This is the case from at least 457.9 to beyond 1550 nm—over this whole range the far-field pattern looks remarkably similar to that shown in Fig. 3, although the numerical aperture of the output increases approximately linearly with wavelength (from  $\sim 0.13$  at 457.9 nm to 0.36 at 1550 nm) and the outer spots become somewhat weaker at longer wavelengths.

In the visible region of the spectrum the modal field pattern in the cladding is redistributed into the higher-index silica regions, decreasing the effective index difference between the core and the cladding. On the other hand, at the longer-wavelength end of the range studied the mode was found to be still tightly confined to the vicinity of the core but unable to accommodate the air holes as directly as in Fig. 2. Instead, the photonic crystal cladding behaves increasingly as a uniform medium with the average refractive index. Consequently, the effective refractive index of

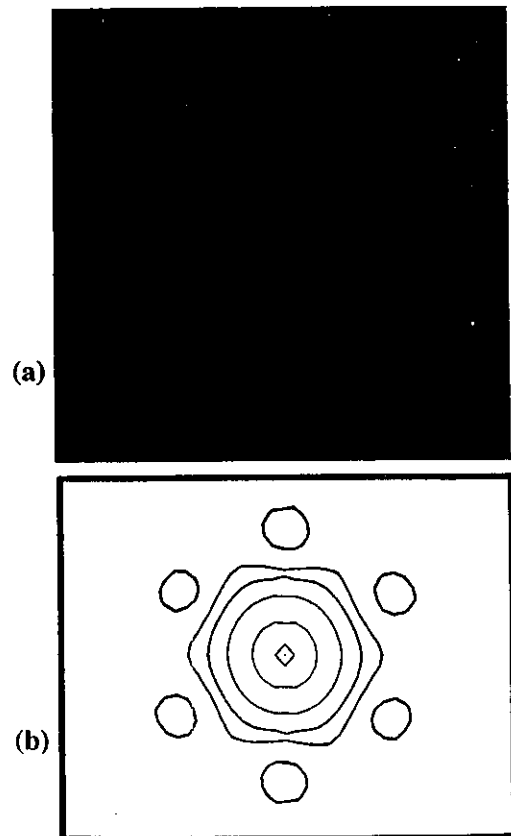


Fig. 2. (a) Contour plot of the recorded near-field pattern of the guided mode ( $\lambda = 632.8$  nm) superimposed upon an approximately scaled portion of a scanning electron micrograph to show the relative orientation of the modal field pattern and the fiber microstructure. The field is strongly peaked in the center, and there is a factor-of-25 difference between the innermost (strongest) and the outermost intensity contours. (b) Calculated Fourier transform of the pattern, again strongly peaked in the center.



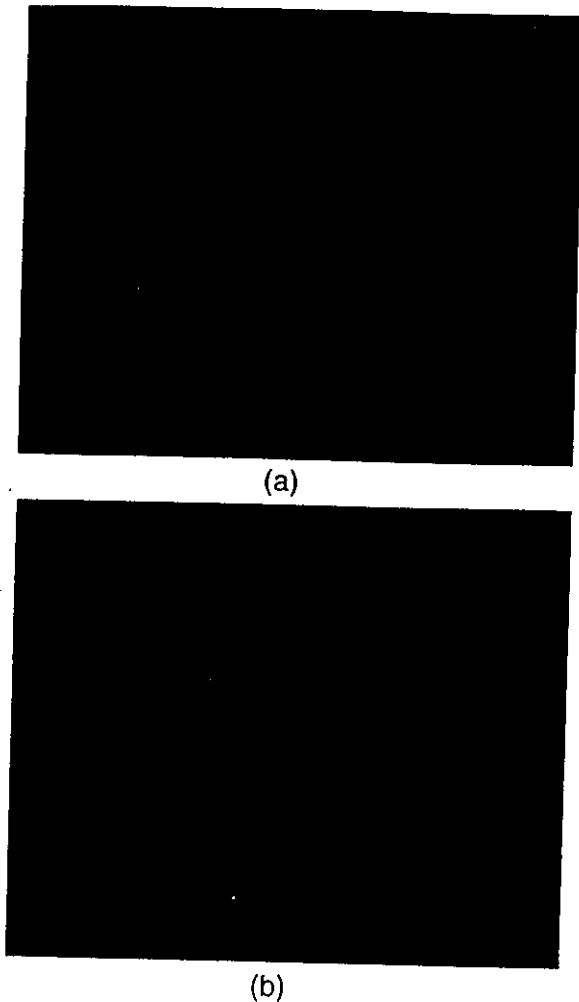


Fig. 3. Photographed far-field pattern at 632.8 nm. (b) Same as in (a) but with the central part of the field overexposed to show the higher-order spots on the fringes of the pattern, which demonstrate the integrity of the periodic structure.

the cladding decreases sharply at longer wavelengths. The wide single-mode wavelength range can now be understood qualitatively with reference to the normalized frequency, or  $V$  value,<sup>7</sup>  $V = (2\pi/\lambda)\rho(n_{co}^2 - n_{cl}^2)^{0.5}$ , that characterizes guidance in a step-index fiber of core radius  $\rho$  and core and cladding refractive indices  $n_{co}$  and  $n_{cl}$ , respectively. The effective decrease of the cladding index at longer wavelengths counteracts the increase in wavelength, keeping the  $V$  value nearly constant and making possible a single robust guided mode over an extended spectral range.

Despite the hexagonal symmetry of the cladding material, the fiber exhibits two perpendicular preferred polarization axes in its transmission properties.

When linearly polarized light is coupled into the fiber with its polarization axis parallel to one of these two axes the output is linearly polarized and parallel to the same fiber axis, even if the fiber is bent or twisted. If the input light is polarized at some other angle the output is in general elliptically polarized. Any coupling owing to defects in the hexagonal structure of the cladding will serve to lift the degeneracy of modes that are rotated apart from each other by  $60^\circ$ . Some evidence of such breaking of hexagonal symmetry is observable in Figs. 1–3.

The fiber presented here could provide a means to enhance the interaction of light with a gas that is in the air holes, for example, for use in a gas sensor or to study nonlinear-optical processes. The support of only a single mode over a broad spectral range is a feature that makes this design of interest in situations in which several different wavelengths are required in the same fiber, such as in frequency-doubling applications. At present we are studying the Bragg scattering from a length of photonic crystal fiber. We intend to fabricate fiber with the correct pitch and air-filling fraction to exhibit a complete band gap for certain values of  $\beta$  and to use this fiber to investigate the possibility of waveguiding by Bragg reflection (the photonic band-gap fiber<sup>5</sup>) at a low-index defect site.

This research was supported by the Defence Research Agency, Malvern, UK. T. A. Birks is a Royal Society University Research Fellow.

\*Present address, School of Physics, University of Bath, Claverton Down, Bath, BA2 7AY, UK.

#### References

1. E. Yablonovitch, *J. Opt. Soc. Am. B* **10**, 283 (1993); P. St. J. Russell, *Phys. World* **5**(8), 37 (1992); J. D. Joannopoulos, R. D. Meade, and J. N. Winn, *Photonic Crystals* (Princeton U. Press, Princeton, N. J., 1995).
2. P. L. Gourley, J. R. Wendt, G. A. Vawter, T. W. Brennan, and B. E. Hammons, *Appl. Phys. Lett.* **64**, 687 (1994); U. Grüning, V. Lehmann, and S. Ottow, *Appl. Phys. Lett.* **68**, 747 (1996).
3. K. Inoue, M. Wada, K. Sakoda, A. Yamanaka, M. Hayashi, and J. W. Haus, *Jpn J. Appl. Phys.* **33**, L1463 (1994); R. Tonucci, B. L. Justus, A. J. Campillo, and C. E. Ford, *Science* **258**, 783 (1992).
4. P. St. J. Russell, T. A. Birks, and F. D. Lloyd-Lucas, in *Confined Electrons and Photons*, E. Burstein and C. Weisbuch, eds. (Plenum, New York, 1995), pp. 585–633.
5. T. A. Birks, P. J. Roberts, P. St. J. Russell, D. M. Atkin, and T. J. Shepherd, *Electron. Lett.* **31**, 1941 (1995).
6. P. Kaiser and H. W. Astle, *Bell Syst. Tech. J.* **53**, 1021 (1974).
7. A. W. Snyder and J. D. Love, *Optical Waveguide Theory* (Chapman & Hall, New York, 1983).

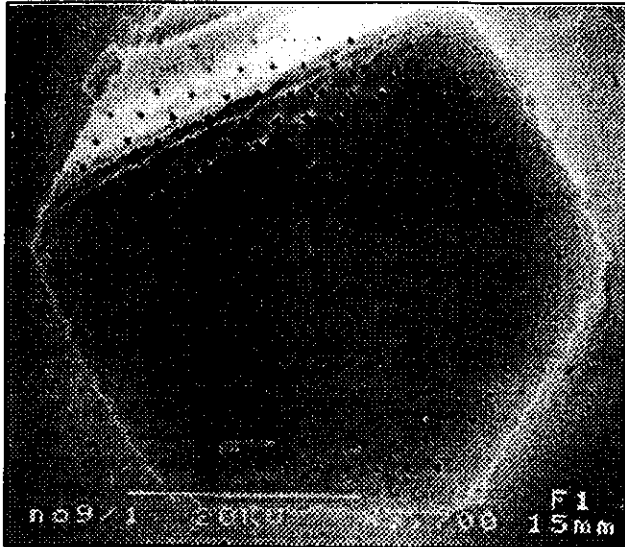


**Figure 3** SEM of photonic crystal fibre

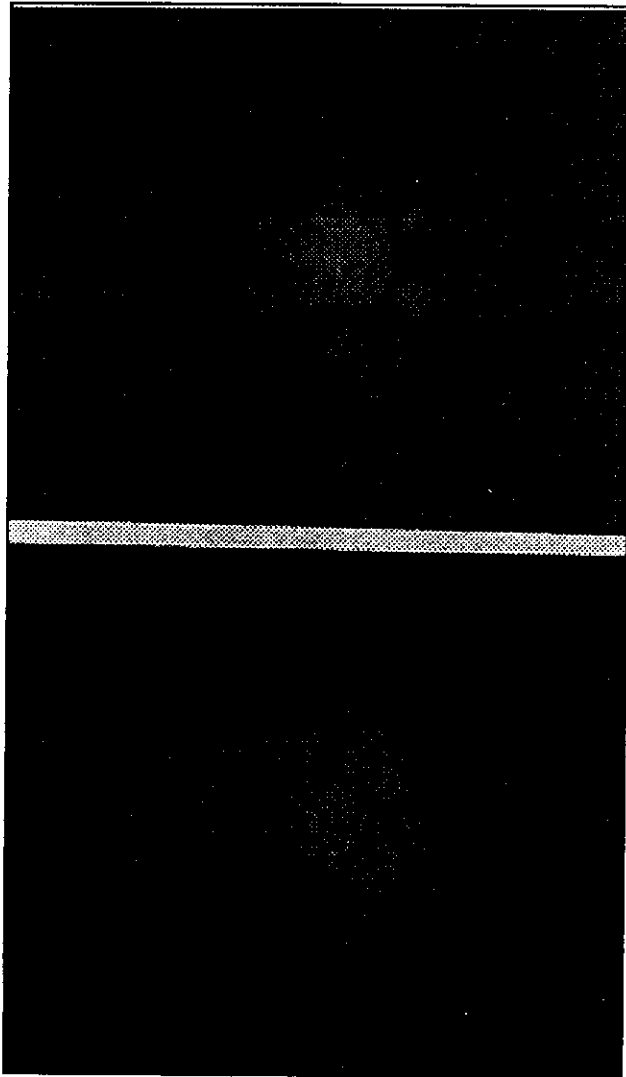


**Figure 1** Photograph of far-field pattern at 633 nm. Note good agreement with calculated Fourier transform of near field

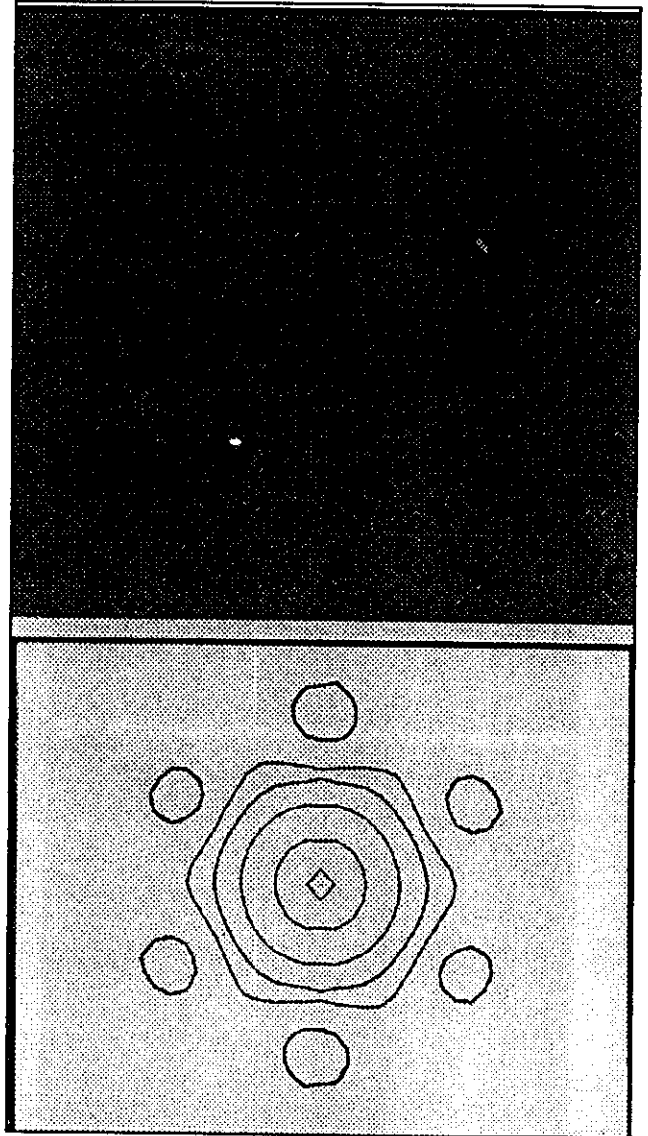


**Figure 2** Contour plot of recorded near field pattern of guided mode at 633 nm superimposed on SEM of fibre end face. Lower plot is calculated Fourier transform of near field.

P2

# Endlessly single-mode photonic crystal fiber

T. A. Birks, J. C. Knight, and P. St. J. Russell

Optoelectronics Group, School of Physics, University of Bath, Claverton Down, Bath, BA2 7AY, UK

Received March 10, 1997

We made an all-silica optical fiber by embedding a central core in a two-dimensional photonic crystal with a micrometer-spaced hexagonal array of air holes. An effective-index model confirms that such a fiber can be single mode for any wavelength. Its useful single-mode range within the transparency window of silica, although wide, is ultimately bounded by a bend-loss edge at short wavelengths as well as at long wavelengths. © 1997 Optical Society of America

In a previous Letter<sup>1</sup> we reported the fabrication of a photonic crystal fiber. This optical fiber was made entirely from undoped fused silica. The cladding was a two-dimensional photonic crystal made of silica with air holes running along the length of the fiber. The holes were arranged in a hexagonal honeycomb pattern across the cross section. The central hole was absent, leaving a silica defect that acted as the core (Fig. 1). The fiber was single mode over a remarkably wide wavelength range, from 458 to 1550 nm at least. Subsequent measurements have extended this range to 337 nm.

In a standard step-index fiber with core radius  $\rho$  and core and cladding indices  $n_{co}$  and  $n_{cl}$ , the number of guided modes is determined by the  $V$  value<sup>2</sup>:

$$V = (2\pi\rho/\lambda)(n_{co}^2 - n_{cl}^2)^{1/2}, \quad (1)$$

which must be less than 2.405 for the fiber to be single mode. Thus single-mode fibers are in fact multimode for light of sufficiently short wavelength. We explained the wide single-mode range of the photonic crystal fiber by considering the effective refractive index of the cladding, loosely understood as the average index in the cladding weighted by the intensity distribution of the light. At shorter wavelengths the field becomes more concentrated in the silica regions and avoids the holes (as we observed by examination of the near-field patterns<sup>1</sup>), thus raising the effective cladding index. This dispersion counteracts the explicit dependence of  $V$  on wavelength  $\lambda$  and so extends the single-mode range. We now quantify this model and demonstrate that photonic crystal fibers can be single mode for all wavelengths. The model's validity is confirmed by bend-loss measurements, which show that the useful spectral range of the fiber is bounded by bend-loss edges at both short and long wavelengths.

Although most interest in photonic crystals has focused on their photonic bandgap properties, we do not consider guidance by photonic bandgap effects<sup>3</sup> here. Instead, because the core index is greater than the average index of the cladding, the fiber can guide by total internal reflection as a standard fiber does, despite the unconventional structure. That is, there are propagation constants  $\beta$  available to light in the core but not to light propagating in the cladding:

$$kn_0 > \beta > \beta_{FSM}, \quad (2)$$

where  $k = 2\pi/\lambda$ ,  $n_0$  is the index of silica (the core material), and  $\beta_{FSM}$  is the propagation constant of the fundamental space-filling mode (FSM). The FSM is the fundamental mode of the infinite photonic crystal cladding if the core is absent, so  $\beta_{FSM}$  is the maximum  $\beta$  allowed in the cladding. Inasmuch as the lower limit of  $\beta$  in a step-index fiber is  $kn_{cl}$ , we identify the effective cladding index  $n_{eff}$  with

$$n_{eff} = \beta_{FSM}/k. \quad (3)$$

The FSM is the generalization of a  $z$ -directed plane wave in an infinite uniform medium, whose  $\beta$  equals  $k \times$  the medium's index. Thus Eq. (3) gives the correct value in this special case. More generally, Eq. (3) is justified because inequality (2) implies that the transverse wave-vector component  $k_T$  in the core lies between zero and  $k_{Tmax} = (k^2 n_0^2 - \beta_{FSM}^2)^{1/2}$  for a guided mode.  $k_T$  is quantized by the boundary conditions between core and cladding, so the number of guided modes is determined by  $\rho k_{Tmax}$ . For a step-index fiber this is simply the  $V$  value of Eq. (1). Thus

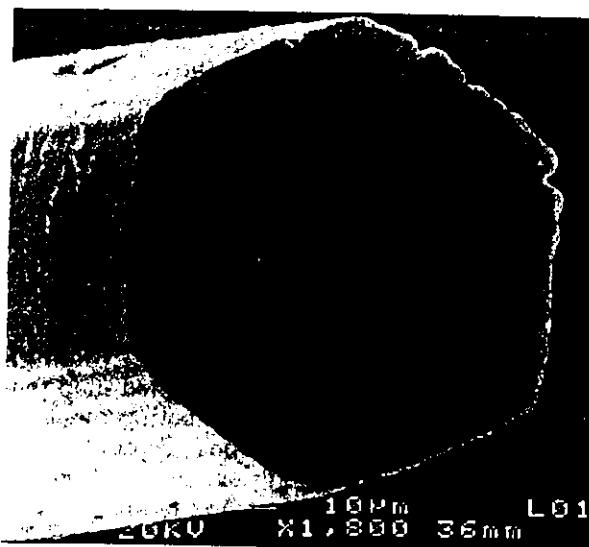


Fig. 1. Scanning electron microscope image of the end of a photonic crystal fiber, showing the central core where a hole has been omitted. The pitch  $\Lambda$  is  $2.3 \mu\text{m}$ , and the fiber is  $\sim 40 \mu\text{m}$  across.

$\beta_{FSM}/k$  plays the role of an effective cladding index when one is counting modes, and so an effective  $V$  value such as Eq. (1) can be defined for the photonic crystal fiber:

$$V_{eff} = (2\pi\Lambda/\lambda)(n_0^2 - n_{eff}^2)^{1/2}, \quad (4)$$

which determines whether the fiber is single mode. As usual, when defining  $V$  values<sup>2</sup> one may choose any transverse dimension for  $\rho$ . Here we use the pitch (center-center spacing) of the holes  $\Lambda$ , which is also roughly the radius of the defect core formed by omitting one of them.

Having found  $n_{eff}$ , we consider the limit  $\lambda \rightarrow 0$ . The scalar wave equation, valid here,<sup>4</sup> gives

$$\Lambda^2 \nabla_t^2 \psi + V_{eff}^2 \psi = 0 \quad (5)$$

for the field distribution  $\psi$  of the FSM in silica regions, where  $\nabla_t^2$  is the transverse part of the Laplacian operator. When  $\lambda \rightarrow 0$ ,  $\psi$  is excluded from the low-index air holes<sup>4</sup> and is confined to the silica region bounded by the edges of the holes. For a given ratio of hole size to  $\Lambda$ ,  $\psi$  is therefore an invariant function of normalized transverse coordinates  $x/\Lambda$  and  $y/\Lambda$  in the short-wavelength limit. Equation (5) then implies that  $V_{eff}$  is finite and independent of  $\lambda$  and  $\Lambda$  under these conditions. This situation contrasts with that for the step-index fiber, for which  $V \rightarrow \infty$  as  $\lambda \rightarrow 0$ . The limiting value of  $V_{eff}$  depends on the relative size of the holes, but a sufficiently small value guarantees single-mode operation for all wavelengths  $\lambda$  and scales  $\Lambda$ .

By averaging the square of the refractive index in the photonic crystal cladding it is simple to show that the long-wavelength limit of  $V_{eff}$  in a scalar approximation is

$$V_{eff} = k\Lambda F^{1/2}(n_0^2 - n_a^2)^{1/2}, \quad (6)$$

where  $n_a$  is the index of air (or whatever is in the holes) and  $F$  is the air filling fraction.

$V_{eff}$  can be calculated in the general case in a scalar approximation. Because the FSM is a fundamental mode with the same symmetries as the photonic crystal itself, one finds it by solving the scalar wave equation within a unit cell centered on one of the holes of diameter  $d$  (Fig. 2). By reflection symmetry, the boundary condition at the edge is that  $\partial\psi/\partial s = 0$ , where  $s$  is a coordinate normal to the edge. We approximate this with a circular outer boundary at radius  $r = b$ , where  $d\psi/dr = 0$ . This is reasonable if the holes are not too large, because the field variation on a circle intersecting the hexagonal boundary will be small. Equating the model's filling fraction to the actual value gives  $b$ . The analysis is little more complicated than that of the step-index fiber<sup>2</sup>. The field in both regions is expressed in terms of Bessel functions of order 0, and the application of boundary conditions yields  $\beta_{FSM}$ . The resulting curves of  $V_{eff}$  against  $\Lambda/\lambda$  for  $n_0 = 1.45$  and  $n_a = 1.00$  are shown in Fig. 3 for various relative hole sizes  $d/\Lambda$ . The  $\lambda \rightarrow 0$  limit of  $V_{eff}$  approaches zero slowly as  $d/\Lambda$  approaches zero.

The fiber described in our earlier Letter<sup>1</sup> has  $\Lambda = 2.3 \mu\text{m}$  and  $d/\Lambda = 0.15$ , and the available wavelength

range corresponds to  $\Lambda/\lambda$  between 1.5 and 6.8.  $V_{eff}$  is therefore less than 2.405 at all wavelengths. Although single-mode operation will not be defined by  $V_{eff} < 2.405$  specifically (perhaps our fiber becomes multimode at shorter wavelengths), some similar cutoff value  $V_{co}$  should apply. It is always possible to adjust  $d/\Lambda$  so that  $V_{eff} < V_{co}$ , thus proving that the photonic crystal fiber can indeed be endlessly single mode.

Larger holes make the fiber likely to be multimoded. The gaps between the holes become narrower, isolating the core more strongly from the silica in the cladding. Smaller holes make single-mode guidance more likely, but the decrease in effective index difference (or in effective N.A.) makes the fiber more susceptible to bend loss. A well-known simple expression gives the critical bend radius  $R_c$  at which bend loss in a waveguide becomes large.<sup>5</sup> Although it is not quantitatively accurate, it does give the correct parametric dependence of  $R_c$  on wavelength, core size, and refractive indices. The condition on bend radius  $R$  for low loss can be written as

$$R \gg R_c = \frac{8\pi^2 n_{co}^2 \rho^3}{\lambda^2 W^3}, \quad (7)$$

where  $W$  is the dimensionless modal parameter of optical fiber theory<sup>2</sup> and is a function of  $V$  only. For long wavelengths, the photonic crystal fiber behaves as a standard fiber, as anticipated in Eq. (6).  $W^3$  decreases more rapidly<sup>2</sup> than  $\lambda^{-2}$  with increasing  $\lambda$ ,<sup>2</sup> so there is a long-wavelength bend-loss edge beyond which the fiber suffers massive bend loss.

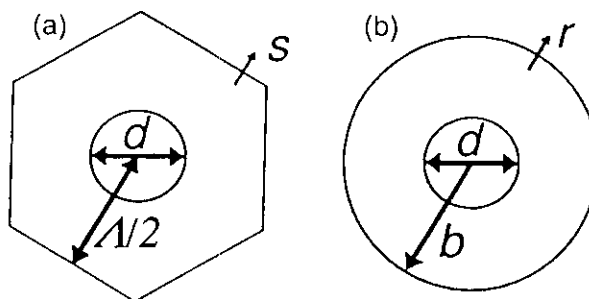


Fig. 2. (a) Actual unit cell in the photonic crystal with (b) its circular approximation.

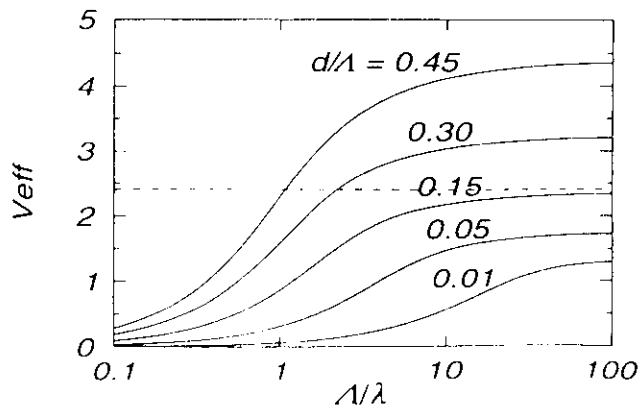


Fig. 3. Variation of  $V_{eff}$  with  $\Lambda/\lambda$  for various relative hole diameters  $d/\Lambda$ . The dashed line marks  $V_{eff} = 2.405$ , the cutoff  $V$  value for a step-index fiber.

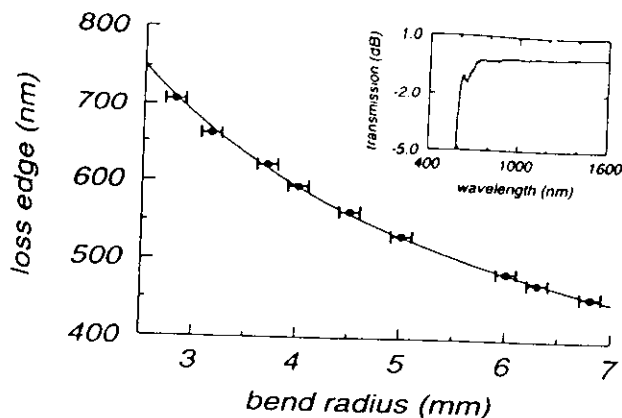


Fig. 4. Measured short-wavelength loss edge (for 3-dB loss) versus bend radius for a photonic crystal fiber with a single-turn bend (points), together with a fit to  $\lambda = \text{constant}/\sqrt{R}$ . Inset: Typical transmission spectrum of the bent fiber, relative to the transmission of the straight fiber. The short-wavelength loss edge lies near 600 nm. The long-wavelength loss edge is beyond the range of the measurement for this sample.

For short wavelengths the fibers are quite different. In standard fiber,<sup>2</sup>  $W \propto \rho/\lambda$ , giving  $R_c \sim \lambda$  independently of the core diameter. However,  $V_{\text{eff}}$  and hence  $W$  are constant in the photonic crystal fiber, so  $R_c$  varies as

$$R_c \propto \Lambda^3/\lambda^2. \quad (8)$$

The reciprocal dependence on  $\lambda$  implies that there is a short-wavelength bend-loss edge also. Measurements of the transmission spectrum of a photonic crystal fiber were taken for a range of single-turn bend radii. A low-loss wavelength range was observed that was bounded by loss edges at short and long wavelengths. The inset in Fig. 4 is an example of such a spectrum

for the very tight bend radius of 4 mm. The variation of the short-wavelength loss edge with bend radius  $R$  is plotted in Fig. 4, together with a fit to  $\lambda = \text{constant}/\sqrt{R}$ . The fit is excellent, confirming the validity of relation (8) and hence of the effective index model.

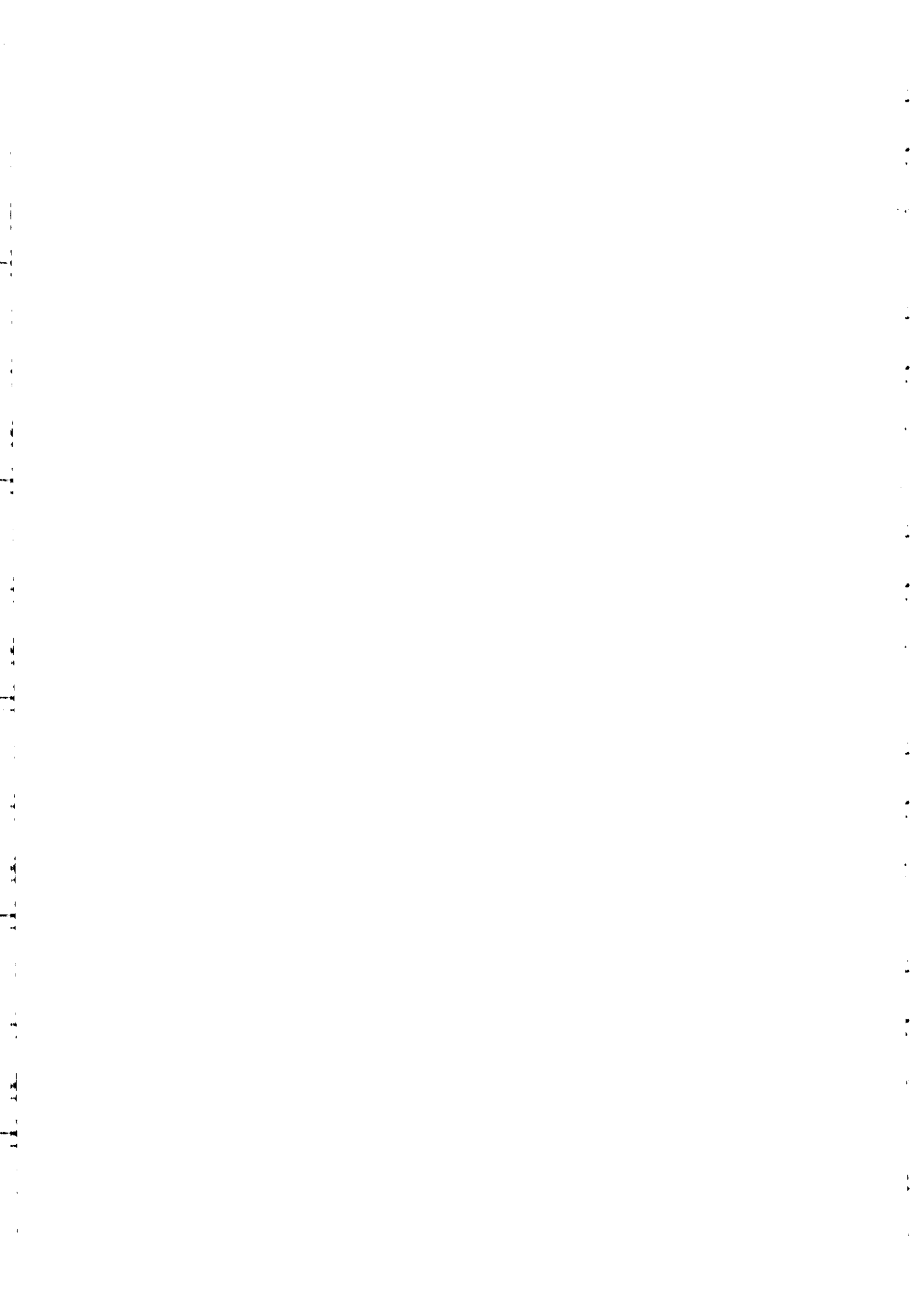
The loss edge for a 5-mm bend radius was at  $\sim 530$  nm. The cubic dependence on  $\Lambda$  in relation (8) indicates that a fiber with a pitch of  $10 \mu\text{m}$  and the same relative hole size would suffer bend loss at a bend radius of approximately half a meter at this wavelength. Thus bend loss limits not only the useful wavelength range of our endlessly single-mode fiber but also the otherwise appealing prospect of a single-mode fiber with a macroscopic core.

We have used an effective-index model to show that the photonic crystal fiber can, as suspected, be single mode at all wavelengths. The useful wavelength range of the fiber within the transparency window of silica, although wide, is ultimately limited by bend loss.

T. A. Birks is a Royal Society University Research Fellow. This research is supported by the UK Defence Research Agency at Malvern and the Engineering and Physical Sciences Research Council. The fiber was made by J. C. Knight at the University of Southampton.

## References

1. J. C. Knight, T. A. Birks, P. St. J. Russell, and D. M. Atkin, *Opt. Lett.* **21**, 1547 (1996); **22**, 484 (1997).
2. A. W. Snyder and J. D. Love, *Optical Waveguide Theory* (Chapman & Hall, New York, 1983).
3. T. A. Birks, P. J. Roberts, P. St. J. Russell, D. M. Atkin, and T. J. Shepherd, *Electron. Lett.* **31**, 1941 (1995).
4. C. Vassallo, *Opt. Quantum Electron.* **15**, 349 (1983).
5. J. D. Love, *Proc. Inst. Electr. Eng. Part J* **13**, 225 (1989).



References

- 1 SIMON, U., MILLER, C.E., BRADLEY, C.C., HULET, R.G., CURL, R.F., and TITTEL, F.K.: 'Difference frequency generation in AgGaS<sub>2</sub> using single-mode diode laser pump sources', *Opt. Lett.*, 1993, **18**, pp. 1062-1064
- 2 BALAKRISHNAN, A., SANDERS, S., DEMARS, S., WEBJORN, J., NAM, D.W., LANG, R.J., MEIJUYS, D.G., WAARTS, R.G., and WELCH, D.F.: 'Broadly tunable laser-diode-based mid-infrared source with up to 31 mW of power at 4.3 μm wavelength', *Opt. Lett.*, 1996, **21**, pp. 952-954
- 3 SIMON, U., TITTEL, F.K., and GOLDBERG, L.: 'Difference-frequency mixing in AgGaS<sub>2</sub> by use of a high-power GaAlAs tapered semiconductor amplifier at 860 nm', *Opt. Lett.*, 1993, **18**, pp. 1931-1933
- 4 TÖPFER, T., PETROV, K.P., MINE, Y., JUNDT, D., CURL, R.F., and TITTEL, F.K.: 'Room-temperature mid-infrared laser sensor for trace gas detection', *Appl. Opt.*, 1997, **36**, pp. 8042-8049
- 5 PETROV, K.P., CURL, R.F., TITTEL, F.K., and GOLDBERG, L.: 'CW tunable 8.7 mm spectroscopic source pumped by fibre-coupled communications lasers', *Opt. Lett.*, 1996, **21**, pp. 1451-1453
- 6 KOPLOW, J., GOLDBERG, L., and KLINER, D.A.V.: 'Compact 1 W Yb-doped double cladding fiber amplifier using v-groove side-pumping', *Photonics Technol. Lett.*, 1998, **10**, (6), pp. 793-795
- 7 GOLDBERG, L., COLE, B., and SNITZER, E.: 'V-groove side-pumped 1.5 μm fibre amplifier', *Electron. Lett.*, 1997, **33**, pp. 2127-2129
- 8 CHU, T.B., and BROYER, M.: 'Intracavity cw difference frequency generation by mixing three photons and using Gaussian laser beams', *J. Physique*, 1985, **46**, pp. 523-533
- 9 ARBORE, M.A., CHOU, M.H., and FEJER, M.M.: 'Difference frequency mixing in LiNbO<sub>3</sub> waveguides using an adiabatically tapered periodically-segmented coupling region'. CLEO Tech. Dig. Series, 1996, Vol. 9, pp. 120-121

solid silica cane to form the fibre core, and drawing the stack down on a fibre drawing tower. The core diameter  $2p$  is greater than twice the pitch  $\Lambda$  because the air holes in the original capillaries were relatively larger than in the final fibre: the holes are allowed to collapse in a controlled fashion during the fabrication process. It is worth emphasising that apart from being a very different size, the fibre shown in Fig. 1 is virtually identical to those fibres described previously [1] which were approximately five times smaller in diameter and which also guided only a single mode over the wavelength range to be described here.

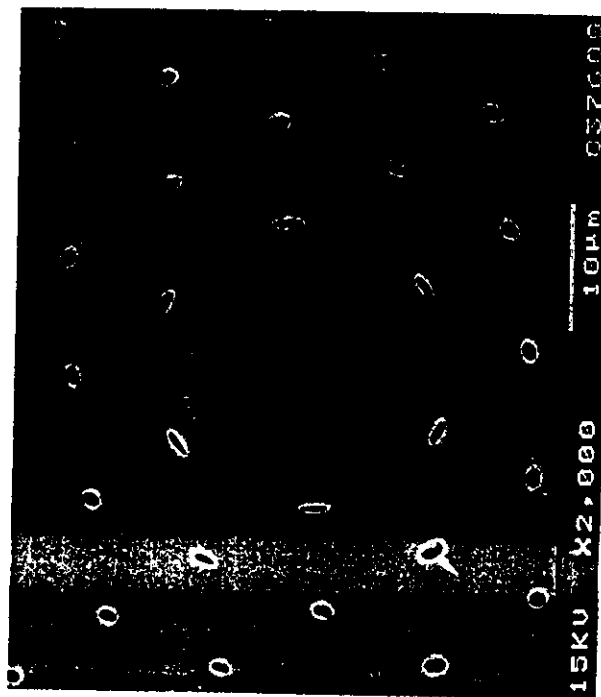


Fig. 1 Scanning electron micrograph of cleaved end face of large mode area photonic crystal fibre

Fibre shown has 22.5 μm core diameter, relative air hole diameter  $d/\Lambda = 0.12$ , and is monomode at all wavelengths  $\lambda > 458$  nm at least

### Large mode area photonic crystal fibre

J.C. Knight, T.A. Birks, R.F. Cregan, P.St.J. Russell and J.-P. de Sandro

The authors report the realisation of a new design for a large mode area monomode optical fibre. This photonic crystal fibre will guide only a single mode, no matter how large the fibre diameter, provided the shape is kept constant. This is demonstrated with a fibre which has a core diameter equal to approximately 50 free-space wavelengths.

A photonic crystal fibre (PCF) is a glass fibre with a regular array of holes running down its length. A single missing hole in the array forms a region which effectively has a higher refractive index than the surrounding photonic crystal. This acts as a waveguide core in which light can become trapped, forming a guided mode [1]. We have previously reported that the PCF remains monomode even for very short wavelengths, and have explained this using an effective index model [2]. We now demonstrate that it remains monomode even for very large-scale fibres. Such large mode area fibres are useful for generating and propagating high optical powers without limitations due to the onset of intensity-dependent nonlinear effects. Monomode photonic crystal fibre can readily be made as large as desired because, unlike conventional optical fibres, the number of guided modes in a PCF is independent of the ratio of core radius  $p$  to optical wavelength  $\lambda$  (provided that the wavelength is sufficiently short). Instead, the number of modes depends only on the ratio of the air hole diameter  $d$  to the spacing between holes  $\Lambda$  [2]. One consequence of this is that no change in the refractive index profile is required to fabricate fibres with different core diameters, and a single preform can be used to fabricate monomode fibres with cores of any size.

An SEM micrograph of a portion of the cleaved face of the fibre reported here is shown in Fig. 1. It has a core of pure silica which is surrounded by an array of air holes in a silica matrix. The fibre shown is 180 μm in diameter and is several metres long. The air holes run along the entire length. The core diameter (defined as the diameter of the ring formed by the innermost air holes) is  $2p = 22.5 \mu\text{m}$ , and the air holes (with diameters  $d = 1.2 \mu\text{m}$ ) are spaced by  $\Lambda = 9.7 \mu\text{m}$  in the periodic region. The fibre was made by stacking a number of silica capillaries into the required hexagonal array, replacing a single one of them with a



Fig. 2 Contour map of near field intensity distribution for guided mode in fibre shown in Fig. 1 at wavelength  $\lambda = 458$  nm

Contours are plotted at 10% intervals in modal field intensity distribution

The fibre shown in Fig. 1 guides only a single mode at a wavelength of  $\lambda = 458$  nm (and at all longer wavelengths within the transparency window of silica). We know this because we have coupled light into one end of the fibre and have used index-matching oil to strip off light in cladding modes. We then find that the near and far field patterns of the light guided in the fibre core are independent of the input coupling conditions or of any bends or twists introduced into the fibre. This is strong evidence of mono-

mode waveguiding. A contour map of the nearfield pattern of the guided mode is shown in Fig. 2. Both the near and far field patterns are very similar to those previously observed in PCF with a conventional core size [1, 2], differing only in scale. The angular divergence of the guided mode in the large-core fibre is  $\theta_a = 0.0065$ , and scales approximately linearly with wavelength and with inverse core size.

The performance of a large-core PCF is limited by bend loss, which unavoidably becomes large for large cores and tight bends [3]. Using the effective index model, [2] the parametric dependence of the critical bend radius for catastrophic loss of power from the fibre core can be shown to be  $R_c \propto \Lambda^3 \lambda^{-2}$ . The, at first surprising, inverse square dependence of the critical bend radius on wavelength is a direct consequence of the fact that for large photonic crystal fibres the effective  $V$ -value is independent of wavelength [2]. We have verified this behaviour in several fibres of different sizes. For the fibre described above we find that  $R_c = 50\text{cm}$  at  $\lambda = 458\text{nm}$  and  $R_c \approx 4\text{cm}$  at  $\lambda = 1.55\mu\text{m}$ . It is worth noting that making such a fibre using conventional technology becomes increasingly difficult for such large cores because of the ever-higher requirements for the uniformity of the doping level as the refractive index difference between the core and the cladding decreases.

We have described the design and fabrication of an ultra-large mode area fibre which guides only a single mode. This was demonstrated for fibre with  $2p/\lambda \approx 50$ . There is no theoretical or technological limit on the mode size for a monomode fibre which can be fabricated in this way, except for bend loss. Our results suggest that far larger core size fibres could be made to guide a single low-loss mode over relatively straight lengths of fibres. We expect the design to be useful in the design of novel high power waveguide lasers and amplifiers.

**Acknowledgments:** This work is supported by the E.P.S.R.C. and by the Quantum Optics Group at D.E.R.A. Malvern.

© IEE 1998

14 January 1998

Electronics Letters Online No: 19980965

J.C. Knight, T.A. Birks, R.F. Cregan and P.St.J. Russell (Optoelectronics Group, Department of Physics, University of Bath, Bath, BA2 7AY, United Kingdom)

E-mail: j.c.knight@bath.ac.uk

J.-P. de Sandro (Optoelectronics Research Centre, University of Southampton, Southampton, SO17 1BJ, United Kingdom)

## References

- 1 KNIGHT, J.C., BIRKS, T.A., ATKIN, D.M., and RUSSELL, P.ST.J.: 'All silica single-mode optical fibre with photonic crystal fibre', *Opt. Lett.*, 1996, 21, pp. 1547-1549 (also erratum *Opt. Lett.*, 1997, 22, pp. 484-485)
- 2 BIRKS, T.A., KNIGHT, J.C., and RUSSELL, P.ST.J.: 'Endlessly single-mode photonic crystal fibre', *Opt. Lett.*, 1997, 22, pp. 961-963
- 3 LOVE, J.D.: 'Application of a low-loss criterion to optical waveguides and devices', *IEE Proc.*, 1989, 136, pp. 225-228

## Model showing effect of impurity sub-lattice topology on upconversion in Er<sup>3+</sup>-doped glasses

P.-M. Binder, L.F. Perondi and T.R. Gosnell

Monte Carlo methods are used to simulate a spatial model of uniform upconversion and commensurate excited-state depletion in high-concentration Er<sup>3+</sup>-doped solids. It is found that the topology of the impurity sublattice affects the value of the upconversion coefficient, a result in accord with recent measurements on samples prepared with identical host compositions and ion concentrations.

Erbium-doped optical amplifiers operating on the  $4I_{13/2} \rightarrow 4I_{15/2}$  transition at  $1.55\mu\text{m}$  suffer an upconversion pump depletion process involving pairs of ions in the excited  $4I_{13/2}$  state. The net effect of upconversion is the rapid annihilation of one of the two  $4I_{13/2}$

excitations in favour of the  $4I_{15/2}$  ground state [1, 2]. At low concentrations of the dopant ions, this process is most likely to occur in isolated pairs and clusters [3, 4], while at high concentrations ( $\geq 0.05\text{mole\% Er}_2\text{O}_3$ ), rapid resonant spatial migration of the  $4I_{13/2}$  excitation over the impurity sublattice combined with occasional near-neighbour encounters of excitation pairs gives rise to so-called uniform upconversion [5, 6].

In this Letter, we investigate the latter regime and show through Monte Carlo simulations of resonant migration and subsequent annihilation of the  $4I_{13/2}$  excitation, that the rate of uniform upconversion depends not only on the concentration of erbium ions but also on their spatial distribution. The latter effect is posited to account for recent experimental findings that sample preparation methods affect the measured value of the upconversion coefficient [7].

We use fully spatial models [8] rather than the more common bulk models. The latter give, for the loss of excitations to radiative decay and upconversion:

$$\frac{dn}{dt} = -\gamma n - Cn^2 \quad (1)$$

where  $n$  denotes the  $4I_{13/2}$  population density,  $\gamma$  is the radiative decay term, and  $C$  is the upconversion coefficient. This equation agrees reasonably well with experiments. However, bulk models fail to explain effects beyond dopant concentration. For this we need spatial models, which are defined by a lattice upon which the erbium ions are located and by a dynamic for the excitations. For the lattice, we have chosen a regular square array whose nearest-neighbour sites are either connected by a 'bond' or disconnected. The former condition permits migration or upconversion between the two sites while the latter condition forbids these processes. With different bond arrangements we attempt to model different topologies of the impurity sublattice.

The dynamic is defined by three transition rates,  $W$ ,  $R$  and  $\Gamma$ , for migration, radiative decay, and upconversion, respectively, so that  $W + R + \Gamma = 1$ . A trial move selects one of these processes, and the direction in which it occurs, the latter two, subject to the conditions of the previous paragraph. We have eliminated long-range exchange processes. This considerably speeds up the simulations, but leaves the question of the effects of this approximation to future work.

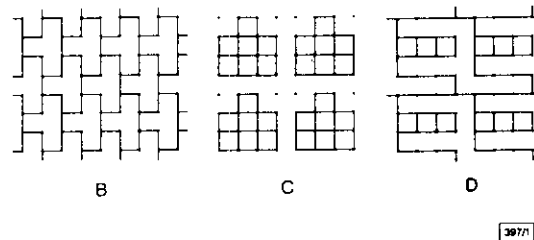


Fig. 1 Lattices B-D used in simulations

All have equal fractions of open and closed bonds

To study the effects of sample preparation, we have simulated the dynamics in square lattices in which all sites are occupied with Er ions, and therefore the dopant concentration is the same, but the connecting bonds occur only with probability  $p = 0.625$ . We concentrate on four lattices with different bond arrangements. In lattice A, the connecting bonds are chosen randomly with probability  $p$ , which produces an infinite cluster, with islands of unconnected sites. Lattices B-D are regular tilings of the square lattice, shown in Fig. 1. We have also performed some simulations on the fully connected square lattice for model validation purposes, which are described here.

We have studied systems of size  $100 \times 100$ , with all sites initially occupied with an excitation. We have simulated several combinations of migration, radiative decay and annihilation rates, typically for 400 MC steps and sometimes much longer, with averages in the range of 20 to 800 configurations per lattice. An MC step is defined as an average of one trial move per particle. We were able to measure surviving excitations ( $n$ , initially with  $n_0 = 10000$ ), average distance travelled before annihilation, and rates of extinction ( $dn/dt$ ) for all time steps.

First, with  $\Gamma = 0$ , theory predicts an expected exponential decay of excitations with time,  $n(t) = n_0 e^{-Rt}$ , independent of migration



## Silica/Air Photonic Crystal Fibres

Philip St.J. RUSSELL, Tim A. BIRKS, Jonathan C. KNIGHT,  
Robert F. CREGAN, Brian J. MANGAN,  
*Optoelectronics Group, School of Physics, University of Bath, Bath BA2 7AY, UK*  
and

Jean-Philippe DE SANDRO  
*Optoelectronics Research Centre, University of Southampton, Southampton SO17 1BJ, UK*

We describe the fabrication, characterisation and applications of silica/air photonic crystal fibres with microscopic arrays of air capillaries running along their length.

### 1. Introduction

We have developed a new kind of all-silica optical fibre which has a hexagonal micron-spaced array of sub-micron diameter air capillaries running along its axis<sup>1-6</sup>. The resulting "2½" dimensional photonic crystal can be many metres (potentially km) in length. Structural defects can easily be introduced during the fabrication stage, either by replacing a capillary with a solid hexagonal rod (high index defect), or by leaving out a capillary entirely (low index defect). Under the correct conditions, light can be guided at both types of defect. If, for example, a full two-dimensional photonic band gap exists over some range of axial wavevector, then confinement can be by Bragg reflection. In the case of the high index defect, however, light can also be confined in the pure silica core by total internal reflection at the core/cladding interface. Excitation of photonic crystals in this manner by evanescent fields, i.e., beyond their critical angle, produces unusual and beneficial effects. For example, the fibre supports a robust single mode over a spectral range very much larger than standard single-mode telecom fibres<sup>3</sup>.

### 1. Background

Yablonovitch's proposal<sup>7</sup> that a photonic band gap could be created, in direct analogy with the electronic band gap, in dielectric materials periodically patterned in 3D, has created wide interest. The subsequent theoretical and experimental demonstration, by several groups, of a PBG at GHz frequencies confirmed the essential soundness of his idea. His pioneering efforts have resulted in a

rekindling of interest in "2½" dimensional photonic crystals, i.e., those in which the normals to the crystal planes all lie in the same plane. An example of such a structure is a planar dielectric waveguide with multiple corrugations etched into its top surface, as discussed in the early 1980s<sup>8,9</sup>. In addition to needing a smaller index contrast to achieve a full two-dimensional PBG, the relative ease with which "2½" dimensional crystals can be made, even at visible and near infra-red wavelengths, and the belief that new physics remains to be discovered, renders them an attractive topic of research in their own right.

With only a few exceptions, published theoretical

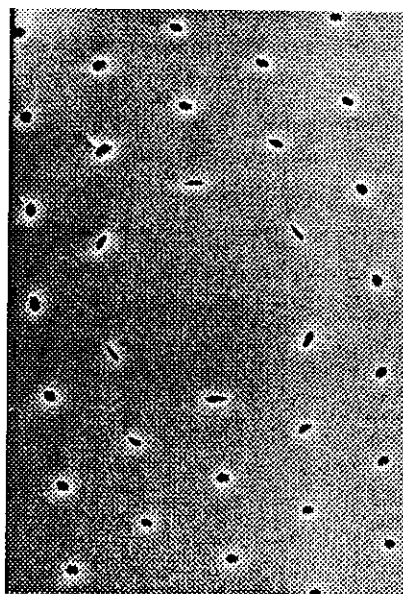


Fig. 1. SEM of photonic crystal fibre with small air filling fraction and a central high index defect; inter-hole spacing 10  $\mu\text{m}$ . We have produced fibres with inter-hole spacings below 2  $\mu\text{m}$ <sup>3</sup>.

studies of  $2\frac{1}{2}D$  photonic crystals have been effectively 2D, i.e., they omit the possibility of propagation along the third *axial* dimension. As pointed out previously<sup>10,11</sup>, propagation along this dimension must be admitted if waveguide modes are to be treated in thin layers of photonic crystal. This is because the transverse resonance condition required for formation of such modes needs a component of wave velocity normal to the film. When properly designed, photonic crystal waveguides can support both perfect waveguiding and strong photonic band-gap effects<sup>11</sup>. Furthermore, since the transverse component of wavevector falls as its axial component rises, the required "inter-atomic" lattice spacing rises while the index contrast needed to create a full 2D band gap reduces. These make it progressively easier to create a  $2\frac{1}{2}D$  structure supporting a full 2D band gap as the axial component of wavevector rises.

In the realisation of these matters, and with funding from the Defence Research Agency in Malvern, we embarked in 1991 on the fabrication of photonic crystal fibres, in what became known as the "holey fibre project." Essentially, the idea was to adapt the technology of glass fibre fabrication to the production of a  $2\frac{1}{2}D$  photonic crystal consisting of a thin thread of fused silica riddled with a hexagonal array of air capillaries running along its length. Calculations show that full 2D band gaps can be achieved with an air filling fraction of 34% – see Figure 3 for the case when it is 45%<sup>12</sup>). The original aim was to incorporate a low index defect state in the centre of this structure, and achieve a novel form of waveguiding in which the light is confined by the full 2D photonic band gap.

### 3. Fabrication

Pure silica fibres supporting guided modes were first investigated in the 1970's<sup>13</sup>, the aim being to achieve low transmission losses. The huge success of chemical vapour deposition in producing extremely low loss fibre has largely eclipsed this early technology. Our original photonic crystal fibre was formed by creating a hexagonal silica/air preform on a macroscopic scale and then reducing its size by several orders of magnitude by pulling it into an optical fibre. The unit cell of the photonic crystal is formed by drilling a hole down the centre of a silica rod and milling six flats on the outside, to give a

hexagonal cross-section. This is pulled down into cane with a diameter of approximately 1 mm and then stacked to give the hexagonal crystal structure. Defect sites are introduced at this stage, and the stacked preform is then drawn twice more to produce the final fibre. SEMs of typical fibres are given in Figures 1 & 2.

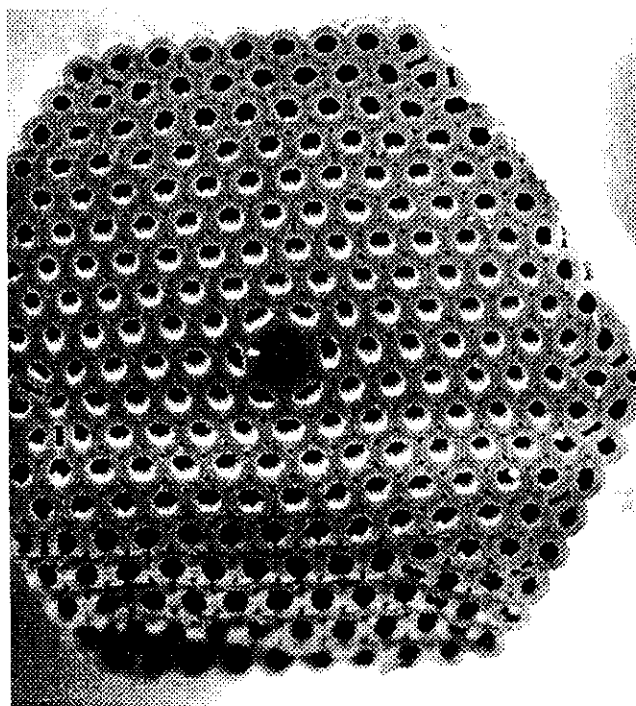


Fig.2. Photonic crystal fibre with central high index defect; inter-hole spacing 7  $\mu\text{m}$ . Made using cylindrical capillaries.

### 4. High index defect

Having succeeded in producing a regular photonic crystal fibre, we realised that it might be possible to produce a waveguide by replacing one of the air capillaries with a solid cane. Viewing the cladding as a material with an "effective index" lower than the core, this structure appears to be a conventional step-index waveguide. On the other hand, allowing that light could escape from the core along the silica bridges, it looks like a leaky waveguide. (In the limit of large air holes, the central core becomes more and more isolated from the cladding and will clearly guide light.) Given that our intuition was sending out conflicting signals, and that we were in the lucky position of being able to make the structure, we tested the fibre experimentally. The

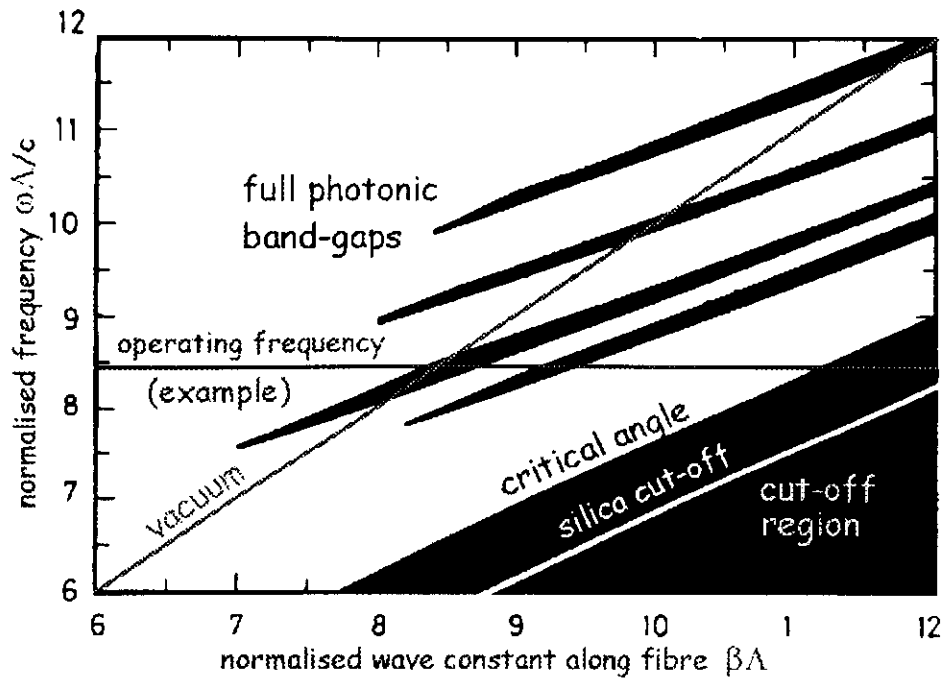


Fig. 3. Band-gap diagram for 2D silica/air crystal with 45% air (after <sup>12)</sup>). At fixed optical frequency (horizontal line), full 2D photonic band gaps exist (slanted “fingers”). A cut-off region also exists between the maximum silica wavevector and the wavevector at the critical angle in the PCF cladding. Guided modes can be created in both the photonic band gaps and this cut-off region by introducing structural defects.

results were quite novel and of wide-reaching technological and scientific interest.

The fibre turned out to be a zero-leakage unconditionally single-mode waveguide, i.e., only one mode was present *whatever the wavelength of the launched light*. The conclusion was that we had produced a fibre structure whose single-mode nature was controlled purely by the geometry of the 2½D crystal and not the wavelength of light. In order to understand the importance of this result it is useful to consider the behaviour of standard single mode fibre<sup>14)</sup>. The normalised frequency parameter

$$V = \frac{2\pi\rho}{\lambda} \sqrt{n_{co}^2 - n_{cl}^2}$$

determines the number of guided modes supported by a step-index fibre ( $\rho$  is the core radius,  $n_{co}$  and  $n_{cl}$  the core and cladding indices and  $\lambda$  the vacuum wavelength). When  $V < 2.405$ , the fibre is single mode.  $V$  increases rapidly as the wavelength falls, and more and more higher order modes appear. For a silica/air photonic crystal fibre, the effective cladding index is a strong function of wavelength<sup>14)</sup>, and  $V$  may be written in the approximate form:

$$V = \sqrt{\left(\frac{2\pi\Lambda}{\lambda}\right)^2 (n_s^2 - 1) f(\lambda) + \left(\frac{\Lambda j_0}{r_c}\right)^2}$$

where  $f(\lambda)$  is the filling fraction of air, weighted by the field distribution in the cladding,  $r_c$  is the radius of each of the regular array of high index resonators that form the cladding, and  $J_0(j_0) = 0$  where  $J_0$  is a Bessel function of the first kind. The pitch of the crystal is  $\Lambda$  and  $n_s$  is the index of silica. At long enough wavelengths,  $f$  is simply the fractional proportion of air by area. As the wavelength decreases, however, light tends to redistribute more and more into the silica parts of the photonic crystal cladding, following  $f(\lambda) \sim \lambda^3$ . In the limit as  $\lambda \rightarrow 0$ , the first term under the square root tends to zero and the  $V$  parameter tends to  $\Lambda j_0 / r_c$ , which is independent of wavelength and directly proportional to one over the square root of the geometrical filling fraction of silica, i.e.,  $\propto 1/\sqrt{1-f(\infty)}$ . Provided the long-wavelength filling fraction is itself small enough, the fibre will remain single mode at all wavelengths. In the language of solid-state physics, the trapped state in the high index defect is akin to a state in the forbidden zero-order photonic band gap, i.e., the one

below the first order Bragg condition. This band gap occurs even in an isotropic medium - for example, in the core of a standard optical fibre. What is, however, novel about modes created in the zero-order band gap of a 2D photonic crystal is the extremely strong dispersion of the effective index in the periodic cladding.

In conclusion, the photonic crystal fibre offers new guiding properties, including guaranteed single mode operation at all wavelengths, subject to certain bend loss considerations<sup>14)</sup>. The wider implications of the technology are the subject of active exploration in our groups.

### Acknowledgements

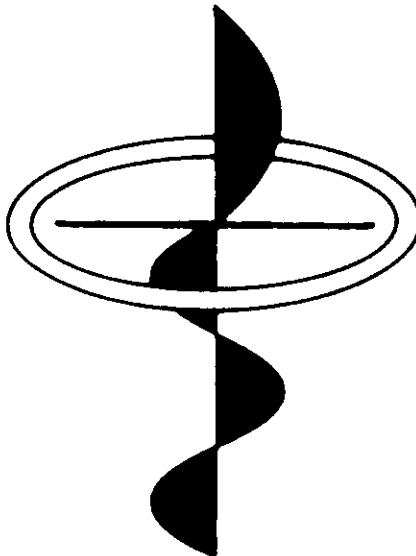
The authors acknowledge the financial support of DERA Malvern and the UK Engineering and Physical Sciences Research Council.

### References

- 1) T.A. Birks, D.M. Atkin, G. Wylangowski, P.St.J. Russell and P.J. Roberts, "2-D photonic band-gap structures in fibre form," in *Photonic Band Gap Materials* (Editor: C.M. Soukoulis) Kluwer 1996
- 2) J.C. Knight, T.A. Birks, P.St.J. Russell and D.M. Atkin, "Pure silica single-mode fibre with hexagonal photonic crystal cladding," postdeadline paper at OFC'96
- 3) J.C. Knight, T.A. Birks, P.St.J. Russell and D.M. Atkin, "All-silica single-mode fiber with photonic crystal cladding," *Opt. Lett.* **21** (1547-1549) 1996; Errata, *Opt.Lett.* **22** (484-485) 1997
- 4) J.C. Knight, T.A. Birks, D.M. Atkin and P.St.J. Russell, "Two-dimensional photonic crystal material in fibre form," presented at CLEO-Europe (Hamburg, Germany, September 1996)
- 5) J.C. Knight, T.A. Birks, P.St.J. Russell and J.G. Rarity, "Out-of-plane Bragg scattering from a photonic crystal fibre," *Applied Optics*, 1997 (to be published)
- 6) J.C. Knight, T.A. Birks, P.St.J. Russell and J.G. Rarity, "Bragg scattering studies of a photonic crystal fibre," paper CFQ6 in *Conference on Lasers and Electro-Optics*, 11 1997 OSA Technical Digest Series (Optical Society of America, Washington, D.C., 1997), pp. 527-528
- 7) E. Yablonovitch, "Photonic band gap structures," *J.Opt.Soc.Am.* **10** (283-295) 1993
- 8) P.St.J. Russell, "Interference of integrated Floquet-Bloch waves," *Phys.Rev. A* **33** (3232-3242) 1986
- 9) R. Zengerle, "Light propagation in single and doubly periodic planar waveguides," *J. Mod. Opt.* **34** (1589-1617) 1987
- 10) D.M. Atkin, P.St.J. Russell, T.A. Birks & P.J. Roberts, "Photonic band structure of guided Bloch modes in high index films fully etched through with periodic microstructure," *J.Mod.Opt.* **43** (1035-1053) 1996
- 11) P.St.J. Russell, D.M. Atkin and T.A. Birks, "Bound modes of photonic crystal waveguides," in *Quantum Optics in Wavelength Scale Structures* (Eds: J.G. Rarity & C. Weisbuch), Kluwer 1996
- 12) T.A. Birks, P.J. Roberts, P.St.J. Russell, D.M. Atkin and T.J. Shepherd, "Full 2-D photonic band gaps in silica/air structures," *Electron. Lett.* **31** (1941-1942) 1995
- 13) P. Kaiser and H.W. Astle, "Low-loss single-material fibers made from pure fused silica," *Bell Syst. Tech. J.* **53** (1021-1039) 1974
- 14) T.A. Birks, J.C. Knight and P.St.J. Russell, "Endlessly single-mode photonic crystal fibre," *Opt.Lett.* **22** (961-963) 1997

Reprinted from

P5



# OPTICAL Materials

---

Optical Materials 11 (1999) 143–151

## Photonic crystals as optical fibres – physics and applications

J.C. Knight <sup>a,\*</sup>, T.A. Birks <sup>a</sup>, R.F. Cregan <sup>a</sup>, P.St.J. Russell <sup>a</sup>, J.-P. de Sandro <sup>b</sup>

<sup>a</sup> *Optoelectronics Group, School of Physics, University of Bath, Bath BA2 7AY, UK*

<sup>b</sup> *Optoelectronics Research Centre, University of Southampton, Southampton SO17 1BJ, UK*



**EDITOR IN CHIEF**

**R.C. POWELL**  
Optical Sciences Center  
University of Arizona  
Tucson, AZ 85721, USA  
Tel: +1-520-6216997  
Fax: +1-520-6219613  
E-mail: rcpowell@u.arizona.edu

**H.J. EICHLER**  
Technische Universität Berlin  
Optisches Institut  
Strasse des 17. Juni 135  
D-10623 Berlin, Germany

**J. FOUSEK**  
Institute of Physics  
Na Slovance 2  
18040 Prague 8, Czech Republic

**J.P. HUIGNARD**  
Thomson-CSF  
Domaine de Corbeville, B.P. 10  
91401 Orsay Cedex, France

**C. KLINGSHIRN**  
Institut für Angewandte Physik  
Universität Karlsruhe  
Kaiserstr. 12  
76128 Karlsruhe, Germany

**H. SAKAKI**  
Institute of Industrial Science  
University of Tokyo  
Tokyo, Japan

**R.J. TWIEG**  
IBM Research Div.  
Almaden Research  
Center K95/801, 650 Harry Road  
San Jose, CA 95120-6099, USA

**ASSOCIATE EDITORS**

**T.T. BASIEV**  
General Physics Institute  
Lab. of Laser Spectr. of Solids  
Vavilov Street 38  
117942 Moscow,  
Russian Federation

**L.A. BOATNER**  
Oak Ridge National Lab.  
Solid State Division  
P.O. Box 2008  
Building 2000, MS 6056  
Oak Ridge, TN 37831-6056, USA

**G. BOULON**  
Physico-Chimie  
des Matériaux Luminescents  
Université Claude Bernard  
Lyon 1, Bât. 205  
69622 Villeurbanne Cedex, France

**L.L. CHASE**  
Lawrence Livermore Nat. Lab.  
P.O. Box 808, L-357  
Livermore, CA 94550, USA

**FUXI GAN**  
Shanghai Inst. of Optics  
and Fine Mechanics  
Academia Sinica  
P.O. Box 800-211  
201800 Shanghai  
People's Republic of China

**D.C. HANNA**  
Optoelectronics Res. Centre  
University of Southampton  
Southampton SO9 1BJ, UK

**J. HEGARTY**  
Dept. of Pure & Appl. Physics  
Trinity College  
University of Dublin  
Dublin 2, Ireland

**K. HILL**  
Communications Research Center  
3701 Carling, P.O. Box 11490  
Station "H", Ottawa, Ontario  
Canada K2H 852

**G.C. RIGHINI**  
IROE-CNR  
via Panciatichi 64  
50127 Firenze, Italy

**J. RUBIO**  
Metropolitan University  
Istapalapa Michoacan  
Purisima Ave.  
Col. Vincentina  
P.O. Box 55534, Istapalapa  
Mexico D.S., Mexico City,  
Mexico 09340

**J.S. SHIRK**  
Naval Research Lab. Code 5613  
4555 Overlook Ave. S.W.  
Washington, DC 20375, USA

**G.I. STEGEMAN**  
CREOL  
University of Central Florida  
12424 Research Parkway,  
Suite 400  
Orlando, FL 32826, USA

**S. UMEGAKI**  
Dept. of Electrical Engineering  
Materials Science Faculty  
of Science and Technology  
Keio University, 3-14-1, Hiyoshi,  
Kouhoku-ku, Yokohama-shi  
Kanagawa 223, Japan

**V. VORLICEK**  
Institute of Physics ASCR  
Na Slovance 2  
180 40 Prague 8, Czech Republic

**M.J. WEBER**  
Lawrence Berkeley Lab.  
1, Cyclotron Road  
Berkeley, CA 94720, USA  
**B.S. WHERRETT**  
Department of Physics  
Heriot-Watt University  
Edinburgh EH14 4AS, Scotland, UK

**A.E. WHITE**  
AT&T Bell Laboratories  
600 Mountain Ave, P.O. Box 636  
Murray Hill, NJ 07974-0636, USA

**Aims and Scope**

The purpose of OPTICAL MATERIALS is to provide a means of communication and technology transfer between researchers who are interested in materials with potential device applications. The journal publishes original papers and review articles on the design, synthesis, characterisation and applications of optical materials.

Abstracted/Indexed in: Chemical Abstracts; Current Contents: Engineering, Technology & Applied Sciences; EI Compendex Plus; Engineered Materials Abstracts (ASM International Materials Information); Engineering Index; INSPEC

**Subscription Information 1999**

Volumes 11 and 12 (8 issues) of Optical Materials (ISSN 0925-3467) are scheduled for publication.

Prices are available from the publishers upon request. Subscriptions are accepted on a prepaid basis only. Issues are sent by SAL (Surface Air Lifted) mail wherever this service is available. Airmail rates are available upon request. Please address all enquiries regarding orders and subscriptions to:

Elsevier Science B.V.

Order Fulfilment Department  
P.O. Box 211, 1000 AE Amsterdam  
The Netherlands

Tel. +31 20 4853642, Fax: +31 20 4853598

Claims for issues not received should be made within six months of our publication (mailing) date.

**Advertising information**

Advertising orders and enquiries can be sent to: *Europe and ROW*: Rachel Gresle-Farthing, Elsevier Science Ltd., Advertising Department,

The Boulevard, Langford Lane, Kidlington, Oxford OX5 1GB, UK; phone: (+44) (1865) 843565; fax: (+44) (1865) 843976; e-mail: r.gresle-farthing@elsevier.co.uk. *USA and Canada*: Elsevier Science Inc., Mr Tino DeCarlo, 655 Avenue of the Americas, New York, NY 10010-5107, USA; phone: (+1) (212) 6333815; fax: (+1) (212) 6333820; e-mail: t.decarlo@elsevier.com. *Japan*: Elsevier Science K.K., Advertising Department, 9-15 Higashi-Azabu 1-chome, Minato-ku, Tokyo 106, Japan; Phone: (+81) (3) 55615033; fax: (+81) (3) 55615047.

**Orders, claims, and product enquiries**

Please contact the Customer Support Department at the Regional Sales Office nearest you:

*New York*: Elsevier Science, PO Box 945, New York, NY 10159-0945, USA; phone: (+1) (212) 6333730 [toll free number for North American customers: 1-888-4ES-INFO (4374636)]; fax: (+1) (212) 6333680; e-mail: usinfo-f@elsevier.com.

*Amsterdam*: Elsevier Science, PO Box 211, 1000 AE Amsterdam, The Netherlands; phone: (+31) (20) 4853757; fax: (+31) (20) 4853432; e-mail: nlnfo-f@elsevier.nl.

*Tokyo*: Elsevier Science K.K., 9-15 Higashi-Azabu 1-chome, Minato-ku, Tokyo 106, Japan; phone: (+81) (3) 55615033; fax: (+81) (3) 55615047; e-mail: info@elsevier.co.jp.

*Singapore*: Elsevier Science, No. 1 Temasek Avenue, #17-01 Millenia Tower, Singapore 039192; phone: (+65) 4343727; fax: (+65) 3372230; e-mail: asiainfo@elsevier.com.sg.

*Rio de Janeiro*: Elsevier Science, Rua Sete de Setembro 111/16 Andar, 20050-002 Centro, Rio de Janeiro, RJ, Brazil; phone: (+55) (21) 5095340; fax: (+55) (21) 5071991; e-mail: elsevier@campus.com.br [Note (Latin America): for orders, claims and help desk information, please contact the Regional Sales Office in New York as listed above].

**US mailing notice** *Optical Materials* (ISSN 0925-3467) is published bimonthly by Elsevier Science B.V., Molenwerf 1, P.O. Box 211, 1000 AE Amsterdam, The Netherlands. Annual subscription price in the USA is US \$549 (valid in North, Central and South America only), including air speed delivery. Periodicals postage paid at Jamaica NY 11431.

US postmasters: Send address changes to Optical Materials, Publications Expediting, Inc., 200 Meacham Avenue, Elmont, NY 11003. Airfreight and mailing in the USA by Publications Expediting.

© The paper used in this publication meets the requirements of ANSI/NISO Z39.48:1992 (Permanence of Paper).

PRINTED IN THE NETHERLANDS



ELSEVIER

January 1999

Optical Materials 11 (1999) 143–151



# Photonic crystals as optical fibres – physics and applications

J.C. Knight <sup>a,\*</sup>, T.A. Birks <sup>a</sup>, R.F. Cregan <sup>a</sup>, P.St.J. Russell <sup>a</sup>, J.-P. de Sandro <sup>b</sup>

<sup>a</sup> Optoelectronics Group, School of Physics, University of Bath, Bath BA2 7AY, UK

<sup>b</sup> Optoelectronics Research Centre, University of Southampton, Southampton SO17 1BJ, UK

## Abstract

We describe the fabrication, characterisation and possible applications of a new type of optical material – a 2-dimensional photonic crystal made of silica and air. This macroporous silica, which is made using the technology of optical fibre fabrication, has properties which differ remarkably from those of conventional materials. We describe how such a material can be used to form waveguides with new and unusual properties, and present some results to illustrate this. Such photonic crystal waveguides could be significant in the design of new lasers and amplifiers. © 1999 Elsevier Science B.V. All rights reserved.

PACS: 42.81.Q; 42.70.Q

Keywords: Photonic crystals; Optical fibre waveguides; Photonic band gaps

## 1. Introduction

The continuing development of optical components requires that they be developed on an ever-smaller scale. Ideally, these components would be engineered on the scale of the optical wavelength. Proceeding to this new generation of active and passive optical components will mean using available materials in novel ways and developing new material systems with the required properties. It is thus important to recognise that one can substantially alter the properties of optical materials by structuring them on the scale of the optical wavelength, fabricating new materials with previously unattainable optical characteristics. This possibility has led to research into so-called photonic crystal materials – materials which have been purposely microstructured so that they have a 2- or 3-dimensional crystal structure, with a

lattice scale of the order of the optical wavelength [1]. The resulting periodic variation in the refractive index results in a strong interaction between the material microstructure and the light field, and can significantly alter the optical properties of the composite material [1,2].

One example of the type of effect which can be observed in such materials is our observation of low-loss waveguiding in an optical fibre which only guides a single mode – independent of the wavelength or fibre size [3,4]. The useful range of monomode operation of this fibre is limited only by the optical absorption of silica and by the bend losses which unavoidably become significant for very short wavelengths and large scale fibres. Another example is the appearance of optical band structure in photonic crystals [1,5]. The appearance of such band structure – which places constraints upon the allowed photon states within the crystalline material – offers the possibility of controlling the spontaneous emission process by engineering the material microstructure, which is

\* Corresponding author. E-mail: j.c.knight@bath.ac.uk.

significant for the design of novel lasers and amplifiers. In general, the most useful effects in photonic crystal materials are observed when the variation in the refractive index is quite large. Consequently one needs to introduce a morphological microstructure into the material. This paper describes the fabrication of a 2-dimensionally periodic photonic crystal material by a novel technique. We report on its unusual optical properties and how it can be used to form new classes of optical waveguides.

## 2. Fabrication

The photonic crystal material being discussed here is in the form of a fine silica fibre with a 2-dimensional array of air holes running down its length [3,6]. The crystal structure is formed on a macroscopic scale as a preform, by stacking half-meter lengths of capillary into a hexagonal shape by hand. Typically we use around 300 capillaries of diameter approximately 0.8 mm to form a preform with an external diameter of perhaps 20 mm. This preform is then drawn at an elevated temperature into a fibre using an optical-fibre

drawing tower, reducing the overall scale of the structure by a factor approaching  $10^4$  while maintaining the crystal structure introduced at the preform stage. Drawing proceeds in two stages: in the first the stack of capillaries is fused together while being drawn into 1 m lengths of cane with a diameter of about 1 mm. Single pieces of this cane are subsequently drawn down a second time, the final fibre having a diameter of between 20 and 200  $\mu\text{m}$ . The pitch is between 1 and 10  $\mu\text{m}$ , and the fraction of air present in the samples is in a range up to around 50%. The maximum attainable air filling fraction is limited by the effects of surface tension which cause the air holes to collapse, so that it is increasingly difficult to fabricate large air-fraction samples for the smaller pitches.

An example of a 2-dimensional photonic crystal material produced in this way is shown in Fig. 1. This scanning electron micrograph shows a portion of the cross-section of a length of fibre which is approximately 80  $\mu\text{m}$  in diameter. The pitch  $\Lambda$  of the crystal structure is 4.2  $\mu\text{m}$  and the large air hole diameter  $d = 2.9 \mu\text{m}$ . The large hexagonal air holes correspond to the originally circular capillary cores, pulled into a hexagonal shape. The smaller triangular air holes are the air gaps which

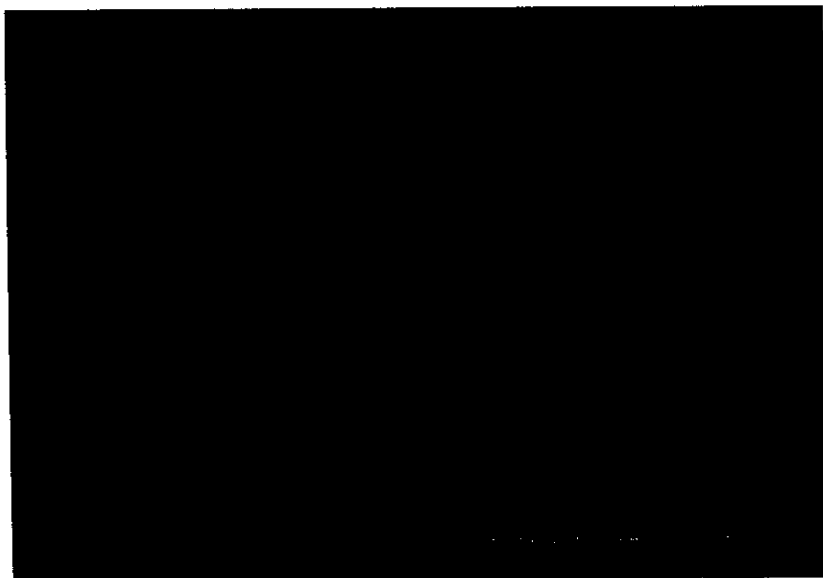


Fig. 1. SEM micrograph of a portion of the cleaved endface of a photonic crystal fibre. The fibre shown here has an external diameter of around 80  $\mu\text{m}$ , a pitch of  $\Lambda = 5.5 \mu\text{m}$ . The apparent distortions on the right hand side of the picture result from a poor cleave in that area.



were formed at the interstitial sites at the “corners” of the stacked capillaries. A crucial parameter during the fabrication process is the temperature at which the preform and the fibre are drawn: higher temperatures lead to the air holes disappearing due to the surface tension forces. The survival of the interstitial holes indicates that the sample in Fig. 1 was drawn at a relatively low temperature (perhaps 1800°C). By increasing the furnace temperature the air hole size can be reduced – we have drawn fibres where the air holes are as small as 50 nm in diameter, but still persist over long lengths of several metres. At such a temperature the interstitial holes no longer exist. Similarly, we can easily vary the final diameter of the fibre – and hence the pitch – by changing the rate at which the fibre is drawn. Because a single stacked preform can – in principle at least – supply kilometre lengths of such fibre, we are in a position to investigate the optical properties of this material for widely varying drawing conditions. Furthermore, it is possible to introduce localised defects into the crystal structure at the stacking stage – for example by leaving out one air hole or by increasing or decreasing the size of a single hole, or by replacing a single capillary with a similar doped capillary. This provides further scope for optical studies, making it possible to observe waveguiding and microcavity effects within the structures.

### 3. Optical properties of 2-D photonic crystals

In a periodically varying medium the allowed (propagating) photon modes are directly linked to the material structure. This means that appropriately microstructured dielectric materials provide an exciting and potentially important way in which to control the propagation of light. We can use an embedded defect in a photonic crystal as a waveguiding core to form an optical waveguide which guides light [3,4,7,8]. To do this, we need to understand the optical properties of the materials for incidence along particular directions of the crystal lattice. It is especially interesting to determine those parameters which will cause light to be totally reflected from the structure, as this can then

be used to confine light in a waveguiding core. It is not sufficient for our purposes to study only the optical properties in the periodic plane, although this has been done previously by many authors. Rather, it is the case where there is a component of wavevector out of the periodic plane (i.e. along the fibre axis) which is of interest for our applications [2]. The band structure in these directions can be studied using now-standard numerical techniques [9,10]. Band structure calculations give the longitudinal propagation constants  $\beta$  of the electromagnetic modes which can propagate in the periodic medium for different directions with respect to the crystal lattice. Specific examples of these calculations for a hexagonal silica–air crystal structure similar to that being discussed here may be found in Ref. [7].

These calculations show that for a given frequency there is a maximum allowed value of the propagation constant,  $\beta_{\max}$ . This mirrors the behaviour of conventional bulk materials, where the maximum value of  $\beta$  is given by  $\beta_{\max} = nk$ , where  $n$  is the refractive index of the material being discussed and  $k$  is the free-space propagation constant. Light which is incident on the material with  $\beta > \beta_{\max}$  (and this is only possible from a higher-index material) cannot propagate in the second material – it is totally reflected. In this case the only field within the second material is the evanescent field associated with total internal reflection. The difference between the familiar bulk case and the corresponding situation in a photonic crystal material is that in the present case the value of the effective refractive index  $\beta_{\max}/k$  is not a constant, but depends strongly on the properties of the crystal material and on the optical wavelength. As we shall demonstrate in the next section this allows for considerable freedom to engineer the material properties to exhibit specific desired optical properties.

For  $\beta < \beta_{\max}$  there can be propagating modes within the periodic material. These occur for fixed values of the direction with respect to the crystal structure and for certain values of the propagation constants. For any particular value of  $\beta$  there may be propagating modes which occur for certain directions of incidence, while in other directions there may be no propagating modes. This is dif-

ferent to the behaviour of light in free space, where there are propagating modes in any direction, because the propagating modes in a periodic medium must of necessity satisfy Bloch's theorem. For certain periodic structures it is possible to find  $\beta$ -values for which there are no propagating modes in any direction. These values correspond to the stop bands of the 2-dimensionally periodic material. This type of effect is currently a subject of great interest world-wide. This arises from the fact that within such a band the density of electromagnetic modes can differ very substantially from that of free space or of a continuous material. This will affect the coupling between an excited atom or molecule within the material and the radiation field, and will thus affect the emission probability of the atoms or molecules into particular directions. In the strongest case the integrated density of photon states and thus the overall transition rate of the ions can be substantially affected. The ability to vary the transition rates of active species virtually at will would have profound technological impact, as well as being of enormous scientific interest. One of our goals in the present work is to demonstrate this type of effect within the photonic crystal fibre. We describe our progress towards this goal in Section 5.

#### 4. Waveguide modes with $\beta > \beta_{\max}$ – the photonic crystal as a fibre cladding

In this section we describe how we have used the photonic crystal fibre material in the regime where  $\beta > \beta_{\max}$  to form a low-loss fibre waveguide. An SEM picture of the structure being described here is shown in Fig. 2. A single pure silica defect site is embedded within the periodic “holey” fibre, by replacing a single hollow capillary with a solid pure silica cane during the stacking stage. When the preform is drawn down into fibre this high-index defect site (pure silica surrounded by silica/air) acts as a low-loss waveguide. The waveguide can be made so as to support a single or several modes: what is remarkable is that a fibre which is designed to support only a single guided mode will be monomode for all wavelengths, no matter how short. This is surprising, because any conventional optical waveguide which is monomode at some wavelength will become multimode at rather shorter wavelengths [11]. A conventional cylindrical optical fibre is monomode if the normalised frequency,  $V = 2\pi\rho(n_{\text{co}}^2 - n_{\text{cl}}^2)^{1/2}/\lambda$ , is less than 2.405 [11]. ( $\rho$  is the fibre core radius and  $\lambda$  the wavelength of the light, while  $n_{\text{co}}$  and  $n_{\text{cl}}$  are the core and cladding refractive indices, respectively.)



Fig. 2. A monomode waveguiding photonic crystal fibre with a pure silica defect. The pitch of the crystal is  $\Lambda \cong 2.3 \mu\text{m}$  and the air hole diameter  $d \cong 500 \text{ nm}$ . The single missing air hole in the centre is sufficient to form a low-loss waveguide core.

Generally, the useful range of monomode operation in conventional fibres is restricted to a variation of the wavelength by a factor of about two [11]. This limitation is imposed by the appearance of higher-order modes for  $V > 2.405$  and by the unacceptable growth of bend losses for increasingly large bend radii as  $V$  decreases below about 1.2. On the other hand, we have verified experimentally that a fibre such as that shown in Fig. 2 is monomode for all wavelengths from 337 nm to beyond 1.55  $\mu\text{m}$  without unacceptable bend losses (the measurement range is limited by laser sources available to us). This was done by coupling different laser sources into one end of the length of fibre, and studying the near- and far-field patterns of the guided mode at the output end. A contour plot showing an example of the near field pattern of the fundamental guided mode in the structure is shown in Fig. 3(a). This pattern was found to be independent of the way in which light was coupled into the fibre, or of any bends or twists in the fibre, and was the only pattern observable over the

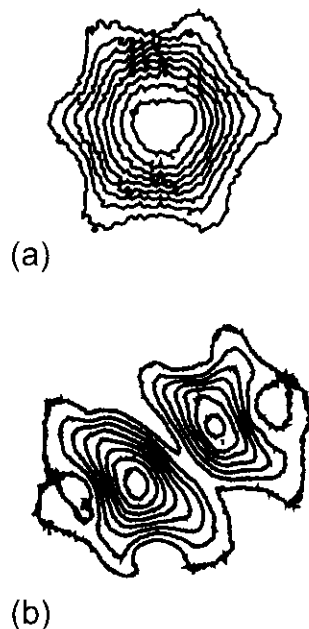


Fig. 3. (a) Near-field pattern of the guided mode in a fibre similar to that in Fig. 2; (b) near-field pattern observed in a similar fibre to that used in (a), but with larger air holes. The input coupling condition has been adjusted so as to optimise the excitation of the second mode. A pattern like this cannot be observed in a fibre such as that in Fig. 2, for any wavelength.

broad range of wavelengths investigated. The fibre used to record this pattern was very similar to that shown in Fig. 2. The mode is well confined to the pure silica core region – the nearest air holes surrounding the core are apparent as deep minima which appear on the modal field distribution. A very different modal field pattern is shown in Fig. 3(b), which was recorded from a different fibre with larger air holes. This plot shows a second guided mode (selectively excited by adjusting the input conditions) with a familiar two-lobe pattern. A mode such as that in Fig. 3(b) could not be excited in the fibre shown in Fig. 2, for any wavelength investigated.

The near-field patterns shown in Fig. 3 provide an important clue to the origin of the observed ultra-broad range of monomode transmission in these fibres. The air holes which form the deep minima in the modal field patterns have diameters  $d$  which are of the same order of magnitude as the wavelength of optical radiation. In the fibre shown in Fig. 2 the air hole diameter is  $d \approx 500$  nm. Clearly, light in the visible part of the spectrum can image features of this size. However, for longer wavelengths the holes are too small to be properly imaged. In the limit of long wavelengths one expects to find that the light sees but an average index in the holey material – in this limit the fibre is quite like a conventional optical fibre with a core index equal to that of silica, and a cladding index given by the average index  $n_{\text{avg}}$  of the periodic holey region (the root-mean-square volume-weighted average of the indices of the air and the silica). At shorter wavelengths one can again think of the fibre as being similar to a conventional fibre, but now with an effective index for the cladding region, where  $n_{\text{eff}} > n_{\text{avg}}$ . The effective index must always be greater than or equal to the average index, because in the regime under consideration (where the microstructured material is being used as a cladding layer for an optical waveguide) the field distribution will always tend to peak in the higher-index silica regions, giving a higher effective index. This tends to extend the range of monomode operation of the fibre, the decrease in the refractive index contrast with decreasing wavelength counteracting the shorter wavelength in calculating the normalised frequency of the fibre.

It is worth quantifying this effect to investigate its extent. We can do this if we take as our definition of the effective index of the cladding material as  $n_{\text{eff}} = \beta_{\text{max}}/k$ , where  $k$  is the free-space propagation constant of the light, and  $\beta_{\text{max}}$  is the propagation constant of the lowest possible mode (the “fundamental space-filling mode”) which could exist in the continuous periodic cladding region. This definition is appropriate because any mode with  $\beta > \beta_{\text{max}}$  would be evanescent in the cladding material. Furthermore, such a definition allows us to quantify the effective index of the cladding without reference to the core size or index. To calculate the numerical value of  $n_{\text{eff}}$  one thus needs to calculate the propagation constant  $\beta_{\text{max}}$ . This can be done because we know the approximate form of the field corresponding to this mode: some details of the calculation have been published in [4]. The curves in Fig. 4 show the predicted variation of  $V_{\text{eff}}$  with  $\Lambda/\lambda$  for different relative values of the air hole size  $d$  – evidently the normalised frequencies  $V_{\text{eff}}$  of the fibre tend to a constant for short wavelengths and for large structures. The effect of the decreasing refractive index difference between the core and cladding exactly counteracts the effect of decreasing wavelength, giving a waveguide which can be monomode for all wavelengths, no matter how short, providing only that the refractive index constant remains approximately constant.

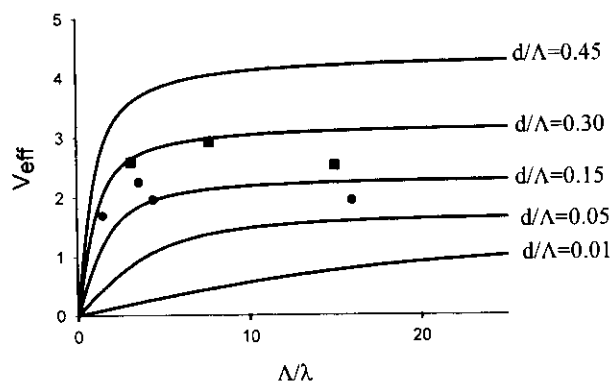


Fig. 4. Calculated values of the effective normalised frequency (curves) plotted as a function of the relative scale of the structure (the pitch divided by the wavelength of the light). Points show observed single mode (circles) or two-moded (squares) operation of various fibres investigated at different wavelengths.

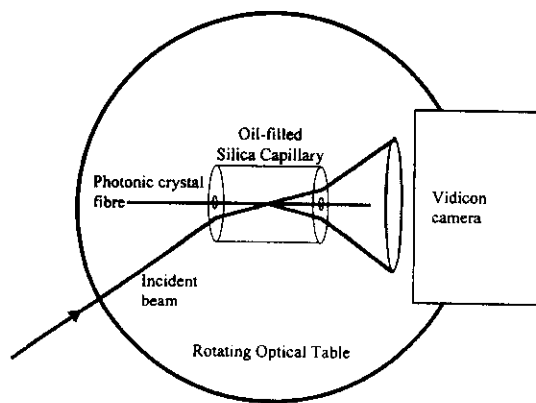
We have shown that in the limit of short wavelengths the normalised frequency of the fibre is independent of the scale of the structure relative to the wavelength. Instead, the crucial parameter is the fraction of air in the holey cladding region, larger air holes giving a lower effective index for the cladding and hence a higher normalised frequency. We expect that as in a conventional fibre a higher normalised frequency will result in more modes being guided in the fibre core. This is borne out experimentally – the points plotted on Fig. 4 correspond to different fibres which support only one mode (circles) or two modes (squares). This was determined for each fibre by studying the near-field patterns in the fibre core. It is apparent that the fibres which support more than a single mode have larger  $V$ -values than those which are monomode: the critical value for the effective  $V$ -value appears to be around  $V \approx 2.4$ , close to the exact value for a cylindrically-symmetric waveguide. Another useful point to be made concerning Fig. 4 is that the number of guided modes is indeed independent of the relative scale of the structure for large structures – data in the figure show that otherwise identical structures with relative scales differing by an order of magnitude can both guide a single robust mode. Such structures are potentially important for the design of high-power fibre lasers and amplifiers.

## 5. From Bragg scattering to stop bands

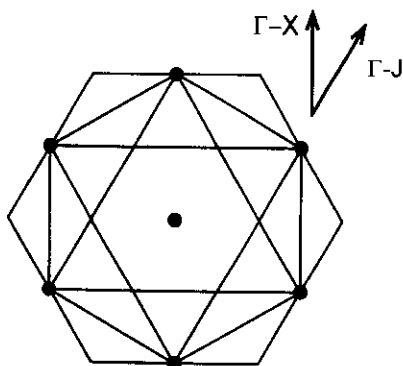
We now describe Bragg scattering effects in the photonic crystal fibre material. The strongest effects from periodically microstructured materials are found when the refractive index contrast between the high and low index phases is large and when the material is composed of roughly comparable volumes of the high and low index materials. Where these conditions are not met, one still observes photonic band structure [12], but the effects are relatively weak and do not extend over a very broad range of  $k$ -space. We can fabricate samples with widely varying morphological parameters, and we expect our samples to display a full range of behaviour from very weak 2-dimensional Bragg scattering to rather strong photonic

band gap effects. We have investigated this range of possible effects by coupling light from a laser beam into the material and studying the 2-dimensional scattering patterns which result. We should emphasise that in these experiments the fibre is not being used as an optical waveguide.

The experimental arrangement is shown schematically in Fig. 5(a). The sample fibre to be probed is placed in the core of a silica capillary with polished end faces. The bore of the capillary is then filled with an oil to match the index of the silica capillary. By introducing a focussed laser beam through one polished end face of the capillary we can illuminate the sample obliquely at



(a)



(b)

Fig. 5. (a) Schematic diagram of the scattering experiment: the output of the vidicon camera is digitised using a frame-grabber. (b) Reciprocal space construction showing the first few Brillouin zone boundaries, which is used to predict the Bragg scattering points in the weak scattering approximation.

different angles, while the sample can be rotated about its own axis in situ to probe different directions of propagation within the crystal structure. The scattered light leaves the far end face of the capillary in the form of a cone (the wavevector component parallel to the fibre axis is preserved) and is allowed to fall on a screen, which is imaged onto a vidicon camera and digitised. In this way we are able to record the entire scattering pattern for a wide range of excitation angles.

For very small air hole structures, we expect that simple Bragg scattering in the first Born approximation should hold good. We thus expect to see well-defined scattering peaks at particular incident angles and into directions which can be simply predicted. The predictions are easily visualised using the  $k$ -space construction in Fig. 5(b). In our experiment increasing the angle between the incident beam and the fibre corresponds to moving out away from the origin in Fig. 5(b). When the incident  $k$ -vector crosses a Brillouin zone boundary one expects a Bragg peak. An example of an observed scattering pattern for a particular angle of incidence along the  $\Gamma$ - $X$  direction (corresponding to crossing the second Brillouin zone boundary at a reciprocal lattice point – the “triple point”) is shown in Fig. 6(a). This sample had very small air holes ( $d/\Lambda < 0.05$ ) and no remaining interstitial holes. Because the air holes are very small, most of the light passes through the sample without being scattered (bright spot on the bottom of the plot). Light is scattered into five other symmetrically positioned directions, as shown in the plot and predicted by simple Bragg scattering theory.

When the sample has much larger air holes the scattering signature becomes much stronger. This is a sign of the enhanced interaction between the light and the microstructured material, and is expected ultimately to result in the appearance of complete 2-dimensional photonic band gaps. The results from such a sample are demonstrated in Fig. 6(b) showing the scattering signature from a fibre with a similar pitch to that in Fig. 6(a), but with considerably larger air holes (31% of air). The presence of interstitial air holes in this sample is expected to broaden the optical stop bands of the material [13]. Two significant differences between

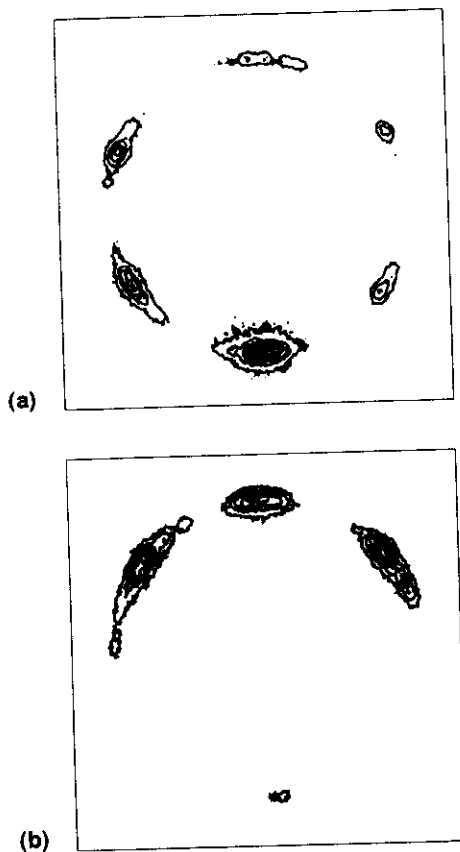


Fig. 6. Scattering patterns observed using a laser with  $\lambda = 1.55 \mu\text{m}$  from samples with a pitch of around  $4 \mu\text{m}$ . The incident angle has been chosen in both cases to coincide with the triple point (coincident with the second Brillouin zone crossing in Fig. 5(b)). The two fibres have filling fractions of (a)  $< 1\%$  and (b)  $32\%$ , respectively. The unscattered/forward scattered light appears at the bottom of each plot, reflections from the sample appearing on the top half.

Figs. 6(a) and (b) are apparent. First, the radiation in the forward direction at the bottom of the plot (which is the sum of the forward-scattered and the unscattered light) is very substantially reduced. (That light which does appear in the forward direction is due to leakage around the edges of the rather small sample, which is about the same size as the focussed laser beam.) Secondly, those Bragg points which are at  $\pm 60^\circ$  to the forward direction are also very weak. These features cannot be explained using Fig. 5(b). They are due largely to the substantial attenuation of the beam as it traverses the sample. (A fraction of the incident light is reflected from the surface of the sample despite our

index-matching oil, but we are at a larger angle than would be required for total internal reflection.) Almost all the light which is incident on the sample is scattered into the backward Bragg points, reflecting the rather strong nature of the photonic stop band in this case. Similar effects are seen when illuminating the sample along other directions with respect to the crystal axis.

Although this does not prove that we have a 2-dimensional photonic stop band, it certainly does show that we are in a strong-scattering regime. Theory suggests that for similar sample parameters to those used here we can indeed expect to observe a complete 2-dimensional stop band, assuming only that the samples are sufficiently regular. However, due to the problems of mode-matching at the interfaces and losses due to incoherent scattering it is difficult to prove the existence of such a stop band using angular or spectral scattering and transmission experiments. We intend to proceed to investigate the effects of the periodic microstructure on the photon modes by studying the fluorescence from Erbium ions embedded within the waveguiding core, and by fabricating a fibre with an air defect, in which it might be possible to form a 2-dimensional Bragg waveguide where the guided mode was confined to the air defect by a full 2D photonic band gap.

## 6. Conclusions

Photonic crystal materials can display remarkable optical properties. Our work with silica/air photonic crystal fibres has shown how they can be used to form low-loss waveguide structures in which the number of guided modes is determined by the geometry of the fibre and not by the relative scale of the structure with respect to the wavelength of interest. Thus one can design and fabricate single-mode waveguides in which the guided mode has a much larger effective mode area than in conventional fibres. We expect such a single-mode large-mode-area structure to be useful in the design of novel high-power lasers and amplifiers. Furthermore, we have demonstrated strong Bragg scattering effects in photonic crystal fibre by scattering experiments, and we expect this to alter the

fluorescence properties of rare earth ions embedded in the fibres. Taken together, these features make photonic crystal fibre of substantial interest for the development of the next generation of optical light sources.

### Acknowledgements

This work is supported by the Quantum Optics Group at the Defence Evaluation Research Agency, Malvern, UK, and the UK Engineering and Physical Sciences Research Council.

### References

- [1] J.D. Joannopoulos, R.D. Meade, J.N. Winn, *Photonic Crystals: Molding the Flow of Light*, Princeton University Press, Princeton, NJ, 1995; see also the special issues, in: C.M. Bowden, J.P. Dowling, H.O. Everitt (Eds.), *J. Opt. Soc. Am. B* 10 (1993) 279–413; G. Kurizki, J.W. Haus (Eds.), *J. Mod. Opt.* 41 (1994) 2; J.G. Rarity, C. Weisbuch (Eds.), *Microcavities and Photonic Bandgaps: Physics and Applications*, Kluwer Academic Publishers, Dordrecht, 1996.
- [2] P.J. Roberts, T.A. Birks, P.St.J. Russell, T.J. Shepherd, D.M. Atkin, Two-dimensional photonic band-gap structures as quasi-metals, *Opt. Lett.* 21 (1996) 507–509.
- [3] J.C. Knight, T.A. Birks, P.St.J. Russell, D.M. Atkin, All-silica single-mode optical fiber with photonic crystal cladding, *Opt. Lett.* 21 (1996) 1547–1549; see also errata *Opt. Lett.* 22 (1997) 484–485.
- [4] T.A. Birks, J.C. Knight, P.St.J. Russell, Endlessly single-mode photonic crystal fiber, *Opt. Lett.* 22 (1997) 961–963.
- [5] E. Yablonovitch, T.J. Gmitter, Photonic band-structure – the face-centered-cubic case, *Phys. Rev. Lett.* 63 (1989) 1950–1953.
- [6] R.J. Tonucci, B.L. Justus, A.J. Campillo, C.E. Ford, Nanochannel array glass, *Science* 258 (1992) 783–785; A. Rosenberg, R.J. Tonucci, H.B. Lin, A.J. Campillo, Near-infrared 2-dimensional photonic band-gap materials, *Opt. Lett.* 21 (1996) 830–832; K. Inoue, M. Wada, K. Sakoda, A. Yamanaka, M. Hayashi, J.W. Haus, Fabrication of 2-dimensional photonic band-structure with near-infrared band-gap, *Jpn. J. Appl. Phys.* 33 (1994) L1463–L1465.
- [7] T.A. Birks, P.J. Roberts, P.St.J. Russell, D.M. Atkin, T.J. Shepherd, Full 2-d photonic bandgaps in silica/air structures, *Elect. Lett.* 31 (1995) 1941–1943.
- [8] P.St.J. Russell, D.M. Atkin, T.A. Birks, P.J. Roberts, Bound modes of two-dimensional photonic crystal waveguides, in: J.G. Rarity, C. Weisbuch (Eds.), *Microcavities and Photonic Bandgaps: Physics and Applications*, Kluwer Academic Publishers, Dordrecht, 1996; P.St.J. Russell, T.A. Birks, D. Lloyd-Lucas, Photonic Bloch waves and photonic band gaps, in: E. Burstein, C. Weisbuch (Eds.), *Confined Electrons and Photons, New Physics and Applications*, Plenum Press, NY, 1995.
- [9] K.M. Ho, C.T. Chan, C.M. Soukoulis, Existence of a photonic gap in periodic dielectric structures, *Phys. Rev. Lett.* 65 (1990) 3152.
- [10] J.B. Pendry, Photonic band structures, *J. Mod. Opt.* 41 (1994) 209.
- [11] A.W. Snyder, J.D. Love, *Optical Waveguide Theory*, Chapman and Hall, New York, 1983.
- [12] A. Rosenberg, R.J. Tonucci, H.-B. Lin, E.L. Shirley, Photonic-band-structure effects for low-index-contrast 2-dimensional lattices in the near-infrared, *Phys. Rev. B* 54 (1996) R5195–R5198.
- [13] C.M. Anderson, K.P. Giapis, Larger two-dimensional photonic band gaps, *Phys. Rev. Lett.* 77 (1996) 2949–2952.

## Instructions to Authors

### Submission of papers

Manuscripts (one original and two copies), should be sent to one of the Editors, whose addresses are given on the inside of the journal cover.

**Original material.** Submission of a manuscript implies that the paper is not being simultaneously considered for publication elsewhere and that the authors have obtained the necessary authority for publication.

**Refereeing.** Submitted papers will be refereed and, if necessary, authors may be invited to revise their manuscript. Authors are encouraged to list the names (addresses and telephone numbers) of up to five individuals outside their institution who are qualified to serve as referees for their paper. The referees selected will not necessarily be from the list suggested by the author.

### Types of contributions

The journal *Optical Materials* publishes regular articles and reviews in the field of optical materials.

### Manuscript preparation

All manuscripts should be written in good English. The paper copies of the text should be prepared with double line spacing and wide margins, on numbered sheets. See notes opposite on electronic version of manuscripts.

**Structure.** Please adhere to the following order of presentation: Article title, Author(s), Affiliation(s), Abstract, PACS codes and keywords, Main text, Acknowledgements, Appendices, References, Figure captions, Tables.

**Corresponding author.** The name, complete postal address, telephone and fax numbers and the e-mail address of the corresponding author should be given on the first page of the manuscript.

**Classification codes/keywords.** Please supply one to four classification codes (PACS and/or MSC) and up to six keywords of your own choice that describe the content of your article in more detail.

**References.** References to other work should be consecutively numbered in the text using square brackets and listed by number in the Reference list.

### Illustrations

Illustrations should also be submitted in triplicate: one master set and two sets of copies. The *line drawings* in the master set should be original laser printer or plotter output or drawn in black india ink, with careful lettering, large enough (3–5 mm) to remain legible after reduction for printing. The *photographs*

should be originals, with somewhat more contrast than is required in the printed version. They should be unmounted unless part of a composite figure. Any scale markers should be inserted on the photograph itself, not drawn below it.

**Colour plates.** Figures may be published in colour, if this is judged essential by the editor. The publisher and the author will each bear part of extra costs involved. Further information is available from the publisher.

### After acceptance

**Important.** When page proofs are made and sent out to authors, this is in order to check that no undetected errors have arisen in the typesetting (or file conversion) process. No changes in, or additions to, the edited manuscript will be accepted.

**Copyright transfer.** You will be asked to transfer copyright of the article to the publisher. This transfer will ensure the widest possible dissemination of information.

### Electronic manuscripts

The publisher welcomes the receipt of an electronic version of your accepted manuscript. If you have not already supplied the final, revised version of your article (on diskette) to the Journal Editor, you are requested to send a file with the text of the accepted manuscript directly to the Publisher by e-mail or on diskette (allowed formats 3.5" or 5.25" MS-DOS, or 3.5" Macintosh) to the address given below. Please note that no deviations from the version accepted by the Editor of the journal are permissible without the prior and explicit approval by the Editor. Such changes should be clearly indicated on an accompanying printout of the file.

### Author benefits

**No page charges.** Publishing in *Optical Materials* is free.

**Free offprints.** The corresponding author will receive 50 offprints free of charge. An offprint order form will be supplied by the publisher for ordering any additional paid offprints.

**Discount.** Contributors to Elsevier Science journals are entitled to a 30% discount on all Elsevier Science books.

### Further information (after acceptance)

Elsevier Science B.V., *Optical Materials*  
Issue Management Physics and Materials Science  
P.O. Box 2759, 1000 CT Amsterdam, The Netherlands  
Fax: +31 20 4852319  
E-mail: f.kop@elsevier.nl



# MICROSCOPIC GLASS FIBRE CRYSTALS

*the world's longest holes*

Professor Philip Russell, Dr Jonathan Knight, Mr Brian Mangan,  
Dr Bob Cregan & Dr Tim Birks

Optoelectronics Group, Department of Physics, University of Bath  
telephone +44 1225 826946; email p.s.j.russell@bath.ac.uk  
www.bath.ac.uk/Departments/Physics/opto/opto1.htm

• OPTICAL FIBRES

---

Optical fibres, which form the individual strands of the world wide communications network, have become a vital – if hidden – part of modern life. Technological maturity does not however preclude innovation, as we have recently shown by developing a revolutionary new kind of optical fibre – the *photonic crystal fibre*. Conventional fibre consists of a *core* of Ge-doped glass surrounded by a *cladding* of pure silica glass and traps light by total internal reflection. Photonic crystal fibre, on the other hand, consists of an elongated honeycomb of hundreds of tiny holes regularly spaced within a thin thread of pure silica. It traps light by imprisoning it behind a “picket fence” of sub-microscopic air holes.

• MAKING PHOTONIC CRYSTAL FIBRE

---

Photonic crystal fibre is made by stacking together glass capillaries and rods, which are then heated to well above the temperature of molten lava and drawn down in size 10,000 times. The process is akin to the spinning of

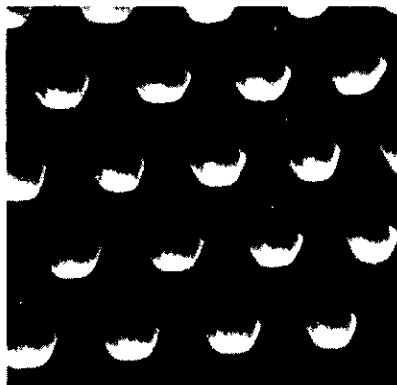


Figure 1: Photonic crystal fibre with small and large holes; large hole spacing 7 microns

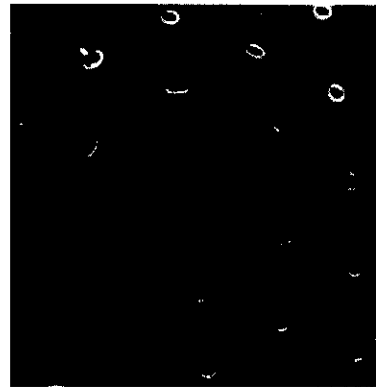


Figure 2: Photonic crystal fibre with 22 micron core for guiding high power blue light

candy-floss, except that the threads are of course inedible – and riddled with holes too small to be seen with the naked eye. The fibres can be pulled to lengths of 10s of km with holes as small as 50 nm across (1000 times narrower than a human hair). The length to width ratio of these holes can be an astonishing 200,000,000,000:1 – making them contenders for the world’s longest. To place this number in perspective, if the Channel Tunnel stretched from London to Jupiter it would have a similar aspect ratio.

• PHOTONIC LATTICES

---

The interaction of photon waves with this regular array of capillaries is closely similar to that of electron waves with an atomic lattice. For example, interesting and useful properties arise if the crystal is made “defective” by incorporating dopants (these control the behaviour of electrons in silicon microchips). In the case of the fibre, dopants are introduced by leaving out, widening or distorting holes. Light can be trapped at these defective sites, and guided along the entire fibre length. It turns out that, unlike in conventional fibres where light can travel at many velocities,

the light trapped at a defect in a suitably designed photonic crystal fibre travels at only one velocity (the phrase used for this is "single-mode") across the entire electromagnetic spectrum of frequencies. The fibre can thus guide multi-colour laser light with unprecedented precision over long distances.

#### • HIGH POWER FIBRES

The amount of laser power a conventional fibre can support without suffering damage is limited by the presence of core dopants and by the maximum core area that can be made while preserving single-mode operation. The photonic



Figure 3: Fibre with three cores (3 missing air-holes), interhole spacing  $\sim 3$  microns

crystal fibre performs much better in this respect, because it is made from pure silica and is guaranteed single-mode no matter how large the core. The fibre in Figure 2 guides single-mode blue light in a core of diameter 22 microns – an area some 20 times larger than is feasible in conventional fibre fabrication.

#### • VERSATILE NEW TECHNOLOGY

The ability of the fibre to support much higher laser powers without damage makes it of great potential importance in applications requiring high laser power such as surgery, laser machining and long-haul fibre telecommunications systems. In addition, the stacking and drawing procedure makes it straightforward to incorporate several cores in one fibre (Figure 3).

These can be used to multiply the transmission capacity of a single fibre, or allow the realisation of elegant fibre-based systems for "smart-sensing" the flexing of, for example, aircraft wings, bridges, undersea cables and oil well drills.

#### • ACKNOWLEDGEMENTS

The work is supported by DERA Malvern (who funded the original "blue-skies" research), EPSRC, British Telecom (who donated fibre drawing equipment to us) and The Royal Society. We also gratefully acknowledge the involvement of our collaborators at Southampton and Heriot-Watt Universities.

#### • BIBLIOGRAPHY

- ❖ P.St.J. Russell, "Photonic Band-Gaps," *Physics World* 5 (37-42) 1992
- ❖ J.D. Joannopoulos, P.R. Villeneuve and S.H. Fan, "Photonic Crystals: Putting a New Twist on Light," *Nature* 386 (143-149) 1997
- ❖ J.C. Knight, T.A. Birks, P.St.J. Russell and D.M. Atkin, "All-silica single-mode fiber with photonic crystal cladding," *Opt. Lett.* 21 (1547-1549) 1996; Errata, *Opt.Lett.* 22 (484-485) 1997
- ❖ T.A. Birks, J.C. Knight and P.St.J. Russell, "Endlessly single-mode photonic crystal fibre," *Optics Letters*, 22 (961-963) 1997
- ❖ P.St.J. Russell, T.A. Birks, J.C. Knight, R.F. Cregan and J.-P. De Sandro, "Silica/air photonic crystal fibres," *Jap. J. Appl. Phys.* 37 Suppl. 37-1, (45-48) 1998

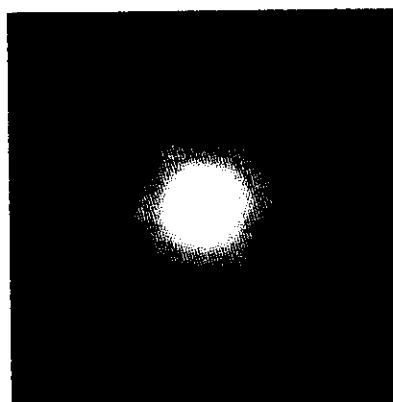


Figure 4: Multicolour pattern produced by photonic crystal fibre supporting several laser colours at once

# Group-velocity dispersion in photonic crystal fibers

D. Mogilevtsev, T. A. Birks, and P. St. J. Russell

*Optoelectronics Group, Department of Physics, University of Bath, Claverton Down, Bath BA2 7AY, UK*

Received June 22, 1998

The dispersion properties of photonic crystal fibers are calculated by expression of the modal field as a sum of localized orthogonal functions. Even simple designs of these fibers can yield zero dispersion at wavelengths shorter than  $1.27 \mu\text{m}$  when the fibers are single mode, or a large normal dispersion that is suitable for dispersion compensation at  $1.55 \mu\text{m}$ . © 1998 Optical Society of America

OCIS codes: 260.2030, 060.2400.

Photonic crystal fiber (PCF) is made from undoped fused silica with a hexagonal array of air holes running along its length. The central hole is missing, leaving a solid silica core to guide light. We have described this fiber's fabrication, structure, and wide single-mode wavelength range,<sup>1</sup> demonstrated that it can be single mode at all wavelengths<sup>2,3</sup> and scales,<sup>4</sup> and constructed versions with as many as six cores.<sup>5</sup> The wide single-mode range is due to the unusual dispersion properties of the cladding's effective index. We therefore decided to investigate the group-velocity dispersion (GVD) of the guided mode itself, and this Letter summarizes our first results. GVD in conventional step-index fibers (SIF's) has received much attention in connection with pulse spread and its compensation, soliton propagation, and the control and harnessing of nonlinear effects.<sup>6,7</sup>

One can describe some of the properties of the fiber by regarding the cladding as an effective-index medium.<sup>2,3</sup> However, with this approach one cannot rigorously determine the propagation constant (and hence the GVD) of a guided mode, and we have found that naive substitution of the effective  $V$  value<sup>2</sup> into known formulas for SIF gives incorrect values for the propagation constant in most cases. General numerical techniques exist for analyzing periodic structures with strong index modulations and have been used to determine photonic band properties.<sup>8</sup> However, we are interested only in guided modes, which are localized near the fiber's core. We take advantage of this localization by modeling the field as a sum of functions localized near the core. These functions are chosen to be close to the experimentally observed fields. This method is less universal than others, but, since a relatively small number of such functions is needed to represent the field accurately, it uses far less computer time and memory.

Maxwell's equations are reformulated as an eigenvalue problem for the propagation constant  $\beta$ , with the refractive index  $n$  depending on the transverse coordinates  $x$  and  $y$  only<sup>9</sup>:

$$[\nabla_{\perp}^2 + k_0^2 n^2 + (\nabla_{\perp} \ln n^2) \times (\nabla_{\perp} \times)] \mathbf{h}_{\perp} = \beta^2 \mathbf{h}_{\perp}, \quad (1)$$

where  $\nabla_{\perp}$  denotes the gradient operator in the  $xy$  plane,  $k_0$  is the free-space wave constant, and the vector

$\mathbf{h}_{\perp} = (h_x, h_y)^T$  gives the transverse magnetic field  $\mathbf{H}_{\perp}$ :

$$\mathbf{H}_{\perp} = \mathbf{h}_{\perp} \exp[i(\beta z - ck_0 t)]. \quad (2)$$

The modal field is expanded by use of the Hermite-Gaussian functions as the set of basis functions:

$$\phi_{mn}(x, y) = \exp[-(x^2 + y^2)/2\Lambda^2] H_m(x/\Lambda) H_n(y/\Lambda), \quad (3)$$

where  $H_m$  is the Hermite polynomial of order  $m$  and  $\Lambda$  is the period of the lattice (i.e., the pitch of the air holes in the cladding). The functions  $\phi_{mn}$  are a complete orthogonal basis set in the transverse plane. They are localized around the origin, which coincides with the core of the fiber. In this basis, Eq. (1) becomes the algebraic eigenvalue problem

$$\sum_{k,l} L_{k,l}^{m,n} \mathbf{h}_{\perp}^{k,l} = \beta^2 \mathbf{h}_{\perp}^{m,n} \quad (4)$$

for the vector of coefficients  $\mathbf{h}_{\perp}^{m,n}$  representing the transverse magnetic field in the Hermite-Gaussian basis.  $L_{k,l}^{m,n}$  are the matrix elements of the operator on the left-hand side of Eq. (1) in this basis. These elements are real and can be found analytically for a wide range of lattices.

The infinite set of Eqs. (4) is truncated (at a maximum value for the order  $m$  of the  $H_m$ ), and we solve it to obtain the propagation constants and fields. The method becomes inaccurate for both low and high frequencies. However, in the intermediate frequency range  $1 \leq \Lambda/\lambda \leq 10$  that is of greatest interest,<sup>2,3</sup> a few hundred basis functions is enough for good convergence of both eigenvalues and eigenvectors.

For speed and simplicity we restricted our initial study to a scalar approximation. This is exact in the high-frequency limit, when coupling between orthogonal field components is negligible and the third term in Eq. (1) can be ignored. The scalar approximation corresponds to paraxial propagation and resembles the weak guidance approximation.<sup>9</sup> The field-coupling term can be shown to scale with the air-filling fraction, so for small air holes the high-frequency limit is reached very quickly. A PCF with less than 10% air is in the high-frequency regime when the wavelength is less than the period of the lattice ( $\Lambda/\lambda > 1$ ).

The overall GVD has two contributions,<sup>6,7</sup> the material dispersion (which is a given function of wavelength  $\lambda$  for all silica fibers and is zero at  $\lambda = 1.27 \mu\text{m}$ ) and the waveguide dispersion (which in a standard SIF shifts the zero of net GVD to  $1.31 \mu\text{m}$ ). However, for a given wavelength and material, the design of a simple SIF has two degrees of freedom, the core radius and the core-cladding index step. The constraint that the  $V$  value must be close to but not greater than 2.405 (to minimize bend loss while staying single mode) leaves one remaining degree of freedom for optimizing the GVD. For example, one can shift the zero of GVD from  $1.31$  to  $1.55 \mu\text{m}$  by increasing the index step and reducing the core size.<sup>7</sup>

We compare the PCF with this simplest SIF because the simplest PCF also has two degrees of freedom that correspond roughly to those of the SIF, the scale (and effective core radius)  $\Lambda$  and the ratio  $d/\Lambda$ , where  $d$  is the diameter of the air holes. In practice, one usually controls GVD in SIF's by adding degrees of freedom, such as extra layers in the cladding. This procedure, which could equally well be adopted for the PCF, is beyond the scope of this Letter. Calculated and experimentally measured field distributions for a typical PCF are drawn in Fig. 1 and are clearly similar.

Propagation constants and hence waveguide GVD's were calculated for different frequency parameters  $\Lambda/\lambda$  for a silica-air PCF and for a range of hole sizes  $d/\Lambda$ . We chose a SIF corresponding to each PCF by matching their effective cladding indices in the limit of low frequency<sup>2</sup> and taking the core radius to be  $\Lambda$ . The GVD of each SIF was also calculated. Graphs of GVD against  $\Lambda/\lambda$  are plotted in Fig. 2, in which GVD is expressed in the normalized form

$$g = \frac{\partial^2(\beta\Lambda)}{\partial(k\Lambda)^2}, \quad (5)$$

which relates to the conventional dispersion parameter<sup>6</sup>  $D$  (usually expressed in units of  $\text{ps nm}^{-1} \text{km}^{-1}$ ) through

$$D = -\frac{2\pi\Lambda}{c\lambda^2} g. \quad (6)$$

Positive  $g$  corresponds to negative  $D$  and normal dispersion. Also indicated in Fig. 2 are the  $\Lambda/\lambda$  ranges in which the fibers are multimode.

The two sets of curves are similar in value and shape. However, there are two key distinctions. First, if the air holes are sufficiently small the PCF is always single mode.<sup>2</sup> Hence PCF's can be simultaneously single mode with anomalous waveguide GVD, whereas SIF's are always multimode when the waveguide GVD is anomalous. One can therefore use PCF's to shift the wavelength of zero net GVD to less than  $1.27 \mu\text{m}$ , where material GVD is normal. This could be significant for soliton transmission (requiring anomalous GVD) in the  $1.3\text{-}\mu\text{m}$  window, dispersionless transmission at shorter wavelengths where fiber amplifiers may be more readily available, and phase matching in nonlinear optics.

Second, the air holes can be large, giving a large effective-index contrast and a large normal waveguide

GVD. This can cancel the anomalous material GVD at  $1.55 \mu\text{m}$  or even overcome it, yielding normal net GVD there. For example, dispersion-compensating fibers have a large normal GVD at  $1.55 \mu\text{m}$ , which cancels the smaller anomalous GVD of installed conventional fibers. In a simple SIF the core must be heavily doped for there to be a large index contrast, making the fiber lossy, apparently because of the thermal mismatch between core and cladding.<sup>7</sup> The PCF, being a single-material structure, will not suffer from this effect. Indeed, if the holes are so large that the thin silica bridges supporting the core scarcely affect the fundamental mode, the large waveguide GVD of a silica core in air can be approached while mechanical

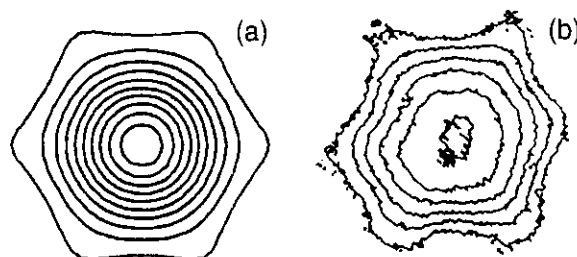


Fig. 1. (a) Calculated and (b) experimentally measured contour plots of the guided mode field at  $\lambda = 458 \text{ nm}$  for a PCF with  $\Lambda = 2.3 \mu\text{m}$  and  $d/\Lambda = 0.23$ .

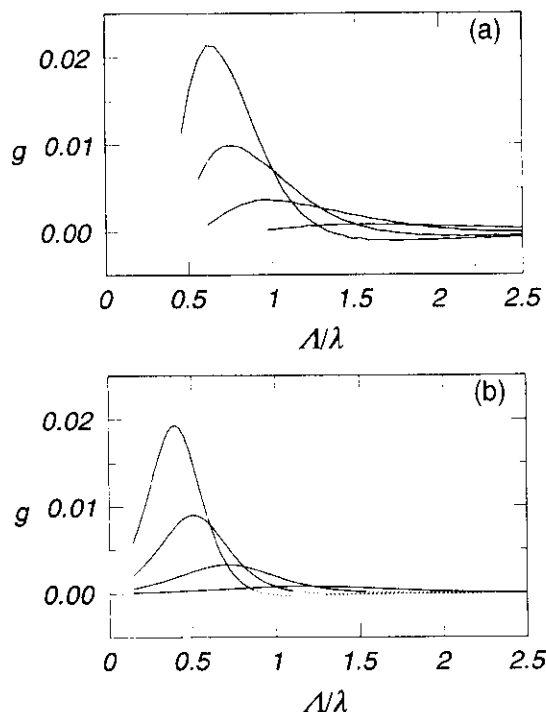


Fig. 2. Normalized waveguide dispersion  $g$  against  $\Lambda/\lambda$  for (a) PCF's with different hole sizes  $d/\Lambda$  and (b) the corresponding SIF's. The values of  $d/\Lambda$  are 0.15, 0.25, 0.35, and 0.45 in order of increasing peak  $g$ . The curves are plotted only where the accuracy is high; the dotted curves indicate regions in which the fibers are multimode. For  $\lambda = 1.55 \mu\text{m}$ , one can convert  $g$  to units of  $\text{ps nm}^{-1} \text{km}^{-1}$  by multiplying by  $-13,500 \times \Lambda/\lambda$ .

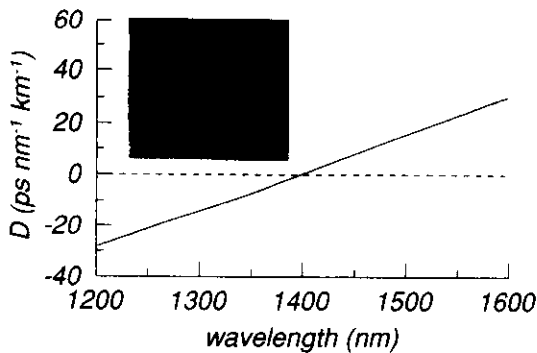


Fig. 3. Calculated net GVD of a real PCF with  $\Lambda = 2.3 \mu\text{m}$  and  $d/\Lambda = 0.15$ . Inset, scanning electron microscope image of the fiber's cross section.

support and protection for the core are retained. A rough calculation based on a silica core in air indicates that the magnitude of the GVD at  $1.55 \mu\text{m}$  for such a PCF could exceed  $1000 \text{ ps nm}^{-1} \text{ km}^{-1}$ , over 50 times that of a standard SIF.

Finally, Fig. 3 is the calculated net GVD versus wavelength for our first reported PCF.<sup>1,2</sup> The fiber had  $\Lambda = 2.3 \mu\text{m}$  and  $d/\Lambda = 0.15$  and was not designed to have special dispersion properties.

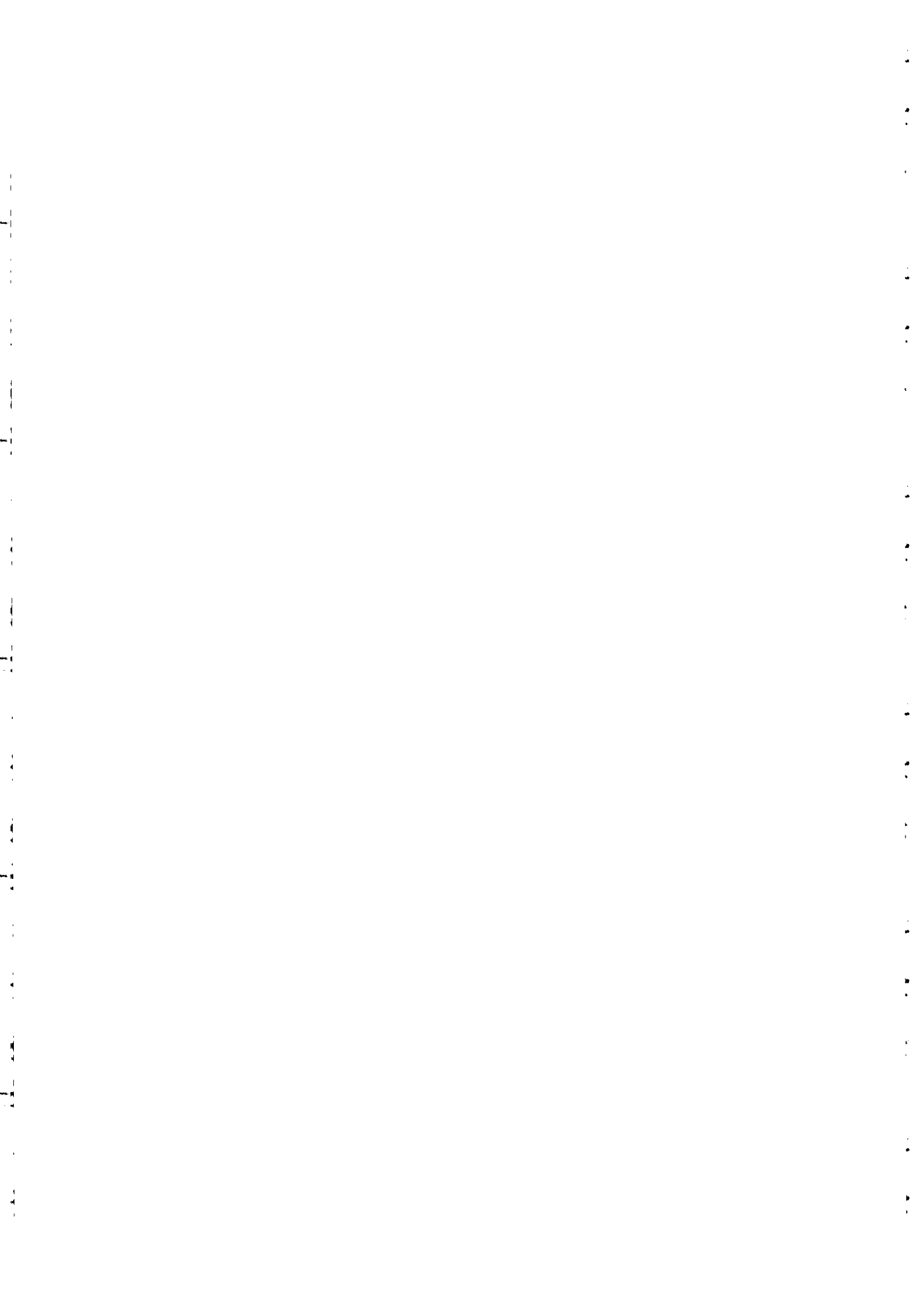
In summary, we have expressed the modes in a photonic crystal fiber as sums of localized orthogonal functions, which cuts down the computer time and memory needed. The dispersion of the fiber was calculated and compared with that of a standard step-index fiber, and the curves were very similar. However, the PCF can have anomalous waveguide GVD while being single mode, permitting the design

of a fiber with the zero of dispersion at wavelengths shorter than  $1.27 \mu\text{m}$ . Also, the PCF design permits the fabrication of fibers with large normal GVD at  $1.55 \mu\text{m}$  for dispersion compensation, without the extra losses associated with the heavy doping of silica.

This work was supported by the UK Engineering and Physical Sciences Research Council. T. A. Birks is a Royal Society University Research Fellow.

## References

1. J. C. Knight, T. A. Birks, P. St. J. Russell, and D. M. Atkin, *Opt. Lett.* **21**, 1547 (1996); erratum, **22**, 484 (1997).
2. T. A. Birks, J. C. Knight, and P. St. J. Russell, *Opt. Lett.* **22**, 961 (1997).
3. J. C. Knight, T. A. Birks, P. St. J. Russell, and J. P. DeSandro, *J. Opt. Soc. Am. A* **15**, 748 (1998).
4. T. A. Birks, J. C. Knight, R. F. Cregan, and P. St. J. Russell, in *Conference on Lasers and Electro-Optics*, Vol. 6 of 1998 OSA Technical Digest Series (Optical Society of America, Washington, D.C., 1998), p. 226.
5. J. C. Knight, T. A. Birks, B. J. Mangan, P. St. J. Russell, G. G. Vienne, and J. P. DeSandro, in *Optical Fiber Sensors*, Vol. 16 of 1997 OSA Technical Digest Series (Optical Society of America, Washington, D.C., 1997), postdeadline paper PD5.
6. G. P. Agrawal, *Nonlinear Fiber Optics*, 2nd ed. (Academic, San Diego, Calif., 1995).
7. B. J. Ainslie and C. R. Day, *J. Lightwave Technol.* **4**, 967 (1986).
8. J. Rarity and C. Weisbuch, eds., *Microcavities and Photonic Bandgaps* (Kluwer Academic, Dordrecht, The Netherlands, 1996).
9. A. W. Snyder and J. D. Love, *Optical Waveguide Theory* (Chapman & Hall, London, 1983).



# Localized Function Method for Modeling Defect Modes in 2-D Photonic Crystals

D. Mogilevtsev, T. A. Birks, *Member, OSA*, and P. St. J. Russell, *Member, OSA*

**Abstract**—We present a novel, general, and numerically efficient treatment of electromagnetic modes localized at defects in two-dimensional (2-D) photonic crystals. The method represents the fields in terms of orthogonal functions localized at the defect and is a fully vector treatment.

**Index Terms**—Holey fibers, optical fiber dispersion, optical fibers, orthogonal functions, waveguide modeling.

## I. INTRODUCTION

TOGETHER with recent spectacular technological advances in the fabrication of photonic crystals, powerful theoretical tools have been developed for modeling their electromagnetic fields. Universal methods such as the plane-wave [1], [2], transfer-matrix [3], and finite difference time-domain [4] methods are examples. However, because of their generality, all demand a lot of computational effort when modeling photonic crystals with localized defects where electromagnetic fields can be confined.

The aim of this work was to develop a fast and numerically efficient method to model optical modes guided by localized defects in two-dimensional (2-D) photonic crystals. The work was initiated and inspired by the need to model the guided modes of the photonic crystal fiber [5], [6]. This novel structure has many potential applications (for example, it has unusual dispersive properties [7]) and typically consists of a hexagonal lattice of microscopic air holes in fused silica. Electromagnetic waves propagating along the fiber are transversely confined by a localized defect in the otherwise periodic structure, due, for example, to a missing (i.e., filled-in) air hole [5] or an additional air hole [6]. Our method is, however, also applicable to a wide range of 2-D periodic structures with localized defects.

The idea behind the method is simple. Since the guided mode is localized in the vicinity of the defect, it is natural to represent the modal field as a superposition of orthogonal functions localized at the defect. As a consequence, only a modest number of such functions is required to achieve an accurate representation. This cuts down the amount of computer time and memory necessary for simulation. This approach was first proposed by Leung [8], who used a set

of basis functions (vector Wannier functions) built from the Bloch solutions for the perfect photonic crystal. Our method is much more simple and straightforward. It uses a predefined set of orthogonal basis functions, which are independent of the geometry of the structure. Earlier we reported the results of a scalar calculation [7], and another scalar implementation of our method has since been described in more detail by others [9], but here we describe a fully vector version of this treatment.

The 2-D photonic crystal is a medium with a dielectric constant  $\epsilon$  that is translationally invariant along the  $z$  axis. To implement the method, we reformulate Maxwell's equations as an eigenvalue problem for the propagation constant  $\beta$ , which is the  $z$ -component of the wavevector [10]

$$\mathbf{L}\mathbf{h}_\perp \equiv (\nabla_\perp^2 + k_0^2\epsilon)\mathbf{h}_\perp + (\nabla_\perp \ln(\epsilon)) \wedge (\nabla_\perp \wedge \mathbf{h}_\perp) = \beta^2\mathbf{h}_\perp \quad (1)$$

where  $\nabla_\perp$  denotes the gradient in the  $x$ - $y$  plane and  $k_0$  is the free-space wave constant. The components of the vector  $\mathbf{h}_\perp = \begin{pmatrix} h_x \\ h_y \end{pmatrix}$  correspond to the components of the magnetic field  $\mathbf{H}$  in the plane of periodicity

$$H_p = h_p \exp[i(\beta z - ck_0 t)]; \quad p = x, y.$$

For the system of basis functions, we used the set of Hermite-Gaussian functions [7]

$$\phi_{m,n} = C_{m,n} \exp[-(x^2 + y^2)/2\Lambda^2] \mathcal{H}_m(x/\Lambda) \mathcal{H}_n(y/\Lambda) \quad (2)$$

where  $\mathcal{H}_m$  is a Hermite polynomial of order  $m$ ,  $\Lambda$  denotes the period of the lattice, and the normalization coefficients  $C_{m,n}$  are

$$C_{m,n} = [\pi\Lambda^2 2^{m+n} m!n!]^{-1/2}.$$

The functions  $\phi_{m,n}$  are well known in the theory of waveguides. They describe modal solutions for a waveguide with a parabolic profile of the dielectric constant [11], they are mutually orthogonal, they form a complete system in the  $x$ - $y$  plane, and they are localized in the vicinity of the point  $x = 0, y = 0$ .

Expressed in the basis of functions  $\phi_{m,n}$ , (1) becomes the algebraic eigenvalue problem

$$\sum_{kl} L_{k,l}^{m,n} \mathbf{h}_\perp^{k,l} = \beta^2 \mathbf{h}_\perp^{m,n} \quad (3)$$

where the vector of coefficients  $\mathbf{h}_\perp^{k,l}$  represents the components of the magnetic field, in the plane of periodicity, in the Hermite-Gaussian basis.  $L_{k,l}^{m,n}$  are the matrix coefficients of the operator  $\mathbf{L}$  in the Hermite-Gaussian basis.

Manuscript received July 9, 1999; revised August 12, 1999.

D. Mogilevtsev was with the Optoelectronics Group, Department of Physics, University of Bath, Bath BA2 7AY UK. He is now with the Quantum Optics Laboratory, Institute of Physics, National Academy of Sciences of Belarus, Minsk 220071 Belarus.

T. A. Birks and P. St. J. Russell are with the Optoelectronics Group, Department of Physics, University of Bath, Bath BA2 7AY U.K.

Publisher Item Identifier S 0733-8724(99)08805-2

An important part of the method is the calculation of these matrix elements  $L_{k,l}^{m,n}$ . Generally, using (1), they can be expressed as

$$[L_{k,l}^{m,n}]_{p,s} = (a_{k,l}^{m,n} + k_0^2 b_{k,l}^{m,n}) \delta_{p,s} + [\theta_{k,l}^{m,n}]_{p,s} \quad (4)$$

where  $p, s = x, y$ . The coefficients  $a_{k,l}^{m,n}$  correspond to the first term in the expression for the operator  $L$  in (1) and can be easily calculated analytically using recurrence relations for the Hermite polynomials

$$\begin{aligned} a_{k,l}^{m,n} = & -(m+n+1)\delta_{m,k}\delta_{n,l} + \frac{\sqrt{(m+1)(m+2)}}{2} \\ & \cdot \delta_{m+2,k}\delta_{n,l} + \frac{\sqrt{m(m-1)}}{2} \delta_{m-2,k}\delta_{n,l} \\ & + \frac{\sqrt{(n+1)(n+2)}}{2} \delta_{m,k}\delta_{n+2,l} + \frac{\sqrt{n(n-1)}}{2} \\ & \cdot \delta_{m,k}\delta_{n-2,l}. \end{aligned} \quad (5)$$

The coefficients that correspond to the second term in the expression for the operator  $L$  in (1)

$$b_{k,l}^{m,n} = \int \int dx dy \phi_{m,n} \varepsilon \phi_{k,l} \quad (6)$$

and to the third term

$$[\theta_{k,l}^{m,n}]_{p,s} = (1 - 2\delta_{p,s}) \int \int dx dy \phi_{m,n} \frac{\partial \ln \varepsilon}{\partial s} \frac{\partial \phi_{k,l}}{\partial p} \quad (7)$$

$p, s = x, y$

are not so simple to calculate. Of course, it is possible to evaluate the integrals numerically. However, it is hard to achieve sufficient accuracy this way, and the computational effort required negates the advantages of the method.

One way to overcome this difficulty is to represent the distribution of  $\varepsilon$  as the sum of the perfectly periodic part and the part corresponding to the localized defect. The periodic part is then represented as a discrete Fourier series, and the integrals over this part in (6) and (7) can be found analytically. The integrals over the localized defect can be found without much effort, either numerically or analytically [9]. We implemented this procedure for our previous scalar version of the method [7], despite a claim to the contrary in [9] (which cannot be substantiated by the references cited therein).

Instead, here we perform these integrals analytically in a straightforward way. To do this we impose periodic boundary conditions on the system by putting it into a finite 2-D box; that is, a supercell. Then we analyze the artificial periodic structure obtained by replicating supercells in the  $x$  and  $y$  directions. Now it is possible to expand the functions  $\varepsilon$  and  $\ln \varepsilon$  in discrete Fourier series

$$\begin{aligned} \varepsilon(x, y) &= \sum_{h,j} \varepsilon_{h,j} \exp(iG_x^{h,j}x + iG_y^{h,j}y) \\ \ln \varepsilon(x, y) &= \sum_{h,j} \nu_{h,j} \exp(iG_x^{h,j}x + iG_y^{h,j}y) \end{aligned} \quad (8)$$

where  $G_{x,y}^{h,j}$  are the components of reciprocal lattice vectors of the periodic supercell structure. Substitution of the expansion

(8) into (6) and (7) gives, after some algebra, the following results:

$$b_{k,l}^{m,n} = \varepsilon_{0,0} \delta_{m,k} \delta_{n,l} + (1 - \delta_{m,k} \delta_{n,l}) \sum_{h,j} \varepsilon_{h,j} \cdot p(h, j, m, n, k, l) \quad (9)$$

$$[\theta_{k,l}^{m,n}]_{x,x} = i \sum_{h,j} G_y^{h,j} \nu_{h,j} \sqrt{\frac{l}{2\Lambda^2}} (p(h, j, m, n, k, l+1) - p(h, j, m, n, k, l-1))$$

$$[\theta_{k,l}^{m,n}]_{x,y} = i \sum_{h,j} G_y^{h,j} \nu_{h,j} \sqrt{\frac{k}{2\Lambda^2}} (p(h, j, m, n, k-1, l) - p(h, j, m, n, k+1, l))$$

$$[\theta_{k,l}^{m,n}]_{y,x} = i \sum_{h,j} G_x^{h,j} \nu_{h,j} \sqrt{\frac{l}{2\Lambda^2}} (p(h, j, m, n, k, l-1) - p(h, j, m, n, k, l+1))$$

$$[\theta_{k,l}^{m,n}]_{y,y} = i \sum_{h,j} G_x^{h,j} \nu_{h,j} \sqrt{\frac{k}{2\Lambda^2}} (p(h, j, m, n, k+1, l) - p(h, j, m, n, k-1, l)) \quad (10)$$

where

$$\begin{aligned} p(h, j, m, n, k, l) &= \sqrt{\frac{2^{m+n-k-l} m!n!}{k!l!}} (iG_x^{h,j}\Lambda)^{k-m} \\ &\cdot (iG_y^{h,j}\Lambda)^{l-n} \cdot L_m^{k-m}([G_x^{h,j}\Lambda]^2/2) \\ &\cdot L_n^{l-n}([G_y^{h,j}\Lambda]^2/2) \exp(-[G_x^{h,j}\Lambda/2]^2) \\ &\cdot \exp(-[G_y^{h,j}\Lambda/2]^2) \end{aligned} \quad (11)$$

and the functions  $L_l^j(x)$  are the associated Laguerre polynomials. Equation (11) is written for the case when  $m \leq k$  and  $n \leq l$ .

Equations (9)–(11) show two interesting properties of the coefficients  $b$  and  $\theta$ . The first is that, as expected, these coefficients are real. Because of the symmetry properties of the structure, they are nonzero only if the differences  $k - m$  and  $l - n$  are both even. In addition, the coefficients  $\theta$  are nonzero only if these differences are also nonzero. The second property is that, due to the presence of exponentially decreasing terms in the expression for the coefficients  $p$ , the sums in (9) and (10) converge quickly. This allows us to model the structure with very good accuracy using large supercells and a large number of plane waves in the representations (8).

To illustrate the method we use two cases as examples. We consider photonic crystal fibers [5] formed by arrays of circular air holes in a bulk dielectric. The defect where the guided modes are localized is formed by one missing hole (Fig. 1). In the first case, the lattice of air holes is square. In the second case, the lattice is primitive hexagonal. We calculated the spatial distribution of the transverse field for the lowest order modes localized within the defect (Fig. 2). It can be seen that the field guided by the defect in this type of structure is well confined within the first row of air holes. In the case of the hexagonal lattice, this result is supported by the experimental data [5]. In Fig. 2(b), it can also be seen that,



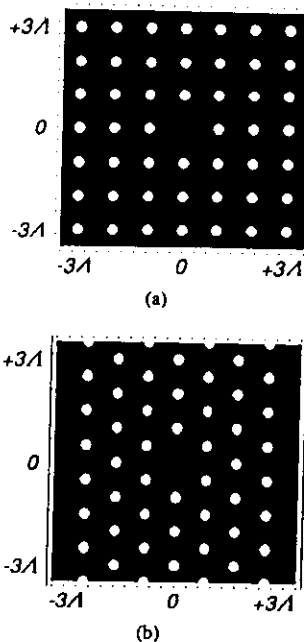


Fig. 1. The outlines of photonic crystal structures with (a) square and (b) hexagonal lattices. The white circles represent air holes in a dielectric background. The absence of an air hole in the central site forms the guiding defect.

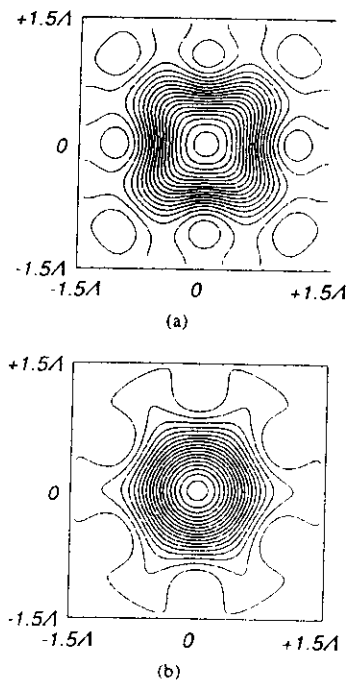


Fig. 2. Calculated transverse field distributions for the  $x$ -polarized fundamental modes of the structures in Fig. 1. In both cases, the diameter of the holes is taken to be 30% of the lattice period, and the wavelength is 31.4% of the lattice period. Four hundred basis functions were used for the plots

even for the comparatively small number of basis functions used, apparently perfect hexagonal symmetry of the mode is achieved.

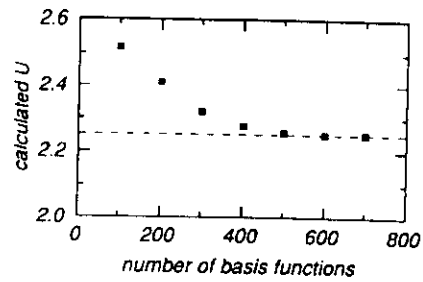


Fig. 3. The core parameter  $U$  of (12) for the fundamental mode of Fig. 2(a) versus the number of basis functions used.

The propagation constant  $\beta$  can be expressed in terms of the dimensionless core parameter  $U$  [10]

$$U = \Lambda \sqrt{k_0^2 \epsilon_b - \beta^2} \quad (12)$$

where  $\epsilon_b$  is the dielectric constant of the "background" dielectric material in the photonic crystal. To illustrate the efficiency of the method, Fig. 3 shows the convergence of  $U$  for the fundamental mode of Fig. 2(a), as the number of basis functions used in the calculation is increased. A few hundred basis functions are sufficient. Since these are products of individual Hermite–Gaussian functions of  $x$  and  $y$  [(2)], each summation in the double sum of (3) can be restricted to just a few tens of terms.

The scalar version of the method is of course also illustrated by the results of [7], for the group velocity dispersion of photonic crystal fibers.

In conclusion, we have presented a detailed account of our localized function method for modeling the full vector modes of defects in 2-D photonic crystals such as photonic crystal fibers. The modal field is represented as a superposition of Hermite–Gaussian functions. A relatively small number of these functions is needed to represent the field accurately, making the method fast and computationally efficient. We have illustrated the method by calculating the fundamental mode fields of two photonic crystal fibers with different lattices.

## REFERENCES

- [1] K. M. Ho, C. T. Chan, and C. M. Soukoulis, "Existence of a photonic gap in periodic dielectric structures," *Phys. Rev. Lett.*, vol. 65, p. 3152, 1990.
- [2] R. D. Meade, A. M. Rappe, K. D. Brommer, J. D. Joannopoulos, and O. L. Alerhand, "Accurate theoretical analysis of photonic band-gap materials," *Phys. Rev.*, vol. B48, p. 8434, 1993.
- [3] J. B. Pendry and A. MacKinnon, "Calculation of photon dispersion relations," *Phys. Rev. Lett.*, vol. 69, p. 2772, 1992; J. B. Pendry, "Photonic band structures," *J. Mod. Opt.*, vol. 41, p. 209, 1994.
- [4] C. T. Chan, Q. L. Yu, and K. M. Ho, "Order- $N$  spectral method for electromagnetic waves," *Phys. Rev.*, vol. B51, p. 16635, 1995.
- [5] T. A. Birks, J. C. Knight, and P. St. J. Russell, "Endlessly single-mode photonic crystal fiber," *Opt. Lett.*, vol. 22, p. 961, 1997; J. C. Knight, T. A. Birks, P. St. J. Russell, and J.-P. de Sandro, "Properties of photonic crystal fiber and the effective index model," *J. Opt. Soc. Amer.*, vol. A15, p. 748, 1998.
- [6] J. C. Knight, J. Broeng, T. A. Birks, and P. St. J. Russell, "Photonic band gap guidance in optical fibers," *Science*, vol. 282, p. 1476, 1998.
- [7] D. Mogilevtsev, T. A. Birks, and P. St. J. Russell, "Dispersion of modes guided in photonic crystal fibres," in *Proc. Conf. Lasers Electro-Opt. Europe*, Glasgow, 1998, paper CFB7; D. Mogilevtsev, T. A. Birks, and P. St. J. Russell, "Group-velocity dispersion in photonic crystal fibers," *Opt. Lett.*, vol. 23, p. 1662, 1998.

- [8] K. M. Leung, "Defect modes in photonic band structures—A Green-function approach using vector Wannier functions," *J. Opt. Soc. Amer.*, vol. B10, p. 302, 1993.
- [9] T. M. Monro, D. J. Richardson, and N. G. Broderick, "Efficient modeling of holey fibers," in *Proc. Opt. Fiber Commun. Conf.*, San Diego, CA: 1999, paper FG3.
- [10] A. W. Snyder and J. D. Love, *Optical Waveguide Theory*. London, U.K.: Chapman and Hall, 1983, pp. 595–606.
- [11] M. J. Adams, *An Introduction to Optical Waveguides*. New York: Wiley, 1981, p. 100.
- T. A. Birks, photograph and biography not available at the time of publication.
- P. St. J. Russell, photograph and biography not available at the time of publication.

D. Mogilevtsev, photograph and biography not available at the time of publication.

# Don't Make Waves, Control 'Em

**SOME 12 YEARS AFTER THE IDEA WAS BORN, RESEARCHERS CONTINUE TO DEMONSTRATE THE VIABILITY AND IMPROVE THE PROCESS OF CONTROLLING LIGHT WITH PHOTONIC CRYSTALS.**

by Charles T. Whipple  
Contributing Editor/Japan

Once upon a time, Eli Yablonovitch of the University of California at Los Angeles had an idea for a new kind of crystal — one that would cut down on the spontaneous emission that causes threshold current in semiconductor lasers. More than a decade later, we're just beginning to see how big an idea it was.

Yablonovitch's crystals promised interesting possibilities. He figured they could act as optical waveguides, improve optical filters and set the stage for completely optical switches — in other words, enable the production of better, smaller optical components. In 1991, he proved that what we now call photonic crystals actually work.

The researcher drew an analogy between electromagnetic wave propagation in multidimensional periodic structures and electron waves in real crystals. "The analogy proved to be a very fruitful one," Yablonovitch said. Initially, he was looking for a "photonic bandgap," a frequency band in three-dimensional dielectric structures that is completely free of electromagnetic waves.

Photonic crystals are like diamonds or graphite in that they have repeating patterns of reflective elements. In natural crystals, the repeating elements are atoms or molecules; in photonic crystals, they're metal or dielectric structures. In the artificially made structures, light of a given wavelength becomes evanescent in all directions.

An experiment by Shawn-Yu Lin's research team at Sandia National Laboratories in Albuquerque, N.M., may offer a better explanation of the photonic crystal phenomenon.

### The logging trail

Lin's group fashioned one photonic crystal of 0.5-mm-diameter columns of alumina set in a grid at a pitch of 1 mm. It looked somewhat like a stack of logs for a bonfire. The pitch of the alumina logs allowed the crystal to manipulate electromagnetic millimeter waves.

When a millimeter wave hit the logs, part of it was reflected and part was allowed to pass through. The pile of logs caused multiple reflections, creating a range of frequencies for which electromagnetic waves cannot exist. The repeating pattern of the logs caused the reflected waves to superimpose out

of step, so peaks met troughs, canceling each other out. The diameter of the logs and the pitch between them determine the frequencies that cancel out. The range of frequencies not allowed to propagate is called a photonic bandgap.

Lin's team confirmed Yablonovitch's seminal work, proving that photonic bandgaps for electromagnetic waves could be created with photonic crystals. "This property enables one to control light with amazing facility, and produce effects that are impossible with conventional optics," said John D. Joannopoulos, who heads photonic crystal research at the Massachusetts Institute of Technology in Cambridge.

Yablonovitch and others say photonic crystals handle photons in much the same way as semiconductors handle electrons. The crystalline structure of a semiconductor controls the flow of electricity, forbidding passage of electrons in a defined energy range. However, the semiconductor material can be doped so it conducts electricity in a precisely defined manner. That's how engineers can make solid-state transistors and computers on a chip.

Like semiconductors, photonic crystals take on their most useful properties with the addition of impurities or defects. One kind of photonic crystal can be created by drilling a diamondlike pattern of holes in a block of silicon. The periodicity (spacing) and size of the holes (columns of



Researchers at Sandia National Laboratories have developed a photonic crystal based on alumina columns set in a grid. The pitch of the alumina logs allows the crystal to manipulate electromagnetic millimeter waves. Courtesy of Sandia National Laboratories.

air) determine the crystal's bandgap. Light in that bandgap sees a perfect crystal in all directions, but if that periodicity is broken by removing one of the columns of air, the forbidden frequency of light can suddenly exist near that defect. And if the defect is a line, photons will be forced to follow that line through the crystal, even if it turns at right angles. This is encouraging news to researchers, indicating that optical integrated circuits are just a matter of time.

### Good news and bad news

According to Joannopoulos, theoretical description of light in photonic crystals involves the solution of Maxwell's equations in a periodic dielectric medium. (The four equations, written by Scottish physicist James Clerk Maxwell, summarize the relationship between electricity and magnetism. They show that like charges repel and unlike charges attract, no single isolated poles exist, electrical currents can cause magnetic fields, and changing magnetic fields can cause electrical currents.)

The good news is that, unlike problems involving electrons in a solid, Maxwell's equations can be solved exactly. In other words, theoretical computations concerning photons are very accurate, and very useful pre-experiment exercises.

The bad news is that, unlike the natural periodic arrangement of atoms in semiconductors, photonic crystals must be created artificially. For millimeter waves, this poses no problem. But for the frequency of light most often used in optoelectronics (1.5  $\mu\text{m}$ ), fabricators must create periodic structures with a lattice constant of about 0.5  $\mu\text{m}$ . That's a thousand times bigger than the atomic lattice constant of a natural crystalline semiconductor, but it's also only a hundredth the width of a human hair. Right now, the only methods that come close to this magnitude entail x-ray or electron-beam lithography. Joannopoulos said that the ultimate goal for optoelectronic



Light passes through an early prototype of the Sandia team's photonic crystal. Courtesy of Sandia National Laboratories.

applications is to design and fabricate 3-D photonic crystals at an operating wavelength of 1.5  $\mu\text{m}$ . Researchers worldwide are working toward that goal.

### What good is it?

The ability to create photonic bandgaps that forbid propagation of electromagnetic or light waves of certain frequencies in one, two or three directions offers interesting possibilities for manipulating those waves. Potential applications include thresholdless lasers, resonant cavities, antenna substrates, optical waveguides, and many kinds of filters and polarizers.

In the years since Yablonovitch postulated and proved the theory behind photonic crystals, research has burgeoned. Yurii A. Vlasov, of the NEC Research Institute in Princeton, N.J., lists groups in 21 countries on his Web-based photonic bandgap research page ([www.neci.nj.nec.com/homepages/vlasov/photonic.html](http://www.neci.nj.nec.com/homepages/vlasov/photonic.html)). His list of US research groups includes eight government organizations, 42 universities and five corporations. Lists for other countries are similar in makeup, with universities leading the way.

Theoretical work and laboratory experiments are all well and good, but what progress has been made

since Yablonovitch's demonstration in 1991?

Following up on their work with crystals to control millimeter waves, Lin's Sandia team finally built a light trap of interlocking silicon bars, each 1.3  $\mu\text{m}$  wide and 1.5  $\mu\text{m}$  high, set at a pitch of 4.8  $\mu\text{m}$ . The device traps infrared light with 10- $\mu\text{m}$  wavelengths.

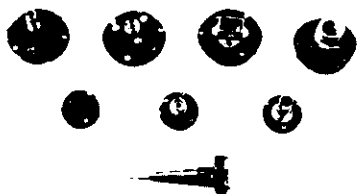
But Lin and his fellow researchers did not settle for just trapping the infrared light. By carefully introducing defects into the lattice, they were able to make the light move up and down and turn corners while traveling through the crystal. The experiments also proved that light can be turned 90° in a one-wavelength radius. MIT's Joannopoulos clarified the possibilities. Waveguides in photonic crystals can guide optical light in air, along narrow channels and around very tight bends — with no losses.

Still, the Sandia researchers must reduce the scale of their crystals even further to manipulate the 1.5- $\mu\text{m}$  infrared light now used for optical communications. To achieve that, they'll have to cut the lattice pitch to one-tenth its current size while reducing the size of the silicon bars by similar numbers. MIT's photonic crystal research group predicts Lin and his colleagues will have crystals for 1.5- $\mu\text{m}$  light by the end of this year.

MIT researchers have come very close to a practical waveguide for infrared light, using a hybrid approach. They took a traditional silicon waveguide and drilled a series of holes in it to form a one-dimensional photonic crystal. Specifically, researcher Jim Foresi drilled four air holes into the waveguide, spacing them 0.22  $\mu\text{m}$  apart. He then left a 0.42- $\mu\text{m}$  gap before drilling another series of four holes.

Here's what happened. A pulse of light with lots of frequencies was sent down the waveguide. When the light hit the four-plus-defect-plus-four configuration, only rays with the frequency of the defect could get through. In this case, the

## FIBER OPTIC COLLIMATORS/FOCUSERS



Fiber optic focusers and collimators are used to package fiber optic devices such as laser and photo diodes, acousto-optic modulators, polarization maintaining splitters, and other devices. Fiber optic collimators collimate light from a fiber, while focusers focus the fiber output at a specified working distance. Adjustable focusers are available, allowing you to change the working distance and spot diameter of the focused spot.

Female receptacle style focusers and collimators are available for a variety of commercially available connectors, such as NTT-FC, AT&T-ST, SMA905 etc. Pigtail style collimators and focusers are also available, and feature 30, 45 or 60dB backreflection levels. Collimators and focusers are offered for both low and high power applications. Collimated beam diameters of 0.2mm and larger are available. Miniature collimator housings as small as 1.6mm diameter are also available. Prices vary from as low as \$55.00 for certain pigtail style collimators and focusers. Volume discounts are available.

## FIBER PIGTAILED U-BRACKET



U-Brackets are designed to transmit light from an optical fiber or source (such as a lasers or laser diodes) across an airgap and into a second fiber with low losses. The U-Bracket is prealigned at the factory for minimum insertion losses, making it very easy to use. A variety of bulk optical devices, including polarizers, isolators, filters, and waveplates, can be simply inserted into the U-bracket, allowing the user to quickly and easily test or prototype systems incorporating fiber and bulk optics.

The U-Bracket assembly consists of three parts: an optional input fiber collimators, (fiber to fiber version), the U-Bracket itself, and an output fiber focuser. Insertion losses of only 0.3dB are achievable across an airgap of 20mm using OZ Optics' patented tilt adjustment technique.



### OZ OPTICS LTD.

219 Westbrook Road  
Carp, Ontario, Canada, K0A 1L0  
Toll Free 800-361-5415  
E-Mail: sales@ozoptics.com  
Website: www.ozoptics.com  
Tel 613-831-0981 Fax 613-836-5089

## tools for the lab **photonic crystals**

frequency was  $1.5 \mu\text{m}$ . This kind of one-dimensional photonic crystal can be used to peel off a certain wavelength of light and send it in a different direction.

### Superprisms

NEC Corp., which has its headquarters in Tokyo and is one of the few companies actively developing photonic crystal devices, recently announced a crystal with a "superprism" effect (see *Photonics Spectra*, December 1998, pp. 31-32) developed in collaboration with NTT Optoelectronics Laboratories, also in Tokyo, and Tohoku University in Sendai, Japan. Where MIT's one-dimensional crystal peels off one frequency, NEC's crystal effectively separates light by wavelength.

"Our intention," explained Hideo Kosaka of NEC's superprism research team, "is to construct photonic crystals with equipment and materials used to make ordinary semiconductors." In Kosaka's experiments, two frequencies of light —  $0.99$  and  $1.0 \mu\text{m}$  — entered the crystal less than  $1^\circ$  apart and exited  $50^\circ$  apart. By the same token, a full spectrum of light exits the crystal widely separated by color frequency.

"It is very difficult to create perfect photonic bandgaps," Kosaka said. "But we thought there might be something usable even with imperfect ones."

The team laid down a silicon substrate, and topped it with a silicon-oxide buffer layer and a patterned layer of silicon with a hexagonal array of holes. Once the pattern was set, 20 pairs of alternating layers of silicon and silicon oxide were laid down. These layers replicated the holes of the patterned layer, resulting in self-organized triangular lattices in a 3-D structure.

"Our method automatically puts the photonic atoms of silicon and silicon oxide directly above each other in consecutive layers," Kosaka said. "It's much simpler than fabrication processes that use artificial opals, etching or micro-manipulation. Our method is also

more eco-friendly. Silicon and silicon oxide leave no toxic waste."

Kosaka agreed that light can be made to turn very sharp corners without loss in waveguides made of perfect photonic bandgap crystals. "But the superprism phenomenon does not need a perfect photonic bandgap," he said. "And they hold the potential of multiple branching and wavelength sensitivity that should inspire novel designs for such functional devices as wavelength division multiplexers/demultiplexers."

NEC is a major supplier of communications equipment to NTT, Japan's national telecommunications utility. Naturally, NEC's research and development program focuses on finding practical applications, in this case, for the photonic crystal phenomenon.

Kosaka and his colleagues envision several applications for their superprism crystals but are concentrating on two: bonding photonic integrated circuits to electronic large-scale integrated circuits and developing a fully photonic add/drop multiplexing device.

### Crystal cavity lasers

The add/drop multiplexer hinges on access to photonic crystal laser diodes. A research team under Hideki Hirayama at the Institute of Physical and Chemical Research (Riken) in Wako, Japan, experiments with photonic crystal cavity lasers. They use Swiss cheeselike photonic crystals, a dielectric material with a lattice of air holes drilled through it. The holes are arranged to form a pair of 3-D photonic crystal mirrors, sandwiching a phase-controlling defect region. The team demonstrated unidirectional radiation patterns and drastic enhancement of spontaneous recombination lifetime with these experimental photonic crystal cavity lasers. And, taken down to the minuscule sizes necessary to handle visible light, they could become important components in integrated optical circuits.

Continuing with developments concerning optical communications, researchers at the University

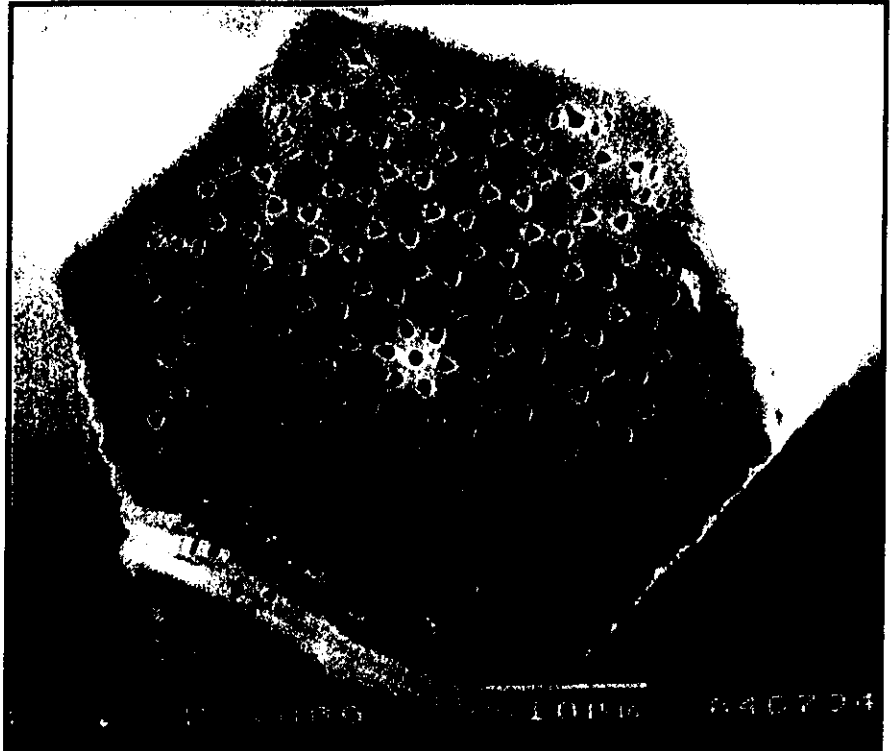
For Free Info, Circle 97  
112 PHOTONICS SPECTRA

MARCH 1999

## tools for the lab **photonic crystals**

of Bath in the UK have created photonic crystal optical fibers. In his report on photonic crystal fiber, Jonathan Knight said his team concentrated on 2-D photonic crystals in its research, which brought it around to photonic crystal fibers. The principle is quite simple: The fiber is merely a 40- $\mu\text{m}$  thread of silica glass with a periodic array of air holes running its entire length.

Ordinary optical fibers consist of a core and cladding. Light waves reflect off the mirror at the intersection of core and cladding toward the center of the fiber. The team's fiber has a "defect" — an extra air hole in the center — that serves as the core. Light waves running down the fiber are confined to the core by the photonic bandgap created by the surrounding array of holes. Tests show the photonic crystal fiber transmits much higher optical power than



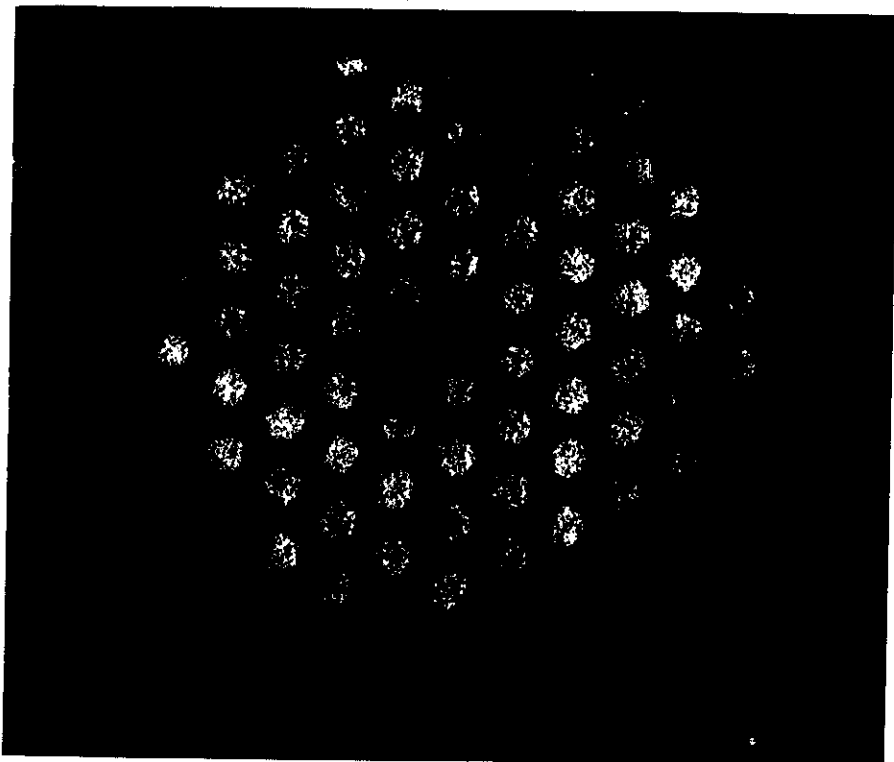
# ITS MOST IMPRESSIVE FEATURES

ELECTRO-CHEMICALLY ETCHED  
ALPHA-NUMERIC GRID

**New**

HIGH DENSITY, SMALL CELL SIZE  
STEEL HONEYCOMB CORE

USER-FRIENDLY  
ROUNDED CORNERS



conventional optical fibers, Knight said.

Now that the principle has been proved, it's probably up to some manufacturer to develop efficient, precise methods for manufacturing these photonic crystal fibers.

Meanwhile, back at UCLA where the whole photonic crystal melee began, Yablonovitch continues to wrestle with the problem that led him to try to find a way to halt

A scanning electron microscope image (opposite page) details a 40- $\mu$ m photonic bandgap fiber created at the University of Bath. The center region with the extra air hole acts as the core, through which light is guided by a photonic bandgap. An optical microscope image (near left) shows the fiber, as the other end is illuminated by white light. Courtesy of the University of Bath.

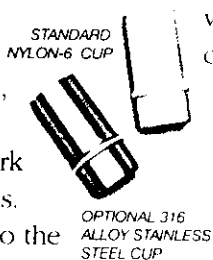
## RE ONLY VISIBLE IN YOUR RESULTS

You can't see the patented breakthrough features that make TMC's CleanTop II the best optical table for demanding applications. But you can depend on them for a trouble-free research environment. That's why CleanTop II is now standard on all TMC tables.

### CleanTop II™

CleanTop II starts clean and stays that way. The ultra-flat stainless steel top plate is cleaned of all manufacturing residue in a proprietary process. And, TMC's patented spillproof feature has been enhanced with new *corrosion free* Nylon-6 cups.

For the ultimate in corrosion protection, we offer 316 alloy stainless steel cups which provide a total stainless steel work surface to handle the harshest chemicals. Cups are epoxy-bonded (not welded) to the top plate. Spills can be quickly and completely removed. There is no potential for contamination or outgassing, as liquids can't reach the honeycomb core.



PATENTED  
CLEANTOP  
SPILLPROOF  
CORE

Precision tapped and countersunk holes accelerate set-up; no wrench is ever required. And radius corners add to user comfort and safety.

Your research results deserve the ultimate in vibration-free optical tables. To request a catalog, contact our Technical Sales Group.

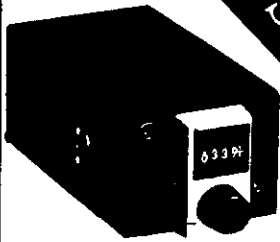
# TMC

**Technical Manufacturing Corporation**

15 Centennial Drive, Peabody, MA 01960 USA  
Tel: 978-532-6330, 800-542-9725, Fax: 978-531-8682  
e-mail: sales@techmfg.com www.techmfg.com

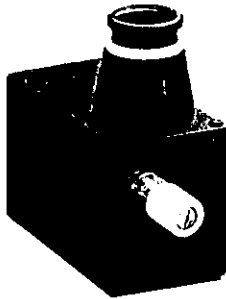
**VIBRATION SOLUTIONS WORLDWIDE**

Over  
20,000 Sold!



## Mini-Chrom Monochromators

Among  
the most  
successful  
ever  
made!



Whether your need is for

- basic research,
- teaching,
- OEM application,

there is a version of the  
**Mini-Chrom** for you!

The combination of excellent performance, small size and low cost make the **Mini-Chrom** monochromators ideally suited for OEM applications.



Email: [opto@optometrics.com](mailto:opto@optometrics.com)  
Web Site: [www.optometrics.com](http://www.optometrics.com)

Nemco Way  
Ayer, MA 01432  
Tel: 978-772-1700  
Fax: 978-772-4017

**Optometrics USA, Inc.**  
A world-class supplier of  
optical components  
for over 30 years.

For Free Info, Circle 95  
116 PHOTONICS SPECTRA

## tools for the lab **photonic crystals**

propagation of electromagnetic waves of certain frequencies. If photonic crystals can manipulate light waves, surely they can also manipulate their longer relatives — radio and microwaves.

In theory, crystals to control radio waves would be about the size of an 18-wheeler. But Yablono-vitch found that photonic crystals with metal elements can be tuned so that small crystals can manipulate long wavelengths. He predicts that cellular telephones with photonic crystal aerials will be in shops before the end of the century. If that happens, people will be able to use their cell phones without subjecting their brains to microwaves.

### Hopeful prospects

Daily, research teams around the world announce developments that use photonic crystal attributes. Armand Rosenberg of the Naval Research Lab in Washington made interesting predictions: "In my opinion, the first applications will involve specialized use of PBG [photonic bandgap] materials as passive optical filters. Clearly, such devices can benefit optical data transmission applications."

Rosenberg also pointed to demonstrations of optical limiters incorporating a nonlinear medium in a photonic bandgap material achieved by the Naval Research Lab. "Ultimately, I think the greatest promise is in integrated optical and optoelectronic circuits, which would incorporate waveguide structures like those discussed by the theory group at MIT."

David J. Norris, a colleague of Vlasov's at the NEC Research Institute, may represent the view of industry. "It is clear that photonic



In experiments with NEC's "superprism" photonic crystal, two frequencies of light — 0.99 and 1.0  $\mu\text{m}$  — enter the crystal less than 1° apart and exit 50° apart. Courtesy of NEC.

crystals can have very special properties," he said. "With these materials, one can inhibit spontaneous emission, a parasitic process in many

optoelectronic devices. Defects introduced into photonic crystals act as extremely efficient optical microcavities that could be used to make thresholdless lasers and extremely low-noise LEDs [light-emitting diodes]."

Then Norris focused on the crux of the matter. "The crystals are very difficult to make, and this difficulty is a big bottleneck for commercialization. This is why we are working to use natural chemical processes such as self-assembly to make photonic crystals, instead of nonlithography."

Nevertheless, Norris added a word of caution: "Some simple, elegant applications have arisen from the field. More exotic applications require more basic materials research to find simple ways to make these crystals."

The time has come for industry to get more involved. As MIT's Shanhui Fan said, "The challenge is to fabricate these micro- and nanostructures reliably, with accurate control over dimensions." Ways to manufacture optical switches, frequency modulators, channel drop filters, low-threshold lasers and integrated LEDs must be devised. This new integrated optics technology needs to be made compatible with integrated circuit technology. The possibilities for telecommunications alone are mind-boggling. □

MARCH 1999



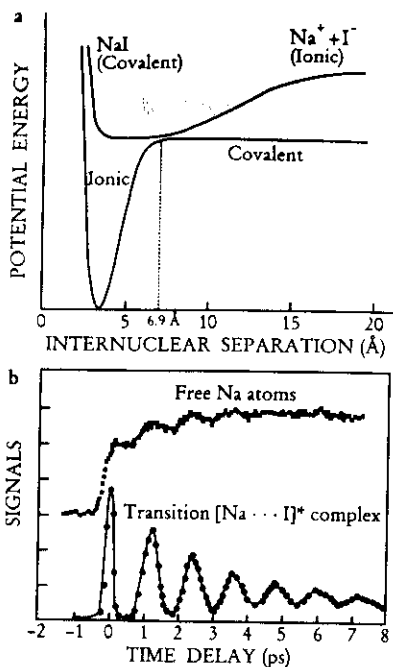
surfaces dictate the confinement or departure of the nuclei, and thus the outcome of the chemical process. For his development of computational techniques that greatly facilitate the calculation of molecular potential-energy surfaces, Northwestern University theorist John Pople shared last year's chemistry Nobel Prize. (See *PHYSICS TODAY*, December 1998, page 20.)

When the potential energy of a diatomic molecule, at a given electronic excitation level, depends only on the distance between the two nuclei, the potential-energy surfaces are simply curves, as we see in the figure at right. For NaI, a prototypical alkali halide molecule, the figure shows the theoretically calculated ground-state potential curve, with a deep ionic-bonding well at an equilibrium nuclear separation of 2.8 Å, and a nearby excited-state potential curve with a broad, shallow well.

In a 1988 experiment,<sup>3</sup> Zewail and coworkers gave a striking demonstration of how femtochemistry can elucidate the dynamics of such a fundamental molecular system. The two NaI potential energy curves come very close to each other when the nuclei are 6.9 Å apart. At this point there's a bonding role reversal, as is often the case at such "avoided crossings": The strong ground-state bond, which is ionic at small separations, becomes covalent, and thus weaker, at separations beyond 6.9 Å. Conversely, the short-distance covalent bond of the excited state becomes ionic, and thus stronger, beyond 6.9 Å. This long-distance creation of an ionic bond in the excited state has been described as harpooning the iodine atom from afar with the sodium atom's valence electron.

The Caltech group's experiment began with a pump pulse that raised NaI molecules in the beam to the excited state. That was followed, at 50 fs intervals for the next 10 ps, by probe pulses at wavelengths chosen to reveal the creation of free Na atoms and of a putative short-lived transition complex of bonding and antibonding states, denoted  $[Na \cdots I]^*$ . The experimental results, shown in part b of the figure, exhibit a remarkably clear and persistent oscillation, with a period of 1.25 ps. The upper data curve signals the liberation of Na atoms, while the lower curve signals the fleeting appearance of the elusive transition complex.

The 1.25 ps periodicity manifests the oscillation period of the NaI molecule in the excited state's broad potential well. Every time the separation approached the 6.9 Å avoided-crossing point, the  $[Na \cdots I]^*$  transition state would form, and there was a



**MOLECULAR DYNAMICS** of NaI at femtosecond resolution.<sup>3</sup> (a) Potential energy curves for the ground state (green curve) and the experiment's excited state (red) come very close to each other at 6.9 Å and trade bonding characteristics. (b) Probe laser pulses at 50 fs intervals detect 1.25 ps oscillations in the population of liberated Na atoms (orange data points) and a short-lived transition complex (blue).

roughly 10% chance that the molecule would jump down to the covalent branch of the ground-state curve and thus finally dissociate.

But—if the experimental signal is a sum over millions of independent molecules—why don't the oscillations wash out? The answer is that, in such

## A New Way to Guide Light in Optical Fibers

Many of our phone conversations and e-mail communications race to their destinations over optical communication links that rely on total internal reflection to guide pulses of light down hair-width fibers of glass. Despite their prodigious bandwidth, these glass fibers will be hard pressed to meet the heavy traffic demands being placed on them by the exploding use of the Internet. Recently, researchers from the US and UK have demonstrated another way to transmit light waves through narrow channels: By surrounding a hollow core with photonic bandgap structure.<sup>1</sup> Their achievement opens the way for guiding light with little or no loss through an evacuated channel.

a femtochemistry experiment, the pump pulse catches all the ground-state molecules at once, all of them very close to the equilibrium 2.8 Å separation at the bottom of the deep potential well. Thus they all start to oscillate in the excited well almost in lockstep, giving us an unprecedented "movie," with angstrom resolution, of a prototypical molecular disintegration in progress.

### Femtosecond diffraction

"Now we're looking at biological systems and other very complex processes," Zewail told us, "and we're hoping to apply electron diffraction techniques on a femtosecond scale. Kent Wilson's [University of California, San Diego] group has recently managed to do lattice-dynamics diffraction experiments with picosecond x-ray pulses."<sup>4</sup> As these diffraction techniques evolve, they should make possible the structural study of crystals and complex molecules on the timescale of their formation.

"Again and again, Zewail's group has shown us how much one can learn by resolving the dynamics of chemical systems on femtosecond scales," says Herschbach. "This inspirational impact is an important aspect of Zewail's contribution."

BERTRAM SCHWARZSCHILD

### References

1. A. H. Zewail *Femtochemistry: Ultrafast Dynamics of the Chemical Bond*, vols. 1 and 2, World Scientific, Singapore (1994).
2. C. V. Shank, *Science* **233**, 1276 (1986).
3. A. H. Zewail, *Science* **242**, 1645 (1988).
4. C. Rose-Petrucci *et al.*, *Nature* **398**, 310 (1999).

▶ A novel form of fiber optics, featuring a hollow core rather than one made of glass, holds promise for communications systems or other applications.

That's important because the interaction of light with glass now limits the maximum power that one can transmit with today's glass-core fibers. It's not possible to have hollow cores with fibers that rely on total internal reflection because the core must have a larger index of refraction than the cladding, and there's no solid material that has an index of refraction less than one.

The recent demonstration is thus

P10

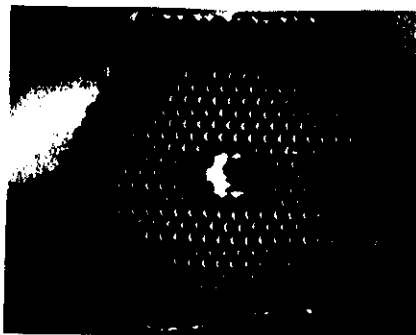
an important step, although so far propagation has been shown only for fibers a few tens of centimeters long. If the technique can be scaled up to long distances, it may help communications companies better keep up with the growing demand on their fiber networks (which is currently met by lightguides, microwaves, and satellite-based systems). Higher power is needed to carry more information in fibers, but the power levels in conventional fiber-optic systems are limited by the nonlinearities of the medium.

Short of replacing conventional fibers, however, photonic bandgap fibers may find niche markets because they have different properties from fibers based on total internal reflection. They allow greater flexibility in the nature of the core, for example, because the index of refraction for the core does not have to be lower than that of the cladding. But they are more restricted in the range of wavelengths they can carry without loss. Aside from lightwave applications, they might be used to guide atoms or small particles down capillary tubes.

### The guiding principle

What serves as the cladding in the new photonic bandgap fibers? As shown in cross section in the figure above, it is a lattice of silica penetrated by a hexagonal close-pack array of holes that surrounds a large central hole (the core). Such arrays of contrasting dielectric materials (in this case, silica and air or vacuum) strongly scatter light rays passing through them. Thanks to their regularity, the structures can have a photonic energy spectrum analogous to that of electrons in a crystal. For certain geometries, the spectrum can even feature a bandgap—that is, a band of wavelengths that cannot propagate within the material. Photonic bandgap materials are attracting increasing interest for applications such as lasers, optical cavities, and couplers (see the news story in *PHYSICS TODAY*, January 1999, page 17, and the article by Sajeev John in *PHYSICS TODAY*, May 1991, page 32).

If a fiber has a photonic bandgap structure as its cladding, light whose wavelength falls within the bandgap cannot leak into the cladding, but must remain within the core. That idea has motivated the team that did the recent demonstration: Philip Russell, Timothy Birks, Jonathan Knight, and their postdocs and students at the University of Bath in the UK, along with John Roberts of the Defence Evaluation and Research Agency in



**PHOTONIC BANDGAP FIBER.** This scanning electron micrograph of the cleaved end face of a light-guiding fiber shows the overall shape (top) and a closeup (bottom) of the honeycomb array of holes in silica. Light is guided down the large central core, which is 14.8  $\mu\text{m}$  in diameter. (Adapted from ref. 1.)

Malvern, England, and Douglas Allan of Corning Inc in Corning, New York. Russell told us that, when he started out toward this goal in 1992, many in the field felt that success would require a bigger contrast in the two indexes of refraction than that between silica and air (1.46 to 1) to get a full bandgap. Nevertheless, Russell's group has shown that it's possible to get a two-dimensional bandgap using these structures.<sup>2</sup>

Finding the right geometric pattern of holes in silica was not straightforward, however, largely because it's not easy to calculate what kinds of structures will give a sufficiently large bandgap in the desired wavelength region. Possible structures differ in the geometrical arrangement of the holes, the size of the holes, and the distances between them. Last year, Knight, Birks, and Russell, together with J. Broeng from the Technical University of Denmark, reported another structure that guided light by a photonic bandgap mechanism, but most of the light traveled through the silica surrounding the central hole, rather than within the hollow core, thus defeating the hoped-for transmission in air that the researchers have now achieved with the new design. One key to their recent success was fabricating a structure with a larger volume frac-

tion of air (around 30%).

To make the fibers, the researchers bundle several hundred hollow capillary rods of silica in a hexagonal close-pack array, each about a millimeter in diameter. They then remove enough rods from the center to leave a hole the size of seven unit cells. The Bath-Corning team then heats this sheaf of rods and draws it out to form long fibers tens of micrometers in diameter. The process introduces additional, small interstitial holes into the gaps between the rods, which have a small effect on the bandgap wavelengths.

### Transmission bands

When Russell and his coworkers shone white light through short lengths of these fibers, they found that the core transmitted colored light—presumably those wavelengths in the bandgap of the cladding—while the cladding transported white light, presumably a mix of all allowed wavelengths. The transmission spectrum showed low-loss peaks in several wavelength bands in the visible and infrared bands of the spectrum. Laser light whose frequencies lay within those bands could be guided through sections of fiber up to 40 cm in length, while maintaining a high degree of spatial coherence. The biggest limitation on the length of transmission is the fluctuation of the fiber parameters down the length of the fiber. That problem should be surmountable with efforts to attain a very evenly drawn fiber, so that the bandgap spectrum remains stable down the fiber's full length.

The Bath-Corning researchers would like to compare the observed transmission bands to the bandgaps predicted theoretically for their structure, but so far the calculations have not been done; the computations are just too difficult, especially for the high frequencies involved.

### Photonic crystal fibers

Several other groups are working with fibers that have solid cores surrounded with periodic dielectric structures (generally called photonic crystals) that do not have bandgaps (typically the volume fraction of air is smaller than in bandgap fibers). Without the bandgap, a photonic crystal cladding must confine light by the conventional method of total internal reflection; the effective index of refraction of the cladding is a volume average of the silica and air.

The earliest photonic crystal fibers studied by Russell and his colleagues had solid cores and they guided light by total internal reflection (TIR).<sup>4</sup>

These photonic crystal TIR fibers exhibit some behavior that's quite distinct from conventional TIR fibers. For instance, the photonic crystal fibers can support single-mode transmission over a wide range of wavelengths, whereas few conventional fibers can transmit at a single transverse mode over a frequency range greater than one octave. Furthermore, Russell commented to us, the photonic crystal cladding allows one to make the core area about ten times larger than that of a conventional fiber, thereby allowing higher power transmission.<sup>5</sup> These differences suggest that the photonic crystal fibers may find some niche markets.

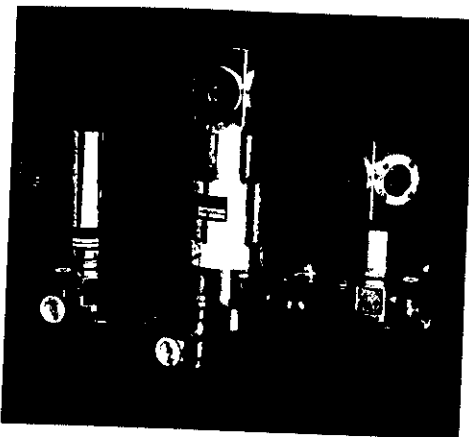
Several other research teams are exploring the properties of photonic crystal fibers. For example, a group from Bell Laboratories, Lucent Technologies, recently made a structure that has a fiber grating in the core and a photonic crystal as its cladding.<sup>6</sup> (A fiber grating is a periodic variation in index of refraction over the length of the fiber.) The grating, which reflects certain wavelengths back on themselves, helps to couple the single modes in the core of the fiber (doped germanium, in this case) with the higher-order leaky modes—those modes that propagate in the cladding. The Bell Labs group is interested in the application of photonic crystal fibers to optical devices as well as to transmission lines. By studying the transmission of various wavelengths through such fibers, the researchers can deduce which modes of the core couple to the cladding. This technique has enabled them to characterize the cladding modes as a first step toward understanding their potential for lightguide devices.

Innovations in fibers are not limited to those with periodic arrays of holes in the cladding: Benjamin Eggleston of Bell Labs told us that he and his colleagues, and similarly a group at the University of Southampton in the UK, are studying yet other types of fibers. **BARBARA GOSS LEVI**

#### References

1. R. F. Cregan, B. J. Mangan, J. C. Knight, T. A. Birks, P. St. J. Russell, P. J. Roberts, D. C. Allan, *Science* **285**, 1537 (1999).
2. T. A. Birks *et al.*, *Electron. Lett.* **31**, 1941 (1995).
3. J. C. Knight *et al.*, *Science* **282**, 1476 (1998).
4. J. C. Knight *et al.*, *Opt. Lett.* **21**, 1547 (1996).
5. J. C. Knight *et al.*, *Electron. Lett.* **34**, 1347 (1998).
6. B. J. Eggleston, P. S. Westbrook, R. S. Windeler, S. Spälter, T. A. Strasser, *Optics Lett.* **24**, 1460 (1999). ■

# JANIS FAMILY OF CRYOCOOLER CRYOSTATS



- Temperature range from 8K to 600K
- Cooling capacities to 3 watts at 20K
- Optical and non-optical
- Top loading samples in exchange gas or samples in vacuum
- Air cooled or water cooled compressors
- Designs for Mössbauer, VSM, FTIR, matrix isolation, Hall effect and others
- Custom systems upon request
- No cryogenics required
- Fast cooldown
- Wide selection of accessories

## JANIS RESEARCH COMPANY, Inc.

2 Jewel Drive, P.O. Box 696  
Wilmington, MA 01887-0696  
Tel: (978) 657-8750 Fax: (978) 658-0349  
E-MAIL: [janis@janis.com](mailto:janis@janis.com)  
WWW: <http://www.janis.com>

Circle number 16 on Reader Service Card

## Laboratory Cryogenic Systems

**Displex®**  
Closed Cycle Cryostats  
(6.5 - 450 K)

**Hell-tran®**  
Flow Cryostats  
(2 - 800 K)

**Advanced Cryogenic Systems, Inc.**  
905 Harrison Avenue, P.O. Box 100, Newtown PA 18103  
Phone: 610-439-8022 Fax: 610-439-1184 E-mail: <[arscryo@aol.com](mailto:arscryo@aol.com)>

Circle number 17 on Reader Service Card

997



# Light

laser or a hosepipe for atoms?

P11

PHILIP RUSSELL's professional life is riddled with holes, but that's the way he likes it. Ask him the secret of his remarkable light-conducting fibres and he'll tell you it is not the material from which they are made, but the lack of it. Where there should be solid silica glass—as in a conventional optical fibre—Russell and his team at the University of Bath have left dozens of tiny holes. Strangely, the holes are there to keep the light in.

Russell's fibres are an impressive piece of engineering—the holes are just tens of nanometres wide and run perfectly for hundreds of metres. This unique design lets them carry far more light than conventional fibres, so in theory they could boost the capacity of fibre-optic networks and even help to create powerful "pocket lasers" for use by surgeons to cauterise tissue or by astronauts to repair orbiting spacecraft. The fibres also let you play some remarkable tricks, such as making light leap from one fibre to another, or squirting atoms through a "hosepipe" of light—tricks that are vital for building high-speed optical computers or super-sensitive gravity detectors.

Conventional optical fibres carry light through a glass core surrounded by a cladding layer—a bit like the insulation on an electrical cable. In most optical fibres both the core and cladding are made from silica glass, but the core has slightly different optical properties, thanks to a sprinkling of atoms known as dopants, usually germanium or phosphorus. These atoms raise the refractive index of the glass so that as light travels through the core, it is reflected from the interface with the cladding by a process called total internal reflection, and is trapped.

Russell's fibres are very different. Core and cladding are still made of silica glass, but there's no need for dopants: instead the fibre has tiny holes running through it. These make the perforated glass impermeable to light.

Why should holes prevent light from passing through an otherwise transparent material? If the holes are arranged in a regular array with a size and separation of roughly the same magnitude as the light's wavelength, they act as a picket fence that stops light from passing through. An orderly array of particles or gaps that excludes light in this way is called a photonic crystal ("Tricks of the light", *New Scientist*, 26 August 1995, p 26).

Photonic crystals were predicted in 1987 by two physicists working independently: Eli Yablonovitch of Bell Communications Research in Red Bank, New Jersey, and Sajeev John of the University of Toronto in Canada. Light passing through a field of obstacles, such as a suspension of particles in water, is scattered if the size of the particles is similar to the wavelength of the light. The researchers realised that if the particles were arranged in a regular lattice, they would scatter incident light of the right wavelength back the way it came, like a mirror. Such crystals have a photonic "band gap"—a band of forbidden wavelengths which they will not allow to pass.

Instead of filling empty space with a regular array of objects, you could make a photonic crystal by peppering a solid block of material with a regular array of holes.

John Miller

js

Photonic crystals offer more than just fancy mirrors: they can confine and guide light too. Disrupt the regularity of photonic materials and you open up a "crack" through which light can squeeze. Missing out a row of holes in a perforated sheet, for example, provides a channel through which light can travel.

This is the principle that Russell and his colleagues, Jonathan Knight and Tim Birks, use to make their photonic crystal fibres. Their strands, each thinner than a human hair, are laced with holes running their length (see Photograph). But through the centre of the fibres runs a solid, light-conducting channel confined by the surrounding photonic crystal. They have made fibres hundreds of metres long, with tiny channels running their entire length. If the smallest of these channels were scaled up to the width of the Channel Tunnel, it would stretch from here to Jupiter.

### Whisker thin

To create this perfect array, the researchers used a neat trick: they packed together narrow glass tubes to make a bundle about two centimetres across. Like logs stacked in a woodpile, the tubes arrange themselves in a hexagonal fashion. To convert this hefty bundle of tubes into a perforated thread three hundredths of a millimetre across, the researchers simply heated the bundle to 2000 °C to make the glass soft and viscous, and then stretched it until it was as thin as a whisker. This preserved the holey cross-section, but shrunk it in scale by a factor of about a thousand. At this temperature, the glass becomes soft enough to ooze into and fill up the very narrow spaces between adjacent tubes whereas their hollow interiors remain. The result: a flexible fibre riddled with channels too small to see.

However, these fibres, first fabricated three years ago, don't operate by setting up a full photonic band gap in the cladding layer. Rather, Russell and his colleagues believe that the picket fence of holes acts like a material with a different refractive index from that of the solid glass core, so the light is confined by total internal reflection.

But they've done far more than create a conventional fibre using unconventional means. They've discovered that no matter how big they make their photonic crystal fibre, it behaves like a conventional fibre with a core just a few micrometres across. This gives their fibre some huge advantages.

Make the core of a conventional fibre too wide and light travelling along it can follow several paths. This sets up patterns

or "modes" in the light—like the patterns of vibration on a drumhead. A fibre with a core more than about 20 micrometres across can support several of these modes and is called a multimode fibre. Send a narrow signal pulse along a multimode fibre and it smears out as it travels, blurring the information content and limiting the amount of data that it can carry.

One solution is to use fibres with cores just a few micrometres across, as light can only follow a single pathway through them. But these "single mode" fibres are so narrow that you can't fit much light into them.

On the other hand, you can make a photonic crystal fibre as wide as you like and it will still behave like a single-mode fibre. The "fundamental" mode remains trapped, but all the light following other pathways leaks out of the core by "squeezing" between the holes, so light pulses don't smear out as they travel along the photonic crystal fibre.

These fibres are also made of pure silica, without the dopants which can absorb light, particularly at blue and ultraviolet wavelengths, and reduce the intensity of the signal bouncing through the fibre. In principle the photonic crystal fibre should behave as a single mode fibre for light from the ultraviolet to the infrared parts of the spectrum—a feat unmatched by any other fibre.

And because the fibre core can be made wider than conventional single-mode fibres, you can squeeze far more light down it—up to 20 times more—opening up new

All of this represents a radical departure from the way light is normally guided around in optical fibres. "Russell's photonic crystal fibres have breathed new life into a well-established field," says Douglas Allan of Corning, a leading glass technology company based in New York. "Their work is an extremely valuable source of new ideas for controlling light in fibres," he adds.

### Totally new

Late last year, the Bath group went one step further. It reported a photonic crystal fibre in which the core was not solid silica but an extra hole (*Science*, vol 282, p 1476). The researchers believe that, whereas in their solid-core fibres the light was still confined by total internal reflection, the hollow-centred fibres trap the light because there is a true photonic band gap in the cladding—a totally new principle of operation for an optical fibre.

Nevertheless, in their new fibre the light is confined inside the glass that surrounds the central hole, rather than in the hole itself. Russell would dearly love to create a fibre in which the light passes down the hollow core—through air instead of silica. There would be almost no absorption or scattering and the power capacity would be vastly increased. This, says Russell, is his team's ultimate aim, the target that he originally envisaged back in 1992. "We're not there yet," he says, "but we're close."

Ultimately, he sees such fibres being used as the amplifying cavity of a laser.

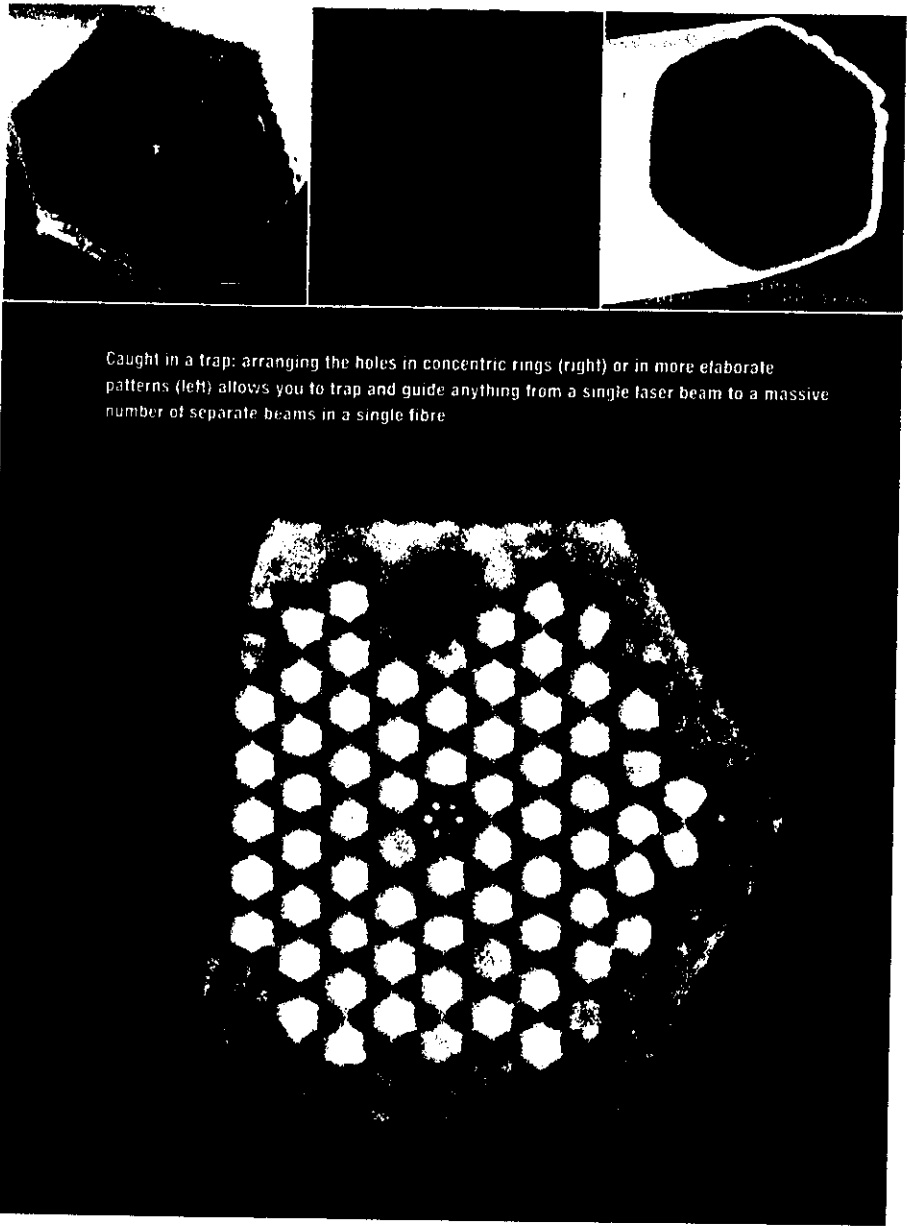
## 'With laser light, the hollow channels in the fibre will confine and guide atoms—a sort of atom hosepipe. As the light bounces along the core, it pushes the atoms along'

possibilities for delivering high-power laser light to cauterise tissue in microsurgery, for instance, or to slice up materials with great precision for engineering.

Higher power also makes the fibres ideal for telecommunications, since it means that fewer amplifiers will be needed along the cable to boost the signal for long-distance transmission. Optical signals must be amplified at regular intervals along the transmission line to compensate for losses through absorption and scattering. This creates technical problems when cables are laid on the seabed, for example. But greater power means the signals can survive for longer between boosts, and because amplifiers are prone to breakdown, fewer of them means fewer costly repairs of undersea cables.

Fibre lasers are already in use, but if they pumped out more power they would be far more useful. The power produced by a hollow-core fibre that carries light through the hole could be at least ten times as great as that from a silica-core fibre, upgrading 50-watt laser beams into the kilowatt region. "There are many applications waiting in the wings for the world's first 1-kilowatt single-mode fibre laser," suggests Russell. They might be used, for example, in cutting and welding tools for repairs to orbiting spacecraft—a kind of pocket light sabre.

Holey fibres can also be used to process light. Simply fill the hollow channels with a gas or liquid, and laser light would interact with it continuously as the light bounces down the fibre. A potential product of "filled" fibres is an all-optical switch. Such



Caught in a trap: arranging the holes in concentric rings (right) or in more elaborate patterns (left) allows you to trap and guide anything from a single laser beam to a massive number of separate beams in a single fibre

J. Knight, P. Russell & T. Birks

switches exist already, but the new fibres could overcome several of their limitations. All-optical switching allows light signals to be rerouted without the need for electronic control, which increases speed and reduces signal loss. It exploits the "optical Kerr effect"—when an intense burst of light triggers an increase in a material's refractive index. This can cause a pulse of light to jump tracks: above some threshold intensity, it leaps from one glass fibre to another when the two run side by side. In other words, a burst of light can be used to flick this switch in an optoelectronic circuit.

But the optical Kerr effect is very weak in glass—its "Kerr coefficient" is small—so the light pulse has to travel over a long distance through the fibre before the cumulative effect is big enough to induce

switching. In the holey fibres the effect could be made much stronger by filling the channels with a liquid such as methanol that has a higher Kerr coefficient. Then, says Russell, it might be possible to achieve switching over one metre of fibre rather than, as is typical at present, over half a kilometre of coiled glass fibre.

Perhaps most intriguing of all is the possibility of using the channels in a photonic crystal fibre as a pipe of light along which cold atoms could be sent. Researchers can use the momentum of photons in a laser beam to pick up small objects such as cells and move them about ("Spin doctors", *New Scientist*, 14 February 1998, p 34). Atoms can be moved about in a similar way. Tuning the energy of the light to one side of an element's atomic absorption line

forces these atoms to move into the bright areas of the beam; tuning it to the other side pushes them out of the light beam.

So Russell's team is collaborating with Kishan Dholakia and coworkers at the University of St Andrews in Scotland to use laser light and the hollow channels in the fibre to confine and guide atoms—a sort of atom hosepipe. The idea is simple: create a vapour of cold atoms and use light to guide the atoms one by one into the channels. Then as the laser beam bounces along the core, it pushes the atoms down the fibre. The atoms are attracted towards the charged glass walls of the channel, but the laser beam nudges them back to the centre of the hole. "They sort of rattle along the channels," says Dholakia.

Potential applications range from the separation of elements or isotopes—tuning the laser light to the right frequency will selectively transport specific atoms or isotopes down the pipe—to ultra-sensitive gravity meters, which would spot changes in gravity using interference. If you cool atoms to a whisker above absolute zero, they display their wavelike nature. When these "atom waves" meet, they generate interference fringes in much the same way that light beams can, but since atoms have more mass than photons, the spacing of these atom fringes is acutely sensitive to the gravitational field in which the atoms sit. Use atom hosepipes to bring beams of cold atoms together—as is done with light in an optical interferometer—and you can make measurements of minute changes in gravity. This could be useful for investigating the structure of the deep Earth, suggests Dholakia, or for detecting tiny changes in sea level.

Although all sorts of photonic materials are under development, most remain a long way from the market. Russell's fibres, on the other hand, could be put to use much sooner. And they should be easy to manufacture in bulk, says physicist Shawn Lin at Sandia National Laboratories in Albuquerque, New Mexico: "This means they should be cheap to produce." Several multinational companies involved in laser design, communications and laser machining have already beaten a path to Russell's door. "Given the level of interest," says Russell, "there is a good chance that the photonic crystal fibre will be commercialised within the next few years." Light sabres, optical computers and gravity detectors may follow in due course. Not bad for a material that's full of holes. □

Philip Ball is Consultant Editor of *Nature*

10-1





pected (that is,  $\pi$  out of phase). This difference becomes even more apparent when we compare the top insets in Fig. 3, A and B, which represent the calculated interferogram amplitudes in the absence of dephasing for the parameters obtained from fitting the data points (26).

The excited state coherence of the artificial "atom" studied here has a decoherence time of 40 ps, which is short compared with atomic coherence times, thus limiting the use of these particular QDs for quantum logic. However, very long electronic spin coherence in semiconductors has recently been measured (27). Furthermore, QD structures with stronger confinement are expected to have reduced coupling to phonons (28) and reduced spontaneous radiative emission (29), and may well have much longer intrinsic coherence times. In addition, doping of dots may result in isolated impurity states with long coherence times associated with more complex states of excitation such as demonstrated in atomic systems (30). Such progress should allow the use of more complicated sequences of control pulses during the coherence time, such as those necessary for performing quantum logic (5) or other coherently controlled processes.

The measurements show that we have successfully demonstrated coherent optical control of the quantum state of a single dot and thus have taken this technique to the ultimate quantum limit. We show that we can extend such an experiment to include more than one excited state and monitor the wave function as it oscillates between two orthogonal states by measuring the autocorrelation function. Finally, we show the feasibility of generating a target wave function by demonstrating control over the quantum mechanical phase of the superposition of states. This work establishes the basic tools for developing more sophisticated control and for creating a more complex wave function such as achieved in atomic systems.

Reference and Notes

1. A. P. Alivisatos, *Science* 271, 933 (1996).
2. K. Brunner *et al.*, *Phys. Rev. Lett.* 73, 1138 (1994); H. F. Hess *et al.*, *Science* 264, 1740 (1994).
3. D. Gammon *et al.*, *Science* 273, 87 (1996).
4. G. Schedelbeck, W. Wegscheider, M. Bichler, C. Abstreiter, *ibid.* 278, 1792 (1997); S. A. Empedocles and M. G. Bawendi, *ibid.*, p. 2114; D. Gammon *et al.*, *ibid.* 277, 85 (1997); J. Hasen *et al.*, *Nature* 390, 54 (1997); E. Dekel *et al.*, *Phys. Rev. Lett.* 80, 4991 (1998); L. Landin *et al.*, *Science* 280, 262 (1998).
5. S. Lloyd, *Science* 261, 1569 (1993); A. Barenco, D. Deutsch, A. Ekert, R. Jozsa, *Phys. Rev. Lett.* 74, 4083 (1995); A. Ekert and R. Jozsa, *Rev. Mod. Phys.* 68, 733 (1996).
6. A. Hache *et al.*, *Phys. Rev. Lett.* 78, 306 (1997).
7. P. C. M. Planken *et al.*, *Phys. Rev. B* 48, 4903 (1993).
8. R. N. Zare, *Science* 279, 1875 (1998); W. S. Warren, H. Rabitz, M. Dahleh, *ibid.* 259, 1581 (1993).
9. F. Wang, C. Chen, D. S. Elliot, *Phys. Rev. Lett.* 77, 2416 (1996).
10. D. M. Meekhof *et al.*, *ibid.* 76, 1796 (1996).
11. J. A. Yeazell and C. R. Stroud Jr., *ibid.* 60, 1494 (1988).

12. T. C. Weinsacht, J. Ahn, P. H. Bucksbaum, *ibid.* 80, 5508 (1998); *Nature*, in press.
13. M. U. Wehner, M. H. Ulm, D. S. Chemla, M. Wegener, *ibid.*, p. 1992.
14. P. G. Huggard *et al.*, *Appl. Phys. Lett.* 71, 2647 (1997).
15. A. P. Heberle, J. J. Baumberg, K. Kohler, *Phys. Rev. Lett.* 75, 2598 (1995); X. Marie *et al.*, *ibid.* 79, 3222 (1997).
16. D. Gammon *et al.*, *ibid.* 76, 3005 (1996).
17. D. Gammon, E. S. Snow, D. S. Katzer, *Appl. Phys. Lett.* 67, 2391 (1995).
18. N. H. Bonadeo *et al.*, *Phys. Rev. Lett.* 81, 2759 (1998).
19. S. V. Goupalov, E. L. Ivchenko, A. V. Kavokin, *J. Exp. Theor. Phys.* 86, 388 (1998).
20. N. F. Scherer *et al.*, *J. Chem. Phys.* 95, 1487 (1991).
21. H. Metiu and V. Engel, *J. Opt. Soc. Am. B* 7, 1709 (1990); J. T. Fourkas *et al.*, 6, 1905 (1989).
22. F. Spano, M. Haner, W. S. Warren, *Chem. Phys. Lett.* 135, 97 (1987).
23. V. Blanchet, C. Nicole, M.-A. Bouchene, B. Girard, *Phys. Rev. Lett.* 78, 2716 (1997).
24. U. Bockelmann, *Phys. Rev. B* 48, 17637 (1993).
25. M. M. Salour and C. Cohen-Tannoudji, *Phys. Rev. Lett.*

- 38, 757 (1977); L. D. Noordam, D. I. Duncan, T. F. Gallagher, *Phys. Rev. A* 45, 4734 (1992).
26. Because the X'- and Y'-oscillator strengths are different, complete cancellation is not observed at the nodes.
27. J. M. Kikkawa, I. P. Smorchkova, N. Samarth, D. D. Awschalom, *Science* 277, 1284 (1997); J. M. Kikkawa and D. D. Awschalom, *Phys. Rev. Lett.* 80, 4313 (1998).
28. U. Bockelmann and G. Bastard, *Phys. Rev. B* 42, 8947 (1990).
29. D. S. Citrin, *Phys. Rev. B* 47, 3832 (1993).
30. T. Mossberg, A. Flusberg, R. Kachru, S. R. Hartman, *Phys. Rev. Lett.* 42, 1665 (1979); B. Young, M. Kashevich, S. Chu, in *Atom Interferometry*, P. R. Berman, Ed. (Academic Press, New York, 1997).
31. We thank P. H. Bucksbaum and R. Merlin for stimulating discussions. Supported by U.S. Army Research Office, Air Force Office of Scientific Research, Office of Naval Research and NSF (Center for Ultrafast Optical Science). J.E. was supported by the Danish Research Council.

10 July 1998; accepted 16 September 1998

# Photonic Band Gap Guidance in Optical Fibers

J. C. Knight, J. Broeng,\* T. A. Birks, P. St. J. Russell

A fundamentally different type of optical waveguide structure is demonstrated, in which light is confined to the vicinity of a low-index region by a two-dimensional photonic band gap crystal. The waveguide consists of an extra air hole in an otherwise regular honeycomb pattern of holes running down the length of a fine silica glass fiber. Optical fibers based on this waveguide mechanism support guided modes with extraordinary properties.

Photonic band gap (PBG) structures offer the opportunity to design new optical properties into existing materials by wavelength-scale periodic microstructuring of the material morphology (1). In three-dimensionally periodic PBG materials, waves of certain frequencies cannot enter into or propagate through the material (1). In two-dimensionally periodic materials, there can be ranges of the propagation constant normal to the periodic plane ( $\beta$ ) where propagation is forbidden (2, 3). One potential application of such materials is a type of optical waveguide where light is confined by surrounding it with a band gap material (4). Two-dimensionally periodic structures in the form of long, fine silica fibers that have a regular array of tiny air holes running down their length (3, 5-8) constitute artificial two-dimensional "crystals" with lattice constants on the order of micrometers. We previously demonstrated an optical fiber waveguide based on total internal reflection from this periodic material—a waveguiding mechanism very similar to that in conventional optical fibers (albeit with some remark-

able features) (5-8). We now report the realization and demonstration of a far more radical optical fiber design, based on light confinement by the PBG effect.

Our fabrication process is related to that reported by Tonucci *et al.* (9) and involves stacking a few hundred solid silica rods and silica capillary tubes by hand in a hexagonal arrangement to form a fiber preform, which is then drawn down at a temperature of around 2000°C to a fiber with a diameter of about 40

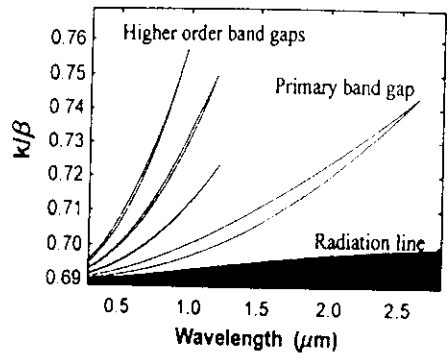


Fig. 1. Computed band gaps in the air-silica honeycomb lattice being discussed here. The parameters used in the computation were a nearest hole spacing of 1.9  $\mu\text{m}$  and an air hole diameter of 0.55  $\mu\text{m}$ .

Optoelectronics Group, Department of Physics, University of Bath, Claverton Down, Bath BA2 7AY, UK

\*Visiting from the Department of Electromagnetic Systems, Technical University of Denmark, 2800 Lyngby, Denmark.

$\mu\text{m}$ . The submicrometer-sized air holes in the final fiber are spaced by a few micrometers. Previous fibers were based on a simple hexagonal array of air holes, made by stacking tubes only. However, we did not observe band gap guidance in a hexagonal structure. Our attention switched to a honeycomb array of holes, which is known to show broader band gaps for in-plane (10) as well as for out-of-plane (11) propagation. Calculations with the plane-wave method show that for realizable scales of structures and air-filling fractions, we expect to observe band gaps at visible light frequencies in ideal structures (11). This is true for out-of-plane propagation, even though the air-filling fraction and refractive index contrast are too small to observe band gaps in the periodic plane (3). Calculations for the parameter range investigated experimentally (Fig. 1) show that band gaps appear for a wide range of wavelengths for values of  $k/\beta$  above the "radiation line," below which one expects to find total reflection from the structure ( $k$  is the vacuum wavenumber). To create a waveguiding "core," one needs to introduce a "defect" into the crystal structure—a localized region with optical properties different from those of the fully periodic structure. This core is surrounded by a "cladding"—the fully periodic region—the purpose of which is to confine the light within the core. Within a properly designed defect, light can propagate with a value of  $\beta$  that falls within the band gap of the surrounding cladding material. Further numerical modeling shows that by introducing an "extra" air hole into a single lattice site within the structure, localized guided modes can appear within the band gaps (11), in certain wavelength ranges.

Experimentally, the honeycomb structure is created by individual positioning of rods as well as capillaries in the stacking stage. An extra air hole is introduced into the center of the honeycomb pattern by replacing a single solid rod with a hollow capillary. This "low-index defect" ensures that there is no possibility of

waveguiding by total internal reflection (6). Because the capillaries and rods are circular in cross section but are stacked into a hexagonal array, there are small air gaps—interstitial holes—that are formed within the structure. These interstitial holes collapse during the fabrication process under surface tension forces, surviving near to the center of the fiber after they have disappeared elsewhere because of the extra forces that result from the presence of the extra air hole (Fig. 2). They appear to play an important role in the optical properties of the samples.

We observe a guided mode in the core of the structure (Figs. 3 and 4). The observed effects are highly sensitive to the precise structure and scale of the core and cladding and are not observed for a range of fibers with slightly different parameters. Small variations in the structure of the fiber over lengths on the order of 10 cm (which are due to variations in conditions within the furnace during fiber drawing) cause the waveguiding properties to change substantially or even to disappear completely. Nonetheless, we can reproducibly fabricate samples that look like that in Fig. 2 and that demonstrate the same optical effects. We are as yet unable to quantitatively model the fabricated structures (Fig. 2). The air holes in our samples are not round (as in our calculations) but are distorted by the effects of surface tension. More problematic are the interstitial air holes within the "core" of the fiber, which have not been modeled accurately because they are so small. However, the band gap plot for the corresponding ideal structure (Fig. 1) does show several band gaps at the visible wavelengths at which we observe waveguiding. The exact frequencies at which theory predicts confined waveguide modes depend on the design of the defect as well as that of the periodic structure, and their determination requires precise modeling of the structure under study.

To demonstrate that these features (Fig. 3) are due to a single guided mode, we focused

visible laser light onto one end of lengths (about 50 mm) of the fiber using a high-power objective lens. Near-field and far-field patterns at the output end were observed (Fig. 4). The relative intensities of the six lobes in the near-field pattern (Fig. 4A) remained fixed as the input coupling was varied and are nearly equal. No other mode field patterns are observed confined to the defect region. The guided mode is tightly confined to a small silica region that is directly connected to a much larger one (Figs. 2 and 4A), demonstrating the unusual nature of the waveguiding process.

The six-lobed far-field pattern (Fig. 4B) remains fixed and unchanging with input coupling, except that the overall intensity of the pattern is extremely sensitive to the precise input coupling. The far-field pattern diverges at an angle of about  $25^\circ$  with respect to the fiber axis, and a similar angle was used for the input coupling. It is worth remarking that the observed far-field intensity pattern (Fig. 4B) can only arise from the near-field intensity pattern (Fig. 4A) by postulating that the fields in opposite lobes of the field pattern have opposite signs. The computed guided-mode profile presented in (11) showed no such phase reversals. However, we found that modal field patterns with a similar symmetry to that observed experimentally can be computed in higher order band gaps. This is consistent with the observation that the mode presented in (11) was computed for a wavelength of  $1.5 \mu\text{m}$ , whereas the mode observed here is guided at about one-third of that wavelength in a structure with a similar scale. The fiber shown (Figs. 2 and 3) guided light for wavelengths between at least 458 and 528 nm (argon-ion laser lines). No confined mode could be observed at a wavelength of 633 nm (helium-neon laser), despite exhaustive attempts. Modal field patterns similar to that in Fig. 4A could be observed by

**Fig. 2.** Scanning electron micrograph of the surface of a cleaved PBC fiber waveguide 5 cm long. The parameters of the fiber shown are a diameter of  $36 \mu\text{m}$ , a nearest air hole spacing of  $1.9 \mu\text{m}$ , and an air-filling fraction in the periodic region of 5.3%. The central air hole is  $0.8 \mu\text{m}$  in diameter and is surrounded by six interstitial holes of diameter of about 75 nm. This fiber guides light at between at least 458 and 528 nm, but not at 633 nm.

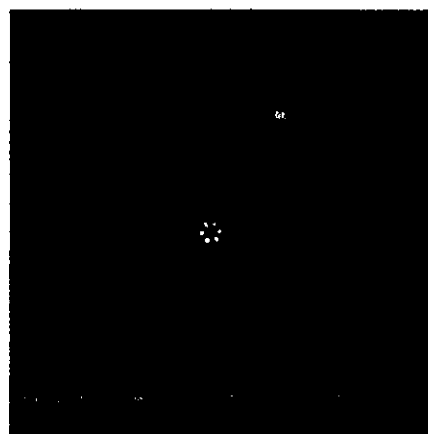
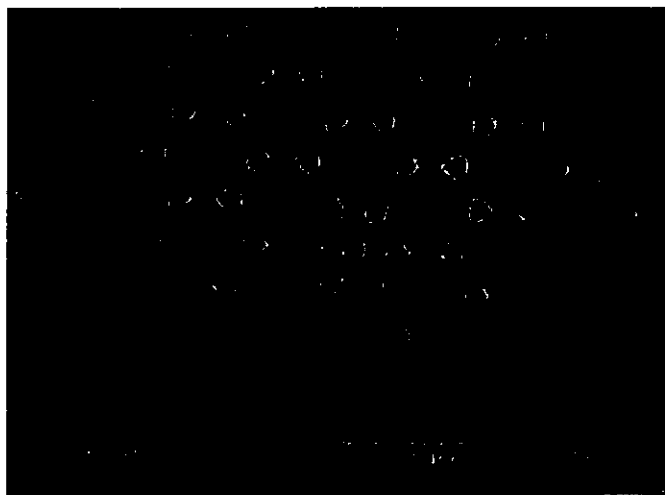


**Fig. 3.** Optical micrograph of a PBC fiber. The fiber is illuminated from below with a white light source, and index-matching fluid on the sides of the fiber is used to strip off some of the light in cladding modes. The fiber shown guides blue and green light in the low-index core.

focusing the light onto the core region, but they were always accompanied by substantial light that filled the whole fiber. No indication of a far-field pattern like that in Fig. 4B was observed. A relatively sharp transition—with wavelength—from a confined to a nonconfined mode is expected to be a feature of this type of waveguiding.

Some qualitative insight into the nature of the guided modes being described here can be gained by considering the honeycomb structure shown in Fig. 2 as a large number of independent silica strands that are strongly coupled together. Each isolated strand would support many distinct waveguide modes, each with a different value of  $\beta$ . When a large number of strands are placed in close proximity, they couple together, and each mode of the single strand opens up into a passband of modes of the

composite structure, each passband now covering a range of  $\beta$  values. The passbands are separated by band gaps. The central silica strand (the "core"), which has a large hole in the middle and six smaller interstitial holes disposed symmetrically around it, would, if isolated, support a different set of waveguide modes because of its different morphology. If the  $\beta$  value of one of these modes falls within one of the bands of modes of the periodic cladding, this mode of the core will be coupled to the extended modes of the periodic cladding. However, if one of the modes of the core region falls in between the passbands of the fully periodic cladding region, then this mode is localized within the core and forms a PBG guided mode. Thus, at some wavelengths, there is a mode trapped within the core (the "guided mode"), whereas at other wavelengths the modes are extended and fill the fiber. A possible reason for the importance of the hard-to-model interstitial holes within the core is that they will affect the  $\beta$  values of the core modes, drawing one of these into the band gap of the continuous material.

Band gap guided modes are expected to have quite different properties to the modes of conventional optical waveguides. For example, we observe that the fiber being described here is strongly birefringent, with a beat length on the order of millimeters (that is, the different polarization modes have rather different propagation constants). We conclude that small imperfections in the structure can have a large effect on the propagation constant of the trapped modes. The dispersion of these fibers is likely to be far

larger than that observed in any previous optical fiber waveguide for the correct choice of fiber design parameters. Other properties of these fibers (for example, their susceptibility to bend loss) remain to be investigated, and even more counterintuitive designs (a silica-air waveguide where the light is trapped within an air hole, for example) are possible. This is only the first of a very broad class of fiber guided modes, which show great technological promise and are of substantial scientific interest.

References and Notes

1. E. Yablonovitch, *J. Opt. Soc. Am. B* **10**, 283 (1993).
2. P. St. J. Russell, D. M. Atkin, T. A. Birks, P. J. Roberts, in *Microcavities and Photonic Bandgaps: Physics and Applications*, J. G. Rarity and C. Weisbuch, Eds. (Kluwer, Dordrecht, Netherlands, 1996), pp. 203–218.
3. T. A. Birks, P. J. Roberts, P. St. J. Russell, D. M. Atkin, T. J. Shepherd, *Electron. Lett.* **31**, 1941 (1995).
4. J. D. Joannopoulos, R. D. Meade, J. N. Winn, *Photonic Crystals: Molding the Flow of Light* (Princeton Univ. Press, Princeton, NJ, 1995).
5. J. C. Knight, T. A. Birks, P. St. J. Russell, D. M. Atkin, *Opt. Lett.* **21**, 1547 (1996) [errata: *ibid.* **22**, 484 (1997)].
6. T. A. Birks, J. C. Knight, P. St. J. Russell, *ibid.*, p. 961.
7. J. C. Knight, T. A. Birks, P. St. J. Russell, J.-P. de Sandro, *J. Opt. Soc. Am. A* **15**, 748 (1998).
8. J. C. Knight, T. A. Birks, R. F. Cregan, P. St. J. Russell, J.-P. de Sandro, *Electron. Lett.* **34**, 1347 (1998).
9. R. J. Tonucci, B. L. Justus, A. J. Campillo, C. E. Ford, *Science* **258**, 783 (1992).
10. D. Cassagne, C. Jouanin, D. Bertho, *Phys. Rev. B* **53**, 7134 (1996).
11. J. Broeng *et al.*, *Opt. Commun.* **156**, 240 (1995).
12. Supported by the Defence Evaluation and Research Agency, Malvern, UK, and the UK Engineering and Physical Sciences Research Council. Donation of fiber drawing equipment from BT Research Laboratories, Martlesham, UK, is gratefully acknowledged.

25 August 1998; accepted 14 October 1998

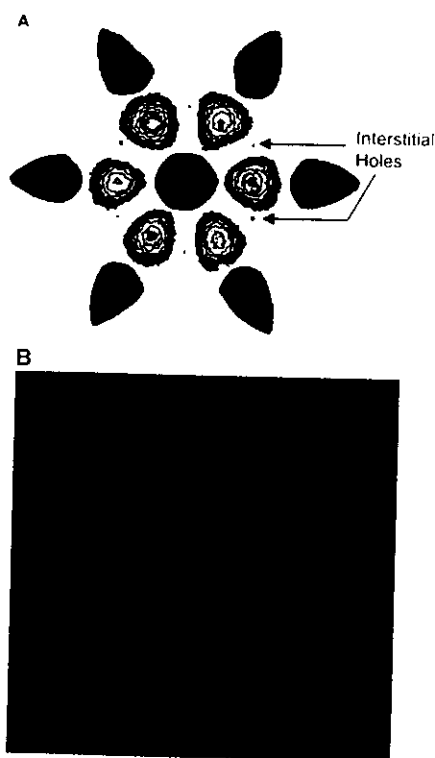


Fig. 4. Near- and far-field patterns observed with laser light (wavelength = 458 nm) to excite the guided mode in a 50-mm length of fiber. (A) A contour map of the observed near-field pattern (color) superimposed on a scanning electron micrograph showing the fiber morphology (black). The interstitial holes in the structure (which appear between the lobes of the guided mode) are clearly visible. The guided-mode field intensity outside the first ring of air holes is at least two orders of magnitude less than the peak intensity shown. (B) A photograph of the observed far-field pattern. The pattern was recorded by allowing the diffracting light emerging from the end of the fiber to fall onto a paper screen, which was then imaged onto photographic film from the back. The orientation of the six main lobes in the far-field pattern is the same as those in the near field.

## Direct Demonstration of Milk as an Element of Archaeological Economies

Stephanie N. Dudd and Richard P. Evershed\*

The stable carbon isotope ( $\delta^{13}\text{C}$ ) compositions of individual fatty acid components of remnant fats preserved in archaeological pottery vessels show that dairying was a component of archaeological economies. Characteristic  $\delta^{13}\text{C}$  values arise from biases in the biosynthetic origins of the  $\text{C}_{18,0}$  fatty acids in milk and adipose fat. Milk and adipose fat from animals raised on similar pastures and fodders have distinct isotopic signatures.

Although sheep are thought to have been domesticated in the Near East at ~9000 B.C. and cattle and goats were domesticated at ~7000 B.C., there is no direct evidence that they were milked. Pictorial and written

records from the Sahara, Egypt, and Mesopotamia show that dairying had begun there by 4000 to 2900 B.C. (1). Evidence of dairying during the prehistoric period in Britain has been limited solely to secondary evidence associated with the procurement and use of dairy products, such as putative ceramic "cheese" strainers, dating from 4500 B.C. (2, 3). Faunal studies have suggested that a high neonatal cull and a bias in the adult cull in domestic ruminant animals may indicate dair-

Organic Geochemistry Unit, School of Chemistry, University of Bristol, Cantock's Close, Bristol, BS8 1TS, UK

\*To whom correspondence should be addressed. E-mail: r.p.evershed@bristol.ac.uk



# 1423

Biological Weapons Convention: A call from U.S. industry

## EDITORIAL

- 1417 **Animal Rights: Reaching the Public**  
P. M. Conn and J. Parker

## LETTERS

- 1419 **Declining Fertility** J. Mitteldorf, S. W. Mosher  
**Laboratory Safety** C. H. Collins and D. A. Kennedy  
**Patenting Genomic Technologies** D. S. Block and D. J. Curran  
**Response** R. S. Eisenberg and M. Heller  
**Corrections and Clarifications**

## POLICY FORUM

- 1423 **BIOLOGICAL WARFARE: Strengthening the Biological Weapons Convention**  
T. P. Monath and L. K. Gordon

## BOOKS AND NEW MEDIA

- 1424 **SCIENCE AND CULTURE: *The Last Dinosaur Book: The Life and Times of a Cultural Icon***  
W. J. T. Mitchell, reviewed by P. Dodson
- 1425 **ARCHAEOLOGY: *Monte Verde A Late Pleistocene Settlement in Chile. Vol. 2: The Archaeological Context and Interpretation***  
T. D. Dillehay, reviewed by D. K. Grayson

## PERSPECTIVES

- ▼ 1426 **PALEOCLIMATE: The Sulfur Cycle and Atmospheric Oxygen** R. A. Berner and S. T. Petsch
- ▼ 1428 **EVOLUTION: Molecular Origin of Species**  
M. Nei and J. Zhang
- ▼ 1429 **QUANTUM DOTS: Controlling Artificial Atoms** F. H. Julien and A. Alexandrou
- ▼ 1430 **DNA REPLICATION: Bringing the Mountain to Mohammed** R. Losick and L. Shapiro

## REVIEW

- 1432 **EVOLUTION: Experimental Evolution of Parasites** D. Ebert

## TECH.SIGHT

- 1436 **COMPUTATIONAL BIOLOGY: Hidden Models in Biopolymers** M. Amitai
- 1438 **TechSightings**

## ONLINE PRODUCTS AND FEATURES

### SCIENCE

THE JOURNAL ONLINE  
[www.sciencemag.org](http://www.sciencemag.org)

### SCIENCENOW

DAILY NEWS SERVICE  
[www.sciencenow.org](http://www.sciencenow.org)

### NEXT WAVE

WEEKLY CAREER UPDATES  
[www.nextwave.org](http://www.nextwave.org)

### GRANTSNET

RESEARCH FUNDING DATABASE  
[www.grantsnet.org](http://www.grantsnet.org)

### NEUROAIDS

EXPERIMENTAL WEB SITE  
[www.sciencemag.org/NAIDS](http://www.sciencemag.org/NAIDS)

# 1476

Guiding light: More than pretty patterns



- 1490 **Role of Mouse Cryptochrome Blue-Light Photoreceptor in Circadian Photoresponses**  
R. J. Thresher, M. Hotz-Vitaterna, Y. Miyamoto, A. Kazantsev, D. S. Hsu, C. Petit, C. P. Selby, L. Dawut, O. Smithies, J. S. Takahashi, A. Sanzar
- 1494 **Induction and Evasion of Host Defenses by Type 1-Piliated Uropathogenic *Escherichia coli*** M. A. Mulvey, Y. S. Lopez-Boado, C. L. Wilson, R. Roth, W. C. Parks, J. Heuser, S. J. Hultgren
- 1497 **Requirement for p53 and p21 to Sustain G<sub>2</sub> Arrest After DNA Damage** F. Bunz, A. Dutriaux, C. Lengauer, T. Waldman, S. Zhou, J. P. Brown, J. M. Sedivy, K. W. Kinzler, B. Vogelstein
- ▼ 1501 **A Rapidly Evolving Homeobox at the Site of a Hybrid Sterility Gene** C. T. Ting, S.-C. Tsaur, M.-L. Wu, C.-I. Wu
- 1504 **Local GABA Circuit Control of Experience-Dependent Plasticity in Developing Visual Cortex** I. K. Hensch, M. Fagioli, N. Mataga, M. P. Stryker, S. Baekkeskov, S. F. Kash

- 1508 **Synaptic Segregation at the Developing Neuromuscular Junction** W.-B. Gan and J. W. Lichtman
- 1511 **The Role of Far1p in Linking the Heterotrimeric G Protein to Polarity Establishment Proteins During Yeast Mating** A.-C. Butty, P. M. Pryciak, L. S. Huang, I. Herskowitz, M. Peter
- ▼ 1516 **Localization of Bacterial DNA Polymerase: Evidence for a Factory Model of Replication** K. P. Lemon and A. D. Grossman

## TECHNICAL COMMENTS

How Pervasive Is "Fishing Down Marine Food Webs"? J. F. Caddy, J. Csirke, S. M. Garcia, R. J. R. Grainger  
**Response** D. Pauly, R. Froese, V. Christensen

[www.sciencemag.org/cgi/content/full/282/5393/1383a](http://www.sciencemag.org/cgi/content/full/282/5393/1383a)



# 1494

*E. coli* in the urinary tract

Change of address: [www.sciencemag.org](http://www.sciencemag.org). E-mail: [sciencemag@aaas.org](mailto:sciencemag@aaas.org). Postmaster: Send change of address to [sciencemag@aaas.org](mailto:sciencemag@aaas.org). Single copy sales: Single copies are prepared on request and postage paid rates are available. Authorization to photocopy items for internal or personal use, or the internal or personal use of specific clients, is granted by AAAS for libraries and registered users of the Copyright Clearance Center (CCC) Transactional Reporting Service, provided that the base fee of \$10.00 per copy is paid directly to CCC, 222 Rosewood Drive, Danvers, MA 01923. For those organizations that have been granted a photocopy licence by CCC, a separate system of payment has been arranged. The fee code for users of the CCC Transactional Reporting Service is 0022-0745/98 \$10.00.

Reprint Series  
3 September 1999, Volume 285, pp. 1537-1539

P13

**Science**

## **Single-Mode Photonic Band Gap Guidance of Light in Air**

R. F. Cregan,<sup>1</sup> B. J. Mangan,<sup>1</sup> J. C. Knight,<sup>1</sup> T. A. Birks,<sup>1</sup>  
P. St. J. Russell,<sup>1\*</sup> P. J. Roberts,<sup>2</sup> and D. C. Allan<sup>3</sup>

# Single-Mode Photonic Band Gap Guidance of Light in Air

R. F. Cregan,<sup>1</sup> B. J. Mangan,<sup>1</sup> J. C. Knight,<sup>1</sup> T. A. Birks,<sup>1</sup>  
P. St. J. Russell,<sup>1\*</sup> P. J. Roberts,<sup>2</sup> D. C. Allan<sup>3</sup>

The confinement of light within a hollow core (a large air hole) in a silica-air photonic crystal fiber is demonstrated. Only certain wavelength bands are confined and guided down the fiber, each band corresponding to the presence of a full two-dimensional band gap in the photonic crystal cladding. Single-mode vacuum waveguides have a multitude of potential applications from ultrahigh-power transmission to the guiding of cold atoms.

To be guided along an optical fiber, light must be confined to a central core by reflection from the cladding that surrounds it. All conventional optical fibers guide light by total internal reflection (TIR), which requires that the core have a higher refractive index than the cladding (1). TIR is perfect in that it causes no loss other than the intrinsic absorptive and scattering losses of the materials themselves. Even these losses (and other material deficiencies) could be largely avoided if the light filled a hollow core. However, this is not possible with TIR, because no solid cladding material exists with a refractive index lower than that of air. Existing hollow fibers (2) use external reflection and are thus inherently leaky; furthermore, they invariably support many different transverse modes; that is, they are highly multimode.

We have developed a fiber in which light can be strictly guided, without leakage, in a hollow core. Light in certain well-defined wavelength bands is trapped in the air by a full two-dimensional photonic band gap (PBG) of the cladding instead of by TIR (3, 4), and it can be guided in a single mode. Here we describe the fabrication and characterization of the fiber and the spatial and spectral properties of the guided modes and compare the results to theoretical models.

The requisite numerical computations for designing a hollow PBG fiber are slow and laborious, and no inverse computational methods exist. The intrinsic need for a two-dimensional (2D) PBG requires that the fiber cladding contain a near-perfect periodic array of air holes (the photonic crystal) with a high air-filling fraction and a small pitch (the distance between adjacent holes in the lattice). Our early photonic crystal fibers (PCFs) had solid cores and guided light by TIR (5, 6). More recently we demon-

strated PBG guidance in a silica PCF with a honeycomb array of air holes (7); however, the light was evanescent in the air, so the observed guided mode was concentrated in the silica surrounding the extra air hole at the core. This appears to be a fundamental limitation of the honeycomb design.

The wave vector component along the waveguide, known as the propagation constant  $\beta$ , determines whether light propagates or is evanescent in any part of the guide. If  $\beta < kn$ , the light propagates at an angle  $\theta$  to the axis in a material of index  $n$ , where  $\beta = kn \cos \theta$  and  $k$  is the vacuum wave constant. If  $\beta > kn$ ,  $\theta$  is imaginary and the light is evanescent. A 1D planar waveguide geometry (Fig. 1) illustrates the different ways in which light can be strictly confined in dielectric waveguides. Conventional TIR, in which the index  $n_1$  of the core is

greater than index  $n_2$  of the cladding, ensures the existence of a range of  $\beta$  where light is propagating in the core while being evanescent in the cladding (Fig. 1A).

In contrast, light can be confined between two multilayer dielectric stacks in a core of arbitrary refractive index (4), if the stacks have a PBG for a range of  $\beta$  at a given optical frequency. We identified two regimes of PBG guidance. In the first (Fig. 1B), light propagates ( $\beta < kn_1$ ) in the layers of high index  $n_1$ , but is evanescent ( $\beta > kn_2$ ) in the layers of low index  $n_2$ . The high-index layers act as individual TIR waveguides, supporting bound modes at specific values of  $\beta = \beta_m$ . Resonant tunneling between adjacent high-index layers permits the leakage of light through them, provided  $\beta$  lies within the pass bands that open up around each  $\beta_m$ . The widths of the pass bands depend on the strength of coupling between the layers. Between the pass bands lie band gaps; if a high-index core layer with a different (maybe smaller) width supports a mode with  $\beta$  inside a band gap, it is not resonant with the other layers and light leakage by tunneling is frustrated. The mode is thus strictly guided by the frustrated tunneling form of PBG. In the second regime of PBG guidance (Fig. 1C), light can propagate in all layers ( $\beta < kn_2$ ). Band gaps occur at the Bragg condition as a result of multiple scattering and interference, leading to the Bragg form of PBG guidance.

In both forms of PBG guidance the refractive index of the core can be chosen much more

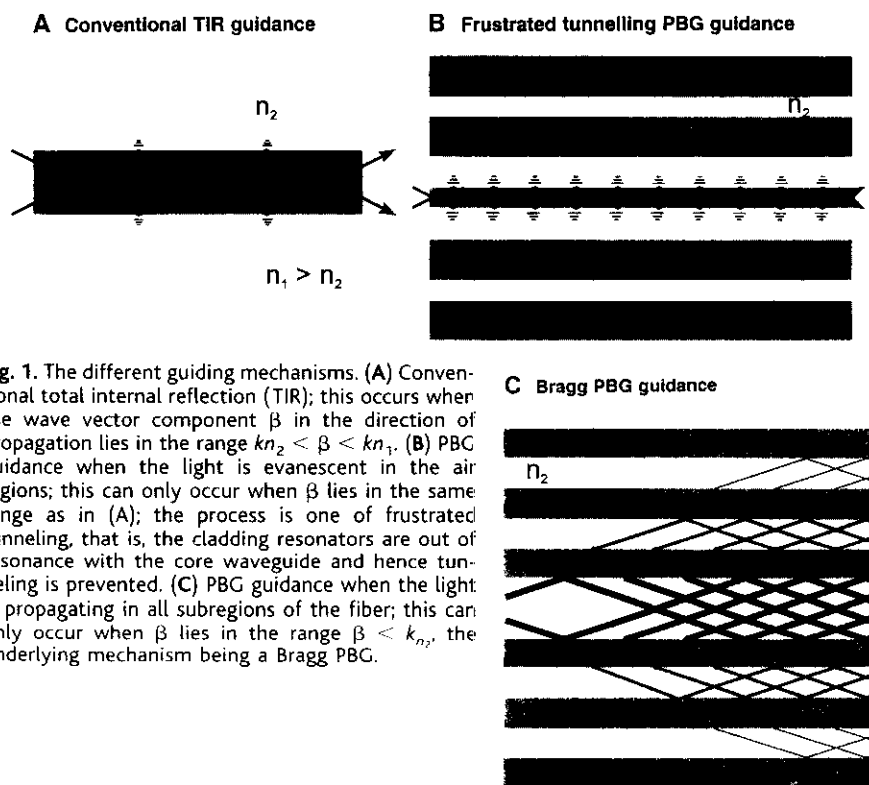


Fig. 1. The different guiding mechanisms. (A) Conventional total internal reflection (TIR); this occurs when the wave vector component  $\beta$  in the direction of propagation lies in the range  $kn_2 < \beta < kn_1$ . (B) PBG guidance when the light is evanescent in the air regions; this can only occur when  $\beta$  lies in the same range as in (A); the process is one of frustrated tunneling, that is, the cladding resonators are out of resonance with the core waveguide and hence tunneling is prevented. (C) PBG guidance when the light is propagating in all subregions of the fiber; this can only occur when  $\beta$  lies in the range  $\beta < kn_2$ , the underlying mechanism being a Bragg PBG.

<sup>1</sup>Optoelectronics Group, University of Bath, Claverton Down, Bath BA2 7AY, UK. <sup>2</sup>Defence Evaluation and Research Agency Malvern, St. Andrews Road, Malvern, Worcs WR14 7HR, UK. <sup>3</sup>Corning Incorporated, Corning, New York 14831, USA.

\*To whom correspondence should be addressed. E-mail: pypsjr@bath.ac.uk

freely than in TIR guidance, because the PBG conditions depend only on the properties of the cladding stacks. Guided modes can exist with mode indices  $\beta/k$  that are lower than the mean index of the stacks (the frustrated tunneling PBG case) or even lower than the lowest index of the stacks (the Bragg PBG case), conferring extra design freedom on PBG compared with TIR guidance and allowing confinement within a hollow core. To the best of our knowledge, every type of conventional low-loss 2D waveguide so far reported uses TIR as the guidance mechanism [including our own "endlessly single-mode" PCFs (6)].

PBG guidance in a fiber requires the existence of a 2D PBG over a range of  $\beta$  values in whichever materials system is used. Although we achieved this with frustrated tunneling PBG guidance in our silica-air honeycomb PCF (7), it is clear (8) that an even greater breakthrough would be achieved if the fiber guided by means of a Bragg PBG, for this would permit the concentration of optical power in air. Such a "vacuum guide" would have many of the desirable features of an empty metal-clad micro-

wave channel guide, including the ability to support extremely high power densities without breakdown, and it would have the potential to push the threshold intensities for stimulated Raman and Brillouin scattering (among other nonlinear effects) up to extremely high levels.

We have shown that simple triangular lattices of air holes in silica (index contrast 1:1.46) can have full 2D PBGs in the Bragg regime of  $\beta$  values (that is,  $\beta < k$ ) if the air-filling fraction is relatively high (3). Theory fails to predict full PBGs in silica-air honeycomb PCFs in the Bragg PBG regime, but this is perhaps not surprising because the honeycomb fiber has a higher proportion of silica and so is less likely to have PBGs at low values of  $\beta/k$ .

The method of fabricating an air-guiding PBG fiber follows our previously reported procedure for PCFs (5, 9). Tubes of silica glass are pulled down to capillary canes on a fiber-drawing tower. These canes typically have external diameters of the order of 1 mm. The PCF preform is constructed by stacking together by hand several hundred capillary canes to form the required crystal structure on a macroscopic scale. The entire stack is then held together while being fused and drawn down into fiber by an optical fiber-drawing tower. A typical fiber diameter is 40 to 100  $\mu\text{m}$ , the total collapse ratio being of the order of  $10^4$ . The final fiber cladding consists of a triangular array of air holes in silica, with interstitial holes that result from stacking circular capillaries. The fraction of air in this part of the fiber needs to be relatively large for the fiber to exhibit a sufficiently broad band gap—typically more than about 30% by volume.

The fiber core was formed by including a larger air hole in the center of the preform. We have studied fibers where this larger hole had an area of one or seven unit cells of the cladding material. In each case, the hole was created by leaving out the appropriate number of canes from the center of the preform stack. The whole

structure was then fused and pulled into fiber. Of the resulting fibers, those formed by omission of just a single cane did not guide modes in the air (at least not at visible wavelengths). From this point on we restrict our discussion to fibers with a seven-unit-cell air core (Fig. 2).

We carried out initial characterization by holding  $\sim 3$ -cm-long samples vertically, illuminating them from below with white light (using a tungsten halogen lamp), and observing the light transmitted through them in an optical microscope (Fig. 3). The central air core is filled with a single lobe of colored light, its transverse profile being smooth, peaked in the center, and falling off to very low intensities at the glass-air boundary. A significant amount of white light is present in the periodic cladding, and it appears colorless in comparison with the mode trapped in the core. Different colors of the vacuum-guided mode were seen, depending on the overall fiber size and the drawing conditions used. The precise color was sometimes hard to assign by eye, and in some cases appeared to be a mixture of different colors, for example red and blue. For appropriate excitation with the white light source, a few samples supported a similarly colored two-lobed mode, which we attribute to a second guided mode falling in the same band gap as the first.

The transmission spectra through the air core of lengths of fiber were measured by linking the microscope by means of a conventional multimode fiber to an optical spectrum analyzer. The spectral dependence of the waveguiding in the air hole (Fig. 4) demonstrated that several well-defined bands of transmission are present, covering the whole visible spectrum and extending into the infrared. Within each transmission band, the losses are small (over fiber lengths of several centimeters) or zero, whereas between these bands the losses are much larger, as expected in the absence of PBG effects (10). We attribute each of these bands to a full 2D PBG. Because the pitch of the crystal is large in

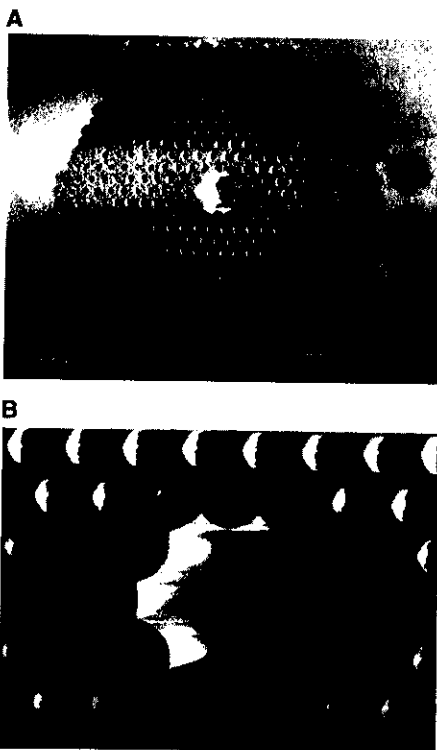


**Fig. 2.** (A) Scanning electron micrograph of the cleaved end-face of a typical vacuum-guiding fiber. The external diameter of the fiber is 105  $\mu\text{m}$  (measured across the flat faces). The solid canes around the outside of the fiber are an aid to the fabrication. This fiber guided light (over lengths of at least several tens of centimeters), as illustrated in Figs. 3 and 4. (B) Detail of the fiber illustrated in (A). The air-filling fraction in the cladding (including the interstitial holes) is  $\sim 39\%$  and the pitch is 4.9  $\mu\text{m}$ . The core has a diameter of 14.8  $\mu\text{m}$  (measured across the largest dimension).

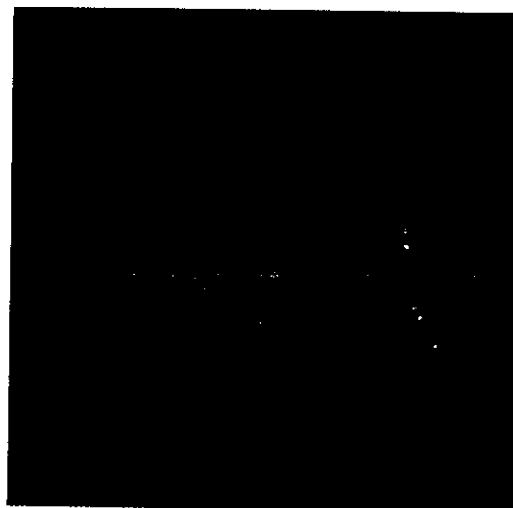


**Fig. 3.** Optical micrograph of the field intensity pattern at the exit face of a  $\sim 3$ -cm-long piece of fiber for white light excitation at the entrance face. White light is in the cladding regions, and the isolated and brightly colored vacuum-guided mode is in the center. Complete removal of cladding modes is difficult because of the incoherent illumination and the relatively large air holes in the structure, but they have been much reduced in the picture (without affecting the guided mode) by the application of index-matching liquid to the sides of the fiber. The effects of chromatic dispersion of the objective lens, structural features on the flat fiber surface, and the color response of the photographic film account for other minor colored features on the fiber end-face.

comparison with the wavelength, the PBGs responsible for the guidance are of high order. By selecting lengths of fiber that had been found to guide light at appropriate wavelengths, we excited this mode using laser sources. The laser light guided in the air core formed a stable, smoothly varying, single-lobed pattern in the far field. Fibers that have maxima in their transmission spectra at a particular laser wavelength guide such laser light in the core over lengths of several tens of centimeters (corresponding to hundreds of thousands of optical wavelengths). The length is presently limited by fluctuations in the fiber parameters, which cause the wavelengths of the guided modes to vary along the length of fiber. Although the short lengths of fiber that we have available preclude systematic study of losses, we transmitted 35% of a laser beam in the guided mode over a 40-mm length of fiber. The biggest contribution to the overall losses in that experiment was the input coupling efficiency. In other fibers that do not support guided modes at the laser wavelength, laser light coupled into the fiber in exactly the same way leaked entirely into the cladding after propagating only a few millimeters, as expected in the absence of PBG effects (10). By incorporating a guiding length of fiber into one arm of a Mach-Zehnder interferometer, we confirmed that the laser light transmitted through the guiding core has a high degree of spatial coherence, giving high-visibility fringes at the interferometer output. This would not be the case if there were many waveguide modes excited in the fiber core.

We observed such confined modes in a variety of samples with similar pitches to

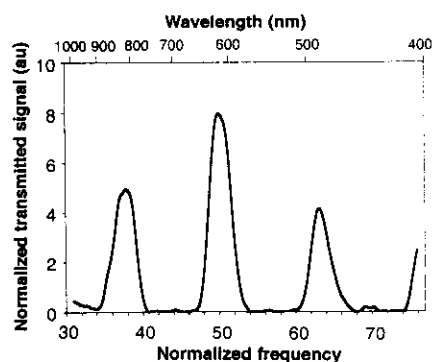


Fig. 4. Intensity spectrum of the light transmitted through the air core, plotted against normalized frequency  $k\Lambda$  and wavelength  $\lambda$ , through a fiber excited with white light. Low-loss transmission bands, widths of  $\sim 3$  frequency units, are separated by regions of much higher loss. The measurement is limited by the low spectral intensity of the white light source in the ultraviolet wavelength region (au, arbitrary units). The spectrum was recorded with a resolution of 10 nm. The relative normalized scales of the different transmission bands reflect the different coupling efficiencies to and from the guided mode at the widely varying wavelengths, and possibly the existence of a second mode in some band gaps.

those in Figs. 2 and 3 and with air-filling fractions in a range from just more than 30% to almost 50%. Theoretical modeling of these structures is difficult and slow because of the very large values for the normalized frequencies (see Fig. 4). Our initial computations of the band structure revealed the presence of narrow band gaps above the light line in this range of frequencies and for the sample parameters studied. Further comparison with the experimental results will require that the presence of the large air hole be modeled, which will take some time and might require the development of new theoretical tools.

It is useful to consider why it is that PCFs with similar cladding parameters but with a defect formed by omitting just a single capillary have not been found to support guided modes. The number of guided modes that a conventional fiber can support is determined by the core-cladding refractive index difference and the size of the core. This follows fundamentally from state-space arguments closely analogous to well-known density-of-states calculations in solid state physics and leads to the result that the approximate number of spatial modes in a conventional fiber is as follows (1):

$$N_{\text{conv}} = \frac{k^2(n_1^2 - n_2^2)r_{\text{co}}^2}{4} \quad (1)$$

where  $r_{\text{co}}$  is the core radius and  $n_1$  and  $n_2$  are the core and cladding indices. (There are of course two polarization states per spatial mode.) In a hollow-core PCF, a similar expression may be derived for the approximate number of spatial modes present in the hollow core:

$$N_{\text{PBG}} = \frac{(\beta_H^2 - \beta_L^2)r_{\text{co}}^2}{4} \quad \text{or} \\ = \frac{(k^2n_1^2 - \beta_L^2)r_{\text{co}}^2}{4} \quad (2)$$

where  $\beta_H$  and  $\beta_L$  are the upper and lower edges of the PBG at fixed optical wavelength, and the second expression applies if the upper PBG edge extends beyond the maximum core wave vector, that is, if  $k^2n_1^2 < \beta_H^2$ . Theory shows that, for a typical triangular array of air holes in silica, the photonic band gap width  $\Delta\beta = \beta_H - \beta_L$  is a small fraction of its average position  $\beta_{\text{av}} = (\beta_H + \beta_L)/2$ . For example, with the data published in (3), at  $\beta_{\text{av}}\Lambda = 9$ ,  $\Delta\beta\Lambda = 0.2$ , and taking  $r_{\text{co}} = \Lambda/2$  for a single missing cane ( $\Lambda$  is the interhole spacing), the expected number of spatial modes is 0.23, making it unlikely that any air-guided mode will be seen. On the other hand, if seven canes are removed, the hollow core area is increased by a factor of 7, the core radius by  $\sqrt{7}$ , and the expected number of spatial modes becomes 1.61, suggesting that a seven-cane hollow core will support at least a single transverse mode (two polarization states) and perhaps a second transverse mode. These predictions are consistent with our observations

that fibers made with a single-cane air hole do not support air-guided modes, whereas those with a seven-cane hole guide light in one or two modes.

The potential practical advantages of a single-mode vacuum guide are myriad. It is easy to couple light into the core, because (unlike the honeycomb PBG fiber, which has a complex six-lobed modal pattern) the phase is constant across the air core (giving a Gaussian-like intensity profile). Fresnel reflections, which are a problem in fiber devices where light is extracted from a fiber and then reinjected after modulation or amplification, will be extremely small in the vacuum-guided fiber, because the refractive index discontinuity between the outside world and the fiber mode can be tiny. Another obvious advantage over other optical fibers is that the performance is much less limited by the interaction (absorptive or nonlinear) between the guided light and the normally solid material forming the fiber core. This will allow transmission of wavelengths and power levels not possible in conventional fibers, and will lead to greatly increased threshold powers for stimulated Raman, Brillouin, and color-center effects. On the other hand, if the hollow core is deliberately filled with a gas, vapor, or low-index liquid, very strong interactions are possible with the light in the guided mode. This may prove useful for gas sensing and monitoring, for the generation of multiple optical wavelengths by nonlinear processes, and more generally in enhanced nonlinear optics. The narrow-band performance of the fiber suggests that it might be useful as a spectral filtering device. The ability to form a single transverse mode in a tube of vacuum offers possibilities in the fields of atom guiding and laser delivery of small particles.

#### References and Notes

1. A. W. Snyder and J. D. Love, *Optical Waveguide Theory* (Chapman & Hall, London, 1983).
2. J. W. Dai and J. A. Harrington, *Appl. Opt.* **36**, 5072 (1997); M. Schnurer et al., *Appl. Phys. B Lasers Opt.* **67**, 263 (1998).
3. T. A. Birks, P. J. Roberts, P. St. J. Russell, D. M. Atkin, T. J. Shepherd, *Electron. Lett.* **31**, 1941 (1995).
4. P. St. J. Russell, T. A. Birks, F. D. Lloyd-Lucas, in *Confined Electrons and Photons: New Physics and Applications*, E. Burstein and C. Weisbuch, Eds. (Plenum, New York, 1995), pp. 585-633.
5. J. C. Knight, T. A. Birks, P. St. J. Russell, D. M. Atkin, *Opt. Lett.* **21**, 1547 (1996); Erratum, *ibid.* **22**, 484 (1997).
6. T. A. Birks, J. C. Knight, P. St. J. Russell, *ibid.* **22**, 961 (1997).
7. J. C. Knight, J. Broeng, T. A. Birks, P. St. J. Russell, *Science* **282**, 1476 (1998).
8. T. A. Birks et al., in *Photonic Band Gap Materials*, C. M. Soukoulis, Ed. (Kluwer, Dordrecht, Netherlands, 1996), pp. 437-444.
9. R. J. Tonucci, B. L. Justus, A. J. Campillo, C. E. Ford, *Science* **258**, 783 (1992).
10. E. A. J. Marcatili and R. A. Schmeltzer, *Bell Syst. Tech. J.* **43**, 1783 (1964).
11. Supported by the Defence Evaluation and Research Agency, Malvern, UK. Donation of the fiber-drawing equipment by BT Research Laboratories, Martlesham, UK, is gratefully acknowledged.

13 May 1999; accepted 14 July 1999



## BLOCH WAVE OPTICS IN PHOTONIC CRYSTALS: PHYSICS AND APPLICATIONS

P.ST.J. RUSSELL and T.A. BIRKS  
*Optoelectronics Research Centre,  
University of Southampton,  
Southampton SO17 1BJ,  
United Kingdom*

### 1. Introduction

We aim in this chapter to provide an introduction to the rich tapestry of physical phenomena involving wave propagation in wavelength-scale periodic structures, and to explore briefly their significance in present day research and technology.

The first clue to the presence of a periodic structure is often the reflection of waves at certain specific wavelengths and angles of incidence. The natural world is full of visually attractive examples of this - moth and butterfly wings [1,2], snake and fish scales [3], bird feathers, and some gem stones [4-6] show bright flashes or "rainbows" of colour upon rotation in sunlight. More and more examples of synthetic self-organised periodic structures are also emerging: certain co-polymer mixtures can form with regular arrays of cavities [7]; suspensions of mono-dispersed particles in liquids can crystallise into three-dimensional lattices [8]; iridoviridae self-organise into crystalline lattices [9]; and multiply periodic intensity patterns produced by interfering laser beams can be used to force atoms into regular arrays [10].

Periodic structures have of course been studied in many different areas of physics and technology, examples being phonons in atomic lattices, acousto-optical diffraction in solids and liquids [11], X-ray, electron and neutron diffraction in crystals [12], distributed feedback lasers [13,14], wavelength filtering in optical communications, spectrometry, transmission electron microscopy, multilayer coatings, phased-array microwave antennae, holograms [15] and — last but not least — electronic band structure [16]. Common to the physics underlying all these devices and phenomena are *stop-bands*: ranges of angle and frequency where waves are blocked from travelling through the periodic structure. The practical consequence is that light incident from an isotropic external medium is either reflected, or tunnels through to the other side; it cannot exist freely in the periodic medium itself. On the  $k$ - $k$  and  $\omega$ - $k$  dispersion diagrams the stop-bands appear as *anti-crossing* points, and are also known variously as band gaps, momentum-gaps and regions of evanescence. In only a few cases, however, do they become so strong and numerous that they coalesce to cover all of wavevector space, forbidding

propagation in all directions within limited bands of frequency — the *photonic band gaps* [17].

Prior to the present interest in photonic band gaps, research had been carried out on photonic band structure and propagation in *strongly modulated* singly and multiply periodic planar waveguides [18-22]. Although the aim of that work was not to achieve a full photonic band gap, it generated a number of fabrication, characterisation and conceptual techniques helpful in working out the wider implications of photonic band structure in optoelectronics. The central theme was the use of Bloch waves (the normal modes of electromagnetic propagation in periodic media) and the development of an optics based on them [20]. Group velocity (which could be derived directly from the wavevector diagram) played a central role, leading to an understanding of phenomena such as negative and multiple refraction and Bloch wave interference [21]. The concepts of Bloch wave optics led to the development of some unique devices [19], and the approach also permitted accurate and detailed explanations for the complex and often beautiful phenomena that were seen in the periodic waveguides [21, 22, 24].

In section 2, a brief illustrative introduction to wavevector diagrams and their uses is given. Simple approximate solutions for the scalar dispersion relation in the two-dimensional square and hexagonal cases are derived in section 3. These are used to illustrate a Hamiltonian optics description of the behaviour of Bloch waves in inhomogeneous photonic crystals (section 4), results which are relevant to the modelling of the fields at defects. Bloch wave interference and scattering are treated in sections 5 and 6, and nonlinear effects discussed in section 7. A brief foray into applications occupies section 8, and conclusions drawn in section 9.

## 2. Wavevector Diagrams and Their Uses

We shall be making extensive use of plots of allowed wavevectors in two dimensions at fixed optical frequency - the *wavevector diagram*. This is very valuable in discussions of the propagation of light in photonic crystals. For an isotropic medium, the diagram is a circle of constant radius. For an anisotropic birefringent medium it is an ellipse with semi-axes of length  $2\omega n_{\text{ord}}/c$  and  $2\omega n_{\text{ext}}/c$  where  $n_{\text{ord}}$  and  $n_{\text{ext}}$  are the ordinary and extraordinary refractive indices. The group velocity corresponding with a point on the curves in wavevector space is given by:

$$\mathbf{v}_g = \nabla_{\delta} \omega(\delta) = \frac{\partial \omega}{\partial \delta} = \frac{d\omega}{d\delta} \frac{\partial \delta}{\partial \delta} = \frac{c}{2n_o} \frac{\partial \delta}{\partial \delta} \quad (1)$$

and points normal to the curves on the wavevector diagram, in the direction of increasing frequency. An illustrative example of how the wavevector diagram assists in working out ray directions and boundary conditions is given in Figure 1. A ray incident from air on a parallel slab of birefringent crystal is refracted in two different ways depending on the state of electric field polarisation. In both cases the component of wavevector parallel to the slab boundaries (the minimum distance joining the origin of wavevector space to the construction line) is conserved. For polarisation in the isotropic plane, Snell's law is obeyed as usual. For

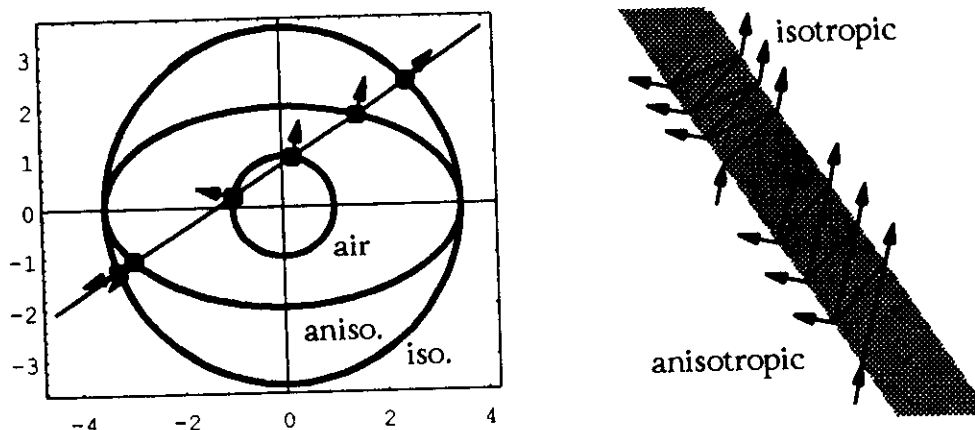


*Figure 1.* Example of the use of the wavevector diagram to predict the ray paths (group velocities) of multiple reflections within a parallel slab of birefringent crystal. The wavevector component along the boundaries is conserved, yielding the construction line that intersects with the circles and ellipse in wavevector space. The normals at these points of intersection give the ray directions and hence the zig-zag paths for isotropic and anisotropic states of polarization.

polarisation in the anisotropic plane, the refracted and reflected ray paths in the crystal, while unusual and difficult to predict, are readily obtained using the wavevector diagram. Another beautiful example of the non-coincidence of group and phase velocity is in ultrasonic pulse propagation in elastically anisotropic materials such as crystalline silicon, as discussed in a recent article [23].

### 3. "Toy models" for dispersion relation in two cases

To illustrate the discussion throughout this chapter, we first derive two approximate solutions for the Bloch wave dispersion relation, one for a two-dimensional (2-D) square crystal, and the other for a 2-D hexagonal crystal. Analytical expressions are accessible through reducing drastically the number of "partial" plane waves in the Bloch wave expansion to three for the hexagonal and four for the square case. Despite the inaccuracies introduced, little of the underlying physics is lost in this approximation, and although we do not have space to show this, it is not difficult to include the case where the electric field is polarised in the plane of the lattice wavevectors.

In each case the structure is described by a relative dielectric constant  $\epsilon$ :

$$\epsilon/\epsilon_0 = 1 + M \sum_{j=1}^N \cos(\mathbf{K}_j \cdot \mathbf{r}) \quad (2)$$

where  $\mathbf{K}_j$  is the lattice vector of the  $j$ -th set of planes with spacing  $2\pi/|\mathbf{K}_j|$ ,  $M$  is the amplitude of the dielectric constant modulation around its average value  $\epsilon_0$ , and  $N=3$  for the hexagonal and 2 for the square cases. The average wavevector in the structure is  $k_0 = \omega n_0/c$ , where  $n_0$  is the average index. In the two-dimensional case,  $n_0$  is given by the square root of the optical path area of a unit cell, divided by the square root of its real area.

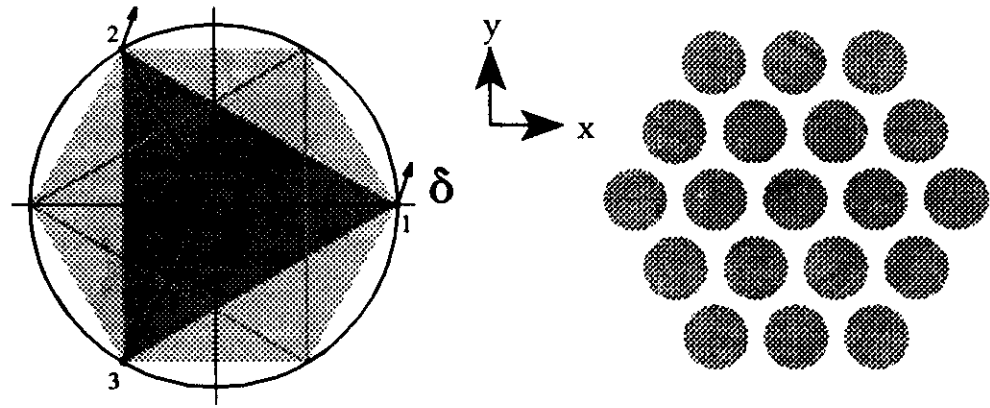


Figure 2. First tileable Brillouin zone (hexagonal lightly shaded region on the left) in wavevector space of the structure on the right. For the calculation it is sufficient to use a triangular sub-zone (darkly shaded region). The average index circle is drawn for the special case when it intersects the three numbered symmetry ( $S$ ) points. The locus of points traced out by  $\delta$  (identical for each  $S$ -point) yields the dispersion surfaces (see section 3.1).

As already mentioned, the wavevector diagram for an isotropic medium is a circle of constant radius  $\omega n_0/c$ : the *average index circle*. In a photonic crystal with a hexagonal or square microstructure, important symmetry points occur at the vertices of the regular polygon formed by concatenated lattice vectors (the Brillouin zone). At one particular optical frequency the vertices of this polygon lie on the average index circle; at the points of intersection, the Bragg condition is satisfied simultaneously at all sets of lattice planes. We shall call the vertices  $S$ -points; in the hexagonal case (Figure 2) there are six, and in the square case (Figure 3) four. As  $M$  increases, the loci of allowed wavevectors (the “dispersion curves”) in the vicinity of the  $S$ -points becomes complicated, stop-bands and other features appearing.

Each point on the dispersion curves within the first Brillouin zone (i.e., the zone straddling the average index circle) is associated with a unique travelling Bloch wave; the featureless regions in between are populated with evanescent waves, which are excited only if boundaries or structural defects occur in the otherwise regular photonic crystal. The full wavevector diagram is obtained by tiling the first Brillouin zone to cover all of wavevector space. Each

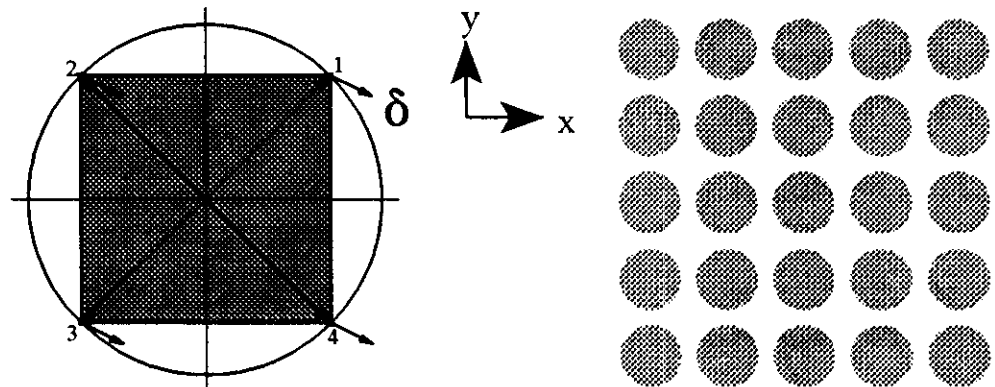


Figure 3. First Brillouin zone (square shaded region on the left) in wavevector space of the square crystal on the right. The average index circle is drawn for the special case when it intersects the four numbered symmetry ( $S$ ) points. The locus of points traced out by  $\delta$  (identical for each  $S$ -point) yields the dispersion surfaces (see section 3.2).

wavevector in the first Brillouin zone thus has an infinite number of associated wavevectors, one in each higher order Brillouin zone, linked by Bloch's theorem.

Thus, one approach to obtaining the Bloch wave function is to expand the fields in terms of an infinite sum of *partial* plane waves, one for each Brillouin zone. This sum is then truncated appropriately, and the resulting eigenvalue problem solved using standard techniques. We now make a drastic reduction in the number of partial waves (to four for the square and three for the hexagonal cases) in order to obtain illustrative analytical expressions for the dispersion relations.

### 3.1 HEXAGONAL CASE

The minimum number of partial waves required in this case is three, their wavevectors being expanded around the three *S*-points:

$$\mathbf{k}_i = \boldsymbol{\delta} + \hat{\mathbf{t}}_i K/\sqrt{3}, \quad K = |\mathbf{K}_j| \quad (3)$$

where  $\mathbf{K}_j$  is the lattice vector from (2),  $\boldsymbol{\delta}$  is the deviation of the Bloch wavevectors from their values when the multiple Bragg condition is satisfied, and

$$\hat{\mathbf{t}}_1 = \hat{\mathbf{x}}, \quad \hat{\mathbf{t}}_2 = (-\hat{\mathbf{x}} + \hat{\mathbf{y}}\sqrt{3})/2, \quad \hat{\mathbf{t}}_3 = (-\hat{\mathbf{x}} - \hat{\mathbf{y}}\sqrt{3})/2 \quad (4)$$

are unit vectors in the three *S*-directions. Substituting an Ansatz consisting of three plane waves with amplitudes  $V_1$ ,  $V_2$  and  $V_3$  and wavevectors (3) into Maxwell's equations, and neglecting higher order terms in  $\boldsymbol{\delta}$ , leads to a  $3 \times 3$  matrix whose determinant must equal zero for solutions:

$$\begin{pmatrix} \vartheta/2 - \boldsymbol{\delta} \cdot \hat{\mathbf{t}}_1 & \kappa & \kappa \\ \kappa & \vartheta/2 - \boldsymbol{\delta} \cdot \hat{\mathbf{t}}_2 & \kappa \\ \kappa & \kappa & \vartheta/2 - \boldsymbol{\delta} \cdot \hat{\mathbf{t}}_3 \end{pmatrix} \begin{pmatrix} V_1 \\ V_2 \\ V_3 \end{pmatrix} = 0 \quad (5)$$

where the coupling constant  $\kappa$  and the dephasing constant  $\vartheta$  are defined by:

$$\kappa = k_0 M/4, \quad \vartheta = 2(k_0 - K/\sqrt{3}). \quad (6)$$

The dispersion relation turns out to have the form:

$$3\delta_y^2 = (\delta_x + \vartheta)^2 + \frac{2\kappa^2(4\kappa + 3\vartheta)}{2\delta_x - \vartheta}. \quad (7)$$

### 3.2 SQUARE CASE

The wavevectors of the four Bloch partial waves in this case are expanded around the four *S*-points:

$$\mathbf{k}_i = \boldsymbol{\delta} + \hat{\mathbf{t}}_i K/\sqrt{2}, \quad (8)$$

where  $\boldsymbol{\delta}$  is the deviation of the Bloch wavevectors from their values when the multiple Bragg

condition is satisfied and

$$\hat{\mathbf{t}}_2 = (\pm \hat{\mathbf{x}} + \hat{\mathbf{y}})/\sqrt{2}, \quad \hat{\mathbf{t}}_3 = (\mp \hat{\mathbf{x}} - \hat{\mathbf{y}})/\sqrt{2} \quad (9)$$

are unit vectors in the four  $S$ -directions; the upper subscript indices are taken with the upper signs. Putting an ansatz consisting of four plane waves with amplitudes  $V_1, V_2, V_3$  and  $V_4$  and wavevectors (8) into Maxwell's equations, and neglecting higher order terms in  $\delta$ , leads to a  $4 \times 4$  matrix whose determinant must equal zero for solutions. Its form is identical to (5), with one extra row for the fourth amplitude. The dephasing constant  $\vartheta$  and coupling constant  $\kappa$  are defined for the square case by:

$$\kappa = k_0 M/4, \quad \vartheta = 2k_0 - K\sqrt{2}. \quad (10)$$

The resulting dispersion relation is:

$$\delta_y^2 = \delta_x^2 + (\vartheta/\sqrt{2})^2 \pm 2(\vartheta/\sqrt{2})\sqrt{\delta_x^2 + 2\kappa^2}. \quad (11)$$

### 3.3 SOLUTIONS FOR THE WAVEVECTOR DIAGRAMS

Some illustrative plots of the resulting dispersion curves (i.e., the locii of  $\delta$  at fixed frequency plotted in 2-D wavevector space) around each  $S$ -point are given in Figures 4 and 5.

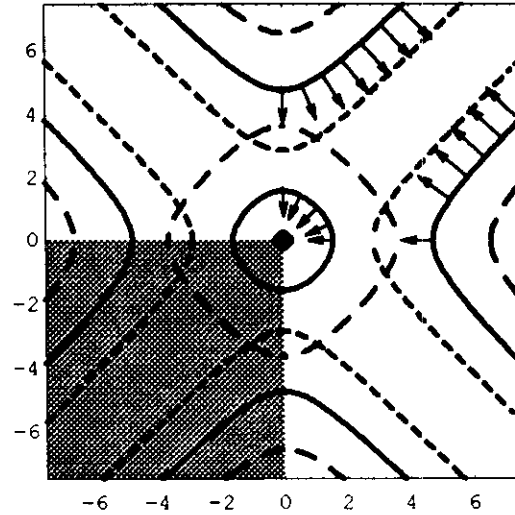


Figure 4. Wavevector diagram about the  $S_1$  point for a square crystal with  $\kappa=1$ ,  $\vartheta=2.5$  (long-dashed curves), 5 (full curves) and 7.5 (short-dashed curves). The vertical and horizontal axes are  $\delta_y$  and  $\delta_x$  respectively. For  $\vartheta=5$ , the direction and relative magnitude of the group velocity is indicated in one quadrant using arrows of variable length. The shaded region is part of the first Brillouin zone (see Figure 3).

In the square case (Figure 4) for  $\kappa=1$  and  $\vartheta=7.5$ , the central region approximates to a circle with equation:

$$\delta_x^2 + \delta_y^2 = \vartheta^2/4 - 4\kappa^2. \quad (12)$$

This is valid so long as terms of third order and higher in  $\delta$  can be neglected. Note that (12) predicts that the circle vanishes for  $(\delta/\kappa)^2 < 16$ . The implications of (12) are intriguing; it states that the Bloch waves behave in many respects like plane waves in an isotropic medium, except that the velocity of light is reduced to a smaller value, and the dispersion with frequency is nonlinear. All the usual classical processes such as diffraction, interference and scattering will be present, except that Bloch waves on the outer stop-band branches not described by (12) will be excited at abrupt interfaces or aperiodicities. The direction of the group velocity at different points on the curves is marked by means of arrows whose length scales with the magnitude. For  $\delta < 0$  they point in the opposite direction, the curves themselves having precisely the same shape (within the approximations of the model) as for  $\delta > 0$ .

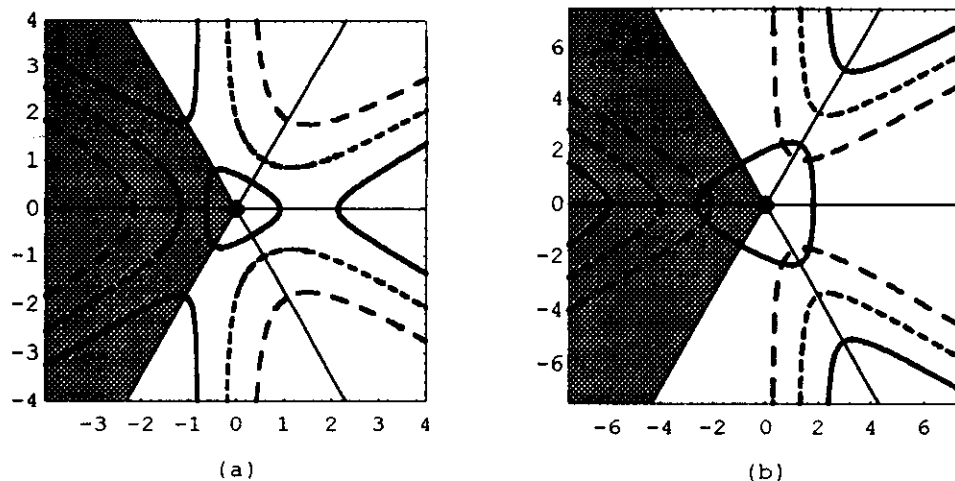


Figure 5. Wavevector diagrams about the  $S_1$  point for a hexagonal crystal with (a)  $\kappa = 1$ ,  $\delta = -1.6$  (full curves),  $-0.5$  (short dashed) and  $0.6$ ; and (b)  $\delta = 4.5$  (full curves),  $2.5$  (short dashed) and  $0.5$ . The vertical and horizontal axes are  $\delta_y$  and  $\delta_x$  respectively. The shaded region is part of the first hexagonal Brillouin zone (see Figure 2).

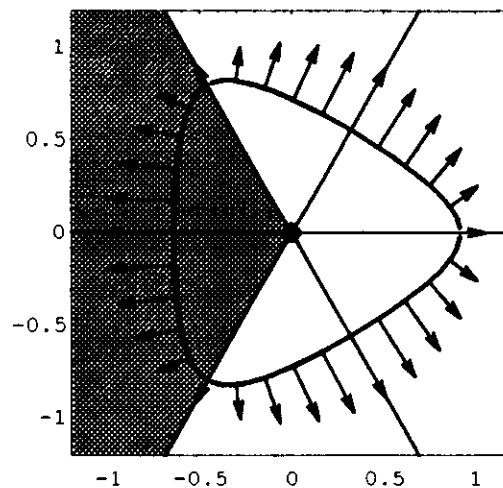


Figure 6. Magnified central rounded triangle from Figure 4 for  $\kappa = 1$ ,  $\delta = -1.6$ , with the group velocity arrows drawn in. Notice the smaller velocities at the points of maximum curvature.

For the hexagonal case, the chosen parameters are  $\kappa = 1$ ,  $\vartheta = 0.6, -0.5$  and  $-1.6$  (Figure 5a) and  $\kappa = 1$ ,  $\vartheta = 0.5, 2.5$  and  $4.5$  (Figure 5b). The central "rounded triangle" is redrawn for  $\vartheta = -1.6$  in Figure 6, along with the group velocity arrows. Note the inverse correlation between curvature and group velocity. As the triangle becomes smaller, eventually disappearing, the curvature becomes tighter and the group velocity tends to zero.

An important consequence of this slowing down of light is that it has more time to interact with matter - dipoles, nonlinearities, scattering centres. Apparently weak perturbations in refractive index can result in strong scattering, and non-linear effects such as Brillouin and Raman scattering, the Pockels effect, and the optical Kerr effect, are enhanced. We shall explore some of these points in sections 6 and 7.

#### 4. Geometrical Optics of Bloch Waves in Inhomogeneous Media

It is well-known that light can spiral around in a waveguide consisting of a cylindrically symmetric bell-shaped refractive index distribution. Because the transverse photon momentum is reduced by the presence of a large axial component of momentum, a weak potential well of higher refractive index is all that is needed to trap the light, as for example in the Ge-doped core of a silica optical fibre [25]. Trapping of light is much easier in photonic crystals, since in the vicinity of the band edge the photon momentum can be very small. Indeed, many important potential applications of photonic band gap materials rely on the use of spatial inhomogeneities to provide intra-band trapped states [26,27]. In addition the effects of inhomogeneities, in the band-windows where propagation is allowed, are not yet well understood. In this section we address the propagation in inhomogeneous periodic media, developing a Hamiltonian optics approach and using it to treat in particular the motion of the Bloch wave rays (given by the group velocity) around circularly symmetrical defects in which the properties vary slowly over many lattice periods.

Hamiltonian optics has been elegantly summarised by a number of authors, including Arnaud in his 1976 book *Beam and Fiber Optics* [28]. It can be applied where the dispersion relation in the homogeneous structure is known, and where, in the inhomogeneous real structure, parameters like average index vary slowly in space. It is essentially an analytical method for stepping through a non-uniform structure, matching phase velocities normal to the gradient of the inhomogeneity at each step, and propagating along the local group velocity to the next point. This process is described by solutions of Hamilton's equations, which take the general form:

$$\frac{d\mathbf{x}}{d\sigma} = \nabla_{\mathbf{k}} H, \quad \frac{d\mathbf{k}}{d\sigma} = -\nabla H \quad (13)$$

where  $\mathbf{x} = \{x, y, z, -t\}$  is the four-vector for space-time,  $\mathbf{k} = \{k_x, k_y, k_z, \omega\}$  the generalised wavevector,  $\sigma$  an arbitrary parameter (see below), and  $H(\mathbf{x}, \mathbf{k})$  the Hamiltonian, which may be expressed directly from the dispersion relation for the waves. Note that in general  $\mathbf{k}$  depends on position. Equation (13) can be re-cast in a Newtonian way [24,28]:



$$\frac{d^2 \mathbf{x}}{d\sigma^2} = [\nabla_k \nabla_k H] : (-\nabla H) = [1/\mathbf{m}^*] : \mathbf{F} \quad (14)$$

in which the reciprocal effective mass tensor depends, in general, on position in real and reciprocal space. The Hamiltonian itself may be written in a number of equivalent ways, subject to the requirement that a phase front is given by the equation  $H = 0$ . In obtaining solutions to (13), it is important to distinguish total from partial differentiation. For the dispersion relation in (12),  $H$  can be chosen in the form:

$$H \equiv \left( \omega n_0 / c - K/\sqrt{2} \right)^2 - \delta_x^2 - \delta_y^2 - 4\kappa^2 = 0. \quad (15)$$

For a central force field  $H$  depends only on distance  $r$  from an origin, and recognising that  $\delta$  in (15) acts as the wavevector, (14) may be re-expressed in the form:

$$\frac{d^2 \mathbf{r}}{d\sigma^2} = 2 \frac{\partial H}{\partial \mathbf{r}} \hat{\mathbf{r}} \quad (16)$$

where  $\mathbf{r}$  is the position vector in two dimensions; if necessary the parameter  $\sigma$  can be related to real time  $t$  by the time component of the four-vector equations (13):

$$c(t-t_0) = - \int_{\sigma=\sigma_0}^{\sigma} \left( 2\omega n_0 / c - K\sqrt{2} \right) n_0 d\sigma \quad (17)$$

where  $n_0$  and  $K$  depend in general on position (and hence on  $\sigma$ ) as given by solutions of (16). The exact meaning of  $\sigma$  is not important if only the ray paths are sought; if, however, position as a function of time is required - such as when calculating the free spectral range of a cavity - (17) must be used. Working in cylindrical polar coordinates, we now follow the standard approach to motion in a central force field. Since the  $\hat{\theta}$  component of the left-hand-side of (16) must be zero, angular momentum  $h$  is conserved:

$$h = r^2 \dot{\theta} = \text{constant} \quad (18)$$

where the dot denotes differentiation with respect to  $\sigma$ . Making the standard substitution  $u = 1/r$ , (16) may be reduced to the form:

$$\frac{d^2 u}{d\theta^2} + u = \frac{2}{h^2} \frac{\partial H}{\partial u}. \quad (19)$$

To illustrate a particular case, we choose a square structure in which the modulation amplitude  $M$ , and hence the coupling constant  $\kappa$ , are radially dependent,  $K$  and  $n_0$  being kept constant:

$$\kappa^2 = (\kappa_0^2 + \kappa_1^2) - \kappa_1^2 u/u_1. \quad (20)$$

This leads to solutions which imitate the elliptical and hyperbolic orbits of a particle in a gravitational field:

$$u(\theta) = u_0 (q + m \cos(\theta + \psi)) \quad (21)$$

where

$$q = 8\kappa_1^2/(h^2u_0u_1), \quad h = -2\delta_{oy}/u_0, \quad (22)$$

$$m = \sqrt{(1-q)^2 + (\delta_{ox}/\delta_{oy})^2}, \quad \psi = \arccos[(1-q)/m]$$

are the definitions of the various parameters. The initial values of  $u$ ,  $\delta$  and  $\theta$  are  $u_0$ ,  $\delta_0 = (\delta_{ox}, \delta_{oy})$  and  $0\pi$  respectively. Equation (21) yields the ray paths  $r(\theta)$ , which may be translated into  $r(\sigma)$  via  $d\theta/d\sigma = hu^2$ , and then into  $r(t)$  via (17). A series of typical ray trajectories are plotted in Figure 7, for attractive ( $u_1 > 0$ ) and repulsive ( $u_1 < 0$ ) central force fields. In each plot, several paths are given for different directions of the initial ray at the point (1,0) and the centre of the force field is at (0,0).

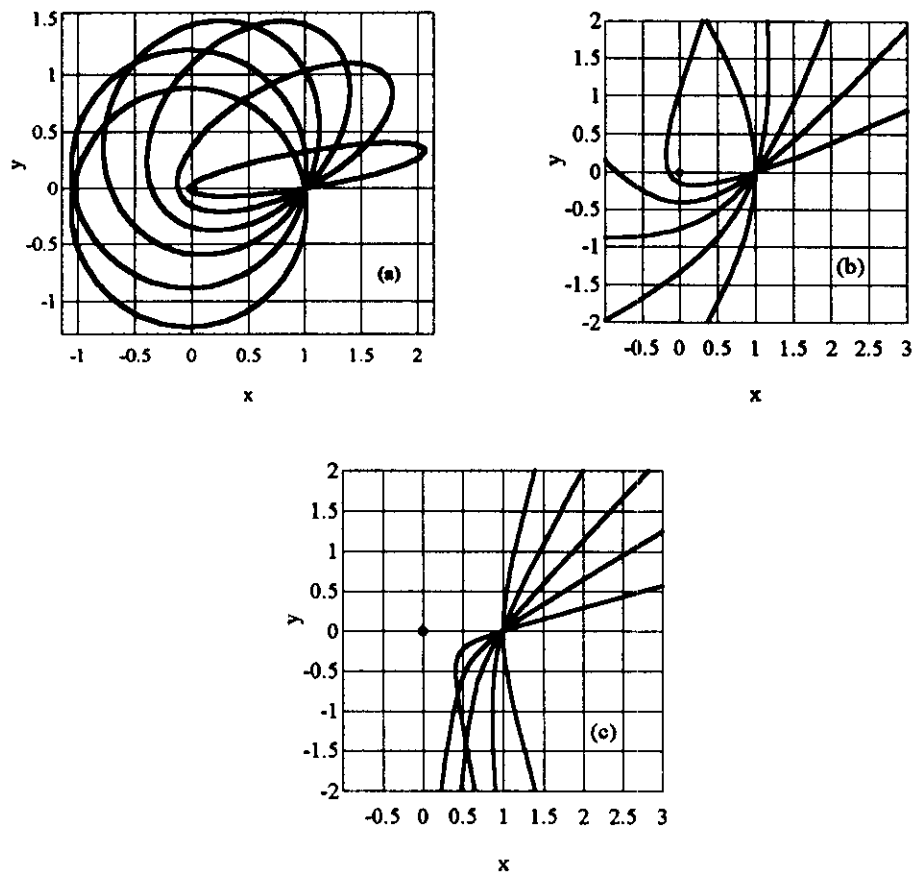


Figure 7. Trajectories of rays around a force field centred at  $x=0$ ,  $y=0$  in a square crystal in three cases: (a) attractive force ( $\kappa$  increasing with radius) at a frequency such that the light cannot escape; (b) attractive force at frequency where light can escape; (c) repulsive force. The parameter values are  $\delta/4\kappa_0 = -2.5$ ,  $u_0 = \kappa_0$  and  $\kappa_1 = 0.2\kappa_0$ , with (a)  $u_1 = 0.004\kappa_0$ , (b)  $u_1 = 0.01\kappa_0$  and (c)  $u_1 = -0.01\kappa_0$ . In each case, the orbits for several different initial directions are given.

We now look in more detail at the case of a circular ray path, which occurs for initial conditions  $\delta_{ox} = 0$  and  $q = 1$ . We shall derive the radius and the time taken for one cycle of

revolution. From (21) for  $q = 1$ , recognising that  $\delta_{oy} = \delta_o$  may be expressed using (15), the inverse radius is:

$$u_o = u_1 \left( (\partial^2/4 - 4\kappa_o^2) / 2\kappa_1^2 \right) \quad (23)$$

and the time taken for one revolution, obtained from (17) using  $d\theta/d\sigma = -2\delta_o u_o$ , is:

$$T = \frac{\pi \partial n_o}{c u_o \sqrt{\partial^2/4 - 4\kappa_o^2}} = \frac{2\pi r_o}{2\delta_o c / \partial n_o} = \frac{2\pi r_o}{v_g} \quad (24)$$

where  $r_o = 1/u_o$ . As indicated in (24),  $T$  can be expressed as the circumference of the circular path divided by the group velocity, exactly as intuition would suggest. The classical nature of the Hamiltonian approach does not predict quantization of these closed orbits; it merely gives us the particle trajectories (governed by the group velocity). In order to establish the optical frequencies at which discrete resonances appear, one must return to considering the underlying field amplitudes (governed by phase velocity). It is, however, possible to predict the frequency spacing between adjacent resonant modes - the free spectral range; this is simply  $1/T$ .

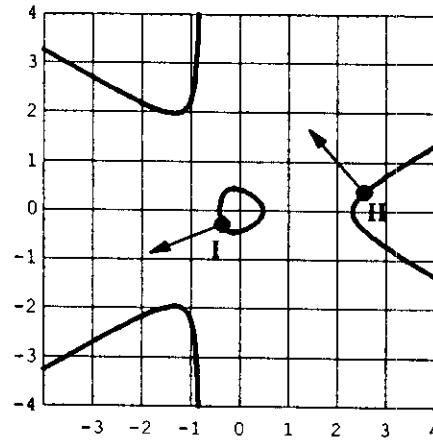
To put some "flesh" on these formulae, we consider a square structure fabricated along the lines of the techniques reported in [21], where coupling constants of 120/mm at an optical wavelength of 633 nm were achieved in etched Ta<sub>2</sub>O<sub>5</sub> waveguides on borosilicate glass. For such a waveguide supporting TM polarised (the fields are then quasi-scalar) modes of effective index 1.7, a structure with  $\Lambda = 260$  nm will have a Bragg wavelength of 624 nm. For  $\partial/\kappa_o = 4.01$ , i.e., operating at 633 nm, the rays will describe a circular trajectory of radius 100  $\mu$ m with a period of 50 psec if the perturbation strength is  $\kappa_1 \sqrt{r_1} = 3.8$  /mm<sup>1/2</sup>. The free spectral range of the associated resonances will be 20 GHz. In a uniform medium of refractive index 1.7, light would take 3.6 psec to travel around a loop of the same dimensions, with a free spectral range of 0.28 THz. This illustrates both the substantial reductions in optical velocity that occur near a band edge, and the associated increase in the optical density of states.

## 5. Interference of Bloch Waves

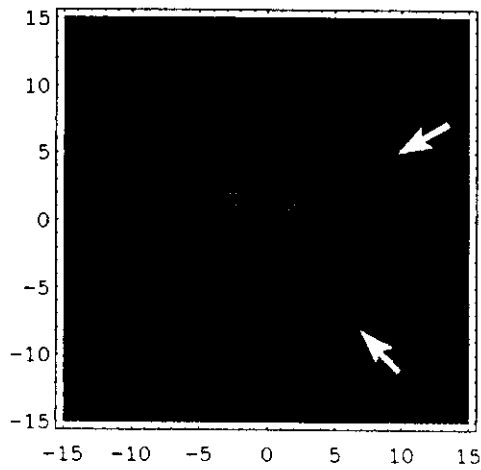
Given their complicated dispersion, it is perhaps not surprising that Bloch waves interfere in a unique and complex manner, and that the characteristics of this interference provide clues to their behaviour when coupled together or scattered. In previous experimental work, singly and doubly periodic planar waveguides were studied [21,22]. Here we treat the two dimensional multiply periodic case. To start our discussion we take first a superposition of two different Bloch waves:

$$E(\mathbf{r}, t) = a_1(\mathbf{r}) \exp[-j(\delta_1 \cdot \mathbf{r} - \omega t)] + a_2(\mathbf{r}) \exp[-j(\delta_2 \cdot \mathbf{r} - \omega t)] \quad (25)$$

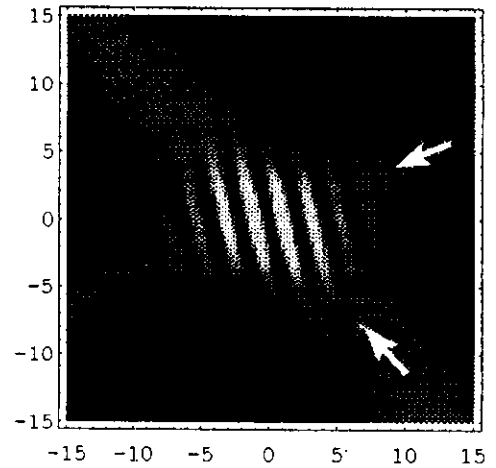
where  $a_1$  and  $a_2$  are time-independent complex periodic functions of position whose structure mimics the lattice. For travelling Bloch waves the wavevectors  $\delta$  are real-valued. If observing scattering from this pattern, coarse fringes would be seen with the form:



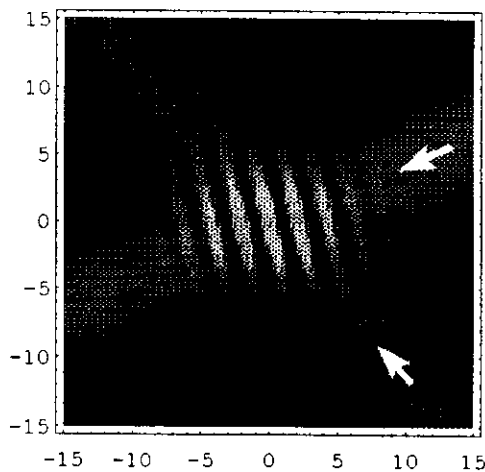
(a)



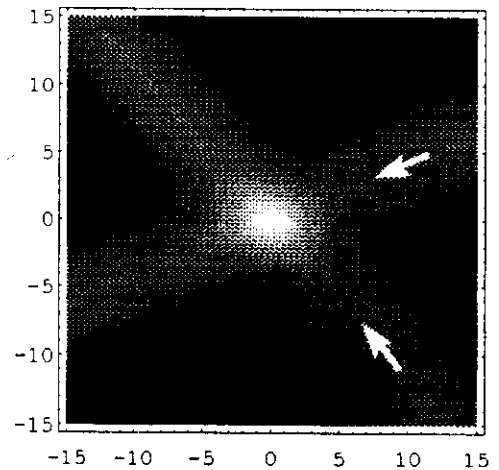
(b) Symmetry point 1



(c) Symmetry point 2



(d) Symmetry point 3



(e) Total field

*Figure 8.* Calculated interference fringes (relative intensities scaled with gray-level) for the two orthogonal Bloch wave beams associated with the points on the wavevector diagram in (a), plotted for  $\kappa = 1$  and  $\vartheta = -1.6$ . In (b), (c) and (d) the fringes created by the groups of partial waves at the 1st, 2nd and 3rd *S*-points are illustrated. In (e), the complete intensity pattern of the superimposed Bloch beams is given; note the complete absence of interference.

$$I(\mathbf{r}) = \langle |a_1(\mathbf{r})|^2 + |a_2(\mathbf{r})|^2 \rangle + \langle a_1(\mathbf{r})a_2^*(\mathbf{r}) + a_1^*(\mathbf{r})a_2(\mathbf{r}) \rangle \cos[(\delta_2 - \delta_1) \cdot \mathbf{r}] \quad (26)$$

where the averaging is over a unit cell and the variation in the argument of the cosine is assumed to be slow. Each of the two terms added together in the amplitude of the cosine turn out to be real, which is why no phase term appears in the argument of the cosine. The orientation of the fringes is given by  $\delta_1 - \delta_2$ , which bears no obvious relation to the directions of propagation as given by the group velocities. This has a number of bizarre consequences when a comparison with conventional plane wave interference is made. For example (defining  $\alpha_1$  and  $\alpha_2$  as the angles between the group velocities and  $\delta_1 - \delta_2$ ), interference fringes can appear even when  $\alpha_1 > 0$ ,  $\alpha_2 < 0$ ; for two plane waves this fringe orientation would be impossible.

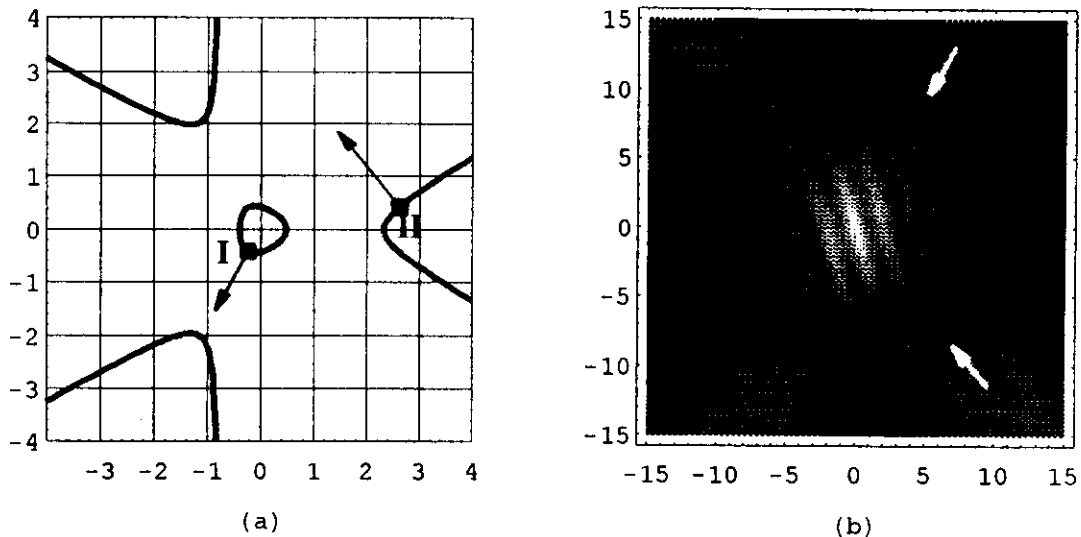


Figure 9. Complete fringe pattern (b) for the two non-orthogonal Bloch wave beams associated with the points on the wavevector diagram in (a). Note the presence, as expected, of visible interference fringes.

The fields forming the fringe patterns may be decomposed into *groups* of partial plane waves sharing approximately the same wavevector, gathered around each of the *S*-points (see e.g. Figures 1 and 2). Each group produces its own set of sub-fringes. If all these fringe sets are spatially in phase, a strong visible fringe pattern will be produced; if however the dips in intensity from one group are filled in by peaks in intensity from the other groups, the result will be a more uniform intensity distribution (orthogonal Bloch waves, with zero overlap integral in (26), produce a perfectly uniform intensity pattern, with no evidence of interference). This means that if a boundary with an isotropic medium is introduced at a point where the intensity from one group is high, a plane wave may appear in the isotropic medium, travelling in the general direction of the partial plane waves of that group. If a boundary cuts across regions where the intensity oscillates between different groups, then beamlets are produced, their directions corresponding to the groups that have the maximum local intensity; the result can often be striking. This process gives rise to the Pendellösung fringes in x-ray diffraction [29], and lies behind the operation of volume transmission gratings [15]; we have previously classified it as *exchange interference* [21], since each sub-group of plane waves interferes

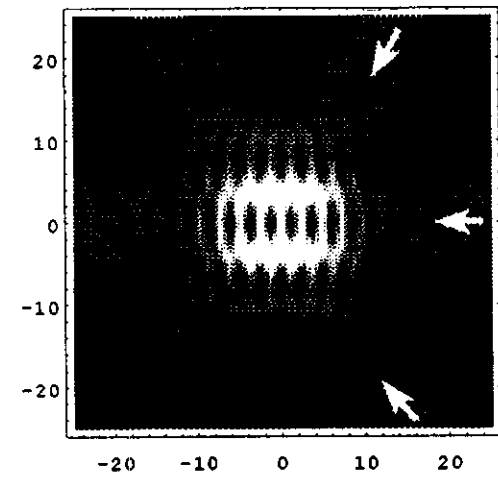
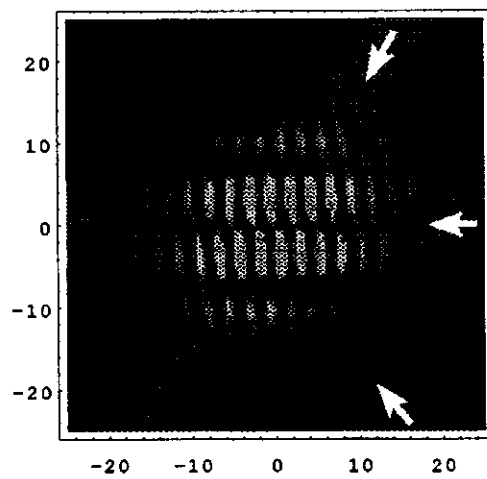
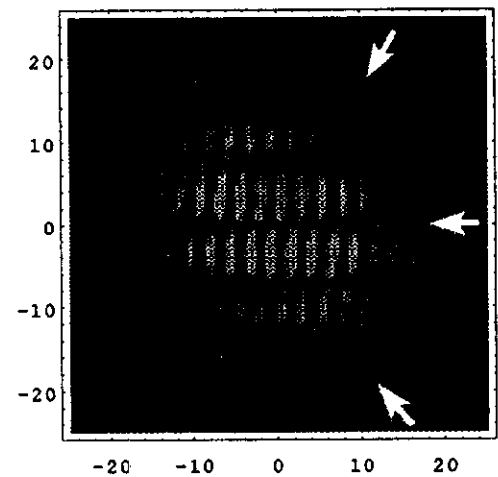
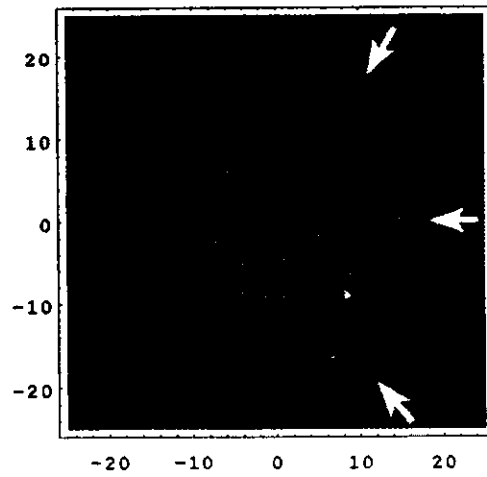
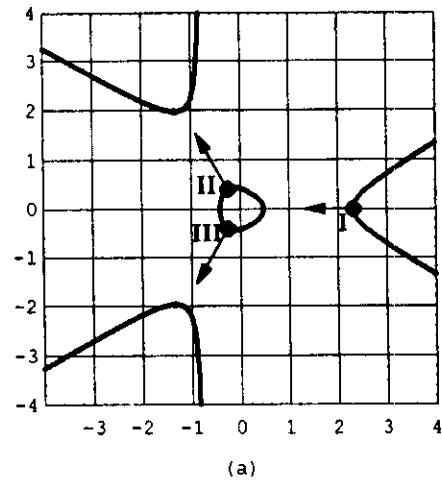


Figure 10. Interference fringes (relative intensities scaled with gray-level) for the three Bloch wave beams associated with the points on the wavevector diagram in (a). In (b), (c) and (d) the fringes created by the groups of partial waves at the 1st, 2nd and 3rd S-points are illustrated. In (e), the complete intensity pattern of the three superimposed Bloch beams is given.

constructively in different regions of space.

To illustrate these arguments, we now look at some specific examples in which the fringe intensity patterns of superimposed Bloch beams, and of their partial wave groups, are plotted for a two-dimensional hexagonal crystal. The points on the wavevector diagram, and the group velocity arrows, are also illustrated. First of all, an orthogonal pair of equal amplitude Bloch waves is selected (Figure 8). The interference patterns from the groups of partial waves at the  $S_1$ ,  $S_2$  and  $S_3$  points are plotted successively in Figure 8b, 8c and 8d. Note the strong visible fringes. When, however, all three patterns are combined, the fringes vanish, leaving a uniform intensity that is higher in the middle simply because the Gaussian beam profiles overlap there. In a second example (Figure 9), a non-orthogonal Bloch wave pair is chosen, and this time the combined intensity field contains fringes. In the third example, three non-orthogonal Bloch waves are taken. The interference patterns here are more complex (Figure 10). Once again, the patterns from each sub-group, and from the combined field, are given. The  $S_1$  subgroup produces a much weaker intensity pattern, as expected since the group velocities of the Bloch waves point predominantly in the  $-x$  direction.

## 6. Coupling and Scattering of Bloch Waves

In this section we derive the coupled mode equations describing the interaction of two different Bloch waves in a two-dimensional periodic structure with a periodic distortion in properties - a *superlattice*. This analysis will provide a useful basis from which to discuss more generally the coupling and scattering of Bloch waves. The analysis is an extension of one presented previously for singly periodic structures [30,31]. The relative dielectric constant of the structure is taken in the form:

$$\epsilon(\mathbf{r}) = \epsilon_0 + \epsilon_p(\mathbf{r}) + \{\epsilon_s = \epsilon_{s0} \cos \mathbf{K}_s \cdot \mathbf{r}\} \quad (27)$$

where the subscript p denotes the undistorted "primary crystal," and s the weak "secondary grating," which together form the superlattice. The time-independent field ansatz is taken in the form of a superposition of two Bloch waves:

$$\begin{aligned} \mathbf{E}(x, z) &= \mathfrak{Y} \sum_{i=1}^2 V_i(x, z) B_i(x, z) \\ &= \mathfrak{Y} \sum_{i=1}^2 V_i(x, z) a_i(x, z) \exp(-j \delta_i \cdot \mathbf{r}), \quad \delta_i \cdot \mathfrak{Y} = 0 \end{aligned} \quad (28)$$

where the  $V_i$  are slowly-varying amplitudes and the  $B_i$  describe Bloch waves of the undistorted crystal; when the  $V_i$  are constant, no coupling is present and (28) is a solution of Maxwell's equations for the primary crystal. Substituting (28) into Maxwell's equations for the structure (27), neglecting second order derivatives of  $V_i$ , multiplying by  $(B_1^* + B_2^*)$  and averaging over a unit cell of the primary crystal, we obtain the coupled Bloch wave equations:

$$\frac{\partial V_i}{\partial p_i} + j \kappa_{sij} V_j \exp(-j \delta_{ij} \cdot \mathbf{r}) = 0, \quad (29)$$

where the coupling constant and dephasing vector are given by:

$$\kappa_{sij} = \frac{\omega \epsilon_{s0} I_{ij}}{4 \epsilon_0 (\hat{\mathbf{p}}_i \cdot \mathbf{v}_{gi}) I_{ii}}, \quad \mathbf{\vartheta}_{ij} = (\delta_j - \delta_i) \pm \mathbf{K}_s, \quad (30)$$

the sign is chosen to minimise the magnitude of the dephasing vector  $\mathbf{\vartheta}_{ij}$ , and

$$I_{ij} = \iint_{\text{cell}} a_i^* a_j dA. \quad (31)$$

The spatial coordinate  $p_i$  has a unit vector  $\hat{\mathbf{p}}_i$  that can be chosen to point in any convenient direction not perpendicular to the group velocity  $\mathbf{v}_{gi}$ . Commonly, both  $p_1$  and  $p_2$  are chosen to lie parallel to one cartesian coordinate; this is useful if the secondary grating region has a straight flat boundary. If, however, two-dimensional coupling is to be treated, a good choice of  $\hat{\mathbf{p}}_i$  points parallel to  $\mathbf{v}_{gj}$ , i.e., parallel to the group velocity of the *other* wave. It is straightforward to show that power is conserved by solutions of (29):

$$\frac{\hat{\mathbf{p}}_1 \cdot \mathbf{v}_{g1}}{I_{11}} \frac{\partial |V_1|^2}{\partial p_1} + \frac{\hat{\mathbf{p}}_2 \cdot \mathbf{v}_{g2}}{I_{22}} \frac{\partial |V_2|^2}{\partial p_2} = 0. \quad (32)$$

The first striking thing is that the coupling constant in (30) is inversely proportional to the group velocity. This means that, close to a band edge, the coupling constant becomes very large. Otherwise expressed: the Bloch waves become highly susceptible to scattering at perturbations which would not significantly affect a plane wave in an isotropic medium. A good example of this is the circle enclosing the Bragg point in the wavevector diagram of the square photonic crystal discussed in section 3.2. In the same waveguide, operating at  $\vartheta/\kappa_0 = 4.01$  with an average index of 1.7, the secondary grating period needed for phase-matched coupling of two Bloch waves travelling at right angles to one another is

$$\Lambda_s = \frac{2\pi}{\delta_0 \sqrt{2}} = \frac{\pi}{2\sqrt{2} \kappa_0 \sqrt{(\vartheta/4\kappa_0)^2 - 1}} \quad (33)$$

which works out at 0.26 mm for a primary grating coupling constant of 120/mm. The group velocity is  $0.07 c/n_0$  and the coupling constant, for  $\hat{\mathbf{p}}_1 = \hat{\mathbf{p}}_2$  bisecting the angle between the two group velocities, is

$$\kappa_{sij} = \kappa_{sji} = \frac{\pi \epsilon_{s0}}{2\sqrt{2} n_0 \lambda \sqrt{1 - (4\kappa_0/\vartheta)^2}} \quad (34)$$

which works out at  $9.3 \times 10^3 \epsilon_{s0}/\text{mm}$  at 633 nm (note that the overlap integral  $I_{12} \approx 1$  for these two waves). A secondary grating with an amplitude  $\epsilon_{s0} = 0.0001$  will couple the Bloch waves together at a rate of 0.93/mm, i.e., 100% coupling will be achieved in 1.7 mm. The effective modulation depth of the primary grating is  $M \approx 0.028$ , which implies that the amplitude of the dielectric constant modulation is 0.08 - some 800 times stronger than for the secondary grating.



The second striking thing is that the coupling constant depends on the overlap integral of the field microstructure of the Bloch waves. As we have seen already, the absence of real interference fringes between two different but co-propagating Bloch waves may be taken as evidence that they are orthogonal, i.e., that their overlap integral is zero. This means, for example, that a superlattice designed to couple together the two Bloch waves whose interference patterns are depicted in Figure 8 will not function. There is thus an intimate relationship between the presence of real interference fringes and the feasibility of coupling.

This analysis may be generalised to the case of superlattices whose secondary grating has multiple periodicities. For example, if the secondary "lattice" matches the hexagonal interference pattern created by interference of three Bloch waves (see, e.g., Figure 10), then coupling between these three waves can be achieved. The ramifications of this extension to the possibilities of optical superlattices (for obvious reasons not feasible in electronic superlattices made by MBE) remain to be explored in detail.

## 7. Nonlinear Scattering

The strong scattering that is possible between Bloch waves because of their very low momentum near a band-edge also means that nonlinear effects such as Brillouin and Raman scattering can be enhanced. There are several different but complementary ways of viewing this. In the first, one argues that the group velocity is low hence the light hangs about much longer; in the second, that the density of states is increased, so that by Fermi's Golden Rule the transition rate is higher; and in the third, that the low momentum of the Bloch photons means that they are easily scattered by weak (possibly nonlinear) perturbations. The first view leads naturally to the idea of an *effective optical path length* governed by the group velocity:

$$L_{\text{eff}} = L n_o \frac{c/n_o}{v_g} = L_{\text{av}} \frac{c/n_o}{v_g}. \quad (35)$$

Since near a band edge  $L_{\text{eff}}$  can be substantially larger than the "physical" path length based on the average index, the effectiveness of a whole range of nonlinear, electro-optic and acousto-optic effects will be enhanced. For example, an electro-optic modulator that needs to be 5 mm long for a desired performance could be reduced in length to 0.5 mm if the group velocity could be reduced by the same factor.

By way of a more detailed example we consider stimulated Brillouin scattering (SBS). In a photonic crystal consisting of holes drilled in high index materials such as Si or GaAs, the presence of significant Brillouin (and Raman) scattering will depend on the optical fields "seeing" the material, not the air. This means that only Bloch waves on the low frequency side of the stop-bands (when the field intensity peaks in the high index regions [32]) will produce a strong SBS signal. We also assume that acoustic waves whose wavelength covers many lattice periods in the photonic crystal see an "average" Young's modulus and density, and hence have a "sensible" dispersion relation. Following the formalism in [33], the Brillouin gain for interaction between two optical waves and an acoustic wave takes the form:

$$G_B = \frac{\omega \Omega_A (\partial \epsilon_r / \partial s)^2}{2 \alpha_A n_o^4 v_g^2 v_{gA} E} \quad (36)$$

in units of m/W. The acoustic frequency and power attenuation rate are  $\Omega_A/2\pi$  and  $\alpha_A$ ,  $E$  is Young's modulus,  $v_{gA}$  and  $v_g$  the acoustic and optical group velocity magnitudes, and the partial derivative of  $\epsilon_r$  with respect to strain  $s$  describes electrostriction. Comparing this expression with the gain in an isotropic medium of average index  $n_o$ , and assuming that all the parameters except  $E$ , the optical group velocities and the acoustic frequency remain unchanged (since both density and stiffness are reduced, the acoustic velocity might not change much), the enhancement in Brillouin gain is:

$$\frac{G_B}{G_{Bav}} = \frac{\Omega_A v_{gv}^2 E_{av}}{\Omega_{Aav} v_g^2 E} \quad (37)$$

If we imagine two counter-propagating Bloch waves that interfere to produce fringes of spacing  $10\lambda/n_o$ , with a reduction in group velocity of  $10\times$  and a reduction in  $E$  of  $2\times$ , an enhancement of around  $20\times$  in Brillouin gain is expected. This is not dramatic, mainly because in the photonic crystal the Stokes frequency shift is reduced and hence the proportion of each pump photon that is converted into an acoustic phonon is smaller, resulting in less power in the acoustic wave and smaller SBS gain.

## 8. Various Applications and Related Issues

One benefit of comparing the behaviour of charge waves in electronic crystals and light waves in photonic crystals is that both the similarities and the differences can lead to interesting possibilities in both fields. For example, in semiconductor crystals the atoms or molecules forming the repeating unit are identical, whereas in a photonic crystal the unit cell can take almost any shape, since it contains a very large number of atoms (in a Si/air structure at a wavelength of  $1\ \mu\text{m}$  each unit cell has  $\sim 10^9$  atoms). In addition, because the period in a photonic crystal is itself nothing special (unrelated to the size of an atom), it can be varied at will, along with all the other parameters typical of a periodic structure (average index, index contrast, crystal orientation and so on). Thus, two-dimensional photonic crystals can be imagined in which the crystal planes bend. An example is a crystal in which the "atoms" have sizes, shapes and positions given by the interference pattern generated by four cylindrical waves - see Figure 11. Electron beam lithography makes the creation of such complex patterns feasible, indeed no more difficult to produce than a perfectly regular periodic structure. Such patterns could be used for complex wavefront conversion within wavelength division multiplexing components, and for the design of microcavities in which spontaneous emission is controlled.

In solid state physics, the traditional emphasis has been on fully trapped states. In optics, because of the need to get light in and out of a device and use it, the emphasis has been on

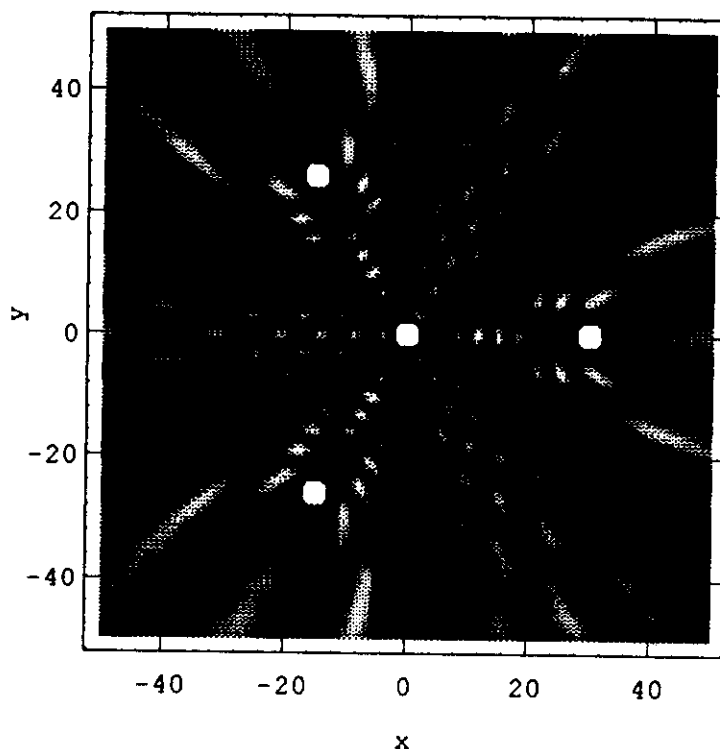


*Figure 11.* The fringe pattern generated by four cylindrical waves emanating from the origin and three points at  $120^\circ$  apart, equidistant from the origin (the white dots). If combined with very high modulation depths of refractive index, such holographically conceived patterns may exhibit rich and unusual behaviour.

semi-trapped states - ones that are coupled strongly to the outside world. The recent development of the quantum cascade semiconductor laser is the result of thinking about semi-trapped states for electrons [34].

The successful manipulation of light is a key ingredient in nearly all optoelectronic components. Photonic crystals, through the strong spatial and temporal dispersion exhibited by the Bloch waves near the band edges, are prime candidates for enhancing the interaction between light and matter and thus improving the performance of a whole range of optoelectronic components (lasers, modulators, wavefront converters). The traditional reservation often expressed about the use of periodic structures for controlling light is that the bandwidth is narrow. While this is true of structures where the step in refractive index is small, it is much less a problem in photonic band gap materials, because the number of lattice periods needed for complete reflection is often in single figures, widening the bandwidth of reflection.

It is clear that the fabrication of extended photonic crystals at optical wavelengths stretches the capability of current nanotechnology, and indeed has not yet been successful. Fabrication of periodically etched high index films is less challenging, and moreover fits more naturally with many current devices produced in waveguide form, including lasers, amplifiers, modulators, couplers, filters and nonlinear elements. It may turn out that the first major uses of photonic crystals will be in thin films; however, before this can be achieved, the problems of maintaining waveguiding in deeply etched layers must be solved. Some recent work addresses this issue [35], demonstrating that solutions already exist.

Major future problems include getting light into a photonic crystal from the external world, and avoiding strong unwanted scattering near the band edges where the photon momentum is very low. An obvious solution to the first is to interpose an adiabatic transition region within which Hamiltonian optics is valid. The second may prove more difficult to manage, since it is likely to place tight tolerances on the fabrication accuracy of each and every unit cell.

## 9. Conclusions

The novelty, timeliness and promise of photonic crystals lies not just in the production of a full photonic band gap, or in the control of the photonic density of states and hence the spontaneous emission rate in active structures, but also in the exploitation of the strong spectral and spatial dispersion that exist near a band edge, and the very rapid spatial transformations in the optical fields this makes possible, to develop new active and passive devices. For example, there are good reasons for thinking it possible to reduce the length of waveguide components such as electro-optic modulators and directional couplers by orders of magnitude. This would allow much greater packing densities on optical chips, leading to large scale integration of optical functions. The Bloch wave optics outlined in this chapter may be a useful basis upon which to design and build this next generation of components in quantum optoelectronics and optical communications.

## Acknowledgments

We gratefully acknowledge the assistance of Sarah Rutt in uncovering examples of periodic structures in the natural world, and the on-going support and interest of John Rarity, John Roberts and Terry Shepherd of DRA Malvern. The Optoelectronics Research Centre is an Interdisciplinary Research Centre of the U.K. Engineering and Physical Sciences Research Council.

## References

1. H. Ghiradella, "Light and color on the wing: structural colors in butterflies and moths," *Appl. Opt.* **30** (3492-3500) 1991
2. H. F. Nijhout, "The developmental physiology of color patterns in lepidoptera," *Adv. Insect Physiology* **19** (181-247) 1985
3. P.J. Herring, "Reflective systems in aquatic animals," *Comp. Biochem. Physiol.* **109A** (513-546) 1994
4. N. Horiuchi, "New synthetic opal made of plastics," *The Australian Gemmologist* **14** (213-218) February 1992
5. P.J. Darragh, A.J. Gaskin and J.V. Saunders, "Opals," *Scientific American* **234** (84-95) 1976
6. J.P. Gauthier, "Natural and synthetic opals: TEM structural study," *Acta Cryst.* **A40** (C248) 1984
7. G. Widawski, M. Rawiso and B. François, "Self-organised honeycomb morphology of star-polymer polystyrene films," *Nature* **369** (387-389) 1994
8. P.N. Pusey, W.C.K. Wick, S.M. Ilett and P. Bartlett, "Phase behaviour and structure of colloidal suspensions," *J. Phys.-Condensed Matter* **6** No 23A (A29-A36) 1994
9. G. Devauchelle, D.B. Stoltz and F. Darcy-Tripier, "Comparative ultrastructure of iridoviridae," *Current Topics*

- in Microbiology and Immunology*, 116 (1-21) 1985
10. M.M. Burns, J.-M. Fournier and J.A. Golovchenko, "Optical matter: Crystallization and binding in intense optical fields," *Science* 249 (749-754) 1990
  11. A. Korpel (Editor), "Selected Papers on Acoustooptics," SPIE Optical Engineering Press, volume MS16, Bellingham, Washington (1990).
  12. J.M. Cowley, "Diffraction Physics," second revised edition, North-Holland (1981).
  13. F.K. Kneubühl, "Theories of Distributed Feedback Lasers," Harwood Academic Publishers, Switzerland (1993).
  14. S.L. McCall and P.M. Platzman, "An optimised  $\pi/2$  distributed feedback laser," *IEEE J. Quant. Electr.* QE-21 (1899-1904) 1985.
  15. L. Solymar and D.J. Cooke, "Volume Holography and Volume Gratings," Academic Press, London (1981).
  16. See, e.g., J.S. Blakemore, "Solid State Physics," Cambridge University Press, Cambridge, 1991; N.W. Ashcroft and N.D. Mermin, "Solid State Physics," Harcourt Brace College Publishers, Fort Worth (1976); H. Haken, "Quantum Field Theory of Solids," North-Holland, Amsterdam (1988); C. Kittel, "Quantum Theory of Solids," John Wiley & Sons, New York (1987).
  17. E. Yablonovitch, "Photonic band gap structures," *J. Opt. Soc. Am.* 10 (283-295) 1993; J.D. Joannopoulos, R.D. Meade and J.N. Winn, "Photonic Crystals," Princeton University Press (1995); for an introduction to the use of wavevector diagrams see P.St.J. Russell, "Photonic band gaps," *Physics World* 5 (37-42) 1992.
  18. P.St.J. Russell and R. Ulrich, "Elementary and coupled waves in periodic planar waveguides," *2nd European Conference on Integrated Optics*, Florence, IEE Conf. Publication 227 (88-91) October 1983.
  19. P.St.J. Russell, "Novel thick-grating beam-squeezing device in Ta<sub>2</sub>O<sub>5</sub> corrugated planar waveguide," *Electr. Lett.* 20 (72-73) 1984.
  20. P.St.J. Russell, "Optics of Floquet-Bloch waves in dielectric gratings," *Appl. Phys.* B39 (231-246) 1986.
  21. P.St.J. Russell, "Interference of integrated Floquet-Bloch waves," *Phys. Rev. A* 33 (3232-3242) 1986.
  22. R. Zengerle, "Light propagation in single and doubly periodic planar waveguides," *J. Mod. Opt.* 34 (1589-1617) 1987.
  23. J.P. Wolfe, "Acoustic wavefronts in crystalline solids," *Physics Today* 48 (34-40) 1995.
  24. P.St.J. Russell, T.A. Birks and F.D. Lloyd-Lucas, "Photonic Bloch Waves and Photonic Band Gaps," in *Confined Electrons and Photons: New Physics and Applications*, E. Burstein & C. Weisbuch (editors), (585-633), Plenum Press, 1995
  25. A.W. Snyder and J.D. Love, "Optical Waveguide Theory," Chapman and Hall, London (1983).
  26. E. Yablonovitch, T.J. Gmitter, R.D. Meade, A.M. Rappe, K.D. Brommer and J.D. Joannopoulos, "Donor and acceptor modes in photonic band structure," *Phys. Rev. Lett.* 67 (3380-3383) 1991.
  27. D.R. Smith, R. Dalichaouch, N. Kroll, S. Schultz, S.L. McCall and P.M. Platzman, "Photonic band structure and defects in one and two dimensions," *J. Opt. Soc. Am.* 10 (314-321) 1993.
  28. J. A. Arnaud, "Beam and Fiber Optics," (Academic Press, New York, San Francisco, London, 1976)
  29. Z.G. Pinsker, "Dynamical Scattering of X-rays in Crystals," Springer-Verlag, Berlin (1978).
  30. P.St.J. Russell, "Bragg resonance of light in optical superlattices," *Phys. Rev. Lett.* 56 (596-599) 1986.
  31. P.St.J. Russell, "Optical superlattices for modulation and deflection of light," *J. Appl. Phys.* 59 (3344-3355) 1986.
  32. P.St.J. Russell, "Bloch wave analysis of dispersion and pulse propagation in pure distributed feedback structures", *J. Modern Optics*, 38 (1599-1619) 1991; Erratum: J. Capmany and P.St.J. Russell, *J. Mod. Optics* 1994.
  33. P.St.J. Russell, D. Culverhouse and F. Farahi, "Theory of forward stimulated Brillouin scattering in dual-mode single-core fibres," *IEEE J. Quant. Electr.*, 27 (836-842) 1991.
  34. J. Faist, F. Capasso, D.L. Sivco, A.L. Hutchinson, C. Sirtori and A.Y. Cho, "Quantum cascade laser - a new optical source in the mid infrared," *Infrared Physics & Technology* (1350-1395) 36 1995.
  35. D.M. Atkin, P.St.J. Russell, T.A. Birks and P.J. Roberts, "Photonic band structure of a periodically etched high-index waveguide layer: stationary resonant modes with a high Q-factor," proceedings of CLEO'95, Baltimore, U.S.A., paper CWF53, (223) 1995; full article in preparation (contact authors for preprint).



## Photonic band structure of guided Bloch modes in high index films fully etched through with periodic microstructure

D. M. ATKIN, P. ST. J. RUSSELL, T. A. BIRKS

Optoelectronics Research Centre, University of Southampton,  
Hampshire SO17 1BJ, England

and P. J. ROBERTS

Defence Research Agency, St. Andrews Road, Malvern WR14 3PS,  
England

(Received 18 October 1995)

**Abstract.** By adapting the well-known 'zigzag' ray model for use with a *periodic* waveguide (i.e. replacing the plane wave rays with Bloch wave rays), we show that thin films of high refractive index, supported by a low index substrate and fully etched through with a periodic pattern, can support guided modes. From the dispersion relation of these guided *Bloch* modes, it is shown that the in-plane modal group velocity can be zero, suggesting applications in enhanced dipole-field interactions and control of spontaneous emission in waveguide lasers.

### 1. Introduction

It is now accepted that, within a band of frequencies known as a photonic band gap (PBG), all the electromagnetic modes in a volume of dielectric material can be suppressed by appropriate periodic patterning, i.e. by the creation of a *photonic crystal* [1-3]. This permits a single intra-PBG electromagnetic mode (or resonance) with high quality factor ( $Q$ ) to be introduced by means of a structural point defect. At the resonant frequency of this mode there can appear a substantial (depending on the  $Q$ -factor) enhancement in vacuum field intensity. If an electronic dipole whose transition coincides with this frequency is introduced, spontaneous emission will be enhanced and low threshold highly efficient lasing achieved [4].

The first such microlaser awaits the realization of a full PBG at optical frequencies, a task which pushes at the limits of what is possible in state-of-the-art nanofabrication. In the face of this considerable technological challenge, a number of groups worldwide are investigating the use of simpler structures supporting PBGs in two dimensions [5-10]. For example, arrays of closely spaced vertical cavity emitting lasers are being constructed in which it is hoped to suppress lateral emission by creating an in-plane PBG [11]. The performance of structures of this sort will, however, only be attractive if *waveguiding* is built into the designs, i.e. if fully trapped transverse resonances are created where the light bounces to and fro between the upper and lower interfaces of the periodic layer. Only a few of the published numerical studies of photonic band structure in two dimensions treat this case [6, 8, 12]. Most do not allow for propagation along the third dimension—essential if guided modes are sought.

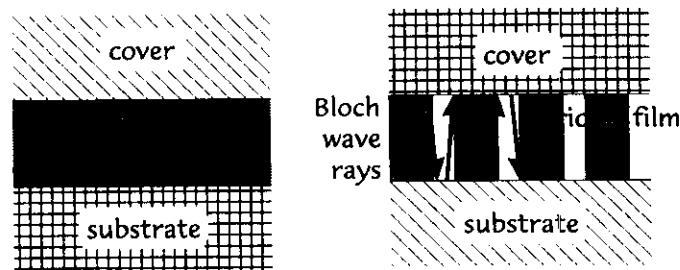


Figure 1. Comparison of (left) the conventional approach to tackling propagation in a weakly periodic guide and (right) the approach adopted in this paper in which the Bloch waves of the periodic layer are used to construct the guided Bloch modes.

Prior analyses on Bragg diffraction in periodic waveguides (e.g. fibre gratings or DFB lasers) start with the assumption that the refractive index modulation is weaker than the index step that forms the waveguide [13]. This allows one to construct a theory based on the coupling of power between a pair of guided modes satisfying a Bragg condition, the essential approximation being that the 'strongly' guided modes are resistant to the weaker periodic perturbation. In this paper, driven by the PBG requirement for large index modulation, we tackle the case (see figure 1) where this is no longer a good approximation. Rather than building *coupled mode equations* from the *guided modes* of a film of the same average index, we construct the *guided modes* of the fully etched layer from the *Bloch waves* of the periodic medium out of which the layer is constructed. The resulting *guided Bloch modes* contain all the salient features of propagation in the periodic layer, including the photonic band structure, dispersion and group velocity. As we shall show, stationary modes can be found (at particular frequencies) that have zero group velocity in the guiding plane. These modes will interact very strongly with a dipole of the correct frequency if it is incorporated into the waveguide.

The generic structure (figure 2) consists of strips of high index dielectric sandwiched between media of lower refractive index, the cover and the gaps between the strips being air. This provides an extremely high modulation depth of the refractive index in-plane. Although there are physical gaps in the waveguiding layer, these turn out—under the correct conditions—to be below the resolution limit of light both in the cover and the substrate, permitting strongly guided modes to be supported. We shall now obtain the field structure and

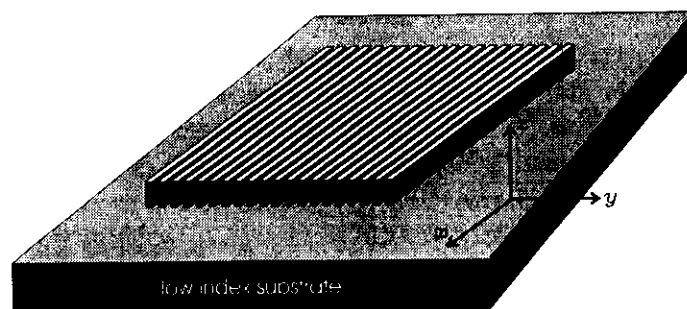


Figure 2. The structure analysed consists of lines of high refractive index placed on a substrate of low refractive index, the other regions being filled with air. Propagation in the  $(y, z)$  plane only is considered.



dispersion of the Bloch modes in an infinite periodic stack, and then use a 'zigzag' ray picture [14] (in which the ray direction is given by the group velocity of the Bloch waves) to derive the dispersion relation of the guided Bloch modes in a slice of this stack placed between two media of lower refractive index.

## 2. Bloch waves of infinite periodic stack

Our starting point is the standard translation matrix technique for a dielectric stack formed from alternating layers of high and low refractive index [9, 15]. We use this to obtain the dispersion relation for the Bloch waves. For completeness we present the main steps in this analysis, relegating most of the details to the Appendix.

The dielectric stack consists of alternating layers of refractive index  $n_1$  and  $n_2$  and widths  $h_1$  and  $h_2$  the stack period being  $\Lambda = (h_1 + h_2)$ . Cartesian axes are oriented with  $y$  normal to the layer boundaries and  $z$  along the layers (figure 2). No field variation with  $x$  is allowed, which allows separation of the fields into transverse magnetic (TM) and transverse electric (TE) states, with respectively  $E_x = H_y = H_z = 0$  and  $H_x = E_y = E_z = 0$ . In each case, all field components can be written in terms of the surviving  $x$ -component,  $f$ , which may be expressed in the  $j$ th layer ( $j = 1, 2$ ) of the  $N$ th period as:

$$f_j^N(y) = a_j^N \cos [p_j(y - y_j^N)] + b_j^N \frac{\sin [p_j(y - y_j^N)]}{\xi_j p_j \Lambda} \quad (1)$$

where  $a_j^N$  and  $b_j^N$  are constants to be determined,  $y_j^N$  is the value of  $y$  at the centre of the  $j$ th layer of the  $N$ th period and  $p_j$  is the wavevector component of the field normal to the interface within each medium:

$$p_j = (k^2 n_j^2 - \beta^2)^{1/2} \quad (2)$$

where  $\beta$  is the propagation constant in the  $z$  direction and  $\mathbf{k}$  is the vacuum wavevector. The TE and TM cases are selected via the parameter  $\xi_j$ :

$$\xi_j = 1 \quad (\text{TE}) \quad \text{or} \quad \xi_j = 1/n_j^2 \quad (\text{TM}). \quad (3)$$

The field throughout the stack is completely specified by a two-component state vector consisting of the constants  $a_j^N$  and  $b_j^N$ . The state vector in one layer is related to the state vector in the corresponding layer in the previous period by operation with a  $2 \times 2$  translation matrix,  $\mathbf{M}$ :

$$\begin{pmatrix} a_j^{N+1} \\ b_j^{N+1} \end{pmatrix} = \mathbf{M} \begin{pmatrix} a_j^N \\ b_j^N \end{pmatrix} = \begin{pmatrix} A & B \\ C & A \end{pmatrix} \begin{pmatrix} a_j^N \\ b_j^N \end{pmatrix}. \quad (4)$$

See the appendix for the elements of  $\mathbf{M}$ , and for the elements of the matrix  $\mathbf{M}_{12}$  relating the state vector in layer  $j = 1$  to the state vector in the neighbouring layer  $j = 2$ . The eigenvalues and eigenvectors of  $\mathbf{M}$  are given simply by:

$$\lambda_{\pm} = A \pm (BC)^{1/2}, \quad \mathbf{f}_{\pm} = \begin{pmatrix} +B^{1/2} \\ \pm C^{1/2} \end{pmatrix} \quad (5)$$

where  $BC = A^2 - 1$  and  $|\mathbf{M}| = 1$ , i.e.  $\mathbf{M}$  is unimodular. This implies that the product of the eigenvalues is unity and thus, without loss of generality, that:

$$\lambda_{\pm} = \exp(\pm jk_y \Lambda), \quad k_y = \frac{\arccos A}{\Lambda} \quad (6)$$

where  $k_y$  is the Bloch wavevector. For a given polarization state at fixed optical frequency and  $\beta$ , the complete field in the structure is expressible as a superposition of two Bloch waves with field distributions:

$$f_{\pm}(y) \exp[-j\beta z] = B_{\pm}(y) \exp[-j(\beta z \pm k_y y)] \quad (7)$$

where the function  $B_{\pm}(y)$  is periodic with period  $\Lambda$ .

### 3. The wavevector diagram

The wavevector diagram is a plot of the loci of real wavevectors at fixed optical frequency in the multilayer stack. It is extremely useful for establishing a clear graphical understanding of the boundary conditions on either side of the periodic layer [9]. First the following set of normalized parameters is adopted:

$$\begin{aligned} n_{av} &= (n_1 h_1 + n_2 h_2) / \Lambda \\ v &= kn_{av} \Lambda, \quad n_R = n_2 / n_1, \quad \tau = h_2 / \Lambda \end{aligned} \quad (8)$$

where  $n_{av}$  is the *weighted average index*,  $v$  is the *normalized frequency*,  $n_R$  the *index ratio* and  $\tau$  the *relative layer thickness*. A series of wavevector diagrams, plotted for a multilayer structure consisting of alternating layers of air and silicon ( $n_R = 3.45$ ) with  $\tau = 0.8$ , is given in figure 3. For a normalized frequency  $v = 2$  and TE propagation, the mode index of the Bloch waves is approximately isotropic and equal to the average index,  $n_{av}$ . The circles repeat in the  $y$  direction at intervals of  $2\pi/\Lambda$  as a consequence of Bloch's theorem. The TM wavevector diagram on the other hand is elliptical, expressing the birefringence of the periodic structure. At a normalized frequency of  $v = 3$  a momentum gap appears within a certain range of  $\beta$  values. In this gap the Bloch waves are evanescent, i.e. if the stack is infinite in extent they cannot exist. The group velocity of the travelling Bloch waves is given by:

$$\mathbf{v}_g = \nabla_{\mathbf{k}} \omega(\mathbf{k}) \quad (9)$$

which indicates that  $\mathbf{v}_g$  is oriented normal to the curves in wavevector space, pointing in the direction of increasing frequency. The points where the momentum gap is narrowest occur at  $k_y \Lambda / \pi = 1$ , and will be referred to as the *symmetric points*; at these points the group velocity points exactly *along* the layers. When the normalized frequency is increased to 4, ellipse-like shapes appear in the momentum gaps. These give rise to an additional pair of symmetric points. We shall refer to the Bloch waves on the 'ellipse' as the fast Bloch waves and those on the outer branches as slow Bloch waves, a naming convention which relates to the phase velocity along the layers.

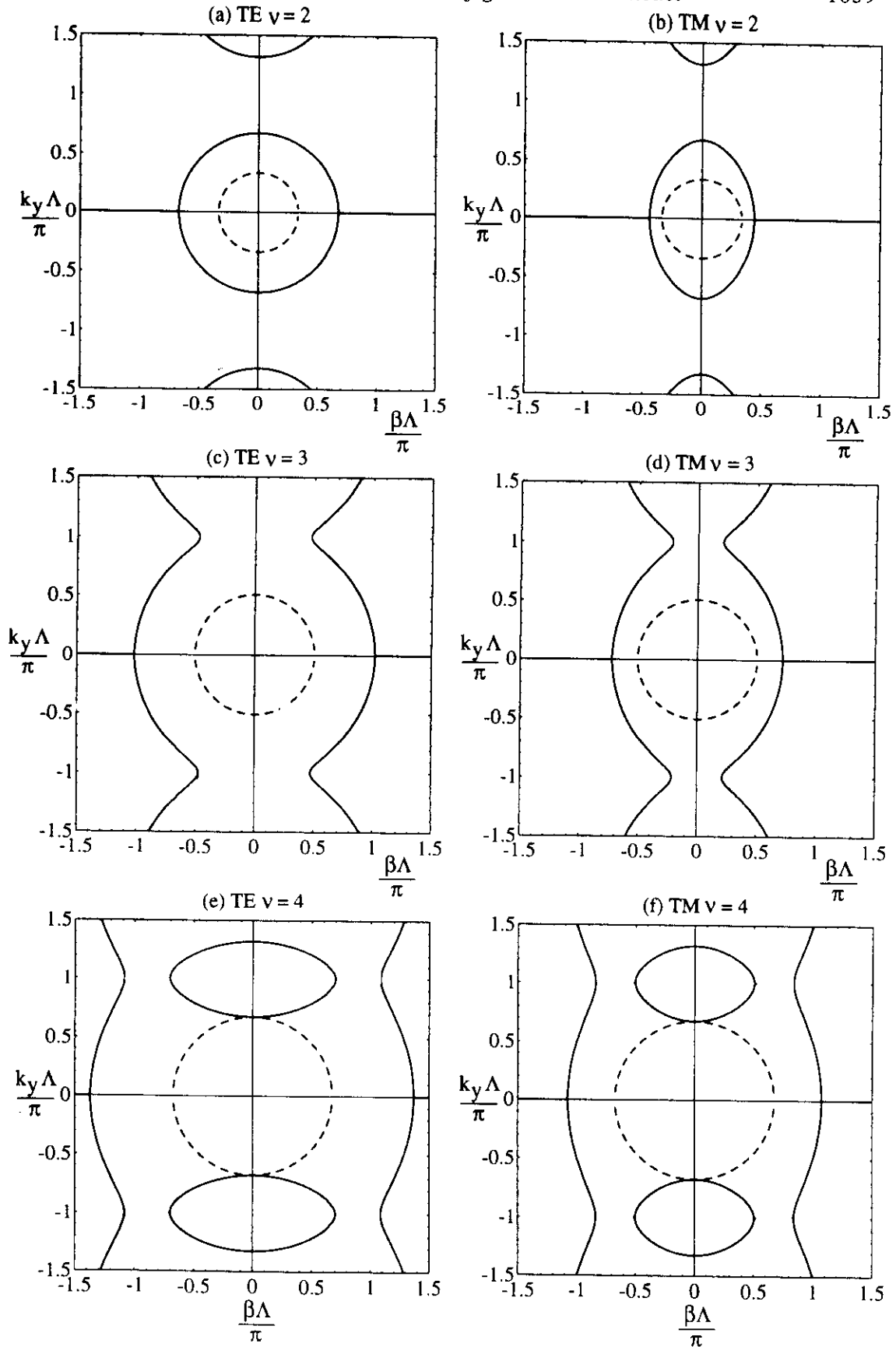


Figure 3. Series of wavevector diagrams for TE and TM cases at three different normalized frequencies  $\nu$  in a multilayer stack with  $n_1 = 1$ ,  $n_2 = 3.45$ ,  $n_{ss} = 1.57$ ,  $n_{co} = 1$  and  $\tau = 0.8$ .

#### 4. Boundary conditions

At fixed optical frequency, boundary conditions specify that the components of wave momentum along a planar interface must be conserved as the interface is crossed. By superimposing the wavevector diagrams for the two adjoining materials, fulfilment of this condition is easy to visualize graphically. In our case the diagram for the substrate is simply a circle:

$$k_y^2 + \beta^2 = k^2 n_{ss}^2 = \left( \frac{n_{ss} v}{n_{av} \Lambda} \right)^2 \quad (10)$$

which is shown (with dotted curves) on figure 3. To treat phase matching at, for example, an interface in the  $(x, y)$  plane, a horizontal construction line is drawn on the  $(\beta, k_y)$  diagram. For  $k_y \Lambda / \pi$  close to 1 this line does not intersect the substrate circle, so that total internal reflection occurs and the Bloch waves are trapped in the periodic layer. As  $k_y \Lambda / \pi$  decreases, the line eventually intersects the substrate circle, and the Bloch waves radiate from the periodic layer into the substrate.

#### 5. Symmetrical points on the frequency versus $\beta$ diagram

On this diagram (figure 4), the positions of the momentum gap edges are plotted as a function of frequency for the same structure as treated in figure 3. In the regions of the diagram that are not shaded  $k_y$  is real and the corresponding Bloch waves propagate freely in the structure. Below the  $k_y \Lambda / \pi = 0$  line the Bloch waves are cut-off. In the shaded regions between the  $k_y \Lambda / \pi = 1$  lines,  $k_y$  is complex and the Bloch waves are evanescent. In the TM case the gap width shrinks to zero at  $\beta \Lambda / \pi \approx 0.3$ , which occurs when the rays in each layer are incident on the interfaces at Brewster's angle.

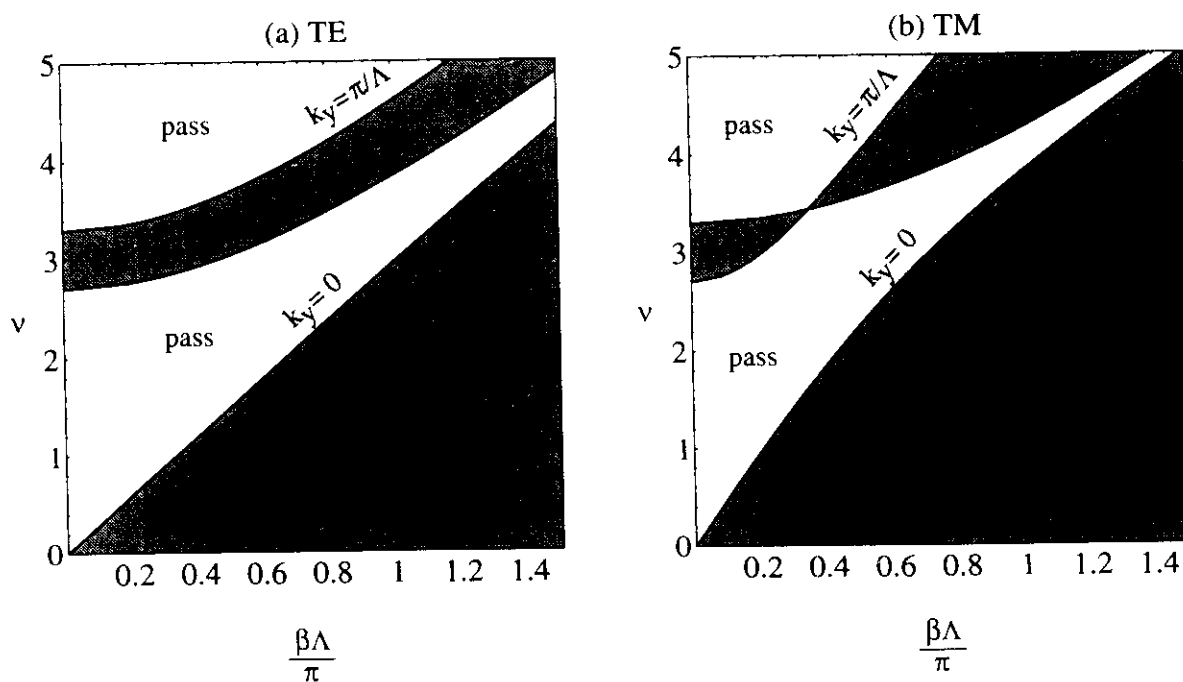


Figure 4. Frequency versus  $\beta$  diagram for the multilayer stack of figure 3 ( $n_1 = 1$ ,  $n_2 = 3.45$ ,  $n_{ss} = 1.57$ ,  $n_{co} = 1$  and  $\tau = 0.8$ ).

## 6. Two-wave approximation for the Bloch waves

To reduce the complexity of the problem, we now take the Fourier transform of the periodic part  $B_{\pm}(y)$  of the Bloch wave fields, and extract the amplitudes of the *two dominant partial waves* in the plane-wave expansion. These are then matched to the fields with *upward* ( $+y$ ) and *downward* ( $-y$ ) progressing phase velocities (evanescent in the  $z$ -direction) in the substrate and cover regions. All the higher order partial plane waves are ignored; as we shall show, the accuracy of this approximation is such that the solutions compare favourably with the results of a numerical finite-difference analysis.

Each Bloch wave can be expanded in terms of an infinite set of partial plane waves whose wavevectors are related by Floquet's theorem:

$$k_n = \beta \hat{z} + (k_y + nK) \hat{y} \quad (11)$$

where  $K = 2\pi/\Lambda$  is the grating vector. This permits us to express the exact solutions from the translation matrix analysis,  $B_{\pm}(y)$  in (7), in the general form:

$$B_{\pm}(y) = \sum_n S_n^{\pm} \exp(-jnKy) \quad (12)$$

where the  $S_n^{\pm}$  are the complex plane wave amplitudes, whose values are easily found by performing Fourier analysis, yielding:

$$S_n^{\pm} = \frac{1}{\Lambda} \int_{-\Lambda/2}^{\Lambda/2} B_{\pm}(y) \exp(jnKy) dy. \quad (13)$$

Retaining the two dominant partial waves, the Bloch wave fields  $b_{\pm}(y, z)$  are given approximately by:

$$b_{\pm}(y, z) \approx \exp[-j(\beta z \pm k_y y)](S_0^{\pm} + S_{\pm 1}^{\pm} \exp(jKy)) \quad (14)$$

where as before the choice of  $+$  or  $-$  determines the group of Bloch waves that progresses (or evanesces) in the  $+y$  or  $-y$  directions.

The percentage errors in amplitude and phase introduced by this approximation are plotted in figure 5 for normalized frequencies of 3 and 4. For slow Bloch waves the amplitude error is less than 3% and the phase error less than 0.5% over the parameter range of interest. For fast Bloch waves the worst case is at the top of the frequency range and gives an amplitude error between 6 and 7% and a phase error less than 0.8%.

## 7. Guided Bloch modes

We are now in a position to obtain the dispersion relation of the guided Bloch modes. The interfaces are considered to be parallel and separated by a distance  $h$ . The boundary conditions require that all wavevector components in the  $y$ -direction be continuous across the interfaces. The most general case (or four participating Bloch waves) is illustrated in figure 6, the arrows indicating the directions of the group velocities in the layer. The upward (U) and downward (D) partial waves in each of the four Bloch waves (labelled by  $f$  (fast) and  $s$  (slow) for  $\beta > 0$ , and  $\bar{f}$  (fast) and  $\bar{s}$  (slow) for  $\beta < 0$ ) are now matched to the upward and downward evanescent waves in the cover (co) and substrate (ss). The surviving  $x$  components  $b_f, b_{\bar{f}}, b_s,$

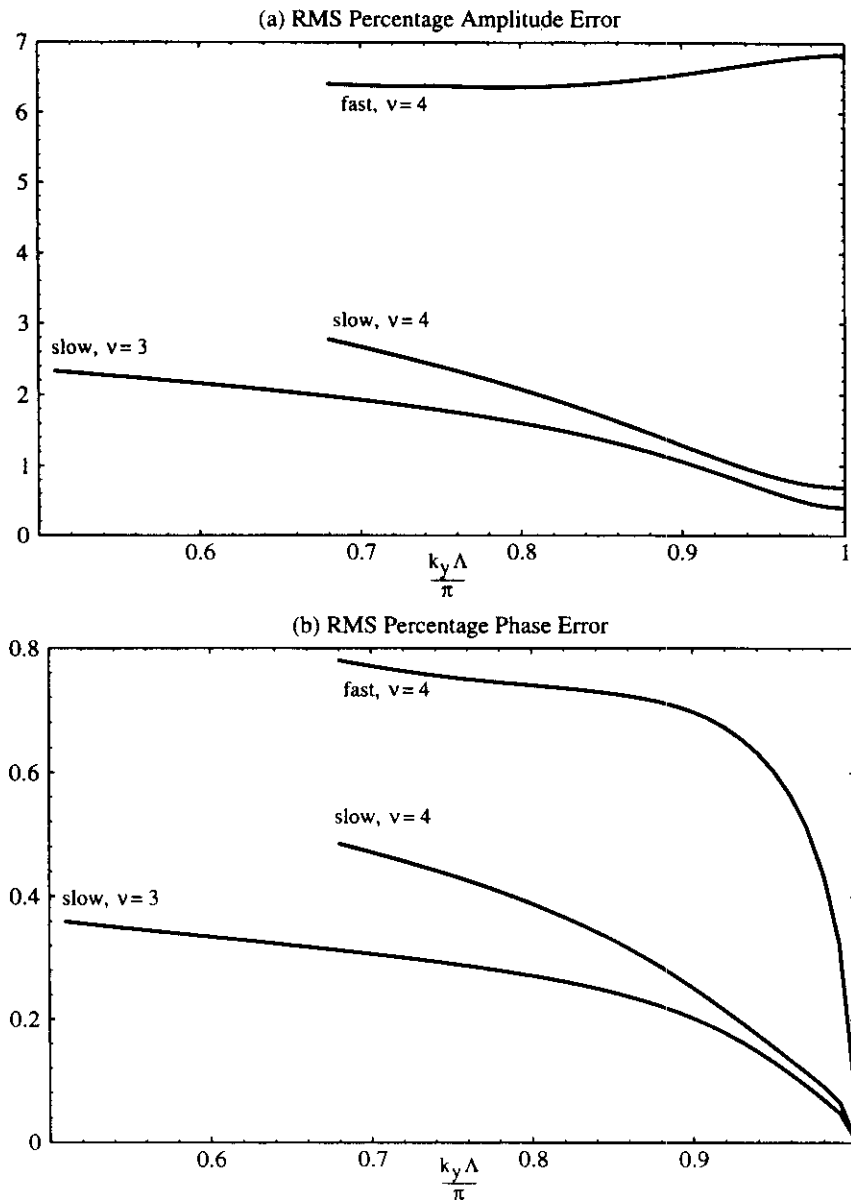


Figure 5. Percentage root mean square errors in (a) phase and (b) field amplitude introduced by truncation of the plane wave spectrum to two partial waves. The mean is averaged over one grating period ( $n_1 = 1$ ,  $n_2 = 3.45$ ,  $n_{ss} = 1.57$ ,  $n_{co} = 1$  and  $\tau = 0.8$ ). At a normalized frequency of 3 only slow waves exist and the errors are less severe. The size of the errors increase with increasing frequency. The errors for fast and slow waves are shown for the highest frequency of interest,  $v = 4$ .

and  $b_s$  of the Bloch wave fields (from (14), taking without loss of generality the + sign and replacing the subscripts  $\pm$  with f or s) are:

$$\frac{b_f}{V_f \exp(-j\beta_f z)} = \frac{b_{\bar{f}}}{V_{\bar{f}} \exp(j\beta_f z)} = \exp(-jk_y y)(F_U - F_D \exp(jKy)) \quad (15)$$

where f and  $F$  are simply replaced by s and  $S$  for the slow Bloch waves. The  $F_U$  and  $F_D$  are the renamed upward and downward partial wave amplitudes (identical for  $\beta = \pm|\beta|$ ) from (14),  $\beta_f$  is the value of  $\beta$  on the inner (fast) stop-band branch,

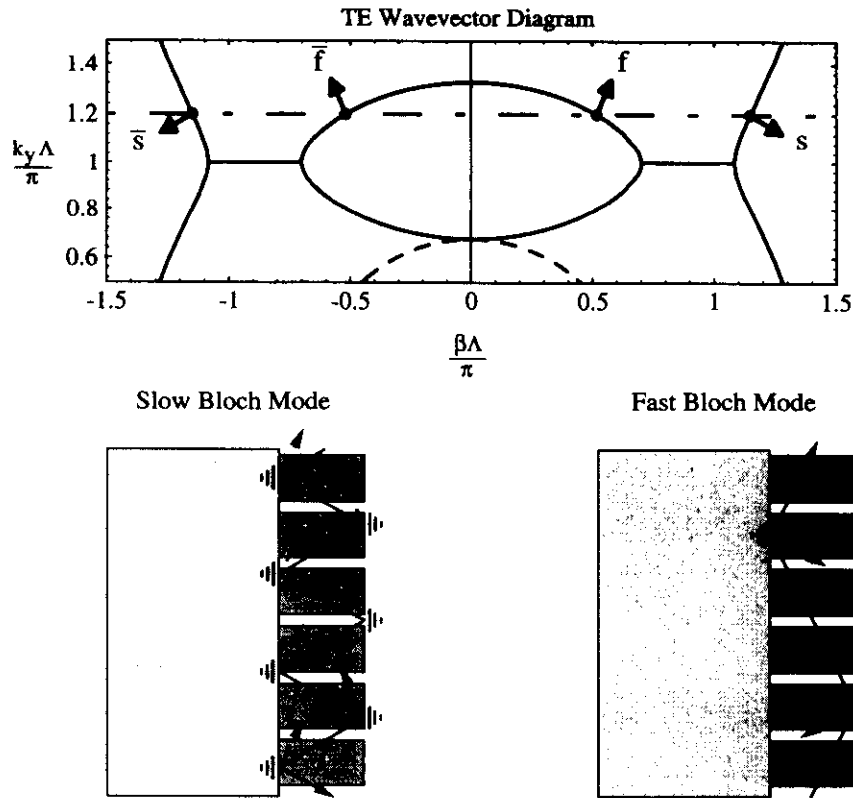


Figure 6. The waveguide modes are found by matching  $k_y$  at the substrate and air interfaces and then satisfying a resonance condition. At each interface four Bloch waves are matched to two evanescent plane waves, i.e. an incident wave of one type scatters partially into a wave of the other type at the interface. However only the waves that satisfy the resonance condition will propagate along the waveguide.

$\beta_s$  is the value of  $\beta$  on the outer (slow) stop-band branch and  $V_j$  are the Bloch wave amplitudes (to be determined). If the 'ellipse' is not present, then  $\beta_f$  is pure imaginary. The Evanescent fields in the cover ( $E_{co}$ ,  $z \geq h/2$ ) and substrate ( $E_{ss}$ ,  $z \leq -h/2$ ) regions are given by:

$$\begin{aligned}
 E_{co} \exp(jk_y y) &= U_{co} \exp[-(k_y^2 - k^2 n_{co}^2)^{1/2}(z - h/2)] \\
 &\quad + D_{co} \exp[-[(k_y - K)^2 - k^2 n_{co}^2]^{1/2}(z - h/2)] \exp(jKy) \\
 E_{ss} \exp(jk_y y) &= U_{ss} \exp[(k_y^2 - k^2 n_{ss}^2)^{1/2}(z + h/2)] \\
 &\quad + D_{ss} \exp[[k_y - K]^2 - k^2 n_{ss}^2]^{1/2}(z + h/2)] \exp(jKy) \quad (16)
 \end{aligned}$$

where  $h$  is the layer width,  $U_{co}$ ,  $U_{ss}$ ,  $D_{co}$ , and  $D_{ss}$  being the upward (+ $y$ ) and downward (- $y$ ) progressing wave amplitudes in the cover and substrate. Requiring continuity of the  $x$ -components and derivatives† of the upward and downward fields

† For the TM case the boundary condition, at the interface between the periodic structure and the cover or substrate, requires continuity of  $(1/n^2(y))(dH_x/dz)$ . In the present analysis it is assumed that, for this boundary condition,  $n(y)$  is constant and equal to the average index,  $n_{av}$ . A more accurate approach would involve finding Fourier components of  $1/n^2(y)$  and incorporating these into the analysis. However, when the results from both methods are compared, the error is very small, validating the initial approximation.

at the substrate and cover interfaces yields eight boundary conditions, which are most conveniently written in the form of a matrix equation:

$$\begin{pmatrix} F_U e^{+\phi} & F_U e^{-\phi} & S_U e^{-\sigma} & S_U e^{+\sigma} & -1 & 0 & 0 & 0 \\ F_D e^{+\phi} & F_D e^{-\phi} & S_D e^{-\sigma} & S_D e^{+\sigma} & 0 & -1 & 0 & 0 \\ F_U e^{-\phi} & F_U e^{+\phi} & S_U e^{+\sigma} & S_U e^{-\sigma} & 0 & 0 & -1 & 0 \\ F_D e^{-\phi} & F_D e^{+\phi} & S_D e^{+\sigma} & S_D e^{-\sigma} & 0 & 0 & 0 & -1 \\ \beta_f F_U e^{+\phi} & -\beta_f F_U e^{-\phi} & -\beta_s S_U e^{-\sigma} & \beta_s S_U e^{+\sigma} & -j p_{ssU} & 0 & 0 & 0 \\ \beta_f F_D e^{+\phi} & -\beta_f F_D e^{-\phi} & -\beta_s S_D e^{-\sigma} & \beta_s S_D e^{+\sigma} & 0 & -j p_{ssD} & 0 & 0 \\ \beta_f F_U e^{-\phi} & -\beta_f F_U e^{+\phi} & -\beta_s S_U e^{+\sigma} & \beta_s S_U e^{-\sigma} & 0 & 0 & j p_{coU} & 0 \\ \beta_f F_D e^{-\phi} & -\beta_f F_D e^{+\phi} & -\beta_s S_D e^{+\sigma} & \beta_s S_D e^{-\sigma} & 0 & 0 & 0 & j p_{coD} \end{pmatrix} \times \begin{pmatrix} V_f \\ V_f \\ V_s \\ V_s \\ U_{ss} \\ D_{ss} \\ U_{co} \\ D_{co} \end{pmatrix} = 0 \quad (17)$$

where

$$\begin{aligned} \phi &= j\beta_f h/2, & \sigma &= j\beta_s h/2, \\ p_{jU} &= \xi_j (k_y^2 - k^2 n_j^2)^{1/2}, & p_{jD} &= \xi_j [(k_y - K)^2 - k^2 n_j^2]^{1/2}, \\ \xi_j &= 1 \quad (\text{TE}) \quad \text{or} \quad \xi_j = n_{av}^2/n_j^2 \quad (\text{TM}) \end{aligned} \quad (18)$$

are the definitions of the various parameters and  $j = \text{co}$  or  $\text{ss}$ . Real values of  $k_y$  for which the determinant of this matrix is zero yield the guided Bloch modes of the periodic layer. At the symmetric points ( $k_y A/\pi = \pm 1$ ), the upward and downward partial waves have equal and opposite wavevectors, which means that the conditions for the upward and downward waves are identical. Since the fast and slow guided Bloch modes are orthogonal at this point and can be considered separately, the problem reduces to a much simpler  $4 \times 4$  matrix yielding the following dispersion equation for the guided modes:

$$\tan(\beta_q h + m\pi) = \frac{\beta_q(p_{ssU} + p_{coU})}{\beta_q^2 - p_{ssU}p_{coU}} = \frac{\beta_q(p_{ssD} + p_{coD})}{\beta_q^2 - p_{ssD}p_{coD}} \quad (19)$$

where  $q = f$  or  $s$  (for the fast or slow Bloch waves) and  $m$  is an integer. This is very similar to the standard dispersion relation for an asymmetric slab waveguide [14].



## 8. Results

### 8.1. Guided Bloch modes at symmetric points

Figure 7 shows plots of normalized frequency  $\nu$  versus  $h/\Lambda$  for a Si structure on a glass substrate ( $n_1 = 1$ ,  $n_2 = 3.45$ ,  $n_{ss} = 1.57$ ,  $n_{co} = 1$ ,  $\tau = 0.8$ , yielding  $n_{av} = 2.96$ ). Since they reside at the symmetrical points on the wavevector diagram, these guided Bloch modes have zero group velocity in the direction parallel to the substrate and are fully confined within the layer. For small values of  $h$  the modes are widely spaced in frequency. The upper set of curves (dashed line style) is for

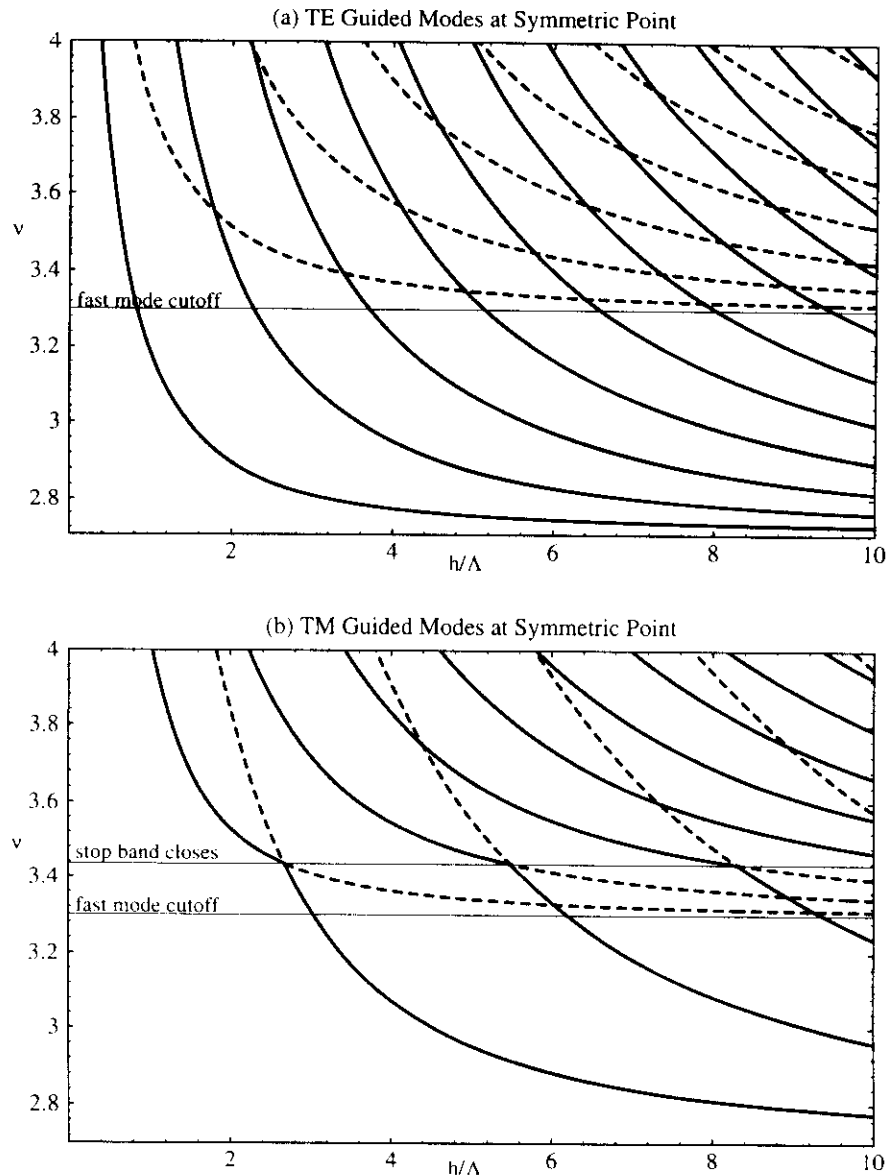


Figure 7. Normalised frequency  $\nu$  versus  $h/\Lambda$  for the guided Bloch modes at the symmetrical points in a Si structure on a glass substrate ( $n_1 = 1$ ,  $n_2 = 3.45$ ,  $n_{ss} = 1.57$ ,  $n_{co} = 1$  and  $\tau = 0.8$ ). The solid lines represent slow modes and the dashed lines represent fast modes. The fast mode cutoff at  $\nu = 3.2996$ . In the TM case (b) the modes switch from fast to slow at  $\nu = 3.435$ . This is a result of the definition of fast and slow modes and the crossing of the  $k_y = \pi/\Lambda$  lines in figure 4 where the stop band closes.

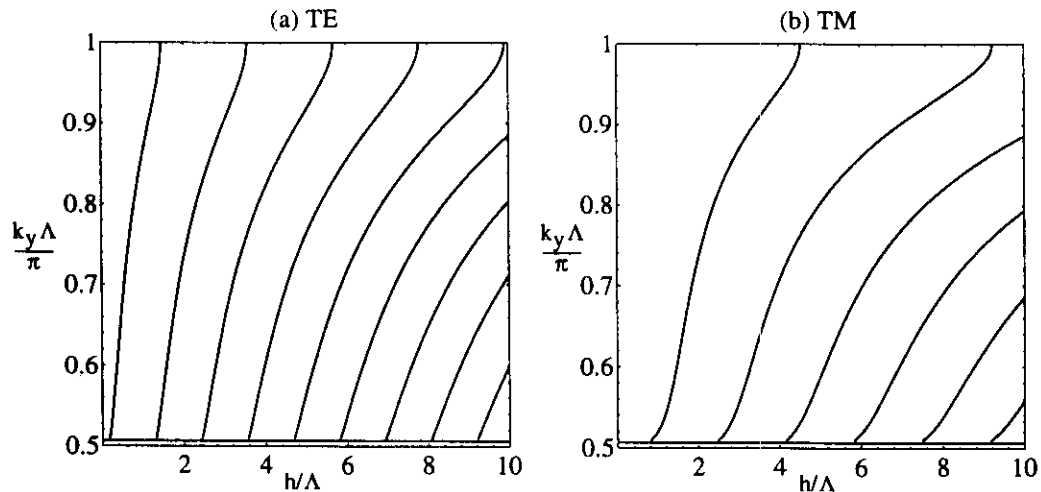


Figure 8. Plots of  $k_y \Lambda / \pi$  versus normalized layer thickness  $h/\Lambda$  for (a) TE and (b) TM modes in a structure with  $n_1 = 1$ ,  $n_2 = 3.45$ ,  $n_{ss} = 1.57$ ,  $n_{co} = 1$  and  $\tau = 0.8$  at a normalized frequency  $\nu = 3$ . The fast modes are evanescent, and the slow modes cut off when the  $k_y \Lambda / \pi$  intersects with the substrate circle.

the fast modes. These disappear at normalized frequencies below  $\nu = 3.2996$ , which corresponds to the disappearance of the 'ellipse' on the wavevector diagram. The lower set of curves (full line style) is for the slow modes. The fast and slow modes occur in pairs, each pair straddling the corresponding mode that would occur in a homogeneous slab waveguide of the same average index.

### 8.2. Behaviour away from symmetric points

Away from the symmetric points, the guided Bloch modes are described by full solutions of (17). Plots of  $k_y \Lambda / \pi$  versus normalized layer thickness  $h/\Lambda$  are presented in figure 8 for TE and TM modes at a normalized frequency  $\nu = 3$ . At this frequency only slow modes exist, there being no 'ellipse' on the wavevector diagram, rendering the fast modes evanescent. Note that for small enough layer thickness only one mode is available over the whole range of  $k_y$ . The guided modes cut off when  $k_y \Lambda / \pi$  intersects with the substrate circle; this condition is indicated by the horizontal line near the base of the figures.

Figure 9 is a repeat of figure 8 for a normalized frequency  $\nu = 4$ . The set of near-vertical curves corresponds to slow modes, and the second set of curves corresponds to fast modes. As the modes move away from the symmetrical point, increasingly strong anti-crossing occurs at the intersection points of the curves. This is due to coupling between fast and slow Bloch waves at the interfaces. When, for example, a fast Bloch wave collides with the cover or substrate interface, it is split by total internal reflection into a mixture of a strong fast and a weaker slow Bloch wave.

### 8.3. Brillouin diagram

Figure 10 shows plots of  $\nu$  versus  $k_y \Lambda / \pi$  for TE modes for a structure of thickness  $1.5\Lambda$  ( $n_1 = 1$ ,  $n_2 = 3.45$ ,  $n_{ss} = 1.57$ ,  $n_{co} = 1$  and  $\tau = 0.8$ ). The shaded regions to the upper left and right occur when  $k_y \Lambda / \pi = \nu n_{av}$ , i.e. when the substrate circle is touched and there is radiation into the substrate. The lowest curve with

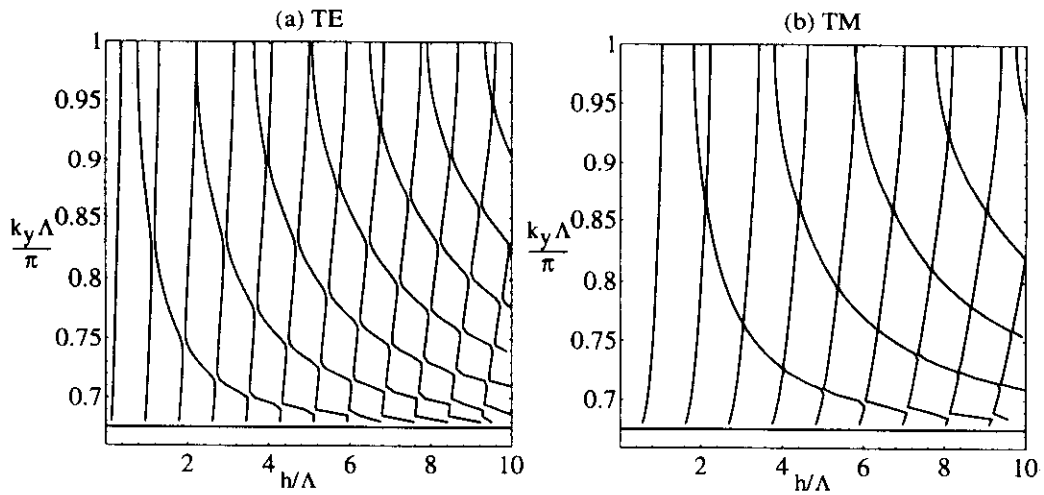


Figure 9. Plots of  $k_y\Lambda/\pi$  versus normalized layer thickness  $h/\Lambda$  for (a) TE and (b) TM modes in the same structure as in figure 8, at a normalized frequency  $\nu = 4$ . Both fast and slow modes are present, and once again they cut off when the  $k_y\Lambda/\pi$  intersects the substrate circle.

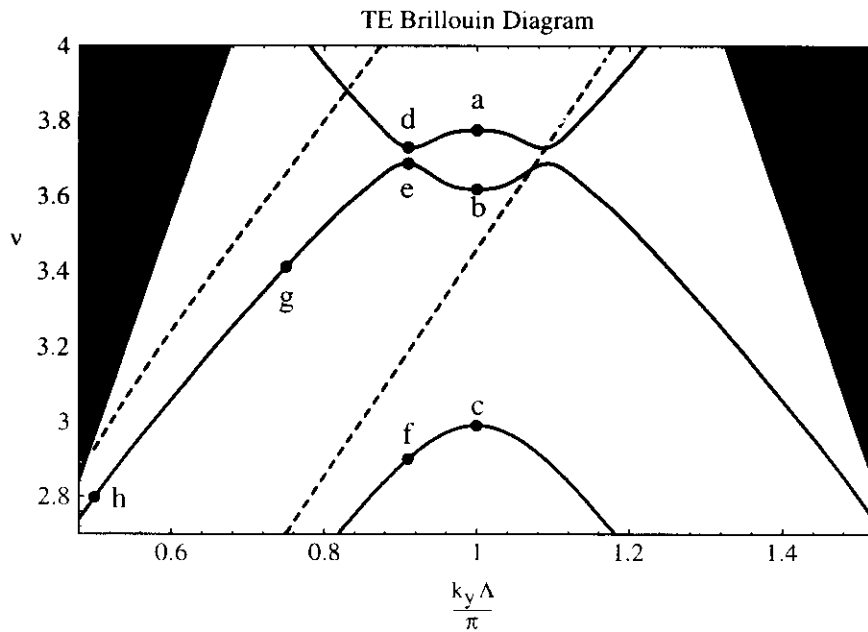


Figure 10. TE Brillouin diagram ( $\nu$  versus  $k_y\Lambda/\pi$ ) for a structure of thickness  $1.5\Lambda$  ( $n_1 = 1$ ,  $n_2 = 3.45$ ,  $n_{ss} = 1.57$ ,  $n_{co} = 1$  and  $\tau = 0.8$ ). The shaded regions correspond to modes that radiate into the substrate. The solid curves are the Bloch wave modes and the dashed curves represent the zero and first order modes in a homogeneous waveguide with index  $n_{av} = 2.96$ . The reference points are marked for table 1 and the field microstructure plots in figure 11.

the point c marked on it corresponds to the zero order slow Bloch wave mode. At points a, b, c, d and e the group velocity of the Bloch wave is zero in the y direction. The vanishingly small group velocity at the symmetric points will result in an enhancement in the interaction between the electromagnetic guided mode and an incorporated dipole of the same frequency. An excitation of finite length will contain a range of frequencies, with a decay time dependent on the bandwidth;

energy will leak away via guided Bloch modes that do not lie precisely on the symmetrical points (see section 9.2). The other two curves on the diagram represent the first order slow mode and the zero order fast mode. Between the points d and e the modes display an anticrossing behaviour. At points a, g and h the mode consists solely of the first order slow mode; at point b there is the zero order fast mode; finally at points d and e there is a mixture of the two modes. This is confirmed by the field microstructure in the next section. An intriguing feature of these plots is the *reduction* in the number of guided modes as the frequency rises. This is the reverse of the behaviour in normal waveguides, where higher frequencies imply a larger number of modes, and is caused by the encroachment of the momentum gap within the permitted range of  $\beta$  values. The modes in a homogeneous waveguide with the same average index are shown as dashed lines on the diagram. In the periodic structure the zero order mode is suppressed between points b and c, and the first order mode is suppressed above a. In thicker layers this mode-suppression effect is even more dramatic [16].

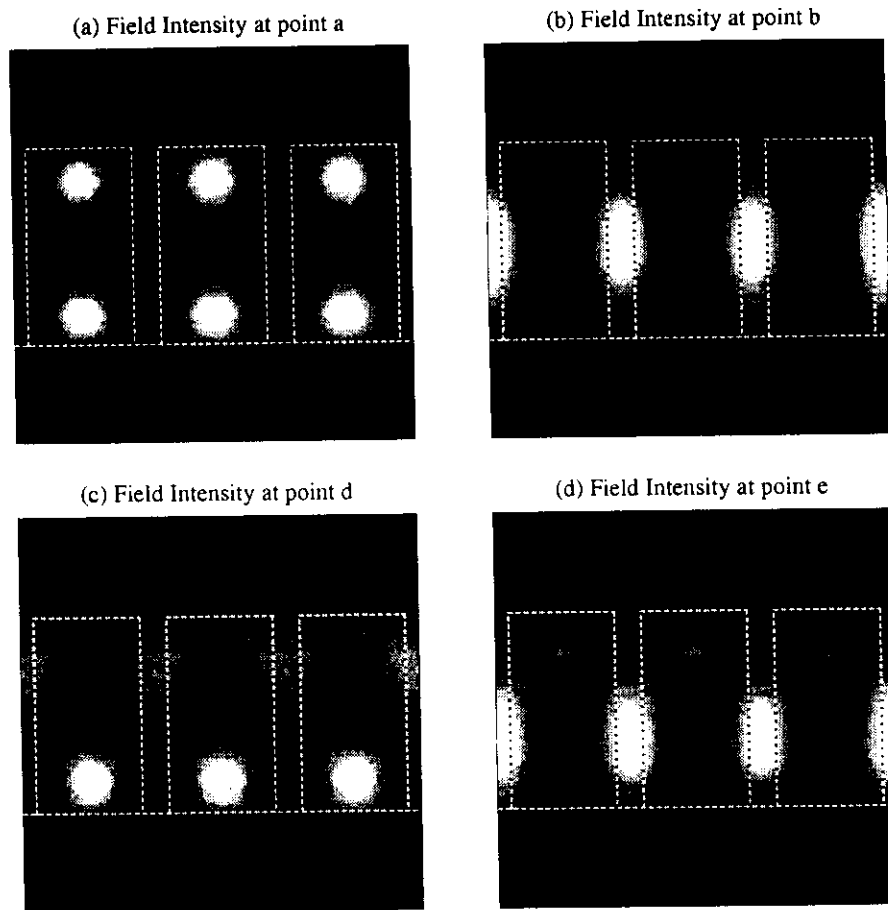


Figure 11. Field intensity distributions of selected TE guided Bloch modes at points a, b, d and e in figure 10. The substrate is below the horizontal dashed line and three periods of the high index waveguide layer are shown. (a) a first order slow mode, (b) a zero order fast mode, (c) a zero-group velocity slow 'mixed' mode and (d) a zero-group velocity fast 'mixed' mode.

#### 8.4. Microstructure of the fields

Figure 11 shows the electric field intensity distribution of the TE guided Bloch modes at points a, b, d and e on figure 10. Figure 11 (a) shows the first order slow mode at point a. This is characteristically concentrated in the high index regions and has a double lobed structure in the  $z$  direction. The zero order fast mode (point b on figure 10) is shown in figure 11 (b); it is guided predominantly in the air gaps. This very unusual behaviour arises because the field pattern is below the resolution limit of free waves in the cover and substrate regions. The modes at points a and b have zero group velocity along the waveguide, as confirmed by the 100% visibility of the modal fringe pattern—no power can flow through regions where the fields are zero.

It is intriguing that four other points of zero group velocity occur, at anticrossing points on either side of the symmetrical point (e.g. d and e). The field intensity patterns of the modes at these points are given in figures 11 (c) and (d). It turns out the anticrossing is caused by the simultaneous resonance of the zero order fast and the first order slow modes, which are then coupled strongly together at the upper and lower boundaries (see figure 6), creating a stopband in  $\beta$ . Since they travel in opposite directions along the guide, a kind of 'tug-of-war' results between the fast and slow modes, giving rise to zero group velocity at the anticrossing point. The overall modal field distributions of these 'mixed' modes are superpositions of fast and slow modes, whose relative phase is such that constructive interference occurs near the substrate in both cases (d and e).

#### 8.5. Comparison with numerical analysis

In order to confirm the accuracy of our simple analytical model, a numerical calculation was performed based on the method of Pendry and MacKinnon [17]. Our analytical model could be extended by generalization of (17) to include the contributions of higher order Fourier components and evanescent (imaginary  $\beta$ ) solutions in the expansion of the field within the grating layer. In practice it is more efficient to recast the equations to relate the Fourier components in the cover to those in the substrate by means of a transfer matrix. The elements of this transfer matrix could be calculated by use of the dispersion relation (A9), the Fourier decomposition (12) and the matching conditions at the substrate and cover boundaries. In practice, due to its availability and flexibility, a finite difference algorithm, initiated by Pendry and MacKinnon, was used to calculate the transfer matrix. This works by discretizing the fields on a real space mesh and has the added advantage of being able to describe more complex grating geometries, such as V-grooves and two-dimensional periodicity. These structures will be considered in future papers.

The condition for appearance of a guided mode is that there be no unphysical exponentially diverging modes in the substrate and cover. This results in a determinantal equation, based on the transfer matrix, which is numerically solved. Table 1 shows a comparison of the resonant frequencies calculated at a number of points indicated on figure 10. The results for both methods correspond very well, close to the symmetric point the error is less than 0.5% and it increases to 3.16% when  $k_y A/\pi$  is reduced to 0.5.

## 10. Conclusions

Deeply etched high index films support two different types of fully guided Bloch modes with zero group velocities in the waveguide plane. Viewed as resonances, these stationary modes have a uniquely high effective  $Q$ -factor (compared to any of the other modes guided in the film) and hence are suitable as micro-resonators for enhancing dipole-field coupling. Although the analysis applies only to singly periodic layers, its general conclusions are relevant to the more general case of two-dimensional multiply periodic thin films, in which resonances that are stationary in all three space dimensions are feasible. The approach used may be helpful in future studies of the behaviour of arrays of vertical cavity surface emitting lasers.

## Acknowledgments

The Optoelectronics Research Centre is an Interdisciplinary Research Centre of the United Kingdom Engineering and Physical Sciences Research Council (EPSRC). D. M. Atkin is the recipient of an EPSRC CASE award with the Defence Research Agency, Malvern.

## Appendix: Translation matrix elements

The matrix  $\mathbf{M}_{21}$  relating the field in the second layer to the field in the first layer is:

$$\begin{pmatrix} a_2^N \\ b_2^N \end{pmatrix} = \mathbf{M}_{21} \begin{pmatrix} a_1^N \\ b_1^N \end{pmatrix} = \begin{pmatrix} A_{21} & B_{21} \\ C_{21} & D_{21} \end{pmatrix} \begin{pmatrix} a_1^N \\ b_1^N \end{pmatrix}, \quad (\text{A } 1)$$

where

$$\begin{aligned} A_{21} &= c_1 c_2 - (\xi_1 p_1 \Lambda / \xi_2 p_2 \Lambda) s_1 s_2, \\ B_{21} &= s_1 c_2 / (\xi_1 p_1 \Lambda) + c_1 s_2 / (\xi_2 p_2 \Lambda), \\ C_{21} &= -\xi_1 p_1 \Lambda s_1 c_2 - \xi_2 p_2 \Lambda c_1 s_2, \\ D_{21} &= c_1 c_2 - (\xi_2 p_2 \Lambda / \xi_1 p_1 \Lambda) s_1 s_2, \end{aligned} \quad (\text{A } 2)$$

$$\det(\mathbf{M}_{21}) = 1,$$

where the terms  $s_j$  and  $c_j$  are shorthand for:

$$c_j = \cos(p_j h_j / 2), \quad s_j = \sin(p_j h_j / 2). \quad (\text{A } 3)$$

The matrix  $\mathbf{M}_{12}$  relating the field in the first layer of the  $(N+1)$ th period to the field in the second layer of the  $N$ th period is then

$$\begin{pmatrix} a_1^{N+1} \\ b_1^{N+1} \end{pmatrix} = \mathbf{M}_{12} \begin{pmatrix} a_2^N \\ b_2^N \end{pmatrix} = \begin{pmatrix} D_{21} & B_{21} \\ C_{21} & A_{21} \end{pmatrix} \begin{pmatrix} a_2^N \\ b_2^N \end{pmatrix}. \quad (\text{A } 4)$$

The analysis can either be based on the translation matrix  $\mathbf{M} = \mathbf{M}_{12} \mathbf{M}_{21}$  (with a state vector representing the field in layers with index  $n_1$ ) or equivalently on the matrix  $\mathbf{M}' = \mathbf{M}_{21} \mathbf{M}_{12}$  (state vector representing the field in layers with index  $n_2$ ).  $\mathbf{M}$  is

$$\begin{pmatrix} a_1^{N+1} \\ b_1^{N+1} \end{pmatrix} = \mathbf{M} \begin{pmatrix} a_1^N \\ b_1^N \end{pmatrix} = \begin{pmatrix} A & B \\ C & D \end{pmatrix} \begin{pmatrix} a_1^N \\ b_1^N \end{pmatrix}, \quad (\text{A } 5)$$

where

$$A = D = A_{21}D_{21} + B_{21}C_{21}, \quad (\text{A } 6)$$

$$B = 2D_{21}B_{21}, \quad C = 2A_{21}C_{21}. \quad (\text{A } 7)$$

$A$  can be re-arranged as

$$A = \cos(p_1 h_1) \cos(p_2 h_2) - \frac{1}{2} \left( \frac{p_1 \xi_1}{p_2 \xi_2} + \frac{p_2 \xi_2}{p_1 \xi_1} \right) \sin(p_1 h_1) \sin(p_2 h_2) \quad (\text{A } 8)$$

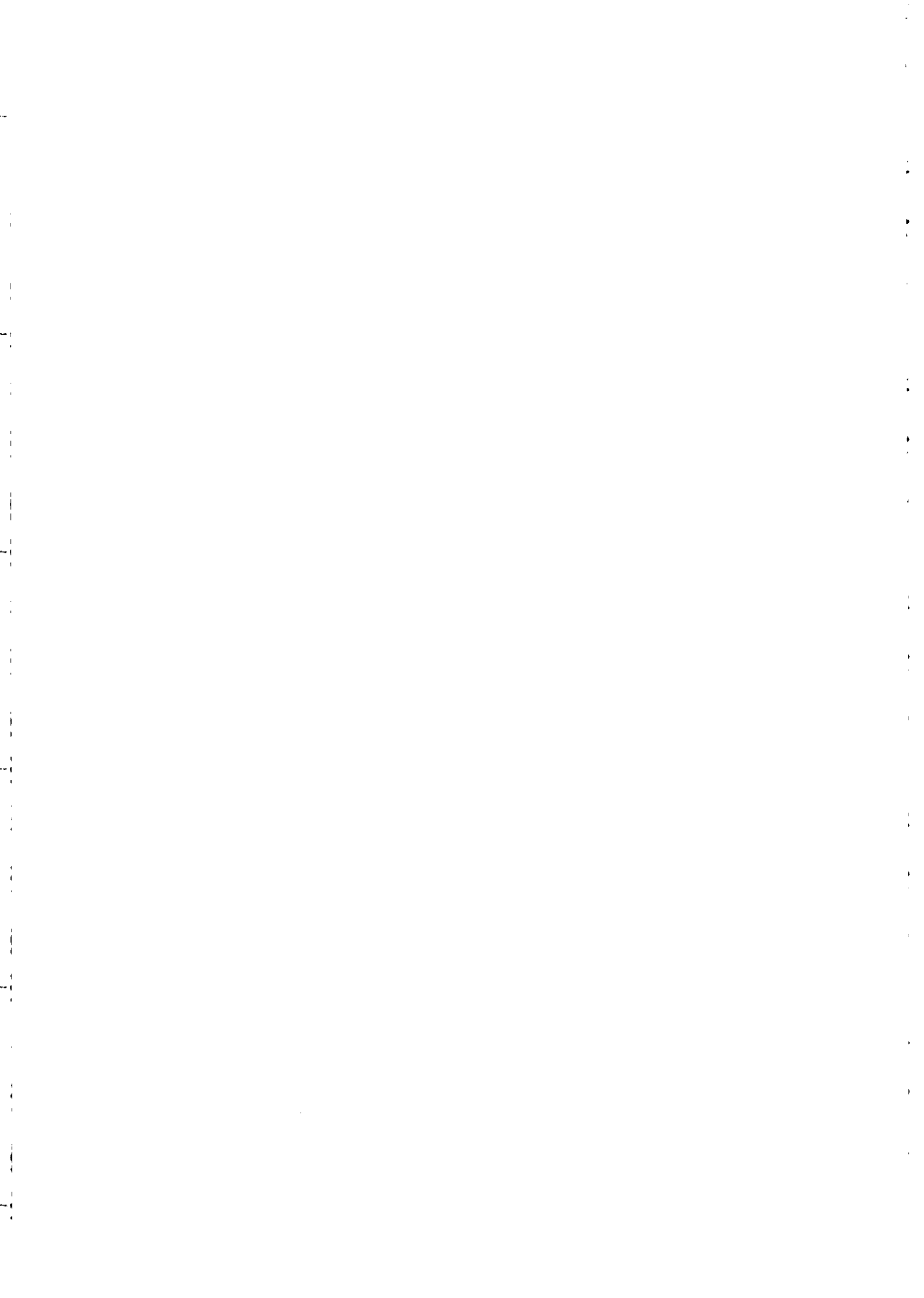
but  $B$  and  $C$  are most conveniently expressed as the product of two factors as above. The elements of the alternative matrix  $\mathbf{M}'$  are:

$$A' = D' = A, \quad (\text{A } 9)$$

$$B' = 2A_{21}B_{21}, \quad C' = 2D_{21}C_{21}. \quad (\text{A } 10)$$

## References

- [1] See special issue: 1993, *J. opt. Soc. Am.* **B 10**, 283–407.
- [2] See special issue: 1994, *J. mod. Optics*, **41**, 195–393.
- [3] JOANNOPOULOS, J., MEADE, R. D., and WINN, J. N., 1995, *Photonic Crystals* (New York: Princeton).
- [4] YABLONOVITCH, E., 1995, *Confined Electrons and Photons: New Physics and Applications*, edited by E. Burstein and C. Weisbuch (New York: Plenum Press).
- [5] GÉRARD, J. M., IZRAEL, A., MARZIN, J. Y., and PADJEN, R., 1994, *Solid State Electron.*, **37**, 1341.
- [6] BIRKS, T. A., ROBERTS, P. J., RUSSELL, P. ST. J., ATKIN, D. M., and SHEPHERD, T. J., 1995, *Electron. Lett.*, **31**, 1941.
- [7] VILLENEUVE, P. R., and PICHÉ, M., 1992, *Phys. Rev. B*, **46**, 4649.
- [8] MARADUDIN, A. A., and MCGURN, A. R., 1994, *J. mod. Optics*, **41**, 275.
- [9] RUSSELL, P. ST. J., BIRKS, T. A., and LLOYD-LUCAS, F. D., 1995, *Confined Electrons and Photons: New Physics and Applications*, edited by E. Burstein and C. Weisbuch (New York: Plenum Press).
- [10] KRAUSS, T., SONG, Y. P., THOMAS, S., WILKINSON, C. D. W., and DELARUE, R. M., 1994, *Electron. Lett.*, **30**, 1444.
- [11] YAMAMOTO, Y., and SLUSHER, R. E., 1993, *Phys. Today*, June, 66.
- [12] FENG, X.-P., and ARAKAWA, Y., 1995, Conference on Lasers and Electro-Optics/Pacific Rim (Piscataway, Orlando: IEEE), paper TuL4.
- [13] YARIV, A., 1991, *Optical Electronics*, Chap. 13 (Saunders College Publishing).
- [14] KOGELNIK, H., 1988 and 1990, *Guided-Wave Optoelectronics*, edited by T. Tamir (Berlin, Heidelberg: Springer-Verlag).
- [15] YEH, P., YARIV, A., and HONG, C. S., 1979, *J. opt. Soc. Am.*, **67**, 423.
- [16] ATKIN, D. M., RUSSELL, P. ST. J., BIRKS, T. A., and ROBERTS, P. J., 1995, *Conference on Lasers and Electro-Optics*, **15**, OSA Technical Digest Series (Washington, D.C.: Optical Society of America) p 223.
- [17] PENDRY, J. B., 1994, *J. mod. Optics*, **41**, 209.
- [18] HOUDRÉ, R., STANLEY, R. P., OESTERLE, U., ILEGEMS, M., and WEISBUCH, C., 1993, *J. Phys. IV Colloque*, **C5 3**, 51.





*Quantum Optics in Wavelength Scale Structures* (Eds: J.G. Rarity & C. Weisbuch), Kluwer 1996

## **BOUND MODES OF TWO-DIMENSIONAL PHOTONIC CRYSTAL WAVEGUIDES**

P.ST.J. RUSSELL, D.M. ATKIN, T.A. BIRKS  
*Optoelectronics Research Centre,  
University of Southampton,  
Southampton SO17 1BJ,  
United Kingdom*

and P.J. ROBERTS  
*Defence Research Agency,  
Malvern WR14 3PS,  
United Kingdom*

### **1. Introduction**

It is now widely recognised that a volume of dielectric material with an appropriately designed periodic microstructure – a *photonic crystal* – will support a full three-dimensional photonic band gap (PBG) [1]. Over the frequency range spanned by the PBG, all electromagnetic modes are suppressed within the volume, allowing a single resonance (or photonic state) to be introduced by means of a structural point defect [2]. This unique ability to tamper strongly with the electromagnetic mode density enables the channelling of spontaneous emission into one or a few electromagnetic modes, and is attractive for enhancing the emission rate from light emitting diodes, and in achieving low threshold highly efficient operation in micro-cavity lasers [3].

Although photonic crystals with full PBG's at optical frequencies seem set to have a revolutionary impact in optoelectronics, they are not yet available, largely because the technological demands on nanofabrication challenge the current limits of the state-of-the-art. As several groups have realised, however, it is less demanding to produce two-dimensional periodic patterns in thin film form (see Figure 1), and thus – perhaps – to achieve a

full PBG in two dimensions [4,5,6,7]. One important potential application of such *photonic crystal waveguides* is in the suppression of lateral emission in arrays of closely spaced vertical cavity emitting lasers [8].

The advantages of waveguiding are well known. Tight confinement of optical power over substantial distances, with precisely controlled parameters of propagation, allows the design and routine production of devices such as modulators, couplers, filters, resonators, mirrors, lasers and amplifiers. Using electron-beam lithography, complex waveguide patterns can be directly written on to a substrate, resulting in multi-functional optical chips. The ready accessibility of every point on the chip means that tapping light in and out, perhaps to interconnect with a neighbouring chip, is straightforward.

There is, however, a fundamental conflict between the requirements for

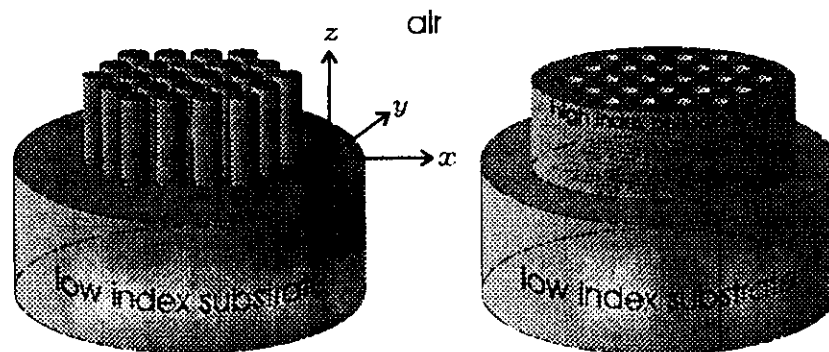


**Figure 1** Examples of the photonic crystal waveguides discussed in this chapter. They consist of high index films on a low index substrate, etched vertically through with various periodic patterns.

waveguiding and those for a full PBG in two dimensions. A waveguide operates by trapping light in a 'potential well' of high dielectric constant, strength  $\Delta\epsilon_{\text{film}}$ . A photonic band gap appears through strongly modulating the dielectric constant so as to create a periodic array of deep wells and high barriers, with dielectric step  $\Delta\epsilon_{\text{pc}}$  (pc = photonic crystal). If  $\Delta\epsilon_{\text{pc}} \ll \Delta\epsilon_{\text{film}}$ , the waveguiding dominates, being perturbed only weakly by the photonic crystal. Given the high values of  $\Delta\epsilon_{\text{pc}}$  needed for a full PBG, this regime is not attainable in practice except in metal-clad waveguides, where owing to ohmic losses the optical absorption is unacceptably high. If  $\Delta\epsilon_{\text{pc}} \gg \Delta\epsilon_{\text{film}}$ , the waveguide is a weak perturbation to the photonic crystal, with the result that waveguiding will be lost; although a full two-dimensional PBG may be attained, it will be of very limited usefulness because of strong diffractive spreading out of the plane of the thin film. In the regime where  $\Delta\epsilon_{\text{pc}} \sim \Delta\epsilon_{\text{film}}$ , it is unclear whether the waveguide or the photonic crystal will dominate. There is at least a chance that some beneficial trade-off can be found where

useful mode suppression is achieved while retaining wave guidance. This is the regime we explore in this chapter.

The approach we use is as follows. Rather than building coupled mode equations from the guided modes of a uniform film of the same average index as the periodic film (the “conventional” approach as described in many textbooks [9]), we construct the guided modes of the periodic film from the Bloch waves of the photonic crystal out of which the layer is constructed (Figure 2). This is done by adapting the well-known “zig-zag” ray model [10] for use with the Bloch wave rays of the periodic film. The resulting *guided Bloch modes* encompass all the salient features of propagation in the periodic waveguide, including the photonic band structure, dispersion, phase and group velocity [11]. They have many unique and useful features, including momentum gaps (at fixed optical frequency) that cause substantial guided mode suppression in thick layers, and in-plane modal group velocities that can be zero.

In order for guided Bloch modes to form, the light must be able to

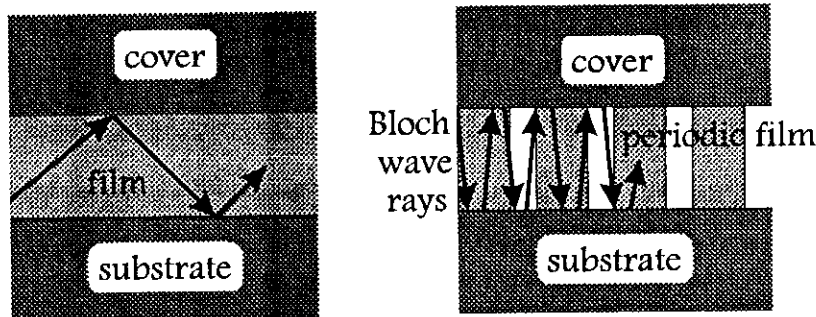


**Figure 2** Conventional (left) and Bloch-wave (right) zig-zag ray pictures of a mode guided in a thin film. Unlike the rays in the isotropic film, the Bloch wave rays (which follow the group velocity) of the photonic crystal film can be normally incident upon the boundary while still undergoing total internal reflection.

bounce to and fro between the upper and lower interfaces of the periodic layer, this requires a non-zero component of wavevector  $\beta$  normal to the film, i.e., along the translationally invariant axis (the  $z$ -axis – see Figure 1) of the two-dimensional photonic crystal. Since very few published numerical studies of two dimensional photonic band structure allow for  $|\beta| > 0$ , we shall devote some space to discussing the wavevector diagrams in that case.

The chapter is organised as follows. First we describe how to obtain the dispersion relations for unbounded two-dimensional photonic crystals (section 2). These are necessary for studying the conditions under which bound modes exist in thin waveguiding layers formed from slices of these crystals (section

3). We develop a new kind of “band diagram” which shows clearly the regions where bound modes may be expected. In the discussion (section 4), we pay particular attention to localised resonances which occur when the in-plane group velocity is zero, and find that the total number of guided modes in a photonic crystal waveguide can be significantly less than in an equivalent layer of the same average index. Conclusions are drawn in section 5.

## 2. Dispersion Relations in Unbounded Photonic Crystals

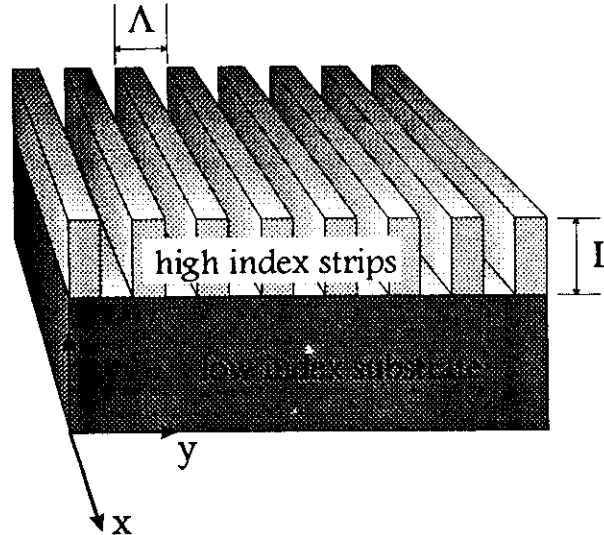


**Figure 3** Singly periodic layer consisting of high index strips on a low index substrate. The  $y$ -axis points normal to the high index planes, and the  $z$ -axis normal to the film.

### 2.1 SINGLY PERIODIC

In this case, the dispersion relation is readily obtained for a multilayer stack using the standard transfer matrix technique, as described (in our own notation) in [12]; see also [13]. It takes the functional form:

$$k_y = \frac{\arccos A}{\Lambda} \quad (1)$$

where  $k_y$  is the Bloch wavevector (pointing normal to the layers),  $\Lambda$  the period and:

$$A = \cos(p_1 h_1) \cos(p_2 h_2) - \frac{1}{2} \left( \frac{p_1 \xi_1}{p_2 \xi_2} + \frac{p_2 \xi_2}{p_1 \xi_1} \right) \sin(p_1 h_1) \sin(p_2 h_2), \quad (2)$$

with  $h_1$  and  $h_2$  the thickness of the layers in each repeating unit

( $A = h_1 + h_2$ ), whose refractive indices are  $n_1$  and  $n_2$ . The *local* wavevector components inside and normal to the layers are  $p_1$  and  $p_2$ , given by:

$$p_j = \sqrt{k_0^2 n_j^2 - (\beta^2 + k_x^2)}, \quad j = 1, 2 \quad (3)$$

where  $\beta$  is the component normal to the *waveguiding* layer of photonic crystal (the  $z$ -direction in Figure 3),  $k_x$  the remaining in-plane wavevector component and  $k_0 = \omega/c$  the vacuum wave constant. The parameters  $\xi_1$  and  $\xi_2$  are defined by:

$$\xi_j = 1 \text{ (TE)}, \quad 1/n_j^2 \text{ (TM)} \quad (4)$$

where TE (TM) polarisation occurs when the electric (magnetic) field points in the plane of the layers. For convenience we define the following parameters:

$$\nu = k_0 n_{av} A, \quad n_{av} = (\tau_1 n_1 + \tau_2 n_2), \quad \tau_j = h_j / A \quad (5)$$

where  $\nu$  is the normalised optical frequency,  $n_{av}$  the average index and  $\tau_j$  the normalised thickness of strip  $j = 1$  or  $2$ .

## 2.2 MULTIPLY PERIODIC

The multiply periodic geometry considered here comprises a hexagonal arrangement of parallel circular-cylindrical "rods" of low index surrounded by a medium of high index. For generality, a normalised propagation constant  $\beta A$  is defined, where  $A$  is the centre-to-centre spacing of adjacent rods. A useful further parameter is the normalised frequency  $\nu$ .

$$\nu = k_0 n_{av} A, \quad n_{av} = \sqrt{\sigma_1 n_1^2 + \sigma_2 n_2^2}, \quad \sigma_j = a_j / A \quad (6)$$

where  $A = a_1 + a_2$ ,  $a_j$  being the unit cell sub area for which the index is  $n_j$ .

The numerical method employed is the *real-space* method [14], in which the field and index distributions within the unit cell are discretised on a grid of points. These are grouped into sub-cells, within which the fields are related by transfer matrices. The sub-cells are small enough to preclude numerical instabilities caused by exponentially growing modes. The fields of adjacent subcells are then related using a numerically-stable scattering matrix. For hexagonal symmetry, the field and index distributions are discretised along non-orthogonal axes, corresponding to the primitive lattice vectors of the underlying hexagonal Bravais lattice.

All possible transverse wavevectors  $\mathbf{k}$  in the  $(x, y)$  plane at given  $\nu$  and  $\beta$  are sought. The calculation thus implicitly considers at once all possible polarisations and transverse directions of propagation, and the results are equally applicable for any orientation of the structure.

### 3. Conditions for Bound Modes in Photonic Crystal Waveguides

We now develop a geometrical tool suitable for establishing the conditions under which a photonic crystal waveguide will support guided modes. It involves adapting the usual band diagram by replacing optical frequency (which we keep constant) with  $\beta$ , the component of wavevector along the axis of invariance of the structure (the  $z$ -axis in our notation).

In reciprocal space at fixed optical frequency, the allowed wavevectors (of the photonic crystal layer) map out a series of one or more curved *dispersion* or *constant photon energy* surfaces  $\beta(k_x, k_y)$ , where the maximum possible value of  $\beta$  is bounded by the product of the vacuum wavevector  $k_0$  and the highest refractive index in the photonic crystal. In a uniform isotropic medium of index  $n$ , the surface is a sphere of radius  $k_0 n$ , since  $\beta^2 + k_x^2 + k_y^2 = k_0^2 n^2$ . At each value of  $\beta$ , the curved intersections of these dispersion surfaces with the constant  $\beta$  plane yield a unique wavevector diagram. The boundaries of the first Brillouin zone, being set by the crystal lattice, are (of course) invariant with  $\beta$ . Each point  $\mathbf{k}$  on the curves in the first Brillouin zone is associated with a single Bloch wave, and is accompanied by equivalent points in all the higher order Brillouin zones, which tile all of reciprocal space. Each of these points represents the wavevector of one of the partial plane waves in the Fourier expansion of the Bloch wave field. Bound modes can appear only if the transverse components of all of these wavevectors have a magnitude greater than  $k_0 n_{\text{ss}}$ , the maximum value in the substrate. It is therefore sufficient to consider only the first Brillouin zone, since the smallest Bloch wavevector will always lie within it. The group velocity component (and hence ray direction) of a Bloch wave in the transverse  $(x, y)$  plane is given by:

$$\mathbf{v}_g = \nabla_{\mathbf{k}} \omega(\mathbf{k}) \quad (7)$$

and points normal to the dispersion surfaces.

Throughout what follows we adopt the normal practice of labelling the points of high symmetry with the letters J and X, the origin of the  $\beta =$  constant wavevector plane (where  $k_x = k_y = 0$ ) being labelled  $\Gamma$ . The group

velocity of the Bloch waves in the  $(x, y)$  plane can be vanishingly small at these high symmetry points, owing to the action of one or more sets of primary Bragg planes. Since low group velocities mean enhanced interactions between matter and light, the high symmetry points are of particular interest in, for example, microcavity lasers.

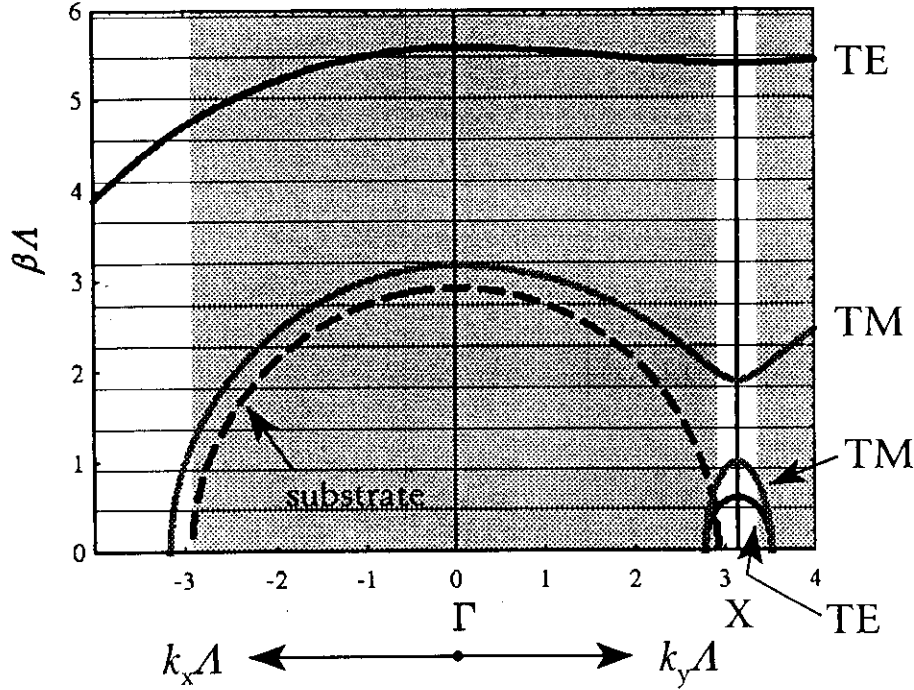


**Figure 4** Plot of  $\beta\Lambda$  along a specific path in the  $(k_x, k_y)$  plane for a singly periodic layer at fixed optical frequency  $\nu = 4$ ; at a vacuum wavelength of 1550 nm this corresponds to a structure with  $\Lambda = 493$  nm – for the other parameters see the text. The trajectory follows the  $k_x$  axis, turning through a right angle at the origin  $\Gamma$ , and progressing along the  $k_y$  axis through  $X$  (the edge of the Brillouin zone). The upper (lower) TE and TM branches at the  $X$ -point give the  $\beta\Lambda$  value for slow (fast) Bloch waves, the slow waves having a larger  $\beta\Lambda$  value. Waveguiding is only possible within the unshaded regions where  $\beta\Lambda$  in the substrate is not real-valued. The horizontal lines approximately represent successive transverse resonances in a layer of thickness  $L = 7\Lambda$ , for which the intermodal spacing  $\Delta\beta\Lambda = \pi/7$ . Note that the total number of  $y$ -propagating modes supported is reduced by the presence of the momentum gap in  $\beta$ .

### 3.1 SINGLY PERIODIC CRYSTAL WAVEGUIDE

As a first example, we consider a singly periodic waveguiding film, consisting of parallel strips of high index material on a low index substrate (see Figure 3

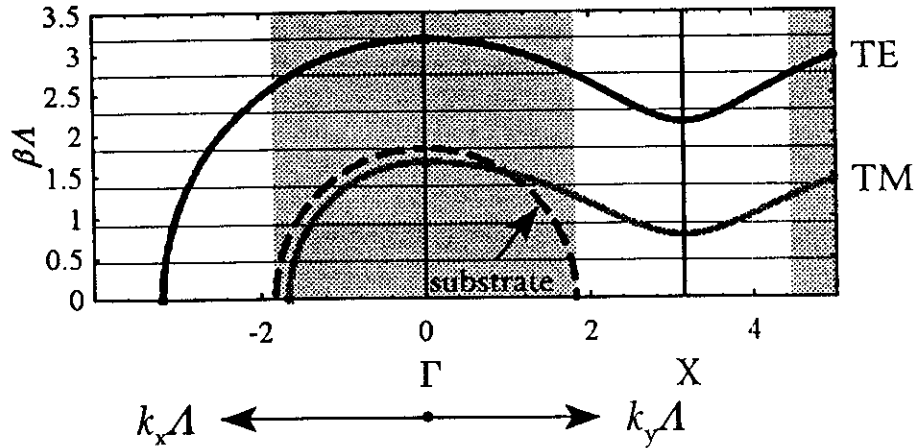


Figure 5 Plot of  $\beta\Lambda$  along a specific path in the  $(k_x, k_y)$  plane for a singly periodic layer at fixed optical frequency  $\nu = 2.5$ ; this corresponds to  $\Lambda = 308$  nm at a vacuum wavelength of 1550 nm. The full black curve is for TE polarisation, the full grey curve for TM and the black dotted curve for the substrate. See the caption of Figure 4 for more details.

In this case the Brillouin zone is an infinitely long rectangle of half-width (the distance from  $\Gamma$  to X)  $k_y\Lambda = \pi$ . In reciprocal space, imagine now an arbitrarily oriented plane containing the  $k_y$  axis. The wavevector diagram in this plane has two forms, depending on the state of polarisation. The  $s$  or TE state occurs when the electric field is normal to the plane of the diagram, and the  $p$  or TM state occurs when it is in the plane. The full three-dimensional TE and TM dispersion surfaces at fixed optical frequency are the *surfaces of revolution* formed by rotating these in-plane wavevector diagrams about the  $k_y$ -axis. The main features of the full three-dimensional dispersion surfaces can be summarised on a two-dimensional plot by showing their intersections with the  $(k_x, \beta)$  and  $(k_y, \beta)$  planes (left and right hand sides of Figures 4 and 5). This is carried out by plotting the position of the intersections of the dispersion surfaces with a trajectory including the  $k_x$  axis, and the line joining the  $\Gamma$  to the X point, i.e.,  $\beta$  versus  $k_y$  for  $k_x = 0$ . As already pointed out, bound modes are possible only in regions where the wavevector in the  $(k_x, k_y)$  plane has a magnitude greater than  $k_0 n_{ss}$ . These regions are easily identified if  $\beta_s$ , the value of  $\beta$  in the substrate, is plotted on the same diagram:

$$\beta_s = \sqrt{k_0^2 n_{ss}^2 - k_y^2 - k_x^2}. \quad (8)$$

Note that this describes the surface of a hemisphere as expected. For  $k_x$  and  $k_y$  values where  $\beta_s$  is real, bound modes in the film are impossible since the light will always leak into the substrate (which is taken as usual to have a higher



refractive index than the cover). Provided a transverse resonance condition can be found, bound modes will occur in regions where  $\beta$  in the substrate is imaginary.

The structure treated in Figures 4 and 5 consists of strips of silicon separated by air, with parameters:

$$\tau_2 = 0.4, \quad n_1 = 1, \quad n_2 = 3.5, \quad n_{av} = 2, \quad (9)$$

the substrate and cover being chosen for illustrative purposes to be silica (index 1.46) and air. At a vacuum wavelength of 1550 nm, these parameters correspond to  $A = 308$  nm,  $h_1 = 185$  nm for  $\nu = 2.5$ , and  $A = 493$  nm,  $h_1 = 296$  nm for  $\nu = 4$ . In these units, the locus of  $\beta_s$  is a sphere of radius  $1.46\nu/n_{av}$ .

At fixed  $\beta$ , any Bloch wave whose transverse wavevector lies within the range spanned by the substrate sphere will be leaky. Since every wavevector in the first Brillouin zone is accompanied by partners in every other Brillouin zone, this means that guided modes can occur *only* within the unshaded regions in Figures 4 and 5. As indicated in (7), the ray directions of the Bloch waves are given by the normals to the dispersion surfaces. One particular mode of the periodic layer thus consists of upward and downward propagating Bloch waves, confined by total internal reflection at the interfaces. One of the most striking things about the loci is the large momentum gap that appears in  $\beta A$ . Within this gap there are no real values of  $\beta$  and hence no guided modes can exist.

The transverse resonance condition for bound modes may be formally written:

$$\beta L - \Phi = m\pi \quad (10)$$

where  $\Phi$  is the sum of the phase changes upon total internal reflection at the two interfaces and  $L$  is the layer thickness. The spacing  $\Delta\beta$  between successive modes is thus (ignoring changes in  $\Phi$ ) roughly  $\pi/L$ . This allows us to count up the number of possible bound modes in each case (see section 4).

### 3.2 HEXAGONAL CRYSTAL WAVEGUIDE

We now extend the results of the last section to layers formed from a hexagonal photonic crystal. On the Brillouin diagram we trace out the usual  $\Gamma$ -J-X- $\Gamma$  wavevector path (Figure 6). As before, waveguiding will exist where

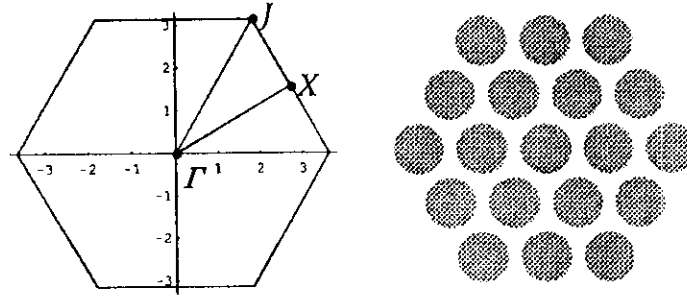


**Figure 6** Brillouin zone of hexagonal crystal with trajectory marked in. The intersections of the dispersion surfaces with the  $\Gamma$ -J-X- $\Gamma$  path, which change as the wavevector component  $\beta$  normal to the layer increases, are used to plot the “band” diagrams in Figure 8. the value of  $\beta_s$  in the substrate is imaginary. To identify these regions, we use (8) to

convert the in-plane wavevector  $k$  (joining points along the  $\Gamma$ -J-X path to the  $\Gamma$  point) into  $\beta_s$ , which is then plotted on the Brillouin diagram along with  $\beta$  in the photonic crystal. Defining the normalised parameters:

$$b = \beta\Lambda, \quad p = k_p\Lambda \quad (11)$$

where  $k_p$  is the scalar distance *along* the path  $\Gamma$ -J-X- $\Gamma$  and  $\Lambda$  is the distance between adjacent cylinder centres, one obtains:

$$b^2 + p^2 = (vn_{ss}/n_{av})^2, \quad \Gamma\text{-J}, \quad 0 \leq p \leq \frac{2\pi}{\sqrt{3}}$$

$$b^2 + \left(\frac{p}{2}\right)^2 + \left(2\pi - \frac{p\sqrt{3}}{2}\right)^2 = (vn_{ss}/n_{av})^2, \quad \text{J-X}, \quad \frac{2\pi}{\sqrt{3}} \leq p \leq \pi\sqrt{3} \quad (12)$$

$$b^2 + (\pi(1+\sqrt{3})-p)^2 = (vn_{ss}/n_{av})^2, \quad \text{X-}\Gamma, \quad \pi\sqrt{3} \leq p \leq \pi(1+\sqrt{3}).$$

Plotting  $b$  versus  $p$  yields the “band diagram” for the substrate, which indicates regions where there are no real-valued wavevectors in the substrate, and hence where guided modes might be expected assuming that  $\beta\Lambda$  is real-valued in the photonic crystal layer. An example of a typical transverse wavevector diagram is given in Figure 7. The complete “band” diagram is plotted in Figure 8 for three different optical frequencies ( $v/n_{av} = 1.4, 1.8$  and  $2.2$ ) at  $n_1 = 1, n_2 = 3.64$  and  $\sigma_1 = 0.8$ .

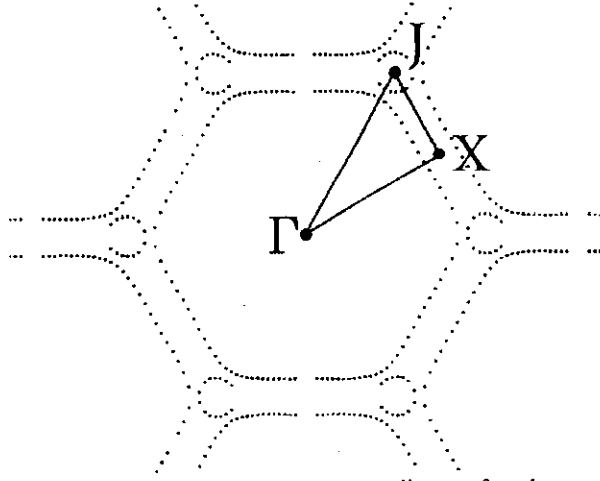


**Figure 7** Numerically calculated transverse wavevector diagram for a hexagonal crystal with  $v/n_{av} = 2.2$  at  $\beta A = 1.76$ ,  $\sigma_1 = 0.8$ ,  $n_1 = 3.64$  and  $n_2 = 1$ .

#### 4. Discussion

To illustrate the quantizing effects of the thin layer, we adopt a simplified version of the transverse resonance condition (10) that ignores phase changes upon reflection (a more rigorous treatment of the singly periodic guide is available in [11]). As already pointed out, under these circumstances the step in transverse wavevector between successive guided modes is  $\Delta\beta = \pi/L$ , where  $L$  is the layer thickness. We draw in a sequence of horizontal lines spaced by  $\pi A/L$  for a layer thickness  $L = 3.7 \mu\text{m}$ , a pitch  $A = 525 \text{ nm}$  and  $v/n_{av} = 2.2$  (Figure 8). Within the rectangular unshaded regions, the intersections of these lines with the loci yield the approximate  $k_p A$  values of the guided modes.

##### 4.1 MOMENTUM GAPS AND GUIDED MODE SUPPRESSION

Significant suppression of guided modes can occur in a photonic crystal waveguide compared to a layer of the same average index and thickness. By way of illustration, refer to Figures 4 and 5 for a singly periodic layer. The precise number of  $y$ -propagating modes that would be supported by a non-periodic layer of the same average index 2 and thickness  $2.1 \mu\text{m}$ , with air cover and silica substrate, is eight (4 TE and 4 TM) at a wavelength of  $1550 \text{ nm}$ . The singly periodic waveguide supports one (fast) TM mode at  $\nu = 4$ , and both a slow TM

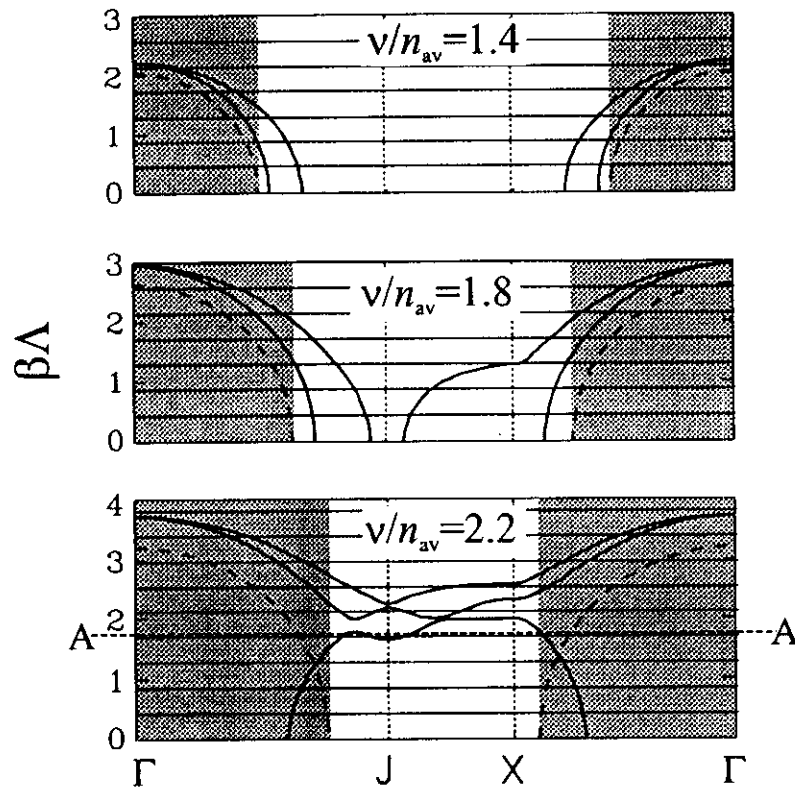


**Figure 8** Sequence of “band” diagrams for a hexagonal crystal layer. The horizontal axis is  $k_p A$ . The unshaded regions represent the parameter ranges where guided modes are possible. The dashed circles are the substrate  $\beta A$  values. The horizontal lines are spaced by an amount appropriate to the mode spacing of a layer  $7A$  thick. Note the anti-crossing points where the slope and hence the in-plane group velocity is zero; photons in the vicinity of these regions will be trapped at resonances. The dashed line AA corresponds to  $\beta A = 1.76$ , the value used in Figure 7. The total number of guided modes is reduced compared to a layer of the same average index, the lower order modes (small  $\beta$ ) being the first to disappear.

and a slow TE at  $\nu = 2.5$ . A thick guide supporting only one mode might be useful for increasing the output of an LED by allowing multiple gain regions while preserving single mode operation.

For the hexagonal crystal waveguide, at  $\nu/n_{av} = 2.2$  all the guided modes which would be present in a layer of the same thickness and average index are suppressed – in all directions – below about  $\beta A \approx 1.7$  (Figure 8).

## 4.2 LOCALISED RESONANCES

The group velocity of the guided Bloch modes along the layer can be very small, equalling zero if the frequency of the light is chosen so that one of the horizontal lines intersects with the momentum gap edges. In the vicinity of these points the light will travel very slowly along the guide, and enhanced interactions with matter (e.g., optical gain, nonlinearity and electrooptic modulation) will result. In the singly periodic case, in addition to stationary modes consisting of one upward and one downward Bloch wave, other modes appear – unexpectedly – consisting of two upward and two downward Bloch waves [11]. They occur because the guided Bloch modes associated with the fast and slow branches on either side of the momentum gaps (Figure 4) can, under the correct circumstances, be simultaneously resonant (the fast mode having a smaller number of lobes across the layer than the slow branch) at a certain optical frequency. *Away* from the Brillouin zone edge (the X point in Figure 4), two such simultaneously resonant modes are coupled together by

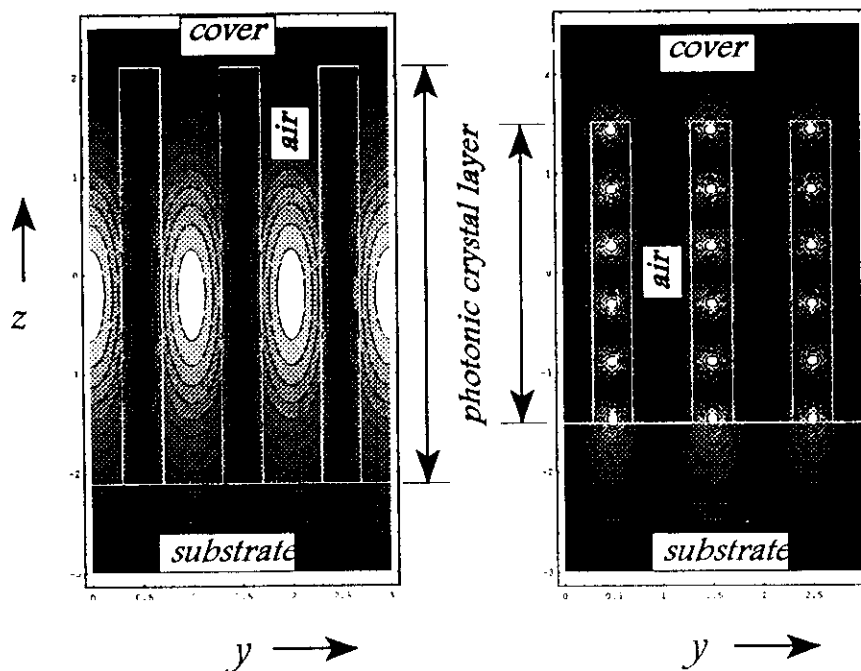


**Figure 9** Example of the field intensity distribution of a *fast* (left) and a *slow* (right) guided Bloch mode in a singly periodic layer at the momentum gap edges. For the fast mode, the light is anomalously concentrated in the air gaps [11].

reflection at the boundaries, and have group velocities that point in *opposite* directions along the layer. This means that the net group velocity can be zero, allowing a stationary guided mode to form.

In the hexagonal case for  $v/n_{av} = 2.2$ , there is a whole series of band

edges, which indicate the positions of stationary resonances and the directions in which momentum gaps appear.

Many of the curious characteristics associated with guided Bloch modes are discussed in [11]. One of their most intriguing features is that the modes associated with the fast Bloch waves (i.e., those on the small ellipsoidal dispersion surface around the X-point in Figure 4) appear to be guided by the *air* gaps in the waveguiding layer. This anomalous behaviour turns out to occur because the period of the field is below the resolution limit of light both in the cover and the substrate, permitting strongly guided modes to be supported. Examples of the field intensity patterns of one of these rather bizarre modes, together with one of the more usual modes (i.e., those concentrated in the high index regions) are available in Figure 9.

In addition to these *intrinsically* resonant (i.e., zero group velocity in the waveguide plane) guided modes, it is possible to *create* a resonance by introducing a structural defect in an otherwise perfectly uniform photonic crystal waveguide. This causes a state to form within the momentum gap, in a manner closely analogous with published reports of intra-band defect states that form at a particular frequency within a conventional photonic band gap [2]. The structural defect that gives rise to these *intra-momentum-gap* resonances can be either a sharply localised point defect, or a smoothly distributed defect. Distributed defects, where a slowly changing aperiodicity with a "bell" distribution is envisaged, may be analysed using a Hamiltonian optics approach [17]. Stationary resonances will allow strong coupling of electromagnetic fields to a dipole of the correct frequency if it is incorporated into the waveguide.

#### 4.3 LEAKAGE MECHANISMS

In order to produce any sort of trapped state (length  $\Delta y$ ) in the waveguide plane, a Fourier spectrum of  $k_y$  wavevectors is needed. And, because of the need for a *guided* mode, the only way a spread of  $k_y$  can be produced is by allowing a finite frequency bandwidth. Of course, a finite bandwidth implies a finite lifetime. Thus, the leakage rate for an excitation of length  $\Delta y$  depends on the curvature at the *energy* band edges [11]. This illustrates the need for a general clarification of the questions being asked about spontaneous emission control in waveguides. The presence of Fourier plane wave components that radiate either laterally along the waveguide (as just described), or into free space (as would be the case for an intra-momentum-gap resonance), precludes the existence of a perfectly confined state within a

waveguide supporting a two-dimensional photonic band-gap. As a result, the key issue to address may be that of *minimising* the effect of the radiating field components so as to *maximise* the Q-factor of the guided resonances.

## 5. Conclusions

The overall conclusion of this chapter is that, despite initial indications to the contrary, strong photonic crystal effects can co-exist together with waveguiding in appropriately designed photonic crystal layers. Furthermore, calculations of the pitch and index contrast needed for a full two-dimensional photonic bandgap, based purely on *in-plane* propagation ( $\beta = 0$ ), are misleading if a thin layer of photonic crystal is sandwiched between two low index media. The actual pitch required in a waveguide is actually *larger* and the index contrast *smaller* than for the in-plane case, owing to there being a substantial component of photon momentum *normal* to the guide plane. This reduces the photon momentum *in* the guide plane, making it easier to attain a full two-dimensional band gap. It also lessens the technological difficulty of making practically useful photonic crystal waveguides. It is even possible to attain a full two-dimensional band gap in the silica/air system, where the index contrast is 1.46:1 [15]. Indeed, in the case of the silicon/air system, two-dimensional hexagonal photonic crystals turn out to exhibit many of the properties normally associated only with a full three-dimensional photonic crystal [16].

The analysis presented in this chapter is also relevant, for example, to the use of photonic band gaps in the suppression of lateral spontaneous emission in arrays of closely spaced vertical cavity emitting lasers, which resemble the structures depicted in Figure 1. The ability to maintain waveguiding in the presence of strong photonic crystal effects may be useful in many applications where miniaturisation of standard optoelectronic components, such as couplers, filters and mirrors, is sought.

Finally – and this may be the most significant point of all given the difficulties associated with producing three-dimensional photonic crystals with full band gaps – a technique already exists (anisotropic photo-electro-chemical etching [18]) which allows extraordinarily precise micron-sized patterns to be etched nm deep into silicon. Some of the effects described in this chapter may thus be within reach technologically in the near future.

## 6. References

1. E. Yablonovitch, "Photonic band gap structures," *J. Opt. Soc. Am. B* **10** (283-295) 1993
2. E. Yablonovitch, T.J. Gmitter, R.D. Meade, A.M. Rappe, K.D. Brommer and J.D. Joannopolous, "Donor and acceptor modes in photonic band structure," *Phys. Rev. Lett.* **67** (3380-3383) 1991
3. See section entitled "Confined Photons" in *Confined Electrons and Photons: New Physics and Applications*, Eds: E. Burstein and C. Weisbuch, (Plenum Press 1995), pp 383-646
4. P. R. Villeneuve and M. Piché, "Photonic band gaps in two-dimensional square and hexagonal lattices," *Phys. Rev. B* **46** (4649-4972) 1992
5. T. Krauss, Y.P. Song, S. Thomas, C.D.W. Wilkinson and R.M. DeLaRue, "Fabrication of 2-D photonic band gap structures in GaAs/AlGaAs," *Electron. Lett.* **30** (1444-1446) 1994
6. K. Inoue, M. Wada, K. Sakoda, A. Yamanaka, M. Hayashi and J.W. Haus, "Fabrication of a two-dimensional photonic band structure with near-infrared band gap," *Jpn.J.Appl.Phys.* **33** (L1463-L1465) 1994
7. A.A. Maradudin and A.R. McGurn, "Photonic band structure of a truncated, two-dimensional, periodic dielectric medium," *J. Opt. Soc. Am.* **10** (307-313) 1993
8. See, e.g., Y. Yamamoto and R.E. Slusher, "Optical processes in microcavities," *Physics Today* **46** (66-73) 1993
9. See, e.g., A. Yariv, *Optical Electronics*, 4th edition (Harcourt Brace College Publishers, Fort Worth, 1991)
10. H. Kogelnik, "Theory of Optical Waveguides," in *Guided-Wave Optoelectronics*, Ed: T. Tamir (Springer-Verlag Berlin Heidelberg 1988 & 1990)
11. D.M. Atkin, P.St.J. Russell, T.A. Birks & P.J. Roberts, "Photonic band structure of guided Bloch modes in high index films fully etched through with periodic microstructure," to be published in *J. Mod. Opt.*, 1996
12. P.St.J. Russell, T.A. Birks and F.D. Lloyd-Lucas, "Photonic Bloch waves and photonic band gaps," in *Confined Electrons and Photons: New Physics and Applications*, Eds: E. Burstein and C. Weisbuch, (Plenum Press 1995), pp 585-633
13. P. Yeh, A. Yariv and C. S. Hong, "Electromagnetic propagation in periodic stratified media: I & II," *J. Opt. Soc. Am.* **67** (423-448) 1977
14. J.B. Pendry, "Photonic band structures," *J.Mod.Opt.* **41** (209-229) 1994
15. T.A. Birks, P.J. Roberts, P.St.J. Russell, D.M. Atkin and T.J. Shepherd, "Full 2-D photonic band gaps in silica/air structures," *Electron. Lett.* **31** (1941-1942) 1996
16. P.J. Roberts, T.A. Birks, P.St.J. Russell, T.J. Shepherd and D.M. Atkin, "Two-dimensional photonic band-gap structures as quasi-metals," to be published in *Opt. Lett.*, 1996
17. P.St.J. Russell and T.A. Birks, "Bloch wave optics in photonic crystals: Physics and applications," in *Photonic Band Gap Materials*, Editor C.M. Soukoulis, (Kluwer Academic, to be published 1996)
18. U. Grüning, V. Lehmann and C.M. Engelhardt, "Two-dimensional infrared photonic band gap structure based on porous silicon," *Appl. Phys. Lett.* **66** (3254-3256) 1995



Reprinted from

# OPTICS COMMUNICATIONS

---

Optics Communications 160 (1999) 66–71

## Full photonic bandgaps and spontaneous emission control in 1D multilayer dielectric structures

P.St.J. Russell <sup>a,\*</sup>, S. Tredwell <sup>a</sup>, P.J. Roberts <sup>b</sup>

<sup>a</sup> *Optoelectronics Group, Department of Physics, University of Bath, Bath BA2 7AY, UK*

<sup>b</sup> *Defence Evaluation and Research Agency, St. Andrews Road, Malvern WR14 3PS, UK*

Received 3 September 1998; accepted 1 December 1998



ELSEVIER

**FOUNDING EDITOR**

F. Abelès

**EDITORS**

J.C. Dainty  
Blackett Laboratory, Imperial College  
London SW7 2BZ, UK

Phone: +44-171-594-7748  
FAX: +44-171-594-7714  
Email: OPTCOMM@IC.AC.UK

L.M. Narducci  
Physics Department, Drexel University,  
Philadelphia, PA 19104, USA

Phone: +1-215-895-2711  
FAX: +1-215-895-6757  
+1-215-895-4999  
Email: LORENZO@WOTAN.PHYSICS.  
DREXEL.EDU

W.P. Schleich  
Abteilung für Quantenphysik, Universität Ulm  
D-89069 Ulm, Germany

Phone: +49-731-502-2510  
FAX: +49-731-502-2511  
Email: OPTCOM@PHYSIK.UNI-ULM.DE

**ADVISORY EDITORIAL BOARD****Argentina**

R.A. Depine, Buenos Aires

**Australia**

C.J.R. Sheppard, Sydney  
A.W. Snyder, Canberra

**Brazil**

L. Davidovich, Rio de Janeiro

**Canada**

J. Chrostowski, Ottawa  
M. Piché, Quebec  
R. Vallee, Sainte-Foy

**China**

Jin Yue Gao, Changchun

**France**

P. Chavel, Orsay  
D. Courjon, Besançon  
P. Glorieux, Villeneuve d'Ascq  
P. Grangier, Orsay  
G. Grynberg, Paris  
J.P. Huignard, Orsay  
T. Lopez-Rios, Grenoble

**Germany**

O. Bryngdahl, Essen  
T.W. Hänsch, Munich  
G. Huber, Hamburg  
J. Jahns, Hagen  
J. Mlynek, Constance  
G. Rempe, Constance  
R. Ulrich, Hamburg  
H. Walther, Garching

**India**

G.S. Agarwal, Hyderabad

**Israel**

G. Kurizki, Rehovot

**Italy**

F.T. Arecchi, Florence  
F. Gori, Rome  
M. Inguscio, Florence  
A. Renieri, Rome

**Japan**

T. Asakura, Sapporo

**Lithuania**

A.P. Piskarskas

**New Zealand**

D.F. Walls, Auckland

**Norway**

J. Stamnes, Bergen

**Poland**

I. Bialynicki-Birula, Warsaw

**Romania**

D. Mihalache, Bucharest

**The Netherlands**

D. Lenstra, Amsterdam  
J.P. Woerdman, Leiden

**Ukraine**

M. Soskin, Kiev

**United Kingdom**

W.J. Firth, Glasgow  
R. Loudon, Colchester  
G.H.C. New, London  
C.E. Webb, Oxford  
B. Wherrett, Edinburgh

**Russia**

Y.I. Khanin, Nizhny-Novgorod  
N.I. Koroteev, Moscow  
V.S. Letokhov, Moscow

**Spain**

M. Nieto-Vesperinas, Madrid  
E. Roldan, Burjassot

**Sweden**

A.T. Friberg, Stockholm  
S. Stenholm, Stockholm

**Switzerland**

P. Günter, Zurich

**USA**

N.B. Abraham, Bryn Mawr, PA  
D.Z. Anderson, Boulder, CO  
H.J. Carmichael, Eugene, OR  
J.C. de Paula, Haverford, PA  
J.W. Goodman, Stanford, CA  
E.P. Ippen, Cambridge, MA  
A.E. Kaplan, Baltimore, MD  
J.S. Krasinski, Stillwater, OK  
N. Lawandy, Providence, RI  
D. Psaltis, Pasadena, CA  
G.I. Stegeman, Orlando, FL  
G. Vemuri, Indianapolis, IN  
E. Wolf, Rochester, NY

**Aims and Scope**

Optics Communications ensures the rapid publication of contributions in the field of optics and interaction of light with matter.

**Abstracted/indexed in:**

Chemical Abstracts; Current Contents: Engineering, Computing and Technology; Current Contents: Physical, Chemical & Earth Sciences; EI Compendex Plus; Engineering Index; INSPEC.

**Subscription Information 1999**

Volumes 159-172 (84 issues) of Optics Communications (ISSN 0030-4018) are scheduled for publication.

Prices are available from the publisher upon request. Subscriptions are accepted on a prepaid basis only. Issues are sent by SAL (Surface Air Lifted) mail wherever this service is available.

**Orders, claims, and product enquiries:** please contact the Customer Support Department at the Regional Sales Office nearest you:

**New York:** Elsevier Science, PO Box 945, New York, NY 10159-0945, USA; phone: (+1) (212) 633 3730 [toll free number for North American customers: 1-888-4ES-INFO (437-4636)]; fax: (+1) (212) 633 3680; e-mail: usinfo-f@elsevier.com

**Amsterdam:** Elsevier Science, PO Box 211, 1000 AE Amsterdam, The Netherlands; phone: (+31) 20 4853757; fax: (+31) 20 4853432; e-mail: nlinfo-f@elsevier.nl

**Tokyo:** Elsevier Science, 9-15 Higashi-Azabu 1-chome, Minato-ku, Tokyo 106-0044, Japan; phone: (+81) (3) 5561 5033; fax: (+81) (3) 5561 5047; e-mail: info@elsevier.co.jp

**Singapore:** Elsevier Science, No. 1 Temasek Avenue, #17-01 Millenia Tower, Singapore 039192; phone: (+65) 434 3727; fax: (+65) 337 2230; e-mail: asiainfo@elsevier.com.sg

**Rio de Janeiro:** Elsevier Science, Rua Sete de Setembro 111/16 Andar, 20050-002 Centro, Rio de Janeiro - RJ, Brazil; phone: (+55) (21) 509 5340; fax: (+55) (21) 507 1991; e-mail: elsevier@campus.com.br [Note (Latin America): for orders, claims and help desk information, please contact the Regional Sales Office in New York as listed above]

Claims for issues not received should be made within six months of our publication (mailing) date.

**Advertising information.** Advertising orders and enquiries can be sent to: **USA, Canada and South America:** Mr Tino de Carlo, The Advertising Department, Elsevier Science Inc., 655 Avenue of the Americas, New York, NY 10010-5107, USA; phone: (+1) (212) 633 3815; fax: (+1) (212) 633 3820; e-mail: t.decarlo@elsevier.com. **Japan:** The Advertising Department, Elsevier Science K.K., 9-15 Higashi-Azabu 1-chome, Minato-ku, Tokyo 106-0044, Japan; phone: (+81) (3) 5561 5033; fax: (+81) (3) 5561 5047. **Europe and ROW:** Rachel Gresle-Farthing, The Advertising Department, Elsevier Science Ltd., The Boulevard, Langford Lane, Kidlington, Oxford OX5 1GB, UK; phone: (+44) (1865) 843565; fax: (+44) (1865) 843976; e-mail: r.gresle-farthing@elsevier.co.uk.

**US mailing notice** - Optics Communications (ISSN 0030-4018) is published semi-monthly by Elsevier Science NL (P.O. Box 211, 1000 AE Amsterdam, The Netherlands). Annual subscription price in the USA is US\$ 4293 (valid in North, Central and South America only), including air speed delivery. Periodicals postage paid at Jamaica, NY 11431.

USA Postmasters: Send changes to Optics Communications, Publications Expediting, Inc., 200 Meacham Avenue, Elmont, NY 11003. Airfreight and mailing in the USA by Publications Expediting Inc., 200 Meacham Avenue, Elmont, NY 11003.

⊗ The paper used in this publication meets the requirements of ANSI/NISO Z39.48-1992 (Permanence of Paper).

Printed in the Netherlands

North-Holland, an imprint of Elsevier Science



ELSEVIER



ELSEVIER

1 February 1999

OPTICS  
COMMUNICATIONS

Optics Communications 160 (1999) 66–71

# Full photonic bandgaps and spontaneous emission control in 1D multilayer dielectric structures

P.St.J. Russell <sup>a,\*</sup>, S. Tredwell <sup>a</sup>, P.J. Roberts <sup>b</sup>

<sup>a</sup> *Optoelectronics Group, Department of Physics, University of Bath, Bath BA2 7AY, UK*

<sup>b</sup> *Defence Evaluation and Research Agency, St. Andrews Road, Malvern WR14 3PS, UK*

Received 3 September 1998; accepted 1 December 1998

## Abstract

It is shown that a layer of low refractive index, sandwiched between two multilayer stacks made from commonly used dielectric materials, can be designed to be completely free of all modes within a band of frequencies, i.e., to support a species of full photonic bandgap. In a slightly thicker layer, only one mode is supported. For in-plane electric field polarisation and a radiating dipole placed in the centre of the layer, the spontaneous emission coupling ratio is  $\beta_{SE} = 0.96$ , very high for such a simple structure. © 1999 Published by Elsevier Science B.V. All rights reserved.

PACS: 42.70.Q; 78.66; 85.60.J

Keywords: Photonic bandgap; Polarisation; Dielectric material

## 1. Introduction

A result which captured the imagination of the scientific community in the early 1990s was the demonstration at microwave frequencies of wavelength-scale periodically microstructured dielectrics which support full photonic bandgaps, i.e., bands of frequency where there are no photonic states [1–4]. Full photonic bandgaps are closely analogous with electronic bandgaps in semiconductors, and only appear in crystals with certain properties, e.g., a face-centre-cubic lattice structure and a strong enough index contrast between ‘atoms’ and ‘interatomic spaces’. A great deal of effort has gone into the microstructuring of materials with high refractive indices, and significant progress has been made [5–7].

Three-dimensional photonic bandgap crystals, being extended media with highly unusual electromagnetic properties, are clearly of the greatest interest and importance. They are however extremely difficult to make in large

volumes at optical frequencies. There is therefore considerable interest in one- and two-dimensional photonic crystals which exhibit some of the same properties. For example, it is possible to design a two-dimensional ‘quasi-metallic’ (QM) photonic crystal which rejects light incident from air no matter what its polarisation state or direction of propagation [8]. It is perhaps less well known that simple, appropriately designed multilayer stacks can also behave like quasi-metals for incidence from, for example, aqueous media [9,10].

The absorption displayed by metals at optical frequencies precludes their use as mirrors for high finesse microresonators. The possibility of replacing them with QM photonic crystals made from low-loss dielectrics is therefore very attractive.

In this paper, we show that *all* the modes (both free and bound) of a low refractive index layer can be suppressed within a limited range of frequencies by sandwiching it between two QM dielectric stacks. Since there are no photonic states in the layer within this range of frequencies, it may be regarded as having a full photonic bandgap. We first briefly develop the transfer matrix approach for a QM stack, and use it to establish the ranges of frequency

\* Corresponding author. E-mail: p.s.j.russell@bath.ac.uk

where the stack supports no modes – of either polarisation state – over all in-plane refractive indices  $n_{\text{eff}}$  in the range  $-n_d < n_{\text{eff}} < +n_d$  where  $n_d$  is the index of the layer. We then show that no real mode (free or trapped) with an effective index less than  $n_d$  can exist within the layer provided the thicknesses of the last layer of the stack and the defect layer are appropriately chosen. We briefly compare the performance of this simple 1D structure with that of a three-dimensionally periodic crystal displaying a full photonic bandgap. Finally, we calculate the spontaneous emission (SE) coupling ratio for a structure with a water layer containing a centrally placed dipole.

### 2. Design of quasi-metallic multilayer stacks

The transfer matrix formalism we use is fully described in Ref. [11]; only the relevant expressions are used in this paper. Consider an infinite stack composed of alternating layers with refractive indices  $n_1$  and  $n_2$  and widths  $h_1$  and  $h_2$ . The  $y$  coordinate points normal to the layers and the  $x$  and  $z$  coordinates are in the plane. The Bloch wavevector  $k_y$  (parallel to  $y$ ) for such a stack may be obtained from the expression:

$$k_y \Lambda = \arccos \left( \cos(p_1 h_1) \cos(p_2 h_2) - \frac{1}{2} \left( \frac{p_1 \xi_1}{p_2 \xi_2} + \frac{p_2 \xi_2}{p_1 \xi_1} \right) \sin(p_1 h_1) \sin(p_2 h_2) \right) \quad (1)$$

where  $\Lambda = h_1 + h_2$  is the pitch of the stack. In this equation,  $p_j = \sqrt{k^2 n_j^2 - \beta^2}$  is the wavevector component normal to the interfaces in layer  $j$ ,  $\xi_j$  is the polarisation parameter ( $\xi_j = 1$  for TE and  $\xi_j = 1/n_j^2$  for TM),  $k$  is the vacuum wavevector and  $\beta$  is the wavevector component parallel to the interface. Eq. (1) is derived by considering the continuity of the field at an interface in the stack [11].

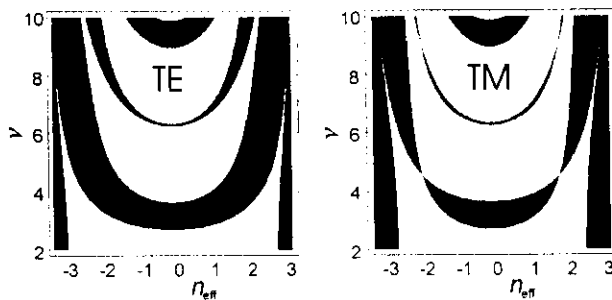


Fig. 1. Plots of  $\nu$  against  $n_{\text{eff}}$  for a stack where  $n_1 = 3.5$ ,  $h_1 = 126$  nm,  $n_2 = 2.2$  and  $h_2 = 190$  nm. In the shaded regions,  $k_y$  is imaginary and the waves in the stack will be evanescent, i.e., no photonic states exist. The diagram on the left is for TE polarisation, and the one on the right for TM. Note that, for TM, the stop-band vanishes at  $\nu \approx 4.5$  because of the Brewster angle.

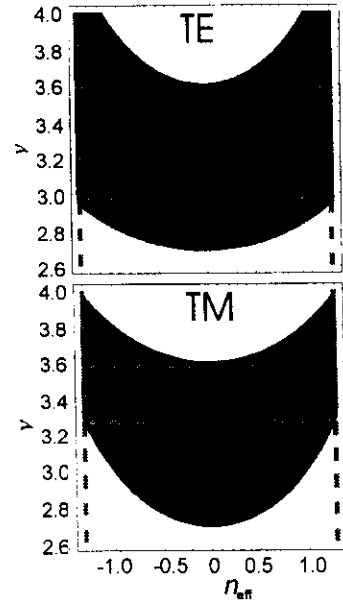


Fig. 2. If waves are incident from a medium with index 1.3, the maximum possible magnitude of  $n_{\text{eff}}$  is 1.3, which limits the effective in-plane indices that can be excited within the stack to the region between the vertical dashed lines. Horizontal dashed lines can then be added to indicate the range of frequencies over which the waves will be evanescent in the stack (the area within the lines must be completely shaded). Owing to Brewster angle effects, the TM case provides a much more limited range of frequencies than TE. In this case, the stack parameters were the same as in Fig. 1.

For real-valued  $k_y$  the stack is able to support propagating modes; however over certain ranges of  $\beta$  and  $k$  there exist regions where  $k_y$  is imaginary, and the field in the stack is evanescent (Fig. 1). For convenience the normalised parameters  $n_{\text{eff}} = \beta/k$  and  $\nu = kn_{\text{av}} \Lambda$  are used, where  $n_{\text{av}} = (n_1 h_1 + n_2 h_2)/\Lambda$ . Suppose that the waves were incident on a semi-infinite stack from some low index medium such as water or air. By drawing the appropriate construction lines on Fig. 1, it is possible to determine a range of frequency,  $\Delta\nu$ , over which all incident waves will be completely reflected (Fig. 2). The lower the index of the layer, the wider the  $\Delta\nu$ .

### 3. Design of low index layer with no photonic states within $\Delta\nu$

Having determined the properties of the QM multilayer stack, a defect layer of index  $n_d$  and width  $h_d$  is now introduced. In addition to this, the width  $h_f$  of the first high index layer on both sides of the defect layer is treated as a design parameter (Fig. 3). In order to eliminate all modes, we must demonstrate that neither bound nor unbound modes exist in the layer. It is straightforward to

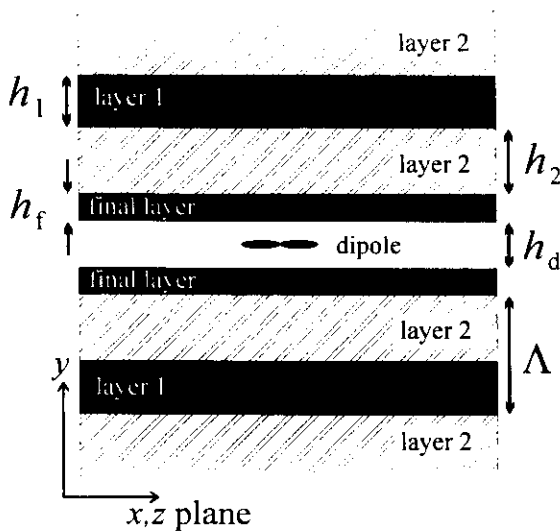


Fig. 3. The symmetrical geometry of the defect layer and the stacks. A low index layer of thickness  $h_d$  is sandwiched between two QM multilayer stacks, in each of which the final layer has a nonstandard thickness  $h_f$ .

eliminate all unbound modes by ensuring that there is QM behaviour over  $-n_d < n_{\text{eff}} < +n_d$ . Eliminating the bound modes is more complex, and requires checking that no real-valued solutions for  $\beta$  exist over  $-n_d < n_{\text{eff}} < +n_d$ . To do this, we need to derive the dispersion relation for guided modes of the low index layer. This is done by matching fields at the interfaces between the low index layer and the stacks. After straightforward manipulation, using symmetry to simplify the dispersion relation, the following form results:

$$\frac{p_d h_d}{2} - \tan^{-1} \left( \frac{p_1 \Lambda \xi_1 a_1^l p_1 \Lambda \xi_1 t_1 - b_1^l}{p_d \Lambda \xi_d a_1^l p_1 \Lambda \xi_1 + b_1^l t_1} \right) = \frac{n\pi}{2},$$

$$t_1 = \tan \left\{ p_1 \left( \frac{h_1}{2} - h_f \right) \right\}. \quad (3)$$

The values  $a_1^l$  and  $b_1^l$  are elements of the state vector  $\{a_1^l, b_1^l\}$  of the evanescent Bloch mode in the stack, which is chosen so as to decay exponentially into each stack from the low index layer (see Appendix A). The integer  $n$  indicates the order of the mode, and whether it has odd or even symmetry. The question arises whether there are any values of the stack parameters for which (3) remains unsatisfied for all  $-n_d k < \beta < +n_d k$ .

The two parameters we chose to vary are  $h_d$  and  $h_f$ . The other parameters were fixed with the following values;  $h_1 = 126$  nm,  $h_2 = 190$  nm,  $n_1 = 3.5$  (Si),  $n_2 = 2.2$  ( $\text{Ta}_2\text{O}_5$ ) and  $n_d = 1.33$  ( $\text{H}_2\text{O}$ ). From Fig. 2, it can be seen that a range of  $\nu$  from  $\nu_{\text{min}} = 3.35$  to  $\nu_{\text{max}} = 3.50$  ensures that no propagating waves in the low index layer can propagate in the stack.

In order to test a particular configuration for guided modes, the LHS of (3) is plotted against  $\beta$  over the range

$0 < \beta < \beta_{\text{max}}$ . If this curve at no point equals  $n\pi/2$ , then no modes exist in the defect layer. Repeating this procedure for a range of  $h_d$  and  $h_f$  allows modeless regions to be identified (Fig. 4). It can be seen that the higher frequencies cause the modes to switch on first, whereas the lower limit is governed by the lower frequencies. In the case presented here, there is a region where no modes exist over the entire range of frequencies  $3.35 < \nu < 3.50$ .

#### 4. Comparison with 3D photonic bandgap structures

In a 3D photonic crystal supporting a full photonic bandgap (such as demonstrated by, e.g., Yablonovitch in Ref. [1] and Özbay in Ref. [3]), there are no photonic states within the range of frequencies spanned by the bandgap. This means that (a) it is impossible for light incident from an external medium to propagate into the crystal; and (b) light cannot be generated within the crystal. In a quasi-metallic multilayer stack, on the other hand, it is impossible for light incident from a *low index* external medium to propagate into the crystal, and light *can* be generated within the crystal provided its index along the planes is high enough (see Fig. 1). The evanescent field intensity in these high index states will have a maximum penetration into the low index defect layer that follows the relation:

$$I(y) = I_0 \exp \left( - \frac{4\pi y}{\lambda} \sqrt{n_{\text{edge}}^2 - n_d^2} \right) \quad (4)$$

where  $n_{\text{edge}}$  is the in-plane refractive index at the stop-band edge and  $I_0$  the intensity at the defect surface  $y = 0$ . The degree of field rejection will depend on the intensity  $I_0$  (likely to be low since there are no resonant states in the defect layer) and how far (measured in terms of in-plane refractive index) the stop-band edge is from the maximum index in the defect layer. Substantial suppression of emission is feasible provided a quasi-metallic stack is designed in which  $\sqrt{n_{\text{edge}}^2 - n_d^2}$  is optimised.

#### 5. SE enhancement factor

In order to test the degree of suppression – and enhancement when only one mode switches on – we have calculated the total emission from a dipole placed at the centre of the water layer and aligned parallel to the planes. The stack design is otherwise identical to those analysed in Section 4. The emission rate is plotted (Fig. 5), for various values of final layer thickness  $h_f/\Lambda$ , against defect layer thickness  $h_d/\Lambda$  at a frequency of  $\nu = 3.40$ . At fixed  $h_f/\Lambda$ , the emission rate drops as  $h_d/\Lambda$  increases, i.e., the dipole moves away from the layer/stack interfaces. Moving the dipole away from the layer/stack interface results in a falling overlap with the evanescent field of the high index ( $n > n_{\text{edge}}$ ) in-plane stack modes, leading to substantial suppression of SE. At  $h_f/\Lambda = 0.4$ , approximately 10

**References**

- [1] C.M. Bowden, J.P. Dowling, H.O. Everitt (Eds.), Development and applications of materials exhibiting photonic bandgaps, *J. Opt. Soc. Am.* 10 (1993) 279–413, feature section.
- [2] E. Burstein, C. Weisbuch (Eds.), *Confined Electrons and Photons*, Plenum, 1995.
- [3] S. Setyahadi, E. Harada, N. Mori, Y. Kitamoto, *Enzymatic*, *J. Mol. Catal. B* 4 (1998) 205.
- [4] J.G. Rarity, C. Weisbuch (Eds.), *Microcavities and Photonic Bandgaps*, Kluwer, 1996.
- [5] M. Boroditsky, E. Yablonovitch, Photonic crystals boost light emission, *Phys. World* 10 (1997) 25–26.
- [6] G. Feiertag, W. Ehrfeld, H. Freimuth, H. Kolle, H. Lehr, M. Schmidt, M.M. Sigalas, C.M. Soukoulis, G. Kiriakidis, T. Pedersen, J. Kuhl, W. Koenig, Fabrication of photonic crystals by deep X-ray lithography, *Appl. Phys. Lett.* 71 (1997) 1441–1443.
- [7] S. Kawakami, Fabrication of submicrometre 3D periodic structures composed of Si/SiO<sub>2</sub>, *Electron. Lett.* 33 (1997) 1260–1261.
- [8] P.J. Roberts, T.A. Birks, P.St.J. Russell, T.J. Shepherd, D.M. Atkin, Two-dimensional photonic band-gap structures as quasi-metals, *Opt. Lett.* 21 (1996) 507–509.
- [9] P.St.J. Russell, presented at UK Quantum Electronics Conference, QE-13, Cardiff, 1997.
- [10] P.St.J. Russell, Functional photonic crystal devices, European Conference on Optical Communications, ECOC '98, Madrid, Spain, September 1998.
- [11] P.St.J. Russell, T.A. Birks, F.D. Lloyd-Lucas, Photonic Bloch waves and photonic band gaps, in: E. Burstein, C. Weisbuch (Eds.), *Confined Electrons and Photons*, Plenum, 1995.

## Instructions to Authors (short version)

(A more detailed version of the instructions is published in the preliminary pages of each volume)

### Submission of papers

Manuscripts (one original and two copies), should be sent to one of the Editors, whose addresses are given on the inside of the journal cover.

**Original material.** Submission of a manuscript implies that the paper is not being simultaneously considered for publication elsewhere and that the authors have obtained the authority for publication, if needed.

**Refereeing.** Submitted papers will be refereed and, if necessary, authors may be invited to revise their manuscript. Authors are encouraged to list the names (addresses and telephone numbers) of up to five individuals outside their institution who are qualified to serve as referees for their paper. The referees selected will not necessarily be from the list suggested by the author.

### Types of contributions

The journal Optics Communications publishes short communications and full length articles in the field of optics and quantum electronics.

**Short communications** are brief reports of significant, original and timely research results that warrant rapid publication. The length of short communications is limited to six journal pages. Proofs will not be mailed to authors prior to publication unless specifically requested.

**Full length articles** are subject to the same criteria of significance and originality but give a more complete and detailed account of the research results. Proofs of all full length articles will be mailed to the corresponding author, who is requested to return the corrected version to the publisher within two days of receipt.

### Manuscript preparation

All manuscripts should be written in good English. The paper copies of the text should be prepared with double line spacing and wide margins, on numbered sheets. See notes opposite on electronic version of manuscripts.

**Structure.** Please adhere to the following order of presentation: Article title, Author(s), Affiliation(s), Abstract, classification codes (PACS and/or MSC) and keywords, Main text, Acknowledgements, Appendices, References, Figure captions, Tables.

**Corresponding author.** The name, complete postal address, telephone and Fax numbers and the E-mail address of the corresponding author should be given on the first page of the manuscript.

**PACS codes/keywords.** Please supply one to four classification codes (PACS and/or MSC) and 1–6 keywords of your own choice for indexing purposes.

**References.** References to other work should be consecutively numbered in the text using square brackets and listed by number in the Reference list. Please refer to a recent issue of the journal or to the more detailed instructions for examples.

### Illustrations

Illustrations should also be submitted in triplicate: one master set and two sets of copies. The *line drawings* in the master set should be original laser printer or plotter output or drawn in black india ink, with careful lettering, large

enough (3–5 mm) to remain legible after reduction for printing. The *photographs* should be originals, with somewhat more contrast than is required in the printed version. They should be unmounted unless part of a composite figure. Any scale markers should be inserted on the photograph itself, not drawn below it.

**Colour plates.** Figures may be published in colour, if this is judged essential by the editor. The publisher and the author will each bear part of the extra costs involved. Further information is available from the full length instructions.

### After acceptance

**Important.** When page proofs are made and sent out to authors, this is in order to check that no undetected errors have arisen in the typesetting (or file conversion) process. No changes in, or additions to, the edited manuscript will be accepted.

**Copyright transfer.** You will be asked to transfer copyright of the article to the publisher. This transfer will ensure the widest possible dissemination of information.

### Electronic manuscripts

The publisher welcomes the receipt of an electronic version of your accepted manuscript (preferably encoded in LaTeX). If you have not already supplied the final, revised version of your article (on diskette) to the Journal Editor, you are requested to send a file with the text of the accepted manuscript directly to the Publisher by e-mail or on diskette (allowed formats 3.5" or 5.25" MS-DOS, or 3.5" Macintosh) to the address given below. Please note that no deviations from the version accepted by the Editor of the journal are permissible without the prior and explicit approval by the Editor. Such changes should be clearly indicated on an accompanying printout of the file.

### Author benefits

**No page charges.** Publishing in Optics Communications is free.

**Free offprints.** The corresponding author will receive 50 offprints free of charge. An offprint order form will be supplied by the publisher for ordering any additional paid offprints.

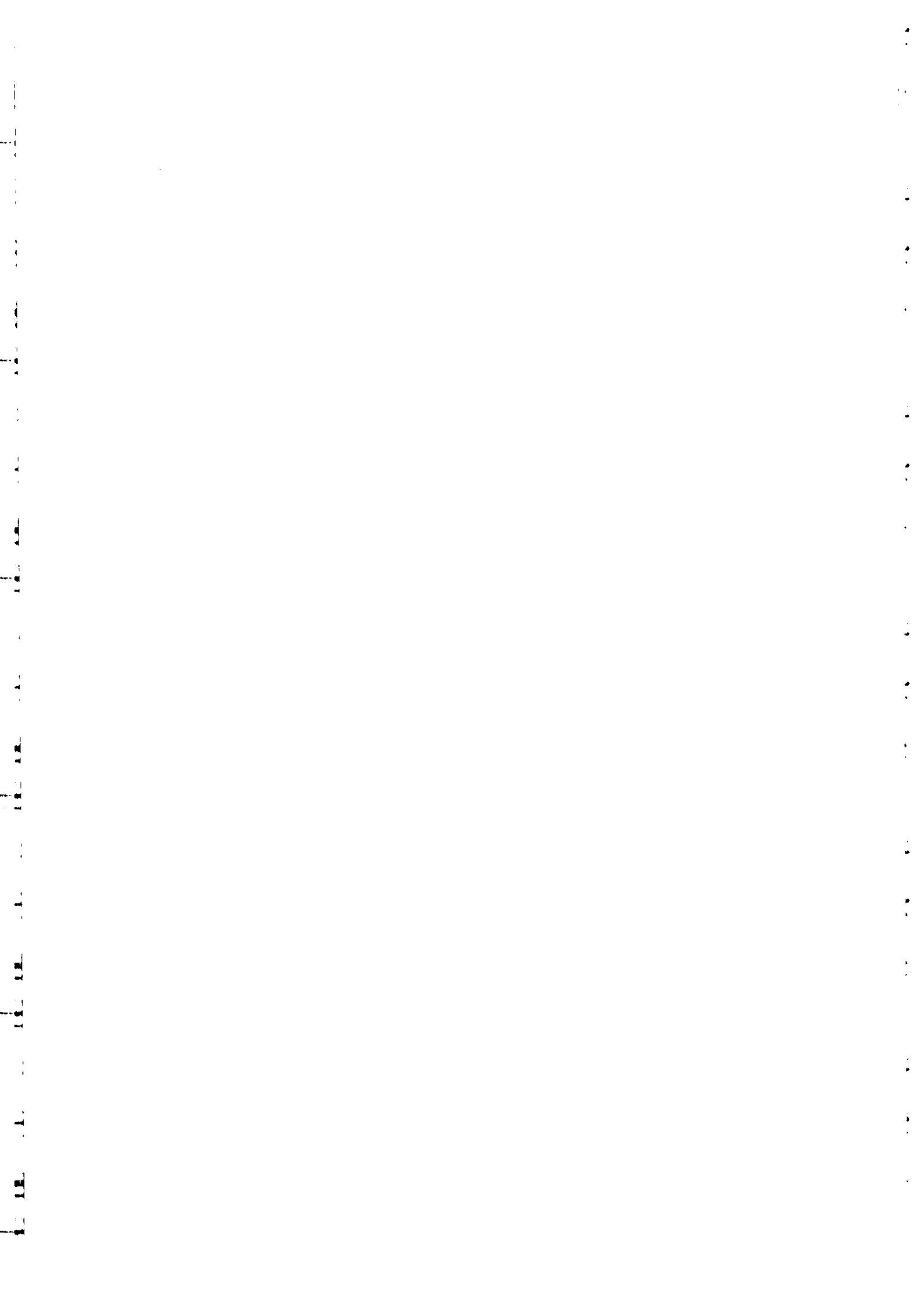
**CONTENTS-Alert.** Journal included in this free Elsevier's pre-publication contents alerting service (for information, please contact [C-ALERT.OPTICS@ELSEVIER.NL](mailto:C-ALERT.OPTICS@ELSEVIER.NL)).

**ContentsDirect.** Journal included in this free Elsevier's pre-publication contents alerting service (for information, please visit the Website <http://www.elsevier.nl/locate/ContentsDirect>).

**Discount.** Contributors to Elsevier Science journals are entitled to a 30% discount on all Elsevier Science books.

### Further information (after acceptance)

Elsevier Science B.V., Optics Communications  
Issue Management Physics and Astrophysics  
P.O. Box 2759, 1000 CT Amsterdam, The Netherlands  
Fax: +31 20 4852319  
E-mail: [PHYSDESK@ELSEVIER.NL](mailto:PHYSDESK@ELSEVIER.NL)





# Acousto-optic superlattice modulator using a fiber Bragg grating

P18

W. F. Liu

Optoelectronics Research Centre, University of Southampton, Southampton SO17 1BJ, UK

P. St. J. Russell

Optoelectronics Group, School of Physics, University of Bath, Bath BA2 7AY, UK

L. Dong

Optoelectronics Research Centre, University of Southampton, Southampton SO17 1BJ, UK

Received April 16, 1997

A modulator is reported in which an extensional acoustic wave is launched along a fiber Bragg grating. The acousto-optic superlattice effect causes an enhancement in reflectivity within a narrow spectral region on both sides of the Bragg wavelength. For a fixed acoustic propagation direction, the Doppler shift can be either positive or negative, depending on whether the wavelength of the incident light lies above or below the Bragg condition. The device can function as a Bragg cell and a tunable filter. © 1997 Optical Society of America

All-fiber acousto-optic devices have potential uses as frequency shifters, multiplexers, modulators, and tunable filters. The ease with which these devices can be spliced into systems, and the consequent low insertion loss, make them an attractive alternative to pigtailed bulk Bragg cells. Previous designs of intermodal coupler include dual-mode fibers supporting an acoustic flexural wave,<sup>1,2</sup> coupling between the polarization normal modes of a high-birefringence fiber by means of a torsional acoustic wave,<sup>3</sup> and a high-performance device based on a four-port fused-taper null coupler.<sup>4</sup> All these devices share the requirement that the acoustic wavelength must match the intermodal beat length,  $L_B = 2\pi/\Delta\beta$ , where  $\Delta\beta = |\beta_2 - \beta_1|$  and  $\beta_1$  and  $\beta_2$  are the propagation constants of the modes.

In this Letter we describe a modulator (briefly reported for the first time in Ref. 5) in which a fiber Bragg grating is excited by an axially propagating extensional acoustic wave. The underlying principle is acousto-optic superlattice modulation (AOSLM), first proposed in 1986.<sup>6,7</sup> In AOSLM the counterpropagating optical modes (the Bloch waves<sup>8</sup>) of the fine-pitch Bragg grating are coupled by a coarse-pitch acoustic wave, the superposition of the two forming a superlattice. Coupling is maximum when the inter-Bloch-wave beat period matches the acoustic wavelength.

The forward-traveling (group velocity in the +z direction) Bloch wave in a fiber Bragg grating can be closely approximated as a constant superposition of two coupled counterpropagating guided modes with wave vectors  $k$  in the form<sup>8</sup>

$$k = \{\pm K + \vartheta[1 - (2\kappa/\vartheta)^2]^{1/2}\}/2, \quad (1)$$

where  $K = 2\pi/\Lambda$  is the Bragg grating vector and  $\Lambda$  is its physical pitch. Coupling constant  $\kappa$  and dephasing parameter  $\vartheta$  are defined as  $\kappa = Mk_0/4$  and  $\vartheta = 2k_0 - K$ , where  $k_0 = \omega n_0/c$  is the average wave

vector in the Bragg grating,  $n_0$  is the modal phase index, and  $M$  is the modulation depth of the dielectric constant, i.e.,  $\epsilon_r = n_0^2(1 + M \cos Kz)$ . Reversing the sign of  $\vartheta$  in Eq. (1) yields the wave vectors of the complementary backward-traveling Bloch wave. The presence of two wave vectors in each Bloch wave, combined with their strong dispersion with frequency (forming a stop band in the range  $-2\kappa < \vartheta < 2\kappa$ ), yields three different acousto-optic resonance conditions as opposed to one in normal fiber. Two of these conditions are at approximately the usual Brillouin frequencies ( $\sim 10$  GHz at 1530 nm). The third, which concerns us in this Letter, is indicated on the  $\omega - k$  diagram in Fig. 1. This condition occurs between the two forward (and the two backward) wave vectors of the two

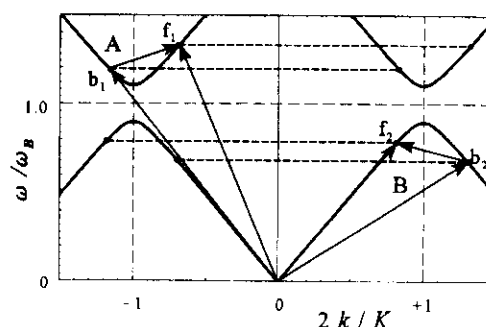


Fig. 1. Frequency wave-vector diagram for a Bragg grating. The group velocity is proportional to the slope of the curves. In case A, a forward-traveling acoustic wave  $[(\omega_s, k_s)]$  vector shown by the arrow from  $b_1$  to  $f_1$  couples a forward-traveling Bloch wave ( $f_1$ ) into a downshifted backward one ( $b_1$ ). In case B, forward Bloch wave  $f_2$  is coupled into anomalously downshifted backward Bloch wave  $b_2$  by backward-traveling acoustic wave. The thick horizontal dashed lines join the  $(\omega, k)$  points of the forward and backward fiber modes of each Bloch wave.

Bloch waves and has an associated frequency shift that can lie between 0 and several hundred megahertz (for clarity, acoustic frequency shift  $\omega_s$  is exaggerated in Fig. 1). Note that in one-dimensional photon-photon scattering the two-vector  $(\omega, k)$  must be conserved, i.e.,  $(\omega_{\text{out}}, k_{\text{out}}) - (\omega_{\text{in}}, k_{\text{in}}) = (\omega_s, k_s)$ , where the frequency components must all be positive (acoustic parameters have the subscript  $s$ ); we ensure this by choosing the input and output two-vectors so as to make  $\omega_{\text{out}} - \omega_{\text{in}} = \omega_s > 0$ . The group velocity of each Bloch mode is given by  $\partial\omega/\partial k = \pm(c/n_o)[1 - (2\kappa/\vartheta)^2]^{1/2}$ , which tends to zero at each stop-band edge and changes sign on opposite sides of the lines  $k = \pm K/2$ . An intriguing feature of superlattice coupling is that the direction of the Doppler shift can be reversed. On the upper stop-band branch, an acoustic wave traveling into the incident Bloch mode will produce a frequency-upshifted reflected Bloch mode. On the lower stop-band branch, however, the reflected mode will be anomalously frequency downshifted. As we show below, these predictions are confirmed by experiment.

An acoustic wave of average power  $P_s$  will produce a peak strain of  $s_o = [2P_s/(EA\nu_{gs})]^{1/2}$ , where  $E$  is Young's modulus,  $A$  is the fiber area, and  $\nu_{gs}$  is the acoustic group velocity. This strain field will sinusoidally modulate both the average index and the pitch of the grating. Close to the stop-band edges, where the group velocity is very small, both of these effects are significant. Further from the stop-band edges, however, pitch modulation dominates. Since the acoustic wave travels some  $10^5 \times$  more slowly than the light, we ignore its temporal dependence (while remembering the Doppler shift). For a strain field in the form  $s(z) = s_o \cos(k_s z)$ , the resulting relative dielectric constant  $\epsilon(z)$  is given by

$$\begin{aligned} \frac{\epsilon(z) - n_o^2}{Mn_o^2} &= \cos[Kz + a \sin(k_s z)] \\ &= J_0(a) \cos Kz + \sum_{n=1}^{\infty} J_n(a) [\cos(Kz + nk_s z) \\ &\quad + (-1)^n \cos(Kz - nk_s z)], \end{aligned} \quad (2)$$

where  $a = Ks_o/k_s$ . It is clear that a sequence of ghosts of the original fiber grating forms at spatial frequencies given by successive spatial sidebands of  $K$ . The amplitudes of these sidebands are given, for small argument  $|a| \ll 1$ , by  $J_n(a) \approx a^n/(2^n n!)$ . The AOSLM resonance occurs when the acoustic wave vector matches the wave-vector difference between two Bloch waves. This leads to the condition

$$\frac{c\Delta\lambda}{\lambda^2} \approx \Delta\nu = \frac{c}{2n_o} \left[ \left( \frac{f_s}{\nu_s} \right)^2 + \left( \frac{\kappa}{\pi} \right)^2 \right]^{1/2} \approx \frac{cf_s}{2n_o\nu_s}, \quad (3)$$

where  $f_s$  and  $\nu_s$  are the acoustic frequency and the phase velocity and  $\Delta\nu$  and  $\Delta\lambda$  are the optical frequency and wavelength shifts from the Bragg condition of the fiber grating. The approximate expression on the right-hand side of Eq. (3) is valid when the AOSLM condition occurs far from the Bragg condition. For bulk silica  $\nu_s$  is 5760 m/s, and given our experimental value of  $\kappa = 1.3/\text{mm}$ , Eq. (3) shows that AOSLM resonance will occur, e.g., at 2 nm from the Bragg wave-

length if the acoustic frequency is 15 MHz (NB:  $\nu_s$  falls when the acoustic wavelength is comparable with the fiber radius<sup>9</sup>). It can be shown that the coupling constant between the counterpropagating Bloch waves at the first sideband in Eq. (2) is given approximately by  $\kappa_1 = \kappa J_1(Ks_o/k_s) \approx \kappa Ks_o/(2k_s)$ . Figure 2 shows the experimental setup. The fiber grating was written with a phase mask in a boron-codoped germanosilicate fiber (N.A., 0.115; cutoff, 1300 nm). The UV source was an ArF excimer laser at 193 nm. The grating was 3 mm long, with a bandwidth of 0.7 nm, a Bragg wavelength of 1526.5 nm, and a coupling constant  $\kappa = 1.3/\text{mm}$ . A piezoelectric transducer, bonded to a silica horn and driven by a rf signal generator, was used as the source of acoustic waves. The diameter of the silica horn was tapered from 3 mm to 125  $\mu\text{m}$  over a distance of  $\sim 7$  cm. One end of the fiber grating was spliced directly to the horn. To test whether the light reflected from the grating is upshifted or downshifted, the light was mixed at a square-law detector with light frequency shifted in a conventional Bragg cell. We found that the interface loss between the transducer and the silica horn is a very important factor in obtaining efficient coupling of the longitudinal acoustic wave to the fiber grating. The light was detected at one of the output ports of 3-dB coupler FC2, with the remaining port being immersed in index-matching oil.

The reflectivity spectrum of the undisturbed Bragg grating and the spectrum of the enhancement in reflectivity due to the acoustic wave are plotted in Fig. 3. AOSLM is observed on both sides of the stop band. The acoustic frequency was 8.02 MHz, and the electrical drive power to the transducer was 350 mW. The wavelengths of AOSLM reflection were at 1525.3 nm on the short-wavelength side and 1527.6 nm on the long-wavelength side. The magnitude of the wave-

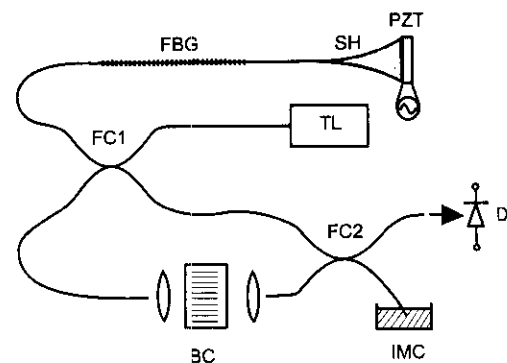


Fig. 2. Experimental setup for monitoring the response of AOSLM. Light from a tunable single-frequency diode laser (TL) is divided at a fused taper coupler (FC1), one half going to the fiber Bragg grating (FBG) and the other to a bulk Bragg cell (BC). The light reflected from the AOSLM is combined with the frequency-shifted light from the Bragg cell at a second coupler (FC2), and the mixed signal is detected at a square-law detector (D); the redundant light in the second arm of FC2 is eliminated in an index-matching cell (IMC). A piezoelectric transducer (PZT) and a fused-silica horn (SH) are used to excite the AOSLM.

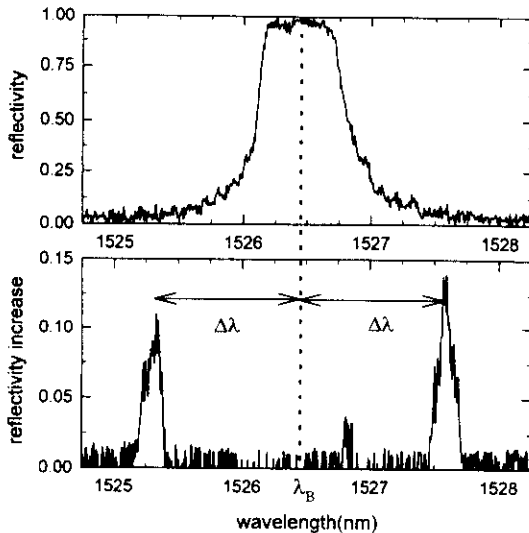


Fig. 3. Reflectivity spectrum of the undistributed Bragg grating (top) and the spectrum of the enhancement in reflectivity due to the acoustic wave (bottom).

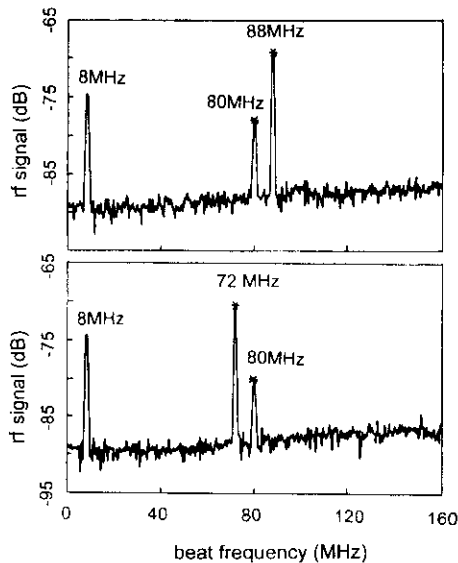


Fig. 4. RF spectra at the detector for sidelobes at  $\lambda > \lambda_B$  (top) and  $\lambda < \lambda_B$  (bottom). The peak at 8 MHz is caused by beating between the unshifted and the shifted Bragg grating reflections. The presence of a band on the low-frequency side of the 80-MHz reference signal indicates that the AOSLM signal is frequency upshifted.

length shift  $\Delta\lambda$  from Bragg wavelength is in each case approximately 1.15 nm, and the bandwidth of the AOSLM effect is  $\sim 0.2$  nm. In a series of measurements of wavelength shift  $\Delta\lambda$  as a function of acoustic frequency (4 to 15.2 MHz in steps of 1 MHz) the agreement between theory [Eq. (3)] and experiment was better than a few percent. The results showed

that AOSLM could be used to form a tunable filter with a tuning rate of 0.15 nm/MHz.

The results of the heterodyne experiment are shown in Fig. 4. A tunable single-frequency laser was used, and the acoustic drive frequency was 8 MHz. On the short-wavelength side of the Bragg condition the reflected light was frequency upshifted (conventional Doppler effect), whereas on the long-wavelength side it was downshifted (anomalous Doppler shift) as predicted by theory.

Since the spatial sidebands produced by the acoustic wave [Eq. (2)] can be regarded as weak ghosts of the strong permanent Bragg grating, the FWHM bandwidth of the AOSLM effect is expected to be that of a weak Bragg grating of the same length, namely,  $\Delta\lambda_{\text{opt}} = 1.39\lambda^2/(\pi Ln_o)$ , where  $L$  is the fiber length and the numerical factor relates to  $\text{sinc}^2(1.39) = 1/2$ . For  $L = 3$  mm at  $\lambda = 1530$  nm this equation predicts  $\Delta\lambda_{\text{opt}} = 0.23$  nm, which is in reasonable agreement with the experimental results.

For small acoustic powers, it can be shown that the efficiency of conversion  $\eta$  can be approximated by  $\eta \approx (\kappa_1 L)^2 = [\kappa L J_1(Ks_o/k_s)]^2$ . For the parameters in our experiment  $\eta \sim 15\%$ , and using the relationship given in the paragraph above Eq. (2) to relate acoustic power to  $s_o$ , it can be shown that of the 350-mW electrical drive power, only 57 mW is actually reaching the Bragg grating as acoustic power. Since the efficiency scales linearly with the power and as the square of length, there is clearly scope for improving the AOSLM efficiency by better acoustic transducer design, increasing the grating length, or using thinner fibers. Some advantages would result if the core was offset from the center of the fiber and flexural waves were used. Substantial improvements are expected with better acoustic transducer design, a longer fiber grating, and thinner fiber.

## References

1. B. Y. Kim, J. N. Blake, H. E. Engan, and H. J. Shaw, *Opt. Lett.* **11**, 389 (1986).
2. J. N. Blake, B. Y. Kim, H. E. Engan, and H. J. Shaw, *Opt. Lett.* **12**, 281 (1987).
3. M. Berwick, C. N. Pannell, P. St. J. Russell, and D. A. Jackson, *Electron. Lett.* **27**, 713 (1991).
4. T. A. Birks, S. G. Farwell, P. St. J. Russell, and C. N. Pannell, *Opt. Lett.* **19**, 1964 (1994); erratum, *Opt. Lett.* **21**, 231 (1996).
5. W. F. Liu, P. St. J. Russell, D. O. Culverhouse, and L. Reekie, in *Conference on Lasers and Electro-Optics*, Vol. 9 of 1996 OSA Technical Digest Series (Optical Society of America, Washington, D.C., 1996), pp. 243-244.
6. P. St. J. Russell, *Phys. Rev. Lett.* **56**, 596 (1986).
7. P. St. J. Russell, *J. Appl. Phys.* **59**, 3344 (1986).
8. P. St. J. Russell, *J. Mod. Opt.* **38**, 1599 (1991).
9. H. Kolsky, *Stress Waves in Solids* (Oxford U. Press, London, 1953), Chap III.



# Hamiltonian Optics of Nonuniform Photonic Crystals

P. St. J. Russell, *Member, OSA*, and T. A. Birks, *Member, OSA*

**Abstract**—The passage of light through slowly varying nonuniform photonic crystal structures is treated using Hamiltonian optics. The approach allows the inverse design of complex and highly compact optical elements as well as providing insight and an appealing physical picture. It can also be used to treat the trapping and deflection of light at distributed defects in one- and two-dimensional (2-D) crystals, and to study the frequency-dependent time delay in chirped one-dimensional (1-D) fiber Bragg gratings (FBG's).

**Index Terms**—Gratings, photonic crystals.

## I. INTRODUCTION

**D**EVICES that rely on the adiabatic evolution of modes through slowly varying media are widespread in optics. Examples include fused tapered fiber couplers (including "null" couplers [1]) and graded index fibers and lenses. In this paper, we treat the propagation of light in photonic crystals with slowly varying properties. The simplest example of a photonic crystal with properties that can be graded is the one-dimensional (1-D) fiber Bragg grating (FBG) [2], [3]. Nonuniform fiber gratings can be used to form dispersion compensators (with wavelength-dependent time delay) in telecommunications [4] and distributed feedback resonators for fiber lasers [5]. Experimental propagation in two-dimensional (2-D) planar waveguides with graded periodic properties has already been discussed qualitatively in the literature [6].

We develop a Hamiltonian optics approach, in which the group velocity (i.e., the ray path) of the light is tracked as a function of time through a nonuniform photonic crystal [3], [7]. For a given launch position, angle, and frequency, the rays travel along a path that adiabatically follows the group velocity of the local Bloch waves—the normal modes of the perfectly periodic photonic crystal medium. Provided that the changes do not occur too rapidly, there is continuous evolution of an individual Bloch wave without any coupling to other Bloch waves. The ray paths are determined by the requirement that the components of Bloch wavevector normal to the local gradient of the slowly varying dielectric function are locally conserved.

Why is it interesting to analyze this type of ray propagation? One reason is the drive toward highly compact components that can be integrated in large numbers onto one substrate, so as to be compatible with, for example, VLSI microelectronic chips and optical fibers. Photonic crystals offer opportunities for reducing (by orders of magnitude) the size of, e.g., couplers, beam splitters, filters, and lenses.

The strong spatial and temporal dispersion of Bloch wave rays makes 2-D photonic crystals of potential importance in components such as beam expanders and add-drop filters for wavelength division multiplexing (WDM) [8], [9]. The Fresnel diffraction rate can also be greatly increased, allowing free-space diffraction to take place over much shorter distances than in normal planar waveguides and therefore allowing compaction of beam-shaping processes. Refraction at interfaces can be controlled in sign and magnitude, and multiple refraction is possible when several Bloch waves are excited at an interface [6]. The optics of Bloch waves is complex and often counterintuitive, offering opportunities for the design of unique optical components. A major problem, however, is managing unwanted scattering at the interfaces between photonic crystal components and nonperiodic regions. One way to do this is to grade the strength of the photonic crystal in the transition regions so as to minimize unwanted effects. Grading the photonic crystal properties also provides, more generally, a means of managing—and making practical use of—the very strong dispersion they offer.

Optical resonators can be designed by grading the photonic crystal properties in a centrosymmetric manner so as to permit closed ray paths [7]. Although the classical nature of the Hamiltonian approach does not predict quantization of these paths, it does allow prediction of the frequency spacing between adjacent resonant modes—the free spectral range.

This paper is structured as follows. First we develop the general Hamiltonian approach (Section II), then we treat nonuniform FBG's (Section III) and nonuniform multiply periodic 2-D photonic crystals for WDM applications (Section IV). Last, we show how the inverse design problem can be solved in a particular case (Section V).

## II. HAMILTONIAN OPTICS

Hamiltonian optics is summarized by Arnaud in [10]. The approach can be applied where the dispersion relation in the homogeneous structure is known and where, in the inhomogeneous real structure, parameters like average index vary slowly in space. It is essentially an analytical method for stepping through a nonuniform structure, matching phase velocities normal to the gradient of the inhomogeneity at each step and propagating along the local group velocity to the next point. This process is described by solutions of Hamilton's equations, which take the general form

$$\frac{dx}{d\sigma} = \nabla_{\mathbf{k}} H, \quad \frac{dk}{d\sigma} = -\nabla H \quad (1)$$

where  $\mathbf{x} = \{x, y, z, -t\}$  is the four-vector for space-time,  $\mathbf{k} = \{k_x, k_y, k_z, \omega/c\}$  is the generalized wavevector,  $\sigma$  is an

Manuscript received August 19, 1999.

The authors are with the Optoelectronics Group, Department of Physics, University of Bath, Bath BA2 7AY U.K. (e-mail: p.s.j.russell@bath.ac.uk).

Publisher Item Identifier S 0733-8724(99)08944-6.

arbitrary parameter, and  $H(\mathbf{x}, \mathbf{k})$  is the Hamiltonian, which may be derived directly from the dispersion relation for the waves. Note that in general,  $\mathbf{k}$  depends on position. Equation (1) can be recast in a Newtonian way [6]

$$\frac{d^2 \mathbf{x}}{d\sigma^2} = [\nabla_{\mathbf{k}} \nabla_{\mathbf{k}} H]: (-\nabla H) = [1/m^*]: F \quad (2)$$

in which the reciprocal effective mass tensor  $[1/m^*]$  depends, in general, on position in real and reciprocal space. This equation shows that the gradient of the Hamiltonian is equivalent to a force  $F$  acting on the rays. The Hamiltonian itself may be written in a number of equivalent ways, subject to the requirement that a phase front is given by the equation  $H(\mathbf{x}, \mathbf{k}) = 0$ . In obtaining solutions to (1), it is important to distinguish total from partial differentiation.

### III. ONE-DIMENSIONAL PROPAGATION IN FIBER BRAGG GRATINGS

For a uniform weakly modulated 1-D grating,  $H$  takes the special form [11]

$$H = \omega n_o/c - K/2 - \sqrt{(k - K/2)^2 + \kappa^2} = 0 \quad (3)$$

where  $\kappa = k_o M/4$  is the grating coupling constant (the coupling rate per unit length between forward and backward waves),  $M$  is the modulation depth of the average dielectric constant,  $K = 2\pi/\Lambda$  is the grating vector ( $\Lambda$  being the grating pitch),  $k$  is the Bloch wavevector, and  $k_o = \omega n_o/c$  is the average wavevector in the grating. This Hamiltonian applies to any weak 1-D periodic structure whose effective index distribution is given by

$$n^2(z) = n_o^2(z)(1 + M(z) \cos [K(z)z]) \quad (4)$$

where all the parameters are assumed to vary very slowly over many periods. Note that the Bloch waves are the normal modes of electromagnetic propagation in periodic media [12], just as plane waves are the modes of isotropic space. Their group velocities describe the ray paths taken by the light, and permit accurate and detailed explanations for the complex and often beautiful phenomena that can be seen in, for example, periodic planar waveguides [13], [14].

The dispersion relation (3) can be written in a form that clearly illustrates the Newtonian nature of Bloch wave propagation. From (3), the group velocity may be found in the form

$$v_g = \frac{\partial \omega}{\partial k} = \frac{c}{n_o} \sqrt{1 - \left(\frac{2\kappa}{\vartheta}\right)^2} \quad (5)$$

where  $\vartheta = 2k_o - K$  is the parameter describing dephasing from the Bragg condition. Substituting this into (3), it is straightforward to show that

$$\left(\frac{2\kappa}{\vartheta}\right)^2 + \left(\frac{v_g n_o}{c}\right)^2 = 1 \quad (6)$$

PE + KE = TE

where the terms can be interpreted successively as potential energy, kinetic energy, and total energy. As the light propagates

through the nonuniform grating, it speeds up or slows down as the standing-wave component (stored or potential energy) falls or rises. At the stopband edges,  $\vartheta/2\kappa = \pm 1$  and  $v_g = 0$ , which implies that all the energy in the Bloch wave is stored in a standing wave, whose fringes turn out to have 100% visibility. Far away from the Bragg condition,  $|\vartheta/2\kappa| \ll 1$ , and the group velocity tends to the average value in the grating, i.e.,  $v_g \rightarrow c/n_o$ , as expected. This general trend is illustrated in Fig. 1, where the field microstructure of the Bloch waves is shown for different frequencies in the vicinity of the Bragg condition and as a function of depth into a uniform Bragg grating. The standing-wave component of the Bloch wave field stores energy, i.e., represents potential energy. It increases as the stopband edges are approached, i.e., as the group velocity tends to zero.

The solution of (1) for the Hamiltonian (3) is particularly simple. Without loss of generality, it is given by

$$\int_{z=z_o}^z \frac{n_o(z) dz}{\sqrt{1 - 1/\delta^2(z)}} = ct \quad (7)$$

where  $\delta = \vartheta(z)/2\kappa(z)$  and  $z = z_o$  at  $t = 0$ . This expression relates time and position in the grating, allowing for example direct calculation of the time taken for light of a given wavelength to be reflected out again from a chirped grating, or the time taken for a complete cycle of oscillation in an inhomogeneous distributed Bragg reflector resonator. The integral in (7) may be evaluated analytically in a number of special cases. Let us now look at three examples.

#### A. Linearly Chirped Grating

The first is a linearly chirped grating. In this case, taking  $\vartheta = \vartheta_o + az$ , the solution is

$$(\vartheta_o + az)^2 = (2\kappa)^2 + \left(-cta/n_o + \sqrt{\vartheta_o^2 - (2\kappa)^2}\right). \quad (8)$$

Time/space plots of this solution for different incident conditions are given in Fig. 2. The diagrams illustrate one of the limitations of the Hamiltonian approach as developed here; since it is classical, tunneling effects are not included. Photons of course do tunnel through the potential barrier created by the grating stopband; this process can be incorporated in the analysis by including an ad hoc tunneling probability near the stopband edge. The case treated in Fig. 2 corresponds to a pulse of bandwidth 10 GHz at 1.55  $\mu\text{m}$  broadened by 350 ps in a fiber link. Notice that as the wavelength varies, the position where the Bloch waves are turned around shifts as expected. The time taken for light at a given frequency to be reflected is

$$\tau = \frac{2n_o \sqrt{\vartheta_o^2 - (2\kappa)^2}}{ca}. \quad (9)$$

For a weak grating [ $\kappa = 0.05/\text{mm}$  and  $\vartheta_o = 0.15/\text{mm}$  for the first-reflected ray, Fig. 2(a)] at  $a = 0.018/\text{mm}^2$ , the compensation is very linear, although the reflection efficiency will be low (strong tunneling); the time-of-flight in the grating corresponds closely to a velocity of  $c/n_o$ , i.e.,  $(\vartheta_o/2\kappa)^2 \gg 1$ . For a strong grating [ $\kappa = 10/\text{mm}$  and  $\vartheta_o = 20.05/\text{mm}$  for the first-reflected ray, Fig. 2(b)] at  $a = 0.1/\text{mm}^2$ , on the other hand, the compensation is significantly nonlinear

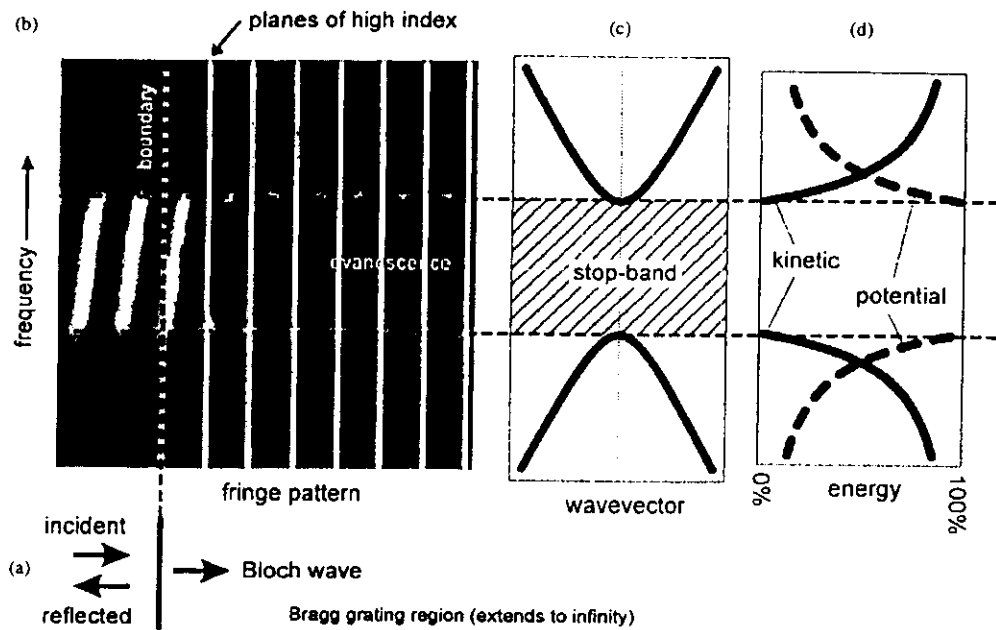


Fig. 1. (a) This figure illustrates the role of "kinetic" and "potential" energy in the propagation of Bloch waves in a uniform, semi-infinite, 1-D Bragg grating. (b) On the left is a density plot of the intensity microstructure of the light, plotted versus distance [horizontal, on a scale to match (a)] and frequency [vertical, on a scale to match (c) and (d)]. In (c) is the frequency-wavevector diagram for the grating, and in (d) is a plot of the kinetic and potential energies following (6). As the stopband edges are approached, the fringe visibility rises, increasing the stored potential energy in the Bloch waves. For a semi-infinite grating, the reflectivity is 100% across the entire stopband. Note that the relative phase between the fringes and the grating changes as the stopband is traversed.

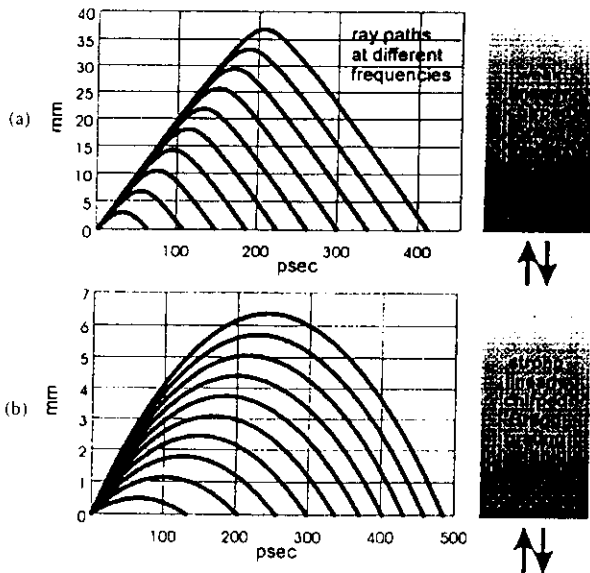


Fig. 2. Space-time plots of ray paths in (a) weak and (b) strong grating—see the text for parameter values. Each ray is spaced by 0.1 GHz from its neighbors. For the weaker grating, the velocity at input and exit is close to the average value  $c/n_o$ , and there will be only weak reflections at the sharp incident boundary, eliminating Fabry-Perot effects caused by Bloch wave reflections. For the stronger grating, the velocity is significantly less than  $c/n_o$ , and there will be strong reflections at the boundary and stronger Fabry-Perot effects.

frequencies in the pulse sees Bragg reflection until it is already well into the grating; this of course implies the need for a longer grating. Notice however that, due to the reduced group velocities near the stopband edge, the grating length required is seven times shorter than in the weak-grating case. The Hamiltonian solution as presented does not treat the reflection at the input boundary to the grating. This causes Fabry-Perot-like interference fringes in the cavity formed between itself and the turning point of the rays in the grating. If, however, the Bragg condition is not satisfied for any of the frequencies in the pulse in the initial few millimeters of the grating, the visibility of these fringes will be insignificant.

*B. Distributed Resonator*

In the second example, we consider a grating in which the coupling constant varies with position as

$$\kappa = \kappa_o \sqrt{1 + bz^2}. \tag{10}$$

The solution in this case takes the form

$$\begin{aligned} z &= (v_o/\gamma) \sin(\gamma t + \arcsin(\gamma z_o/v_o)) \\ \gamma &= 2c\kappa_o \sqrt{b}/(n_o v) \\ v_o &= (c/n_o) \sqrt{1 - (2\kappa_o/\vartheta)^2} \end{aligned} \tag{11}$$

where  $z_o$  is the initial position and  $v_o$  is the initial group velocity if  $z_o = 0$ . These solutions are plotted in Fig. 3 against  $t$  and  $v_o n_o/c$  for  $z_o = 0$  and  $b = 0.15/\text{mm}^2$ . As the launch velocity decreases (moving closer to the stopband edge), the amplitude (in millimeters) of the oscillation and the cavity round-trip time both decrease as expected. The absolute

(owing to the proximity of the strong stopband), although the efficiency will be much higher. This nonlinearity may be eliminated to a large degree by operating so that none of the

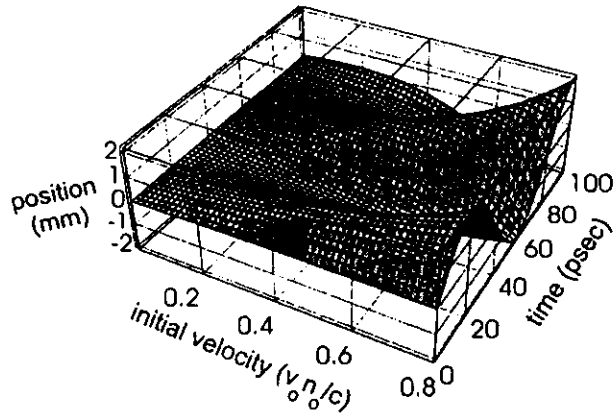


Fig. 3. Space-time surface for different values of initial Bloch wave velocity in a resonator formed by quadratically chirping the grating strength. For a given initial velocity, the graph gives the position of the light as a function of time. The faster waves—with higher initial kinetic energy—travel further up the "potential hill" than the slower waves, which therefore oscillate at higher frequencies, although with lower amplitudes.

quantized frequencies of oscillation will be determined by the usual requirement that the round-trip phase be a multiple of  $2\pi$ , a matter we do not address here. The free spectral range of the resonances, however, is determined by the group time delay around the cavity and is given by  $2\pi/\gamma$ .

### C. Coupled Resonators

In the third example, we consider two resonators side by side and sufficiently close to couple to each other. The grating coupling constant is assumed to vary as follows:

$$\kappa = \kappa_0 \sqrt{1 - 2bz^2 + d^2 z^4} \quad (12)$$

where  $b$  and  $d$  are constants with dimensions of  $m^{-2}$ . This yields two adjacent potential wells and leads to the solution

$$\frac{c(t - t_0)}{n_0} = \frac{-j}{dz_{c+}} F \left( j \arcsin \left( z \frac{dz_{c+}}{\sqrt{\delta_0^2 - 1}} \right) \middle| -1 - \frac{2bz_{c+}^2}{\delta_0^2 - 1} \right) \quad (13)$$

where  $F(\phi|m)$  is an incomplete elliptic integral of the first kind

$$z_{c\pm}^2 = \frac{b \pm \sqrt{b^2 + d^2(\delta_0^2 - 1)}}{d^2} \quad (14)$$

$$\delta_0^2 = \frac{\vartheta^2}{4\kappa_0^2}$$

and  $t_0$  is chosen so that  $z = z_0$  at  $t = t_0$ . The stopband edges occur at positions  $z = \pm z_{c\pm}$ , i.e., when  $\delta^2 = (\vartheta/2\kappa)^2 = 1$ . The Bloch waves are propagating at  $z = 0$  if  $\delta_0^2 > 1$ , and are evanescent if  $\delta_0^2 < 1$ . Thus, when  $\delta_0^2 > 1$ , there are two turning points for the rays, at  $z = \pm z_{c+}$ , and the rays cross from one resonator to the other. When  $\delta_0^2 < 1$ , there are two outer turning points at  $z = \pm z_{c+}$  and two inner ones at  $z = \pm z_{c-}$ . This means that the rays are trapped within one or the other of the resonators but cannot cross the intervening potential barrier. This behavior is illustrated in

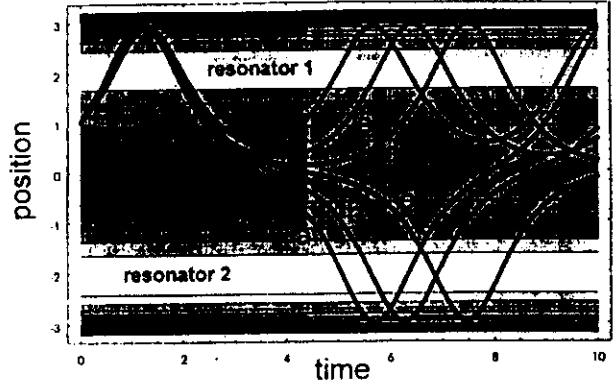


Fig. 4. Space-time paths in a pair of coupled cavities for (a)–(f):  $\delta_0 = 1.2, 1.1, 1.02, 0.98, 0.9$ , and  $0.6$ . Darker regions are at lower potential energy. As the frequency of the light changes, the ray paths oscillate more and more slowly to and fro between the potential wells, eventually being permanently trapped within the initial well, where they oscillate more and more quickly as  $\delta_0$  falls further.

Fig. 4 for  $z_0 = 1, b = 1, d = 0.48$ , and a range of values for  $\delta_0$ .

Note that tunneling can cause power to transfer between the two resonators even when  $\delta_0^2 < 1$ . This nonclassical behavior is not accounted for in the Hamiltonian approach.

### IV. MINIATURE WDM DEVICE USING SQUARE CRYSTAL

It is well known that light can spiral around in a waveguide consisting of a cylindrically symmetric bell-shaped refractive index distribution [15]. Because the transverse photon momentum is reduced by the presence of a large axial component of momentum, a weak potential well of higher refractive index is all that is needed to deflect the rays, as, for example, in the Ge-doped core of a silica optical fiber. Deflection of light is much easier in photonic crystals, since in the vicinity of the band edge, the photon momentum can be very small. Indeed, many important potential applications of photonic bandgap materials rely on the use of spatial inhomogeneities to provide intraband trapped states. We showed in [7] that centrosymmetric force fields, created by varying the crystal properties in a cylindrically symmetric manner, can be used to create resonators. In this section, we give results on the wavelength-dependent properties of such photonic crystals with square lattices.

Close to the band edge of a square photonic crystal lattice, i.e., in the vicinity of the high-symmetry corners of the Brillouin zone at fixed optical frequency,  $H$  can be chosen in the approximate form [7]

$$H^2 = \vartheta^2/4 - \delta^2 - 4\kappa^2 = 0 \quad (15)$$

where  $\kappa$  is related to the strength of index modulation. The parameter describing dephasing from the 2-D Bragg condition is

$$\vartheta = \left( \frac{2\omega n_0}{c} - K\sqrt{2} \right) \quad (16)$$

and the wavevector  $\delta = (\delta_x, \delta_y)$  is measured from the corners of the square Brillouin zones; it describes circles centered at



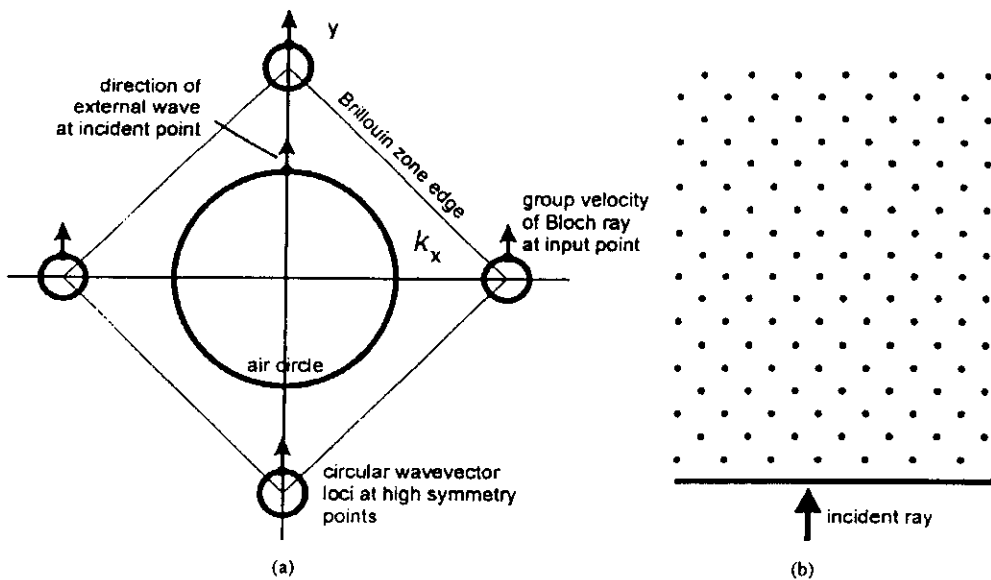


Fig. 5. (a) Reciprocal space diagrams for a square photonic crystal near a band edge. The loci of allowed wavevectors lie on circles centered at the high-symmetry points. The diameter of these circles varies as the ray point moves away from the center of symmetry. An external wave, incident from an isotropic medium, has a wavevector that lies on a circle centered at the origin of reciprocal space. The initial Bloch wave rays in the crystal point normal to the small circles. (b) The orientation of the square lattice relative to the input boundary, the incident ray direction being marked in.

the high-symmetry points (see Fig. 5). The reciprocal lattice vector is  $K = 2\pi/\Lambda$ , where  $\Lambda$  is the lattice spacing. For a central force field,  $H$  depends only on distance  $r$  from an origin and (2) may be re-expressed in the form

$$\frac{d^2\mathbf{r}}{d\sigma^2} = 2 \frac{\partial H}{\partial \mathbf{r}} \quad (17)$$

where  $\mathbf{r}$  is the position vector in two dimensions. If necessary, the parameter  $\sigma$  can be related to real time  $t$  by the time component of the four-vector equations (1)

$$c(t - t_0) = - \int_{\sigma=\sigma_0}^{\sigma} (2\omega n_o/c - K\sqrt{2}) n_o d\sigma \quad (18)$$

where  $n_o$  and  $K$  depend in general on position (and hence on  $\sigma$ ) as given by solutions of (17). If only the ray paths are sought, the exact scaling of  $\sigma$  is not important; however, (18) must be used if position as a function of time is required—such as when calculating the free spectral range of a cavity. The full analysis is given in [7].

To illustrate the wavelength-dependent properties of this crystal in a particular case, we choose a structure in which the coupling constant  $\kappa$  is radially dependent,  $K$  and  $\sigma$  being kept constant

$$\kappa^2 = (\kappa_o^2 + \kappa_1^2) - \kappa_1^2 r_o/r \quad (19)$$

where  $\kappa_o$  is the value of the coupling constant at  $r = r_o$  and  $\kappa_1$  is a constant describing the strength of the variation in crystal properties with position. For incidence from an isotropic external medium, the crystal being oriented as shown in Fig. 5, the initial Bloch wave rays point normal to the input surface. As illustrated in Fig. 6, the incident point is at  $r = r_o$ , directly to the right of the center of the force field, i.e., at

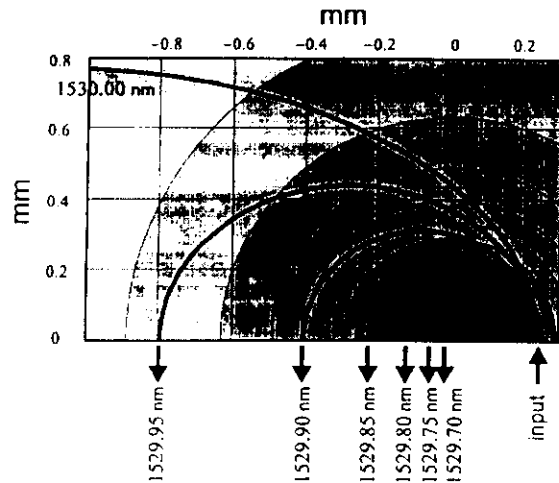


Fig. 6. Calculated ray paths for different wavelengths, each incident normal to the boundary. Notice the large change in output position for only 50-nm changes in wavelength. See text for more details. The center of symmetry of the variation in crystal strength is at the origin. Note that the shading saturates to a uniform shade in the center where the potential increases very rapidly toward  $\pm\infty$  as  $r \rightarrow 0$ ; darker regions are at a lower potential energy.

$\theta = 0$ . It may be shown that the ray paths within the crystal take the form

$$r(\theta) = r_o / (q + (1 - q) \cos \theta) \quad (20)$$

where

$$q = \frac{(\kappa_1/\kappa_o)^2/2}{(\vartheta/4\kappa_o)^2 - 1} \quad (21)$$

For  $r_o = 242 \mu\text{m}$ , a grating pitch  $\Lambda = 628 \text{ nm}$ , an average index  $n_o = 1.697$ , a grating constant  $\kappa_o = 49.6 \text{ mm}^{-1}$ ,  $\kappa_1/\kappa_o = 0.18$  and operating at a wavelength in the vicinity

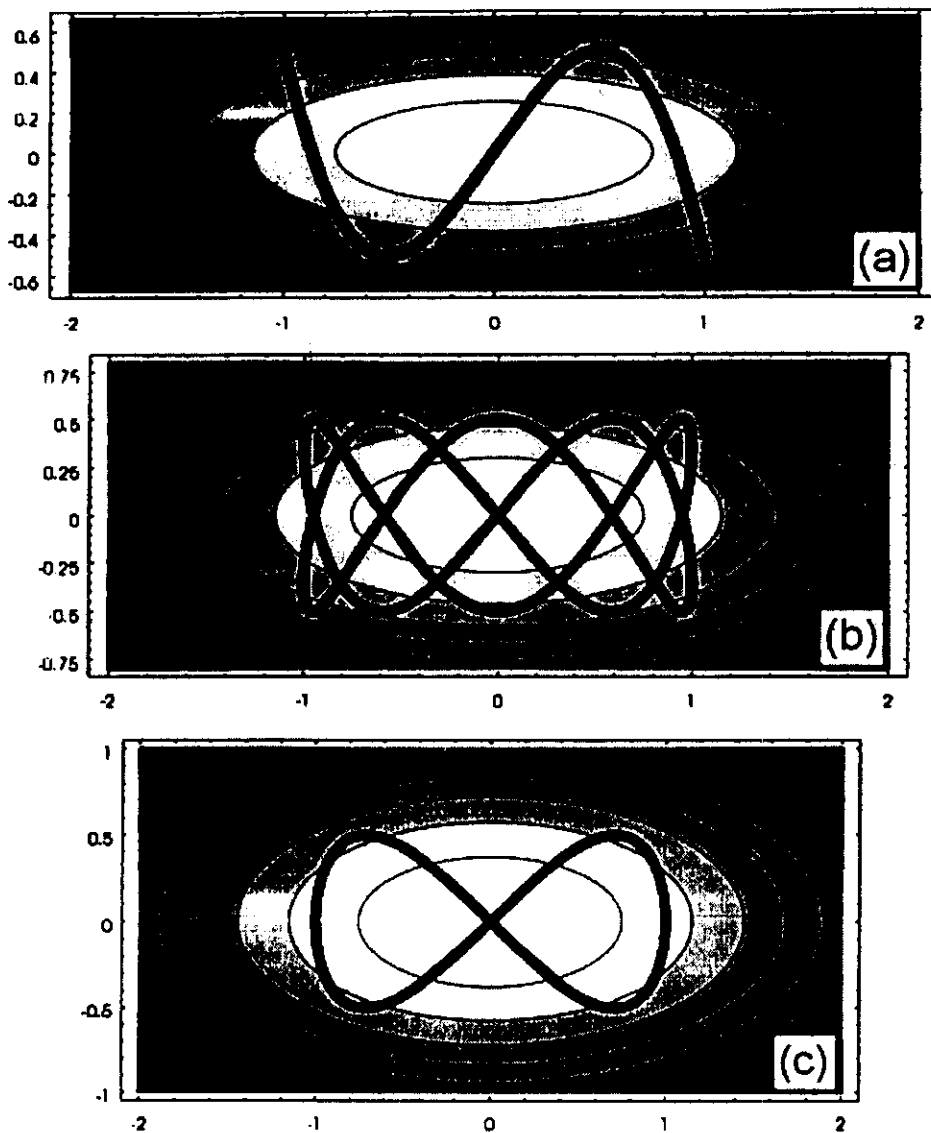


Fig. 7. Lissajous ray paths in nonuniform photonic crystal specifically designed, using inverse Hamiltonian techniques, to support them. Darker regions are at higher potential energy. The parameter  $a$  is (a) 3, (b) 2.5, and (c) 2. In case (a), the ray paths turn around abruptly because the band edge is encountered in a region where the group velocity has no transverse component to the gradient of the Hamiltonian. See text for more details. Note that chaotic ray paths will occur if the ratio of horizontal and vertical Lissajous frequencies is noncommensurate.

of 1530 nm, the ray paths in Fig. 6 are obtained. Notice the high sensitivity of output ray position to wavelength—a 0.05-nm change in wavelength shifts the output rays by a large fraction of a millimeter. The behavior is reminiscent of that seen in [9]. The parameter values used are adapted from those already achieved experimentally [13], [14] in etched Ta<sub>2</sub>O<sub>5</sub> waveguides on borosilicate glass, taking account of a change in wavelength from 633 to 1530 nm.

V. INVERSE PROBLEMS

The Hamiltonian approach is convenient for solving inverse problems, i.e., design problems where one seeks the correct distribution of photonic crystal properties that will yield specified ray path dispersion. This would allow precise design of,

for example, time delay as a function of frequency in a FBG. As an example of this, we choose Lissajous curves in the form

$$x(t) = x_o \sin[\Omega t], \quad y(t) = y_o \sin[a\Omega t] \quad (22)$$

where  $a$  is a number and  $\Omega$  is an angular frequency. The curves described by these formulas are chaotic if  $a$  is irrational. The question is: How do we design a photonic crystal that supports ray paths described by (22)? Taking the Hamiltonian for a square lattice near a band edge (at the high-symmetry point) in the form of (15), and applying Hamilton's equations (1), it is straightforward to show that the ray path (22) is obtained for

$$\kappa^2(x, y) = \left(\frac{\vartheta_o \Omega}{2}\right)^2 (a^2 y^2 + x^2) + \text{constant} \quad (23)$$

where  $\vartheta_o$  is the value of dephasing specified in the design.

Pictures illustrating the ray paths for different values of  $a$ , superimposed on contour plots of the function (23), are given in Fig. 7.

## VI. CONCLUSION

In conclusion, the Hamiltonian approach outlined in this paper provides an elegant viewpoint from which to analyze and understand the behavior of light in spatially inhomogeneous photonic crystals. Its limitations are that the properties must vary slowly over many lattice periods, that tunneling (not a classical concept) cannot be treated easily, and that quantization of closed orbits in resonators is not predicted. The free spectral range between adjacent resonances can, however, be obtained straightforwardly from the path integral of the reciprocal group velocity

$$\nu_{fsr} = \left( \oint_{\text{path}} dl/v_g \right)^{-1}. \quad (24)$$

More complicated spatial inhomogeneities can be treated by numerical integration of (1), and three-dimensional (3-D) photonic crystals can be straightforwardly analyzed. Solutions to the inverse problem allow complex WDM, resonator or lens-like functions to be designed into a photonic crystal. Time-varying photonic crystal properties can also be treated, which could lead to novel electro-optic modulator designs. Last, it is perhaps worth emphasizing that the ray paths in inhomogeneous photonic crystals are much more sensitive to wavelength than equivalent ray paths in traditional graded-index media. This permits increased functionality, applicability, and design freedom.

## REFERENCES

- [1] T. A. Birks, D. O. Culverhouse, and P. St. J. Russell, "The acousto-optic effect in single mode fiber tapers and couplers," *J. Lightwave Technol.*, vol. 14, pp. 2519–2529, 1996.
- [2] P. St. J. Russell and J.-L. Archambault, "Fiber gratings," book chapter in *Optical Fiber Sensors Vol. III: Components & Sub-Systems*, B. Culshaw and J. Dakin, Eds. Norwood, MA: Artech House, 1996, pp. 9–67.

- [3] P. St. J. Russell and T. A. Birks, "A Hamiltonian approach to propagation in chirped and nonuniform Bragg gratings structures," in *Proc. Topical Meeting Photosensitivity and Quadratic Nonlinearity in Glass Waveguides (PQNGW'95)*, Portland, OR, 1995, paper PMD2-1.
- [4] J. Lauzon, S. Thibault, J. Martin, and F. Ouellette, "Implementation and characterization of fiber Bragg gratings linearly chirped by a temperature gradient," *Opt. Lett.*, vol. 19, pp. 2027–2029, 1994.
- [5] J. T. Kringlebotn, J.-L. Archambault, L. Reekie, and D. N. Payne, "Er<sup>3+</sup>:Yb<sup>3+</sup> co-doped fiber distributed feedback laser," *Opt. Lett.*, vol. 24, pp. 2101–2103, 1994.
- [6] P. St. J. Russell, T. A. Birks, and F. D. Lloyd-Lucas, "Photonic Bloch waves and photonic band gaps," in *Confined Electrons and Photons: New Physics and Applications*, E. Burstein and C. Weisbuch, Eds. New York: Plenum, 1995.
- [7] P. St. J. Russell and T. A. Birks, "Bloch wave optics in photonic crystals: Physics and applications," in *Photonic Band Gap Materials*, C. M. Soukoulis, Ed. Norwell, MA: Kluwer, 1996, pp. 71–91.
- [8] P. St. J. Russell, "Novel thick-grating beam-squeezing device in Ta<sub>2</sub>O<sub>5</sub> corrugated planar waveguide," *Electron. Lett.*, vol. 20, pp. 72–73, 1984.
- [9] H. Kosaka, T. Kawashima, A. Tomita, M. Notomi, T. Tamamura, T. Sato, and S. Kawakami, "Superprism phenomena in photonic crystals," *Phys. Rev. B*, vol. 58, pp. 10096–10099, 1998.
- [10] J. A. Arnaud, *Beam and Fiber Optics*. New York/San Francisco/London: Academic, 1976.
- [11] P. St. J. Russell, "Bloch wave analysis of dispersion and pulse propagation in pure distributed feedback structures," *J. Mod. Opt.*, vol. 38, pp. 1599–1619, 1991; Erratum, J. Capmany and P. St. J. Russell, *J. Mod. Opt.*, vol. 41, pp. 163–164, 1994.
- [12] ———, "Optics of Floquet-Bloch waves in dielectric gratings," *Appl. Phys.*, vol. B39, pp. 213–246, 1986.
- [13] ———, "Interference of integrated Floquet-Bloch waves," *Phys. Rev.*, vol. A33, pp. 3232–3242, 1986.
- [14] R. Zengerle, "Light propagation in single and doubly periodic planar waveguides," *J. Mod. Opt.*, vol. 34, pp. 1589–1617, 1987.
- [15] A. W. Snyder and J. D. Love, *Optical Waveguide Theory*. London, U.K.: Chapman and Hall, 1983, p. 37.

P. St. J. Russell, photograph and biography not available at the time of publication.

T. A. Birks, photograph and biography not available at the time of publication.

